Transient and Long-Term Behaviour of the World Ocean under Global Warming

By

DAOHUA (DAVE) BI

Submitted in fulfilment of the requirement
for the degree of
Doctor of Philosophy

Antarctic CRC and IASOS
University of Tasmania

March, 2002

Declaration

I hereby declare that this thesis contains no material which has been accepted for the award of a degree or diploma by any tertiary institution. To the best of my knowledge and belief, this thesis is solely the work of the author, and contains no material previously published or written by another person except where due acknowledgement and reference are made in the text.

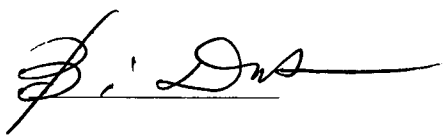

Daohua (Dave) Bi

Authority of Access

This thesis may be made available for loan and limited copying in accordance with the Copyright Act 1968.

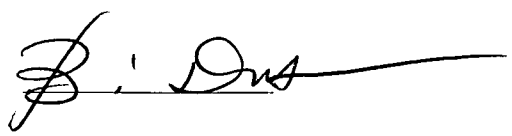

Daohua (Dave) Bi

Acknowledgements

This thesis has been supported by an Overseas Postgraduate Research Scholarship/Australian Postgraduate Award and an Antarctic CRC Scholarship.

Sincere thanks go to Professor Bill Budd (supervisor, Antarctic CRC), Drs. Tony Hirst (research supervisor, CSIRO Atmospheric Research) and Xingren Wu (associate supervisor, Antarctic CRC/Antarctic Division) for their excellent supervision. It is their deep insight and enthusiasm for the project, their lasting encouragement, strong support and assistance throughout the course of my PhD candidature that greatly aided in the progress and completion of this work.

I have highly appreciated discussions and advice from Drs. Wenju Cai, Siobhan O'Farrell, Yingping Wang, Ian Smith, Hal Gordon, Peter Whetton, Peter Bains, Steve Wilson, Mr. Mark Collier (CSIRO Atmospheric Research), Dr. Ian Simmonds (University of Melbourne) and Dr. John Church (CSIRO Marine Research) on various matters related to my research.

I thank the CSIRO Atmosphere Research Climate Impact Program, especially the program leader Dr. Barrie Hunt and the Ocean Modelling Group for providing me with a 'long-term' office and access to all facilities at the CSIRO Atmosphere Research.

Long integrations of this work have been conducted on supercomputers NEC-SX4 at the High Performance Computing and Communications Centre (HPCCC), Bureau of Meteorology/CSIRO, and Cray-J90 at the University of Tasmania. Help and assistance from staffs of these computing centres are also sincerely acknowledged.

My family has been a constant source of motivation towards my work. I thank my wife Jingxi Wu and our daughter Cathy Bo Bi for their love, support and patience.

Finally I would like to say THANKYOU to my father who has given me the strongest and the most persistent support all the time!

Abstract

The thermohaline circulation (THC) of the oceans plays a crucial role in adjusting the global thermal and hydrological budget in the climate system. Knowledge about its stability and change is very important for understanding the evolution of past climates and assessing possible climate changes in the future. In this study, we investigate the transient and long-term behaviour of the THC, particularly the Southern Ocean overturning in the CSIRO climate model, under increasing atmospheric greenhouse gases (as equivalent CO_2, referred to simply as CO_2) following the IPCC/IS92a scenario to stabilisation at three times preindustrial CO_2 ($3\times CO_2$) then continuing at that level of stabilisation.

Firstly the CSIRO ocean model is further developed by modifying the surface boundary forcing, for the purpose of ensuring a stable and realistic ocean climate to be used as the initial condition of the ocean for coupled model climate change studies. The new formulation leads to a significantly improved spinup solution and coupled control climate of the ocean. The world ocean water mass properties, in particular the Southern Ocean stratification, the THC, and the Antarctic Circumpolar Current (ACC) are all in broad agreement with observations.

In the following global warming experiment, pronounced changes of the global THC occur during the CO_2 increase period: the North Atlantic Deep Water Formation (NADWF) weakens rapidly and the Antarctic Bottom Water Formation (AABWF) collapses completely before CO_2 triples. During the subsequent period of 1100 years with stabilised $3\times CO_2$, the NADWF intensity shows a tendency to recover gradually in the upper part of the ocean but the AABWF shows no sign of returning and the residual deep overturning dies away. Also evident is the change of ACC transport under CO_2 forcing: it increases along with the CO_2 increase and keeps increasing steadily for a few centuries after CO_2 tripling. While both the surface freshening and heating from above are responsible for the weakening of NADWF, the surface freshening around Antarctica, including the enhancement of precipitation over evaporation (P - E), runoff from continents and reduction in the sea ice

formation and outflux, suppresses the deep convection off Antarctica and causes the shutdown of AABWF. The strengthening of the ACC transport is attributable to the enhanced meridional density contrast across the ACC due to the uneven warming in the Southern Ocean, both at the surface and in the interior. This change in density structure leads to an acceleration in the upper layer currents which outweighs the deceleration in the mid-depth layer caused by the weakening and shutoff of the AABWF.

Using the Bryan (1984) technique to accelerate the convergence of the deep ocean towards equilibrium under the $3\times CO_2$ condition, it is found that the global THC eventually reaches a near-stable state in which the NADWF is fully recovered, the AABWF is also partly re-established and deep ocean ventilation is activated again. The recovery of the THC is attributed to the slow but persistent warming in the deep ocean which gradually destabilizes the water column. After thousands of years, a stratification structure close to the initial state becomes re-built in the high latitude Southern Ocean, which allows deep convection and hence overturning off Antarctica to occur, bringing the system into a new regime. However, this regime needs some more time to further adjust and settle down to a more stable and slightly different normal mode solution. This is verified by an extension to the accelerated run for 500 years with the acceleration switched off. This result shows the development of a possible new quasi-equilibrium for the ocean under long-term global warming induced by the anthropogenic CO_2 increase.

Comparison has been made with the results from an earlier version of the coupled model which has a clearly different initial climate for the ocean. We conclude that, for the CSIRO coupled model (mark2), the oceanic response to global warming is not strongly dependent on the basic state of the ocean. However, some differences in the oceanic behaviour under CO_2 forcing between the two versions are of scientific interest and have been discussed in detail.

List of Acronyms:

AABWF	Antarctic Bottom Water Formation
ACC	Antarctic Circumpolar Current
AGCM	Atmospheric General Circulation Model
HB	Horizontal Background diffusion (model version)
H-R	Hellerman and Rosenstein (1983)
GM	Gent and McWilliam scheme (model version)
NADWF	North Atlantic Deep Water Formation
NCEP	National Center for Environmental Prediction
NH/SH	Northern/Southern Hemisphere
OGCM	Ocean General Circulation Model
P-E	Precipitation minus Evaporation
SSD	Sea Surface Density
SSS	Sea Surface Salinity
SST	Sea Surface Temperature
THC	ThermoHaline Circulation

Nomenclature of the runs [1]:

GM2/	Ocean spinup with GM verison No.2
GM3	Ocean spinup with GM verison No.3
CGM2	Coupled Control run with GM2 ocean
CGM3	Coupled Control run with GM3 ocean
TGM2	Coupled Transient run with GM2 ocean
TGM3	Coupled Transient run with GM3 ocean
ATGM2	Accelerated TGM2 run
ATGM3	Accelerated TGM3 run

[1]The author states that the nomenclature of the experiments and/or model versions listed here is not 'official'. It is used for the purpose of this thesis only.

Contents

List of Tables

List of Figures

Chapter 1

Introduction

The Earth's climate changes. It is vastly different from what is was 100 million years ago when the high latitudes were heavily covered by tropical plants and most of the continents were playgrounds for the dinosaurs. During the last million years the Earth has experienced repeated extensive glaciation in the Northern Hemisphere (NH). Today's climate is largely different from what it was 18000 years ago when the last glaciation reached its peak and the NH was covered with much more ice sheets. Even over the past 2000 years the Earth has seen a variation in the global temperature up to 1 °C on either side of the present value. In the more recent past, say, since the late 19th century, the global average surface temperature has increased by 0.6±0.2 °C and it is very likely that the 1990s was the warmest decade and 1998 the warmest year in the instrumental record since 1861, as suggested by observations (IPCC 2001). Changes or variations of climate in the long history of the Earth have been largely attributable to the evolution of the Earth's geography, to fluctuations or periodicities in the Earth's orbit, and to long-term changes in the composition of the atmosphere.

In the future the global climate will surely continue to change. Apart from the natural causes, a new, *external*, driving force has been introduced since the Industrial Revolution and will probably play a much more important role in causing the climate change. This force is human activities. Human beings have realized the potential

effect of their own activities on the climate since the early 19th century. By the end of the 19th century and the early 20th century, it had been discovered that the amount of CO_2 in the atmosphere affected the global temperature through the greenhouse effect and that human activities were increasing the atmospheric CO_2. Since the late 1960s, climate change induced by atmospheric CO_2 (which lately has been broadened to include the effect of other greenhouse gases and referred to as equivalent CO_2 or simply CO_2) has drawn more and more attention and has been investigated extensively by various means. One of the many objectives of these studies is to answer the question as to how and where the global climate evolves under the increasing CO_2 condition. This is also the main target of the present study, which focuses on oceanic response to the long-term CO_2 forcing.

1.1 Ocean Circulation and the Climate System

The world ocean covers 71% of the surface area of the globe. It is evidently the dominant primary source of water supplies for the Earth's ecosystem. Meanwhile, its huge amount of water mass makes it an immense reservoir of heat for the Earth's climate system. This heat storage capacity, working as a giant flywheel to the climate system, acts to maintain, or say stabilize the state of the global climate: moderating change but prolonging it once the change commences. Net thermal energy obtained by the ocean in tropical latitudes is transported to the polar latitudes, where part of the heat is released back into the atmosphere and part is transported into the deep ocean. In this process, ocean circulations, especially the meridional thermohaline circulations (THC) play a crucial role.

The THC, driven by density differentials in the ocean, acts as a giant conveyer belt (Broecker 1987, 1991), efficiently transporting heat and salt great distances between basins and globally. In the Atlantic Ocean, the THC is manifested as warm, saline surface water transported by the Gulf Stream and the North Atlantic current system from the tropical region towards high latitudes. Therefore the sea surface

temperature (SST) and sea surface salinity (SSS) in the northern North Atlantic are considerably higher than that of the northern North Pacific at comparable latitudes where no such strong THC is evident. When the high latitude North Atlantic saline surface water cools, particularly in late winter, it becomes denser, destabilizing the water column and triggering deep convection and hence the overturning. The sinking branch of the overturning circulation brings the surface salty water into the deep layer of the occean, thereby producing the North Atlantic Deep Water (NADW). This process is the so-called NADW formation (NADWF). The formed NADW can be carried (and distributed) by the southward return flow at depth to other places and eventually penetrates the Southern Ocean until it is blocked by a zonal 'wall' in the Circumpolar Ocean, i.e., the Antarctic Circumpolar Current (ACC). Only a minor part of this salty water can penetrate through the ACC and reach high latitude regions off Antarctica. Most of this water joins the ACC, flowing around Antarctica and ventilating the Indian and Pacific Oceans, mainly through large-scale diffusion and meso-scale eddies. For compensation, upwelling occurs in the North Pacific, and a shallow return current is thus formed, which flows into the Indian Ocean (through the Indonesian passages) and reaches the region off South Africa. There it joins the western boundary flow, i.e., the Agulhas Current. While most of the warm water transported from the Indian Ocean is swept into the confluence of the ACC and turns east, some is spun off into eddies that enter the Atlantic and then flows northwards into the North Atlantic. The above process roughly features a closed large-scale meridional cell originating from the North Atlantic, which dominates the world ocean meridional heat transport.

At the other side of the ACC, i.e., high latitude Southern Ocean off Antarctica, another branch of the THC system is in operation. In the Weddell and Ross Seas, for example, when sea ice forms or grows in winter, brine is rejected into the underlying surface water, and the shallow water columns on the continental shelves lose buoyancy so rapidly that they plummet to the bottom of the shelves and then keep sinking (along the continental rise) down the bottom of the ocean, forming the Antarctic Bottom Water (AABW). This AABW formation (AABWF) process involves deep

convection and overturning circulation off Antarctica, and the so formed AABW, which has the highest density in the world ocean (except for the Arctic Ocean), is spread northward by the deep meridional overturning cell and ventilates the bottom ocean of all basins with cold and relatively low salinity water.

Since the THC, especially the NADWF and AABWF are determined by the vertical density contrast between the surface and the deep depths, perturbations to the sea surface thermohaline conditions in the North Atlantic and the high latitude Southern Ocean will naturally affect their intensities and even the basic pattern of the world ocean circulation. On the other hand, the THC change causes new distributions of heat and salt in the ocean, and the associated variation in the surface state such as the SST pattern changes the ocean-atmosphere heat and moisture exchange and balance, thereby changing the Earth's climate. An example that associates the oceanic state with climate changes may be the well known Younger Dryas event (Broecker et al. 1985; Boyle and Keigwin 1987; Keigwin and Lehman 1994; Sarnthein et al. 1994), which occurred during the last deglacial periods, about 13000 years ago. Isotopic analysis of Greenland ice cores (Grootes et al. 1993) suggests that large and rapid changes of climate occurred frequently during the last glacial and deglacial periods. Characterized by very low surface temperature in the NH, the Younger Dryas lasted only several hundred years and ended abruptly. Broecker et al. (1985) speculated that the abrupt climate change in the Younger Dryas period, as well as other events, resulted from the abrupt shift of the THC, i.e., North Atlantic overturning from one mode of operation to another. Furthermore, they suggested that meltwater from the continental ice sheets caused the capping of the oceanic surface by relatively fresh water in high latitudes and thus led to the rapid weakening of THC and the sudden change of climate, i.e., cooling. In addition to that of the Younger Dryas event, another mode of the oceanic circulation and climate significantly different from the present state is found in the last glacial maximum period, which is characterized by not only the absence of lower deep water production and enhanced northward penetration of the AABW, but also significant ventilation of the upper deep water, as suggested by paleoceanographic data (Boyle

and Keigwin 1987; Duplessy et al. 1988).

1.2 Stability of the Thermohaline Circulation

The above mentioned paleoclimatic evidence has raised the possibility of multiple equilibria of ocean circulation and rapid transition between different modes under certain external forcing, especially anomalies in the hydrological cycle over the North Atlantic. This, together with the importance of the THC in maintaining the global climate, has inspired a large number of studies on the stability of THC, in particular, the NADWF.

Most of these studies have been based on ocean-only models, with a focus on the sensitivity of NADWF to high latitude fresh water flux perturbations caused by local changes such as the Great Salinity Anomaly (GSA) [1] (e.g., Bryan 1986; Wright and Stocker 1991; Power et al. 1994; Rahmstorf and Willebrand 1995; Cai 1996b). However, results are highly model-dependent: the NADWF can be either extremely stable or very unstable. As can be understood, large uncertainty exists in the stand-alone ocean model results due in part to the lack of many important atmospheric feedbacks that operate in reality and strongly modify behaviours of the ocean.

To more realistically simulate the effects of high latitude freshening (either GSA-like events or variations in large scale atmospheric moisture transport) on the THC, coupled models of various complexity, from highly idealised atmosphere-ocean coupled models (e.g., Nakamura et al. 1994; Saravanan and McWilliams 1995; Rahmstorf 1996; Wang et al. 1999) to comprehensive three dimensional fully coupled models (e.g., Manabe and Stouffer 1995; Cai et al. 1997), have been used such that feedback processes and interactions between the atmosphere and ocean are allowed. Although the results are diverse, the NADWF is found to be very sensitive to the imposed

[1] The GSA event was a large freshening of surface water of the North Atlantic during 1968-72 (Dickson et al. 1988) and is believed to have been initiated by an anomalous outflux of sea ice from the Arctic (Walsh and Chapman 1990). It is a natural occurrence of the coupled ocean-atmosphere-sea ice climate system.

freshening in most models. It can either be largely but temporally reduced or completely shut off and then recover, indicating the existence of multiple equilibria in the model ocean. These results also provide some useful indications to the behaviour of world ocean under atmospheric CO_2 forcing which has been shown to enhance poleward transport of the atmospheric moisture and thus freshen the surface water of high latitude oceans.

The past two decades have witnessed a growing concern about anthropogenic influence on the global climate. Thanks to the rapid advance in computing technology and the development in human understanding of the climate system, coupled models have become one of the most powerful tools for climate research and have been widely used to study climate change induced by atmospheric greenhouse gas increases (e.g. Bryan et al. 1982; Spelman and Manabe 1984; Bryan and Spelman 1985; Bryan et al. 1988; Washington and Meehl 1989; Stouffer et al. 1989; Manabe et al. 1990, Manabe et al. 1991; Cubasch et al. 1992; Manabe and Stouffer 1993, 1994; Murphy and Mitchell 1995; Gordon and O'Farrell 1997; Hirst 1999; Mikolajewicz and Voss 2000), based on a variety of radiative forcing scenarios (IPCC 1990; IPCC 1996). Basically, these studies have been conducted to answer a pivotal question: how sensitive is the climate to the intensifying greenhouse effect? In other words, how big is any pending climatic disruption likely to be? Although answers to these questions do not completely agree, all models show a commonality that anthropogenic CO_2 increase is changing the climate: it causes an increase in the surface temperature, at least in terms of the global average, i.e., global warming.

How does the ocean respond to the global warming? Most models simulate a remarkable weakening, even complete shutoff of the NADWF under CO_2 increase forcing, although there are also models with a small change in the THC or even no response of the NADWF intensity at all (e.g., Latif et al. 2000). Since the CO_2 increase is not expected to stop in the near future and its impact will be persistent and far-reaching, a natural question, not only of scientific interest and importance, is therefore raised: what will be the long-term response of the ocean? Will there be a final, new equilibrium for the ocean and thus the whole climate system under persistent CO_2 forcing?

Due to the large time scale of the THC response to surface perturbations, to answer these questions needs integrations extending over multi-centuries and millennia. Such integrations (still) take a large amount of computational time. Therefore, only a few studies have been carried out so far to investigate the long-term behaviour of the world ocean THC under global warming using three dimensional fully coupled models. One report on this topic is by Manabe and Stouffer (1994) who observed the collapse of the NADWF in a CO_2 quadrupling integration covering 500 years using the GFDL model. Lately, this integration had been extended to over 5000 years (Manabe and Stouffer 1999), and the NADWF is found to reintensify after year 900 of the simulation and fully recovers by year 1600, suggesting that the THC shutoff state is not a stable equilibrium in their model. More recently, Voss and Mikolajewicz (2001) found that, in their 850-year CO_2 quadrupling integration using the ECHAM3/LSG model, the NADWF temporarily weakens by up to 50% at around year 140 (i.e., 20 years after CO_2 quadrupling), and then slowly recovers, in contrast to the complete and lasting shutdown simulated in the GFDL model.

1.3 Southern Ocean and the Climate System

While most attention has been paid to the North Atlantic and the NADWF in the above mentioned studies, Hirst (1999) carried out an integration covering 850 years using the CSIRO fully coupled climate model, with a transient increasing CO_2 followed by a three time CO_2 stabilization forcing scenario, to examine the response of the Southern Ocean to global warming. He found that deep convection is suppressed and the downwelling adjacent to Antarctica associated with the AABWF nearly ceases by the time of CO_2 tripling. During the subsequent period of elevated stable CO_2, both the convection and AABWF do not recover at all. As a result, the water of the entire ocean below about 1.5 km depth remains relatively stagnant, retaining a density which is too great to allow renewal from any source. The NADWF is found to be substantially reduced and become shallower in the first half of the integration but show a weak and steady recovery thereafter (but still primarily in the

upper layers). These results are in contrast to the finding of Manabe and Stouffer (1994) that, under the four times CO_2 condition in the GFDL model, the Antarctic overturning cell becomes weaker and shallower but never shuts off, whereas the NADWF collapses completely and stays inactive for a long time.

Although most previous studies, for some well-understood reasons, focus on the central role of the North Atlantic in climate change, all coupled global models suggest an important role for the Southern Ocean change in determining the global pattern of surface atmospheric response. It has been shown that changes in the Southern Ocean thermal advection and convection make the surface temperature there particularly resistant to the CO_2 induced warming, contributing to a marked inter-hemispheric asymmetry in the pattern of global warming (e.g., Manabe et al. 1990, 1991; Manabe and Stouffer 1994; Murphy and Mitchell 1995). The commonly simulated feature that the NH as a whole warms much faster than the SH has significant potential consequences for regional climate change (e.g., Whetton et al. 1997).

Another potential effect of the Southern Ocean change would be the response of carbon cycle. The world ocean is known to be an important net absorber of the additional CO_2 added to the atmosphere each year by human activities. Much of the CO_2 that enters the ocean surface waters from the atmosphere is transfered by mixing and deep water formation into the ocean interior. The long time scale of deep water overturning, together with the greater solubility of CO_2 in water under pressure, makes the ocean a giant reservoir of CO_2, and thus a damper of climate change associated with CO_2 increase. However, the converse can also occur: when the CO_2 induced climate change develops to such a large extent as discussed above, the ocean's CO_2 capacity will be reduced due to both the reduction in the water solubility of CO_2 under higher temperature and the reduction in CO_2 uptake and downward transport with weakened or even closed deep convection and deep water formation. Such a feedback between the atmospheric CO_2 increase and the oceanic CO_2 uptake would naturally lead to a higher atmospheric CO_2 content for a given emission scenario than otherwise envisaged (e.g., Sarmiento and Quere 1996; Sarmiento and Hughes 1999; Matear and Hirst 1999).

Apart from affecting the carbon cycle, the Southern Ocean change has also potential impact on the ocean ecosystem. In the longer term, the possibility of deep ocean stagnation over many centuries raises the issue of development of extensive anoxia, with potential severe deleterious effects for marine biota. The associated changes in biological production may exert significant influence back on the climate system because the marine organisms, such as phytoplankton, are very important in the control of atmospheric CO_2 via oceanic uptake. In particular, a reduced biological production leads to less consumption of CO_2 in the near surface waters, reducing air-sea gradients in CO_2 content, hence lessening further sequestration of CO_2 in the ocean and increasing its build-up in the atmosphere. This feedback process is not included in the current generation of 'physical' models, but it does occur in reality [2]. In any case, the Southern Ocean is an extremely important region for both the climate system and the ecosystem, especially in a long term view. Knowledge about the stability and change of the Antarctic overturning and the associated AABWF is critical for understanding the evolution of past climates and assessing possible climate changes in the future.

The Hirst (1999) integration highlights a possible long-term response of the ocean, especially the Southern Ocean, to the global warming forcing. However, the ongoing warming in the ocean interior indicates that the climate system is far from a final equilibrium state in the model. An important question for the long-term ventilation of the deep ocean is thus whether or not AABWF eventually resumes under stable elevated CO_2 levels.

[2]Phytoplankton fix carbon from dissolved CO_2 through photosynthesis. When these organisms and their 'predators', i.e., the larger species that use them as a food source, die, their remains sink to the seafloor as detritus, adding to the sediment, transferring carbon from the surface waters to the deep ocean and the geosphere reservoir. It is estimated that without this natural sink of carbon the equilibrium atmospheric CO_2 concentration before the Industrial Revolution would have been 450 ppm rather than 270-280 ppm (e.g., Bigg 1996).

1.4 Aims of This Study

This PhD program studies the response of the world ocean, in particular the Southern Ocean, to CO_2 induced global warming, making use of the CSIRO fully coupled climate model (mark2). An initial goal of this study was to modify the CSIRO OGCM in order to obtain an as realistic as practicable oceanic climate in terms of water properties, especially density structure in the Southern Ocean, for the use in coupled model climate research. This was partly motivated by the above mentioned differences in response of the global THC to increasing CO_2 forcing between the CSIRO climate model and other models such as the GFDL model. Since the coupled ocean control climate of the CSIRO model used by Hirst et al. (2000) represents a water stratification significantly weaker than in the observations (Levitus 1994), particularly in the high latitude Southern Ocean, due mainly to a low salinity bias in the deep oceans, it may be thought that the Southern Ocean overturning is unrealistically sensitive to the surface perturbation induced by CO_2 anomaly forcing. A reasonable speculation is that a more realistic representation of the world ocean stratification in the control run could lead to a weaker response of the THC to global warming forcing–for example, the AABWF may not shut off as quickly or completely or, if it does collapse, may recover sooner after CO_2 stabilization.

Our effort to reformulate the ocean model does lead to an appreciable improvement in the ocean climate, i.e., very stable and matching the observations very closely, especially in the Southern Ocean in terms of the water column stratification. However, when used for climate change simulations in the coupled model, it turns out that the modified ocean responds to global warming in a way generally similar to that with the 'poorer' control climate, in spite of some differences in the details of the results. Hence, our result supports the finding of Hirst (1999) that the continual increase in atmospheric CO_2 concentration may eventually cause a closedown of the AABWF, and the resultant deep ocean stagnacy may last for long time under the elevated CO_2 level. More importantly, it is widely recognised that any model used to investigate climate change must be able to represent reasonable large scale

features of the THC, and, naturally, a realistic representation of temperature and salinity (and thus density) distributions in a prognostic ocean model is one of the central indices for validating the performance of models. In this context, our result with the new ocean formulation is to some extent more convincing, and allows the small changes to the water masses which are already appearing in the observations to be more clearly compared with the changes simulated by the model (Wong et al. 1999).

In general, the primary objectives of this PhD program include:

- to modify the CSIRO ocean model, with the aim of yielding a more realistic spinup climate than earlier versions in terms of water mass properties on basin to global scales for use in coupled model climate change studies;
- to initialise the ocean in the CSIRO climate model with the above obtained spinup solution and perform a long control integration to examine the stability of this new ocean climate;
- to carry out a long integration based on the above control run, with a transient/stabilization CO_2 scenario to examine the expected 'more realistic' responses of world ocean THC, especially the AABWF to global warming.
- to perform additional runs, accelerating the deep ocean convergence to *equilibrium*, to examine the possible final state of the ocean in particular, under stable elevated CO_2 condition;
- to compare the behaviours of the ocean under CO_2 forcing in the new version model with that of an earlier version which has a quite different control climate for the ocean, hence examining the dependence of ocean climatic responses to global warming on the representation of the basic state of ocean.

1.5 Overview of This Thesis

Chapter 2 briefly introduces the CSIRO ocean model GM2 version from which this program is started. We have no intention of restating lengthy formulations such as the physical framework–the governing equations, numerical techniques and so on because this model is developed from the Cox-Bryan model and its basic configuration has been described in detail in a wide range of publications. In stead, some relevant details such as the surface conditions, (new) developments in the model parameterizations are discussed. However, the focus of this chapter is on the modifications of the surface thermohaline forcing fields. It is based mainly on the changes made in the surface forcing fields, together with the adjustments of some physical parameters, based on which the new version ocean model GM3 is formulated.

Chapter 3 documents the new ocean climate obtained using the GM3 version ocean model. Through comparison between the GM3 spinup solution, the GM2 climate and other spinup results achieved under different surface forcing conditions, success of the GM3 version in producing water properties closely matching the observations is highlighted. This comparison is presented in section 3.1. The following sections examine some other important elements of the ocean climate such as surface fluxes (section 3.3), meridional heat and freshwater transports, and the world ocean THC in particular (section 3.5.1). Also examined are the wind driven circulations (section 3.5.2). For this purpose, the Sverdrup model is used to estimate the wind driven depth-integrated flow. Comparison is made between this flow and the model simulated barotropic flow, and the difference is discussed. Further comparisons are made between the GM3 and GM2 versions in terms of the above important thermodynamic and dynamic fields, aimed at revealing the respective advantages and weaknesses of these two versions in representing the ocean climate on basin and global scales.

Chapter 4 reports the ocean climatologies of two coupled control runs (CGM3 and CGM2) which are initialized with the different GM3 and GM2 spinup solutions, respectively. Comparison in the prior chapter between the ocean-alone models is

extended further in this chapter between the coupled control climates. It is shown that the noted differences or contrasts between GM3 and GM2 are generally well maintained through the course of the two control integrations, both covering 800 years. Although both runs show very stable annual mean globally averaged climate, with negligible long-term trends in terms of all major quantities at the surface and in the ocean interior, CGM3 is demonstrated to have a generally more realistic solution compared against the observations with results from other coarse resolution coupled models. This strengthens our confidence in the performance of the new model when used for climate change simulations. We note that appreciable regional drift can still exist, mainly in high latitudes such as the Arctic Ocean.

In Chapter 5 we represent the results of a global warming experiment TGM3. This run is initialized with the control (CGM3) solution at the end of model year 100, and subsequently is forced by an increasing (equivalent) CO_2 level according to the IPCC/IS92a radiative forcing scenario for greenhouse gases for the period 1880-2082. By model year 302 (calendar year 2082), CO_2 concentration is triple the control level, and TGM3 is continued thereafter for another 1100 years with the CO_2 concentration held constant at this elevated level (referred to as $3\times CO_2$). Also presented are the results from a parallel run TGM2 which is initialized from CGM2 and employs an identical CO_2 scenario, but with a shorter stabilization duration (650 years). The TGM3 integration may be taken as an extension of Hirst (1999) (which may be referred to as TGM1) except for the use of the 'updated' ocean component (with a more realistic spinup climate in the Southern Ocean in particular, as repeatedly addressed) and some refinements to the ice model which can better represent the sea ice-ocean interaction process. The gradual reintensification of NADWF and the complete shutoff of AABWF noted in TGM1 are still evident in both the TGM3 and TGM2 runs. Moreover, the shutoff state of AABWF in TGM3 lasts through the whole period of the 1100 year $3\times CO_2$ stabilization with no sign of returning, and the associated deep overturning cell dies away, leaving a isolated bottom ocean with no ventilation. Details of other oceanic responses, both at the surface (i.e., the heat and hydrological budgets, SSS and SST, sea ice) and in the ocean interior

(i.e., temperature, salinity, density, and horizontal currents), are documented, and relevant mechanisms for these changes are examined. Differences in changes between TGM3 and TGM2 are noted and discussed.

Chapter 6 presents results of two additional runs AGM3 and AGM2. These runs stem from the TGM3 and TGM2 (i.e., initialized with the state from the end of year 700), respectively, and make use of the Bryan (1984) technique to accelerate the deep ocean convergence to equilibrium. We show that, under acceleration, the deep ocean warms more rapidly than the upper water in due course. After 230 years accelerated integration (equivalent to 6300 years for the deepest ocean), the Southern Ocean water column becomes destabilized to such an extent that deep convection is reactivated and the AABWF is able to operate again, and thereafter the whole climate system evolves into a new, quasi-stable state. This is the case for both runs. To examine if this state is the same as what can be expected from the normal time-stepping integration, further extensions to these accelerated runs are conducted and made to continue for 500 years with the acceleration switched off. We show that the accelerated solution does need some time with normal time-stepping running to adjust and finally settle down to a more stable but slightly different state. Reasons of the resumption of AABWF is discussed in detail.

Finally, chapter 7 presents the overall conclusions of this study. Major achievements are highlighted and further discussed. Also included in this chapter are remarks on some possible caveats for the model (and simulations) and the potential resultant uncertainties.

Two appendices are provided to present the surface adjustments for the coupled models, and to discuss the salinity drift in the global warming experiments, especially the accelerated runs, and its potential effects on the model results, respectively.

Chapter 2

The CSIRO Ocean Model

2.1 General Description

The CSIRO global ocean general circulation model is a coarse resolution, gridpoint, z-coordinate model. It is developed from the Cox (1984) code for the primitive equation general circulation model of Bryan (1969) and is described in detail by Moore and Reason (1993) and Moore and Gordon (1994). For the version as a component of the CSIRO coupled model (mark2), the model domain consists of a global coverage of the world ocean and the horizontal grid has a resolution of 5.625° longitude by about 3.2° latitude, corresponding to the R21 Gaussian grid of the spectral atmospheric GCM.

In addition to the major Eurasian/African/American land masses, the model features three islands (Antarctica, Australia/New Guinea, and New Zealand), with nonzero net circulation permitted around each of them. The bottom topography is derived by interpolating the Scripps $1° \times 1°$ dataset (Gates and Nelson 1975) onto the model grids with additional slight smoothing. The smoothing is needed to ensure convergence of the model's barotropic streamfunction as per Cox (1984) and Killworth (1987). Bering Strait is closed and there is no flow between North America and Greenland. Important sill depths include the Indonesian passage (1900 m)

and the Greenland-Scotland sill (800 m). Several inland seas (Baltic Sea, Black Sea, Caspian Sea) included in the model are not linked to the world ocean and act on the world ocean only via affecting the heat flux adjustment when coupled to the atmospheric model. Due to the coarse resolution of the model, the Mediterranean Sea, Hudson Bay and the Persian Gulf are also not linked directly to the world oceans but the effect of water exchange between these water bodies and the world ocean is parameterized via a mixing of tracers between the closest adjacent grid points across the unresolved straits. For example, the rate of exchange between the Mediterranean Sea and the North Atlantic is calculated assuming a total volume transports of 0.8 Sv, with outmixing depth assumed to be 800 m for the Gibraltar Strait, whilst the other unresolved straits have smaller exchange rates and shallower outmixing depths. Drake Passage extends from 65°S to 56°S in the model (compared to the actual width from 63°S to 57°S) so as to accommodate three velocity grid boxes.

This model prognoses potential temperature, salinity, the two horizontal velocity components, and diagnoses the vertical velocity by using the continuity equation. At the sea surface, the rigid-lid approximation is employed and the bottom is assumed to be insulating. No-slip and insulating conditions are applied at lateral boundaries. The flow variables are Fourier filtered in the northern high latitude (north of 74.9°N) for the purpose of relaxing the severe time step restriction associated with advective numerical stability due to the convergence of meridians toward the North Pole. No filtering is applied in the Southern Oceans.

Some important physical parameters used in the CSIRO OGCM are listed in Table 2.1. A relatively weak, depth-dependent vertical diffusivity κ_v is prescribed, following that of Bryan and Lewis (1979), generally ranging from 0.3 cm^2s^{-1} in the subsurface water to near 1.3 cm^2s^{-1} in the deep ocean below 3500 m. Slightly larger values are used between the upper three levels to roughly mimic some wind-forced surface mixing effects. It is worth mentioning that vertical diffusivity is very important for the diapycnal mixing which is the mixing process essential for the maintenance of the overturning circulations in the ocean. The above prescribed vertical diffusivity

Table 2.1: Ocean model physical parameters (in units of cm^2s^{-1}): vertical diffusivity κ_v, isopycnal thickness diffusivity κ_e, isopycnal tracer diffusivity κ_i, lateral viscosity A_h, and vertical viscosity A_v. Note the last column gives accelerating scales (dimensionless) used in Chapter 6 for speeding up the ocean convergence.

Level	Depth (m)	κ_v [a]	κ_e (10^7)	κ_i (10^7)	A_h (10^9)	A_v	K_{ac}
1	12.5	20.0	0.0	1	8	20	1
2	37.5	1.50	0.0175	1	8	20	1
3	65	0.30	0.0450	1	8	20	1
4	98.5	0.30	0.0725	1	8	20	1
5	138.5	0.30	0.1050	1	8	20	1
6	185	0.30	0.1459	1	8	20	1
7	240	0.30	0.1925	1	8	20	1
8	310	0.31	0.2495	1	8	20	1
9	410	0.31	0.3255	1	8	20	1.33
10	545	0.31	0.4395	1	8	20	2.07
11	710	0.32	0.582	1	8	20	3.48
12	905	0.32	0.6	1	8	20	5.16
13	1130	0.33	0.6	1	8	20	7.09
14	1395	0.35	0.6	1	8	20	9.45
15	1720	0.39	0.6	1	8	20	12.9
16	2125	0.60	0.6	1	8	20	18.8
17	2575	1.11	0.6	1	8	20	22.3
18	3025	1.23	0.6	1	8	20	24.6
19	3475	1.26	0.6	1	8	20	25.9
20	3925	1.28	0.6	1	8	20	26.8
21	4375	1.28	0.6	1	8	20	27.4

[a] Value *at* level k should be understood as *between* level k *and* level k+1.

profile has the weakness that it does not respond to the potential influence of local physical factors such as the stability on the diffusivity. Some studies have employed a scheme that relates the vertical diffusivity to the Brunt-Vaisala frequency (buoyancy frequency) N by setting κ_v to be proportional to the inverse of N (e.g, Gargett 1984; Moum and Osborn 1986; Kraus 1990; Hirst and Cai 1994, Hirst et al. 2000). However, this scheme is still not well physically validated and Hirst and Cai (1994) found little change in the resulting ocean solution. Thus, the N^{-1} dependence of vertical diffusivity is switched off in this study and instead the Bryan and Lewis profile is preserved, based on the judgement that it leads to generally better result after a series of trial experiments were performed to test different profiles for our

model. Convective mixing in this model is simulated by setting an enhanced local vertical diffusivity value of 10^6 cm^2s^{-1} in regions of static instability, whenever diagnosed during the integration, letting temperature and salinity be mixed vertically over the unstable portion of the water column. In this adjustment process heat and salt are conserved by mixing adjacent unstable levels completely. Although some researchers (e.g., Marotzke 1991) reported that the parameterization for convection is important to the thermohaline circulation, we do not include such a scheme in our model as per England (1993), who used a model similar to ours and found little adjustment of the model solutions from the switch in convection schemes.

The Cox (1987) scheme for isopycnal tracer diffusion is incorporated, via the small angle approximation to the Redi (1982) diffusion tensor, to represent more realistically the tendency for heat and salt to be mixed on surfaces of constant density. We set the isopyncal diffusivity κ_i to be spatially uniform with the value of 1×10^7 cm^2s^{-1} although some other researchers (e.g., England 1993) adopt a depth dependent isopycnal diffusivity in their models. This parameterization is discussed further in the following section.

This model version employs the Gent and McWilliams (1990) scheme for eddy-induced advection, which is also discussed in more detail in the following section. The isopycnal thickness diffusivity κ_e is set to be 0.6×10^7 cm^2s^{-1} below 800 m, above which it decreases linearly to zero at the surface as required by the continuity constraint imposed on the eddy-induced transport. This is in contrast to that of GM2 and an earlier version (Hirst et al. 2000, referred to as GM1) where κ_e is set to be 1×10^7 cm^2s^{-1} below 270 m. In addition, a weak and depth-dependent background horizontal diffusivity is used to replace the isopycnal thickness diffusivity in the high northern latitude region (beginning from 74.9°N) to avoid spurious temperatures and salinities.

The lateral viscosity A_h and vertical viscosity A_v are set to the typical values of 8×10^9 cm^2s^{-1} and 20 cm^2s^{-1}, respectively, as per previous studies (e.g., Bryan et al. 1975).

2.2 Parameterizations

It is widely accepted that rapid tracer diffusive mixing in the real ocean occurs primarily along neutral surfaces (locally referenced constant potential density surfaces, McDougall 1987) which are generally not horizontal, and this is referred to as isopycnal mixing. In contrast, mixing across the neutral surfaces is believed to be weak in the real ocean (McDougall and Church 1986). The prescribed large horizontal diffusivity, which used to be commonly employed in ocean models for numerical reasons, may cause unrealistically strong diapycnal mixing, especially in regions of steeply sloping neutral surfaces, thus resulting in serious distortion of the solution for both eddy-permitting and coarse-resolution models (Cummins et al. 1990; Hirst et al. 1996). To parameterize the oceanic tracer transport by mesoscale eddies and eliminate, or at least reduce the effects of the above spurious horizontal diffusive fluxes, two more physically based schemes have been employed in the CSIRO OGCM, as has also been done in many other models around the world.

The first parameterization, referred to as "isopycnal tracer diffusion" (the tracer mixing along neutral surfaces), is a scheme introduced by Cox (1987) based on the analysis of Redi (1982). Many researchers have implemented this scheme in their large-scale ocean models (e.g., Cummins et al. 1990; England 1993; Hirst and Cai 1994; Böning et al. 1995) and reported marked improvement in the tracer distributions in terms of comparison with observations or eddy-resolving modelling. However, an explicit background horizontal diffusivity is still needed to maintain the numerical stability, and the scheme is found to allow only minor reduction in this diffusivity in coarse-resolution global models (e.g., England 1993; Hirst and Cai 1994). Moreover, Hirst and Cai (1994) showed that, although introduction of isopycnal mixing considerably improves the water mass structure, in particular by freshening and cooling water in intermediate depths towards realistic levels, it hardly changes the vertical stratification, density fields, current structure and meridional overturning. This means the isopycnal mixing scheme has a major effect on the tracer distribution but a very minor effect on the ocean dynamics. So, OGCMs

with this scheme still suffer deficiencies such as unrealistically weak stratification at high southern latitudes, which leads to extensive deep convection and large flux adjustment needed to damp the climate drift when coupled to an atmospheric model, which potentially distorts the global warming pattern in transient experiments for climate change induced by green-house gases. The version of CSIRO OGCM with both isopycnal mixing and the artificial horizontal background diffusivity (Gordon and O'Farrell 1997) is referred to as version HB.

A more recent development which helps to overcome the above problem of spurious diapycnal mixing is the implementation of the Gent and McWilliams scheme (Gent and McWilliams 1990; Gent et al. 1995, hereafter referred to as the GM scheme), which parameterizes the adiabatic transport of oceanic tracers by mesoscale eddies. The GM scheme expresses the additional eddy-induced advection as a function of the resolved density and has an effect on the large-scale density field like diffusion of neutral density thickness along the neutral surfaces (Gent et al. 1995). This scheme is physically based and acts on an OGCM akin to imposing a very large vertical viscosity, and therefore allows for substantial reduction or complete elimination of the unphysical large horizontal diffusivity in the model used for numerical purposes. Many researchers (e.g., Danabasoglu and McWilliams 1995; Duffy et al. 1995; Böning et al. 1995; England 1995; Robitaille and Weaver 1995; Hirst and McDougall 1996) have implemented GM schemes in their OGCMs and show that their Cox-Bryan-Code based z-coordinate OGCMs can be run with a realistic dianeutral mixing rate, without the prescribed high horizontal diffusivity.

With the GM scheme, eddy-induced horizontal transport velocity is diagnosed and added to the usual resolved-scale (referred to as "large-scale" or "Eulerian-mean") horizontal velocity to give the "effective transport velocity" (Gent et al. 1995; Hirst and McDougall 1996; Hirst et al. 2000). The vertical component of either the eddy-induced transport or the effective transport velocity is obtained using the continuity equation.

Hirst and McDougall (1996), amongst other researchers, reported significant im-

provements upon the implementation of GM scheme in their OGCM. The major achievements include generally smaller and less noisy surface fluxes near Antarctica, more realistic deep water properties and a substantial reduction of deep convection near Antarctica, which, in the version with fictitious horizontal diffusivity, seriously depletes the salinity of Circumpolar Deep Water (CDW), leading to marked salinity deficiencies in the deep Indian and Pacific Oceans, and severely distorting the surface flux patterns near the Antarctic as mentioned above. The GM scheme also has a substantial effect on model dynamics. Hirst and McDougall (1998) showed that the meridional overturning circulation, when viewed in density coordinates, changes remarkably upon the implementation of the GM scheme, e.g., the evident residual Deacon cell in the earlier versions like HB, which is induced by the horizontal diffusivity, disappears completely and the separate direct Antarctic and deep circulation cells in the HB model are fully merged in the GM version. This solution is believed to represent the real ocean better than that of the HB version, and is also in broadly better agreement with that of the eddy-permitting FRAM Southern Ocean model (Döös and Webb 1994; McIntosh and McDougall 1996).

Moreover, Hirst et al. (1996) and Hirst et al. (2000) examined the performance of the GM scheme in the ocean under coupled conditions. Their experiments demonstrated that the beneficial effects of the GM scheme mentioned above are all generally well maintained during the coupled integration and these improvements are especially pronounced in the high latitude Southern Ocean. In addition, the coupled model with the GM version ocean (referred to as the GM version coupled model) requires smaller surface flux adjustments and displays markedly reduced climate drift in comparison to the earlier HB version ocean as reported by Gordon and O'Farrell (1997).

As we know, the ocean model is by no means perfect due to the limitation of our understanding and representation of the complicated ocean physics and in particular the difficulty of parameterizing some important physical processes in a coarse resolution model. Despite the improvements achieved with the better model physical configuration, there are still deficiencies in many aspects relating to poor represen-

tation of ocean circulations and tracer distributions. One of the initial goals of this study is to obtain an oceanic climate which is as realistic as possible, using the above described state-of-the-art OGCM with proper surface boundary conditions, and to incorporate it in the CSIRO coupled model for the purpose of climate change simulations and sensitivity experiments.

2.3 Surface Boundary Conditions

The most traditional and still commonly used boundary condition for the OGCM is relaxation forcing for the model surface tracers, that is, the surface temperature and salinity values are restored towards observed climatology via a Newtonian damping law, with a constant timescale ranging from days to months. The implied effective surface fluxes of heat and salinity/freshwater can then be diagnosed via the restoration, and the specified tracer climatologies, or say the *apparent* salinities and temperatures (Haney 1971), which vary temporally and spatially, are often designed to give observed surface fluxes when surface tracer values match observations (Han 1984). This technique was firstly used for surface thermal forcing based on the justification of Haney (1971) that there is direct feedback between the oceanic surface temperature and the air temperature above the sea surface, and it allows for large-scale thermal coupling of the ocean and atmosphere. However, its use in forcing the model surface salinity is not physically justified because the freshwater flux, which is determined from precipitation and evaporation (i.e., P - E), is essentially independent of the surface salinity.

A kind of mixed boundary condition is sometimes used in ocean modelling studies. Such forcing keeps the temperature restoring but replaces the unphysical salinity relaxation with a prescribed freshwater flux which is either diagnosed from the spinup under relaxation forcing or derived from a surface freshwater budget (P - E) compiled from observations. However, this mixed forcing does not necessarily ensure a realistic ocean solution. On the contrary, it may lead to unexpected and model-

dependent behaviours in the ocean, including the polar halocline catastrophe (Bryan 1986), low-frequency oscillations (Marotzke 1989) and decadal timescale oscillations (Weaver and Sarachik 1991a,b; Cai 1995). Moreover, under such mixed boundary conditions, the model solution is very sensitive to the surface freshwater forcing magnitude, and the model solution can either be unstable or reach multiple equilibria. So, although it may be a useful approach to investigate ocean response to the change in the hydrological cycle of the atmosphere, mixed boundary conditions are not suitable for ocean spinup integrations that aim to obtain a stable and realistic ocean equilibrium for the coupled model.

Another type of forcing for surface tracers is the flux boundary condition, which specifies the net heat and freshwater fluxes over the whole model domain. The heat flux can be specified in the way that derives the freshwater flux, i.e., it can be either the observed climatology or simply diagnosed from an initial ocean spinup with relaxation forcing. Furthermore, both the heat and freshwater fluxes can be specified via the product of an atmospheric GCM. This is of particular interest for climate change experiments using an atmosphere-ocean coupled model. If the pre-coupling ocean spinup, driven by the AGCM implied fluxes, can reach a reasonable equilibrium, flux adjustments, which are widely used to damp the climate drift upon coupling, will naturally vanish. Unfortunately, the ocean model tends to behave erratically under fixed flux forcing, with the SST evolving far from the observed surface temperature (e.g., Rosati and Miyakoda 1988). This drift in SST occurs because the specified fluxes may have large errors or uncertainties due to the limitations in observations and because the air-sea feedback which operates under the Haney (1971) thermal forcing is switched off under the fixed flux forcing.

A more realistic surface tracer boundary condition may be configured using bulk forcing. Bulk forcing is a kind of flux forcing but the heat flux in the bulk formulas can adjust according to the evolving surface temperature, which reflects the air-sea feedbacks and therefore constrain the SST drift mentioned above, resembling the sea-air coupling process in the model and in reality. This thermal forcing has been used by Hirst and Godfrey (1993) and Oberhuber (1993a) in their OGCMs, but the heat

and freshwater fluxes are not linked via evaporation process as they are in reality. Barnier et al. (1995) designed standard bulk formulas to configure OGCM thermal boundary conditions, which express the net heat flux as a function of SST, with the climatologies of SST and net heat flux calculated using the European Center for Medium-Range Weather Forecasts (ECMWF) analyses. Large et al. (1997) employ bulk forcing in the NCAR OGCM, utilizing the evolving model SST and monthly atmospheric fields based on both the reanalyses of the National Center for Environmental Prediction (NCEP) and satellite data products. It needs to be mentioned that for the OGCMs that are not coupled to an explicit sea ice model, such as the NCAR model and CSIRO model, bulk forcing is used only for open (ice free) sea water and a strong restoring in temperature and salinity is still needed under sea ice. In addition, a weak salinity relaxation is also applied to open water for the purpose of damping the potential instability which would otherwise occur. Large et al. (1997) found that, compared to relaxation forcing, bulk forcing produces poleward heat and salt transports in better agreement with most oceanographic estimates and maintains the abyssal tracer distributions closer to observations.

In this study, the ocean model is forced at the surface by modified observed annual cycle climatologies of the British Meteorological Office (BMO) SST and Levitus (1982) sea surface salinity (hereinafter referred simply to as BMO SST and Levitus SSS, respectively). The modifications to relaxation fields are moderate and employed in high latitude especially the water mass formation regions, as detailed in the following section, to set realistic upper-surface properties which are central to the deep water formation there. We choose the relaxation thermohaline forcing because it is believed to be the most suitable tracer boundary condition for our model with the view of ensuring a stable and realistic ocean solution, as addressed by Cai (1996b) and based on comparisons between observations and model results from our trial experiments under various forcing conditions. It is widely accepted that a realistic ocean solution is the basic requirement for the study of the oceanic response to changes in atmospheric conditions using atmosphere-ocean coupled models. The reason that we choose the BMO SST rather than Levitus temperatures to restore

the model surface temperature towards needs to be mentioned. Firstly, although it may seem a more natural choice, the Levitus SST and SSS together do not supply our model with a proper surface relaxation forcing under which formation of realistic water masses can be simulated. Previous studies (e.g., Hirst and Cai 1994) reveal serious inconsistencies between the Levitus values and some other observations. For example, the Levitus values at 10 m depth (which dominates in the interpolation to the top level of our model) give a peak winter density remarkably lower than that of observations in many important water mass formation regions such as the Labrador Sea and Norwegian/Iceland/Greenland Sea (and in some regions the surface density is even higher than that at 10 m depth). We found that the combination of Levitus SSS and BMO SST gives a generally better density field, especially for the winter density peak greater than 28.0 $\mathrm{kg\,m^{-3}}$ which is featured in the Norwegian/Iceland/Greenland Sea and close to that of observations (Rudels et al 1989; Clarke et al. 1990). Secondly, the BMO SST is used for the CSIRO AGCM spinup and thus is a natural choice for the ocean spinup, considering the compatibility between these two components for the CSIRO coupled model.

The dynamic boundary condition for our model is configured with the climatology of atmosphere to ocean momentum flux (windstress). Contrasting many earlier studies (e.g., Gordon and O'Farrell 1997; Hirst et al. 1996, Hirst et al. 2000) where Hellerman and Rosenstein (1983) windstress monthly climatology (referred to as H-R wind data hereinafter) is used, this study employs the windstress climatology determined from the NCEP 1951-1990 monthly mean and interpolated onto the model grid points. Compared to the H-R wind which is too strong over tropical oceans and too weak over the Southern Ocean especially near Antarctica, the NCEP windstress is believed to be more realistic in terms of the general distribution pattern and magnitude, especially in the near Antarctica region. In addition, the NCEP climatology is closer to the CSIRO AGCM windstress than the H-R data. So its use in our model will reduce the required momentum flux adjustment for coupling, and help in diminishing the possible impact of change in windstress upon coupling in the case with no windstress correction. The adjustment of ocean solutions upon

using different windstress forcing data in the spinups will be described briefly in next chapter.

2.4 Modification of the Surface Forcing Fields

Trial experiments showed that, under the (original) BMO SST and Levitus SSS forcing, our model still fails to produce realistic world ocean water mass properties and thermohaline circulations. Although the relaxation tracers indicate a high enough winter peak density that generally matches observations as mentioned above, the restored model upper-level tracers can only give a peak density of 27.90 $\mathrm{kg\,m^{-3}}$ in the Norwegian/Greenland Sea, and a peak value of 27.5 $\mathrm{kg\,m^{-3}}$ in the Labrador Sea, both are much lower than the observed counterparts, i.e., over 28.0 and 27.78 $\mathrm{kg\,m^{-3}}$, respectively. This inconsistency in the North Atlantic is hypothesized to be one of the main factors causing the weak deep convection and thus too shallow penetration of North Atlantic overturning. To test this hypothesis, we make some further adjustments to the forcing, aimed at obtaining more realistic model upper-level temperature and salinity fields (and therefore better surface density features). Obviously this pursuit also favours our endeavour to provide a reasonably realistic simulated SST for the coupled model in climate studies.

It is well known that the model SST and SSS simulated under relaxation forcing always suffer a more or less "shift" from the climatological values, especially the peak and trough values. This is due partly to the mixing between neighbouring grid points with different properties, and partly to surface fluxes lagging observations caused by *the unreality of a posteriori restoring the model surface tracers to the observed*, both depending on the relaxation timescale. It is from this deviation that the implied surface fluxes are diagnosed. Using a shorter relaxing timescale, e.g., of a few days rather than about one month as commonly used, can help to reduce this departure. However, it will lead to noisy and unreasonably large fluxes in many regions which will cause too large and too extensive flux adjustments when coupled

to the atmosphere and is therefore taken as inappropriate for our purposes. The alternative method used to reduce this departure, in particular the SST anomaly, is to adjust the forcing fields so as to tie the resultant model surface solution close to observations. We choose to *adjust the surface forcing fields*, instead of using too short relaxation timescales, for our ocean spinup integration, in such a way that the mean computed surface value at a point corresponds to the corresponding mean observed value. In principle, this is equivalent to imposing a time centered restoration rather than a time lagged restoration.

A series of short time integrations are performed to modify the thermal forcing field, using an intermediate relaxation time scale of 20 days. Firstly a short run is conducted under the original BMO SST climatology forcing and the model SST anomaly is diagnosed, i.e., BMO SST minus model top level temperature in our case. This anomaly is then imposed on the old forcing field for the subsequent short run, from which a new SST anomaly can be obtained and used to modify the forcing values again. Repeat this precess a few times until a model SST field closest to the original BMO climatology is reached. The final forcing field is what we need for the long term ocean spinup to be coupled to the atmosphere. We initially employed the above modification to the SST forcing globally and found the adjustment is very large and noisy in the middle latitudes and equatorial regions, and results in unreasonably large and noisy heat fluxes there. So we constrain the modification to within the high latitudes in both hemispheres (north of 40°N and south of 60°S) where the deep water masses are formed, with the change in forcing values at the demarcation smoothed. In addition to the above adjustment, the BMO SST dataset is also carefully tuned 0.5 – 2.0 °C higher in the North Sea to reduce the false high density center there which appears when forced under the original BMO SST data and may lead to spurious water mass formation at that location.

Fig.2.1a and 2.1b show the annual cycle of the BMO SST averaged over the North Atlantic (60°W–40°E, 50–80°N) and the Southern Ocean (south of 60°S), respectively, for both the original and modified fields. Also shown are the modelled near surface temperatures under original and modified BMO SST data, identified as GM2

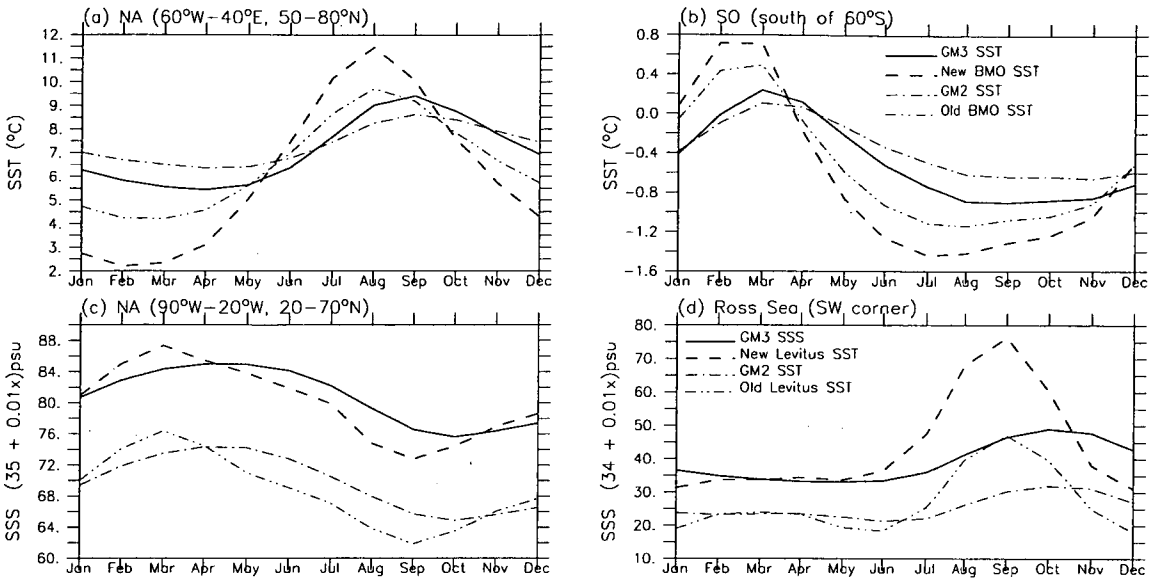

Figure 2.1: Annual cycle of SST and SSS for relaxation data and model results over the North Atlantic (NA) and Southern Ocean (SO)/southwestern corner of the Ross Sea.

and GM3, respectively. The lag of the model SST to the surface forcing is evident. The annual cycle of the final forcing SST is substantially modified and so is the resulting model temperature. In the North Atlantic, if we neglect the impacts from other factors, such as the salinity forcing change and the slight differences of model physics between GM2 and GM3, the cooling by 2 °C of the forcing can lead to a decrease of 0.95 °C in the model temperature in March, and 1.7 °C warming in August making the model temperature 0.8 °C higher in September. The overall improvement in model temperature in the North Atlantic is achieved at the cost of larger heat fluxes in that region, as indicated by the larger temperature difference, and clearly, with such an adjustment, we still see too high model (GM3) winter temperature compared to the original BMO SST, due mainly to the freezing point constraint for the relaxation SST. A similar situation occurs in the Southern Ocean where the modified model winter temperature is significantly cooled but is still not cold enough. This shows the limitations of the above modification schemes to the SST, which is a characteristic of sea ice freezing regions.

Modification is also made to the restoration SSS field so as to achieve more realistic model SSS which, together with the improved SST results, will lead to a better rep-

resentation of the model surface density distributions. However, the abovedescribed method for SST forcing adjustment is found unsuitable for the SSS forcing because it causes a very noisy freshwater flux distribution over the global ocean. We thus constrain the modification to within the North Atlantic region and some grid points near Antarctica, with the principle that the resulting model SSS distributions in these regions capture both the temporal and geographical characteristics of the Levitus SSS climatology. In the North Atlantic (20–70°N, 20–90°W), the adjustment made to the Levitus SSS ranges from -0.78 to 0.85 psu in the annual cycle. Significant changes are made in high latitudes, with the largest enhancement (0.5 psu in late winter and 0.85 in early summer) employed at a point (50.6°W, 55.7°N) in the central Labrador Seas and the largest reduction (0.78 psu for all seasons) imposed on a point (61.9°W, 58.9°N) near the mouth of Hudson Strait. In the southeastern Greenland coastal region the Levitus SSS is also subject to a reduction from 0.2–0.5 psu year round. In lower latitudes, modification is weak (0.1–0.2 psu) but extensive so as to yield a realistic winter salinity distribution there. The overall change in the Levitus SSS forcing in the North Atlantic is about 0.1 psu enhancement year round, as displayed by Fig.2.1c, making the model surface about 0.1 psu saltier as well. Such changes made to restoration SSS and SST do result in reasonable model water properties near the surface, and more importantly, keep the model winter peak density close to observations in the NADWF regions and consequently result in a stronger and deeper overturning circulation there compared to solutions under other surface forcing conditions.

In the Southern Ocean, especially the ice covered region near Antarctica, due to the difficulty in observation (particularly in winter), there exist large uncertainties in all the available SSS climatologies, including the Levitus SSS used here. For example, Levitus SSS (at our model resolution) shows that there are only two narrow regions in the western Ross and Weddell Seas where SSS is over 34.0 psu in winter (with maximum value of only about 34.78 and 34.72 psu, respectively, at their southwestern corners) and very low values in other coastal regions (generally 33.7–33.9 psu). This gives surface water around Antarctica which is too fresh to reflect the win-

ter salt rejection from ice formation. Such a deficiency results in poor deep water properties near Antarctica in our model, i.e., too warm and fresh and therefore too buoyant at depth, which gives too weak stratification at high southern latitudes and, as a consequence, it becomes too easy to trigger false and excessive deep convection in the Southern Ocean. Our trial experiments show that largely enhanced salinity forcing (e.g., up to 34.2–34.7 psu around Antarctica in ice covered regions) does improve the thermal status considerably at depth near Antarctica with cold enough bottom water (i.e., -1 – -2 °C), but at the same time the salinity structure becomes worse due to strong freshening (i.e., down to 34.5–34.6 psu) at depth and therefore the weak stratification is not improved at all. This is not surprising because the enhanced surface forcing intensifies the convective mixing near Antarctica and makes the surface cold and fresh water penetrate into the depth to the deep water, which is typically 0–0.5 °C, 34.7 psu in our model. After failing to achieve both a reasonable surface solution and satisfactory deep water properties in terms of realistic temperature and salinity at depth without causing surface flux errors, we finally gave up the attempts to modify the Levitus SSS more extensively. In this study, we just enhance the winter salinity forcing by 0.1–0.3 psu for three coastal grid points at the southwestern corner of the Weddell Sea and increase the values at three points in the southwestern corner of the Ross Sea by 0.1–0.2 psu for summer and 0.2–0.5 psu for winter, respectively. Note these adjustments are all restricted to points adjoining the coast, where the seafloor is above 800 m and the neighbouring points have a seafloor above 1900 m. This follows the three rules addressed by Hirst and Cai (1994), which are based on the assumption that the high-salinity dense shelf water induced by near-coastal salt exclusion can only be mixed and flow downslope into the deep ocean, in accordance with observations (Killworth 1983; Carmack 1986).

Fig.2.1d represents the annual cycle of the original Levitus SSS at the southwestern corner of the Ross Sea and the enhanced feature, together with the modelled near surface salinities of GM2 and GM3. The obvious error is the false trough in early winter (June) for the old SSS forcing but our modification to this trough is moderate

(0.18 psu) considering the continuity with the surrounding points. The September value is enhanced by 0.3 psu to capture the large salt exclusion from the ice formation in the winter season. The overall enhancement at this corner is about 0.16 psu year round and the resulting model salinity is thus that much saltier.

2.5 Procedure for Ocean Spinup

The ocean model experiments in this study consist of a series of preliminary integrations and a final spinup experiment. The short preliminary runs are designed to determine a set of surface forcing fields appropriate for the final long spinup aimed at obtaining a reasonably realistic ocean climatology.

We start the preliminary runs from a quasi-equilibrium state of the model version GM2, using annual cycle surface forcing data of the original BMO SST, Levitus SSS and NCEP windstress, and employing the prescribed vertical diffusivity profile and a reduced isopyncal thickness diffusivity discussed above. The BMO SST and Levitus SSS are modified gradually following the process and principles described in the last section to make the model approach an acceptable surface solution, in particular a reasonable winter peak density distribution in the water mass formation regions. At this stage, a hierarchy of longer integrations are also performed to determine the 'most appropriate' pre-specified vertical diffusivity profile which, together with the modified surface forcing, is expected to produce realistic global ocean water properties and circulations. While the other variants benefit the model solution more or less in various aspects, the standard Bryan-Lewis profile is finally employed due to its overall better performance globally.

The final ocean spinup involves two stages. Firstly, an asynchronous time stepping run is conducted following the last preliminary run from which the final modification of restoring fields is made. Different time steps are used for velocity (U, V) and tracer (T, S) integrations: the barotropic streamfunction and baroclinic velocity equations are integrated with a time step of 20 minutes while tracer equations use a time step of

1 day. Note the Bryan (1984) acceleration technique to speed up abyssal convergence of the model solution is turned off here for the purpose of ensuring true seasonal behaviour of the ocean under the annual cycle surface forcings. This asynchronous run is continued for about 6000 (tracer) years and reaches a satisfactory equilibrium under the convergence criterion that the rates of change in the global mean T and S at each level are negligible (less than 0.005 °C and 0.001 psu per century). Secondly, a synchronous run, using a time step of 1 hour for both the momentum and tracer equations, is conducted to continue the above asynchronous run and lasts for 500 years. This run is designed to further adjust the pre-coupling state of the model ocean, helping minimize residual drift at high latitudes upon changing from the stand-alone ocean mode into the coupled mode which adopts synchronous time stepping for all fields. This spinup, using the new formulation of the ocean, is referred to as GM3.

In the above spinup process, the e-folding decay timescale for the surface tracer relaxations is set to 20 days, which is used for our modification of the relaxation fields before the spinup and, together with the adjusted forcing fields, is judged to be efficient in keeping the model surface solution close to observations. Such an intermediate time lag for our model leads to a Haney heat flux of about 57 $\mathrm{W\,m^{-2}\,K^{-1}}$. This compares, for example, with the Haney coefficient of 70 $\mathrm{W\,m^{-2}\,K^{-1}}$ used for the spinup of the GFDL ocean model (Manabe and Stouffer 1991). A weaker relaxation such as one with a time lag of 30 days or longer is inappropriate for our purpose due to either its inefficiency in producing realistic surface properties or its demand for larger adjustments to the forcing fields. Similarly, a stronger relaxation with a time scale shorter than 10 days (e.g., Hirst and Cai 1994, England 1994; Hirst and McDougall 1996) is proven to yield fluxes which are too strong and noisy globally in our model and which could cause more difficulties in coupling to the atmosphere.

In addition to GM3, a few more spinups using different model versions and/or surface configurations are also conducted for the purpose of comparison. Results from these runs are validated against the Levitus climatology (Levitus et al. 1994) mainly in

terms of temperature and salinity distributions, as presented in next chapter.

Chapter 3

Ocean Spinup Climatology

The annual mean GM3 ocean climatology, including water properties, surface fluxes and global circulations, is documented in this chapter. The improvements in model performance from the new formulation, in particular the modification of surface forcings, will be illustrated mainly on the basis of comparisons between the GM3 results, the Levitus et al. (1994) climatology (hereinafter referred to as Levitus) and results from the other three integrations with different model configurations.

3.1 Spinup Runs

Table 3.1 lists and briefly describes the four spinup experiments involved in our discussions and comparisons. In summary, GM2 is an earlier version based on which the GM3 is developed. It uses the seasonal surface forcing fields of the original Levitus SSS and BMO SST climatologies and the H-R windstress; CW3 and BF3 are variants of the GM3 version. BF3 employs a bulk-flux forcing scheme (Large et al. 1997) at the surface as used in the NCAR Climate System Model (NCAR CSM) (e.g, Gent et al. 1998), and CW3 is identical to GM3 but with the CSIRO AGCM spinup windstress forcing. BF3 is provided to examine the suitability of using the so-called (physically) "most realistic" boundary conditions in our coarse

resolution model, whilst CW3 is compared to GM3 to demonstrate the sensitivity of our model to the change in windstress forcing, which may reveal the possible response of our ocean model to coupling to the atmospheric component with no adjustment on windstress employed. Note that the difference in presentation of results, i.e., synchronous for GM2 and GM3 versus asynchronous for BF3 and CW3, has little effect on the comparison presented here.

Table 3.1: Ocean spinup runs with different model configurations

NAME	Description (configuration)	Duration
GM3	GM version No.3. κ_e = 0–0.6×10^7 cm^2s^{-1}, prescribed B-L κ_v profile, modified BMO SST and Levitus SSS relaxation, NCEP windstress	6000 years (asynchronous) + 500 years (synchronous)
CW3	same as GM3 but with the CSIRO atmosphere model windstress	4000 years (asynchronous)
BF3	same as GM3 but with bulk-flux-forcing at the surface (using the NCEP reanalysis data)	4000 years (asynchronous)
GM2	GM version No.2. κ_e = 0–1.0×10^7 cm^2s^{-1}, static stability-dependent κ_v, original BMO SST Levitus SSS, H-R windstress	5000 years (asynchronous) + 300 years (synchronous)

In the following discussions, the GM3 and GM2 solutions are taken from the average of their last 100 year synchronous integrations, while the CW3 and BF3 results are the average of their last 1000 year (asynchronous) integrations.

3.2 Water Properties of the Oceans

Water mass thermohaline properties in the world ocean have been investigated extensively due to their vital role in affecting many important physical processes and the global circuations. It is commonly recognized that whether or not a prognostic ocean model can realistically represent the heat and salt distributions is one of the central indices for the validation of its performance. In this context, we start with the assessment of the GM3 solution from the examination of the structures of temperature, salinity and density and compare them with the results from other runs where appropriate.

To exhibit the general behaviour of our model, we focus on the results for the global ocean and three individual ocean basins, i.e., Atlantic, Indian-Pacific and Southern Oceans. In our analysis, the Atlantic Ocean extends from 50°S to the North Pole, containing Baffin Bay and the whole Arctic; the Indian-Pacific Ocean consists of the two vast water bodies north of 50°S, sharing one boundary at around 20°E with the Atlantic; and the Southern Ocean includes all the oceans south of 50°S. The reason why the Indian ocean and Pacific ocean are taken as one water body here is that they have generally more similar water properties in terms of the temperature and salinity distributions. Note no inland seas are taken into consideration. In addition, in our expressions hereinafter we refer to potential temperature and potential density as temperature and density, respectively, for simplicity.

3.2.1 Density Distributions

The ultimate purpose of our modification to the surface relaxation fields is to reproduce as realistically as possible the stratification in the ocean, on the basis of reasonable temperature and salinity distributions. Fig.3.1 shows the vertical distributions of the annual and horizontal mean density fields (σ_t, referenced to the surface) from the Levitus data and the spinup solutions. As expected, GM3 and CW3 demonstrate a general better agreement with observations than GM2 and BF3 in all ocean basins, particularly below the depth of around 1000 m, reflecting the joint effect of improved temperature and salinity solutions, which will be shown in the following subsections, with the modified model surface formulation.

Below the uppermost level, the global ocean subsurface water of all model solutions is subject to a significant density shortfall due mainly to the deficiency of salinity to be shown later. This light bias reaches a maximum of 0.39 and 0.43 $\mathrm{kg\,m^{-3}}$ at 185 m depth for GM3 and GM2, respectively, indicating a stratification weakening above this level for both model configurations in the world ocean, with GM2 suffering slightly more weakening than GM3. Down from this level, the GM3 low density bias is gradually reduced to zero at 1395 m depth and then changed into a very

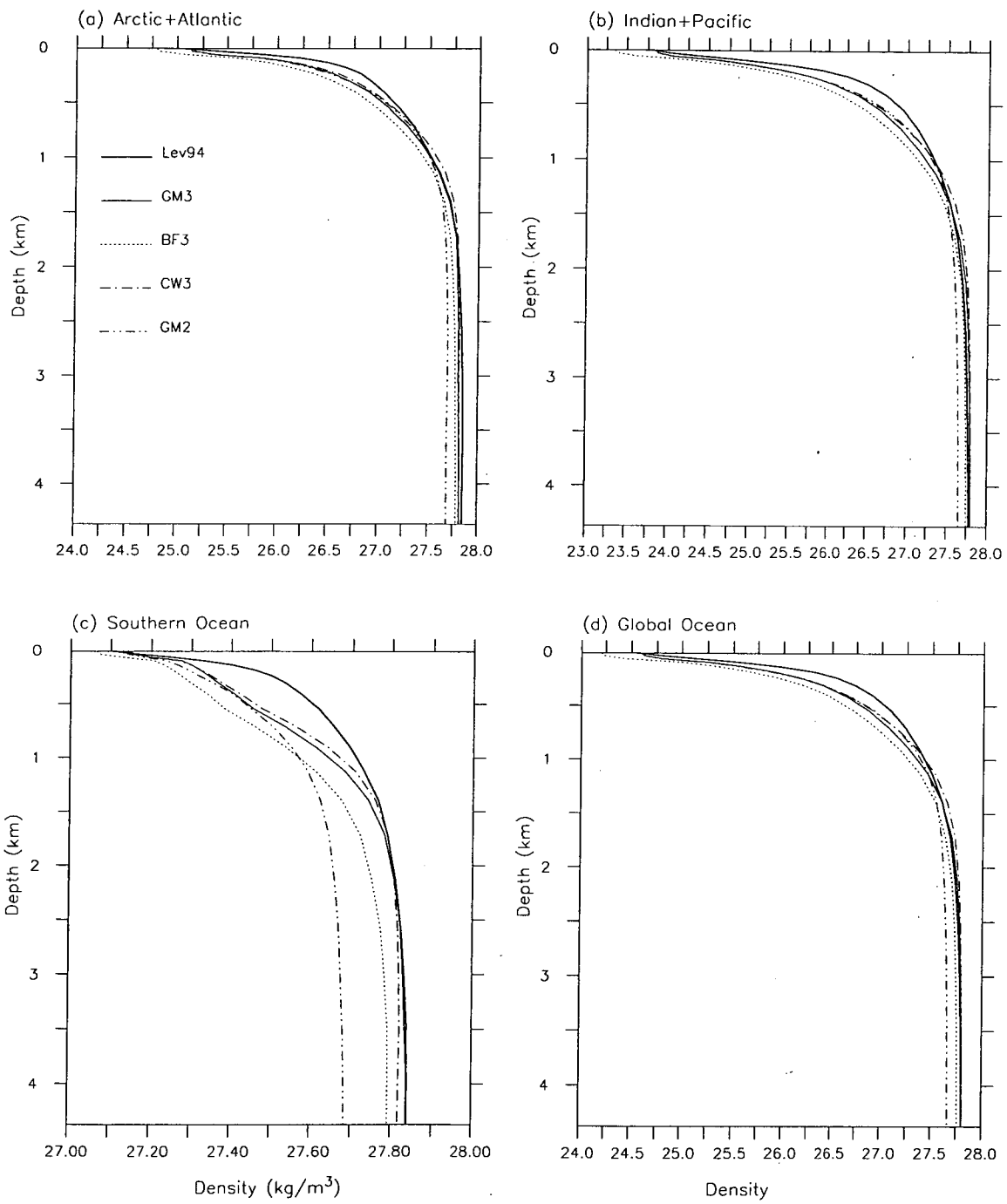

Figure 3.1: Vertical distribution of annual mean density (σ_t) in (a) Atlantic, (b) Indian-Pacific, (c) Southern Ocean, and (d) global ocean.

small positive bias (0.01–0.02 $\mathrm{kg\,m^{-3}}$) which extends further down to the bottom, showing a slightly strengthened stratification in the mid-depth and little impacted stratification in the deep ocean. In this global mean water column, GM2 bears a clear distinction from both the Levitus and GM3, as shown by its notable reduction in density gradient.

The stratification difference between GM2 and GM3 is of special interest and importance in the Southern Ocean. As shown in Fig.3.1d, GM2 produces an unrealistically weak stratification, particularly below the depth of about 600 m, with a large negative density bias of 0.16 $\mathrm{kg\,m^{-3}}$ near the bottom and a close to realistic density near the surface as expected from the relaxation, whilst GM3 is in good agreement with Levitus in both the uppermost and deep water. Clearly the GM3 configuration results in a striking improvement to the whole water column stratification in the Southern Ocean. Since the Southern Ocean is the major focus of this study, such an improvement achieved here is critical.

To further examine the basin and global mean vertical structures of the model density fields in comparison with the Levitus climatology, we divide the whole ocean column into three depth intervals. They are the upper layer (0–800 m), mid-depth layer (800–2350 m) and deep layer (2350–4600 m). The volume-weighted root-mean-square (RMS) differences of density within these three layers and the whole water column for the individual basins and the world ocean are thus calculated and listed in Table 3.1, together with that of temperature and salinity.

Compared to GM2 and BF3, the GM3 configuration gives generally better vertical distribution features of density in all basins and nearly all water columns. The global total column as a whole has the density distribution slightly closer to Levitus in GM3 than GM2. The most dramatic improvement of density field occurs in the abyssal oceans, with the RMS differences of the GM3 solution being 0.04, 0.03, 0.00 and 0.01 $\mathrm{kg\,m^{-3}}$ in the deep layer of Atlantic, Indian/Pacific, Southern and the World Oceans, respectively, in contrast with their GM2 counterparts of 0.15, 0.11, 0.15 and 0.13 $\mathrm{kg\,m^{-3}}$. The mid-depth layer, except for that in the Indian/Pacific

Table 3.2: Root-Mean-Square differences of the model T, S and σ_t from Levitus (1994) climatology for the means in each domain. (units: °C, psu and kg m^{-3} for T, S and σ_t, respectively.)

		Ocean Basins											
		Atlantic+Arctic			Indian+Pacific			S. Ocean			Global Ocean		
Layer	Run	T	S	D	T	S	D	T	S	D	T	S	D
(upper)	BF3	0.51	0.40	0.39	1.47	0.43	0.59	0.61	0.30	0.21	0.95	0.39	0.48
0	CW3	0.25	0.18	0.19	1.49	0.08	0.33	0.31	0.14	0.12	0.95	0.10	0.26
–	GM2	0.48	0.16	0.23	1.41	0.07	0.32	0.38	0.17	0.16	1.02	0.09	0.27
800m	GM3	0.47	0.15	0.22	1.62	0.08	0.34	0.32	0.16	0.14	1.14	0.09	0.28
(mid)	BF3	0.48	0.03	0.06	0.32	0.11	0.11	0.15	0.13	0.10	0.24	0.09	0.09
800	CW3	0.18	0.02	0.04	0.24	0.06	0.06	0.34	0.03	0.02	0.16	0.04	0.04
–	GM2	0.14	0.10	0.09	0.25	0.10	0.06	0.22	0.16	0.15	0.12	0.11	0.08
2350m	GM3	0.20	0.02	0.01	0.44	0.03	0.06	0.41	0.03	0.04	0.34	0.02	0.04
(deep)	BF3	0.52	0.13	0.07	0.29	0.06	0.03	0.12	0.05	0.05	0.28	0.08	0.04
2350	CW3	0.41	0.08	0.03	0.14	0.03	0.03	0.26	0.01	0.01	0.15	0.01	0.01
–	GM2	0.83	0.26	0.15	0.37	0.18	0.11	0.17	0.20	0.15	0.44	0.20	0.13
4600m	GM3	0.22	0.07	0.04	0.03	0.04	0.03	0.38	0.03	0.00	0.01	0.01	0.01
(total)	BF3	0.50	0.21	0.20	0.72	0.21	0.28	0.30	0.17	0.12	0.50	0.19	0.23
0m	CW3	0.30	0.10	0.10	0.70	0.06	0.16	0.30	0.06	0.06	0.46	0.05	0.12
–	GM2	0.58	0.19	0.16	0.70	0.13	0.17	0.25	0.18	0.15	0.55	0.15	0.16
4600m	GM3	0.29	0.09	0.11	0.79	0.05	0.16	0.38	0.08	0.07	0.57	0.04	0.13

Ocean, also sees a significant reduction in density deviations from Levitus under the GM3 configuration. For example, the RMS differences in this layer are reduced from 0.09 and 0.08 kg m^{-3} in GM2 to 0.01 and 0.04 kg m^{-3} in GM3 for the Atlantic basin and global ocean, respectively. The upper layer as a whole sees no marked effect of the GM3 configuration on the density field in all individual basins and the world ocean in terms of the RMS indices compared to GM2. However, the impact of surface forcing modification in GM3 on the model near surface density is evident and constrained to local regions. For example, in the North Atlantic region (60°W-0°E, 20°N-70°N), where the the major forcing adjustment is employed, the model uppermost level density is enhanced by up to 0.10 kg m^{-3} (GM3 - GM2), whilst the overall enhancement is only 0.04 kg m^{-3} in the whole Atlantic Ocean from 50°S to 70°N and the global scale effect is just 0.01 kg m^{-3}. The increase of near surface density in the North Atlantic is the first goal of the GM3 configuration and it intensifies the local convective mixing and deepens the thermohaline overturning penetration in that important NADW formation region.

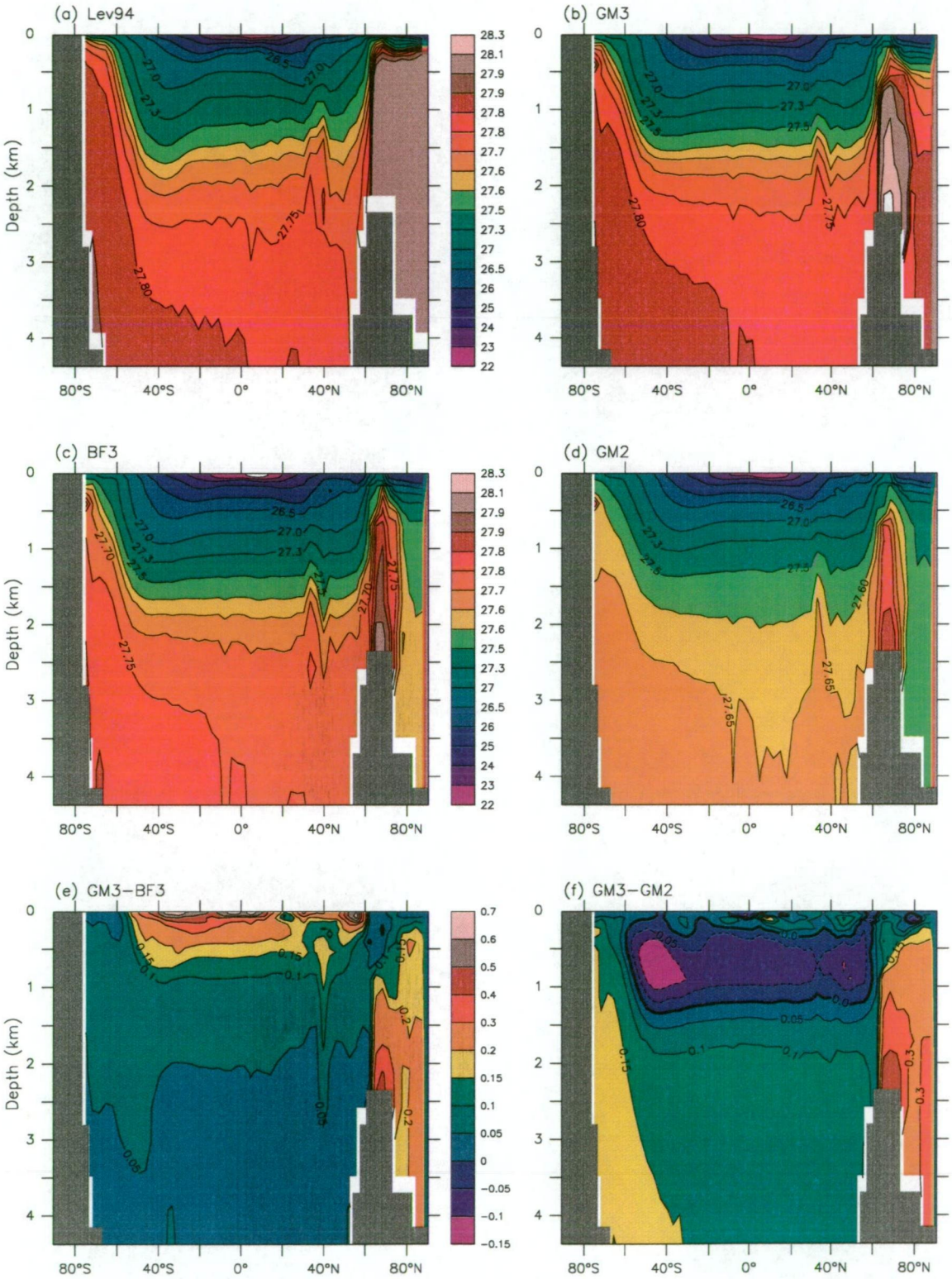

Figure 3.2: Zonally averaged annual mean density (σ_t, in $\mathrm{kg\,m^{-3}}$). (a) Levitus, (b) GM3, (c) BF3, (d) GM2, (e) GM3 - BF3, and (f) GM3 - GM2.

Amongst all the solutions presented here, BF3 shows the largest density deviation from Levitus in the upper layer of all oceans. Although it gives RMS differences comparable to that of GM2 in the mid-depth layer and even much better features in the bottom layer, BF3 suffers a density deviation as large as 0.23 $kg\,m^{-3}$ from Levitus for the whole column of the global ocean, 77% and 44% more than that of GM3 and GM2, respectively, indicating a poor representation of upper density features under the bulk-forcing configuration in our model. Finally, the similarity between the density features of CW3 and GM3 indicates that the CSIRO AGCM windstress can be used to replace the NCEP windstress climatology without causing any significant negative effects in producing a realistic ocean stratification.

Fig.3.2 presents Levitus and the modelled zonal and annual mean density distributions for the global ocean, together with the results of GM3 - GM2 and GM3 - BF3. The CW3 solution is excluded due to its generally close similarity to GM3. Comparing 3.2a and 3.2b, we see clearly that GM3 simulates the vertical structure of density strikingly well in terms of both the pattern and magnitude in most of the global zonal mean section especially for the main oceans south of 60^{o}N and below 1000 m depth. Even in the Arctic, where the large light bias is a common deficiency for all spinups resulting from the poor simulation of the temperature and salinity (i.e., large fresh and warm errors to be shown later), GM3 displays encouraging improvement in the density field due to the better simulated salinity. Overall, this indicates that a fairly realistic stratification has been simulated successfully, in particular below 1000 m, with the GM3 configuration. In contrast, the GM2 result suffers a large density insufficiency (from more than 0.1 $kg\,m^{-3}$ in middle latitudes to over 0.15 $kg\,m^{-3}$ in southern high latitudes) at mid-depth and the abyssal ocean, as shown in Fig.3.2d, implying unrealistically weak stratification below the 2000 m depth in the world ocean. Fig.3.2f exhibits the overall enhancement of stratification in the whole column at all latitudes achieved with the GM3 configuration compared to the GM2 solution. Except for the layer above about 500 m in low and mid-latitudes, where GM3 gives weaker stratification than GM2, all basins show much stronger stratification in GM3 than GM2, as indicated by the significantly strengthened vertical

contrast of density. Of particular importance is that the spuriously weak stratification off Antarctica in the GM2 solution is corrected. The improvement in the southern latitudes water column stratification with the GM3 configuration has a substantial effect on the local convective adjustment and may result in slower (and therefore more realistic) ventilation over the depth of the Southern Ocean.

The BF3 density zonal mean features illustrated in Fig.3.2c and 3.2e are strongly associated with the poor solutions for the tracers, in particular the salinity field, and will be discussed in the following sections.

3.2.2 Temperature Features

Fig.3.3 shows the vertical structure of the Levitus and the modelled temperature. The success of GM3 is achieved below around 1500 m in the main basins (Atlantic and Indian/Pacific Oceans) where, as can be seen from the global ocean profiles, GM3 gives the temperature closest to Levitus, with a minimum warm bias of less than 0.1 °C at 1720 m and 0.02 °C below 2350 m. In contrast, BF3 and GM2 show notable cold bias in this column, with the maximum departures being about -0.3 and -0.55 °C, respectively, near the bottom.

A common deficiency of all spinups in the main basins is the marked warm biases in subsurface water from under the uppermost level to around 1000 m depth. All models fail to represent the water thermal status realistically in this layer, with the largest global mean errors ranging from 1.12 to 1.52 °C at around 240 m.

In addition, GM3 still seems to perform relatively poorly for the upper layer in the Southern Ocean, with a generally warm error below 50 m. The largest bias (0.78 °C) is observed at around 100 m and notable errors (0.3–0.5 °C) can be found below 1000 m. However, such a noticeable warm bias actually does not have much negative impact on the deep Southern Ocean stratification (as already shown) because in the cold water near Antarctica the density structure is dominated by the salinity. BF3 gives the best profile below 1500 m in the Southern Ocean, but it suffers a large cold

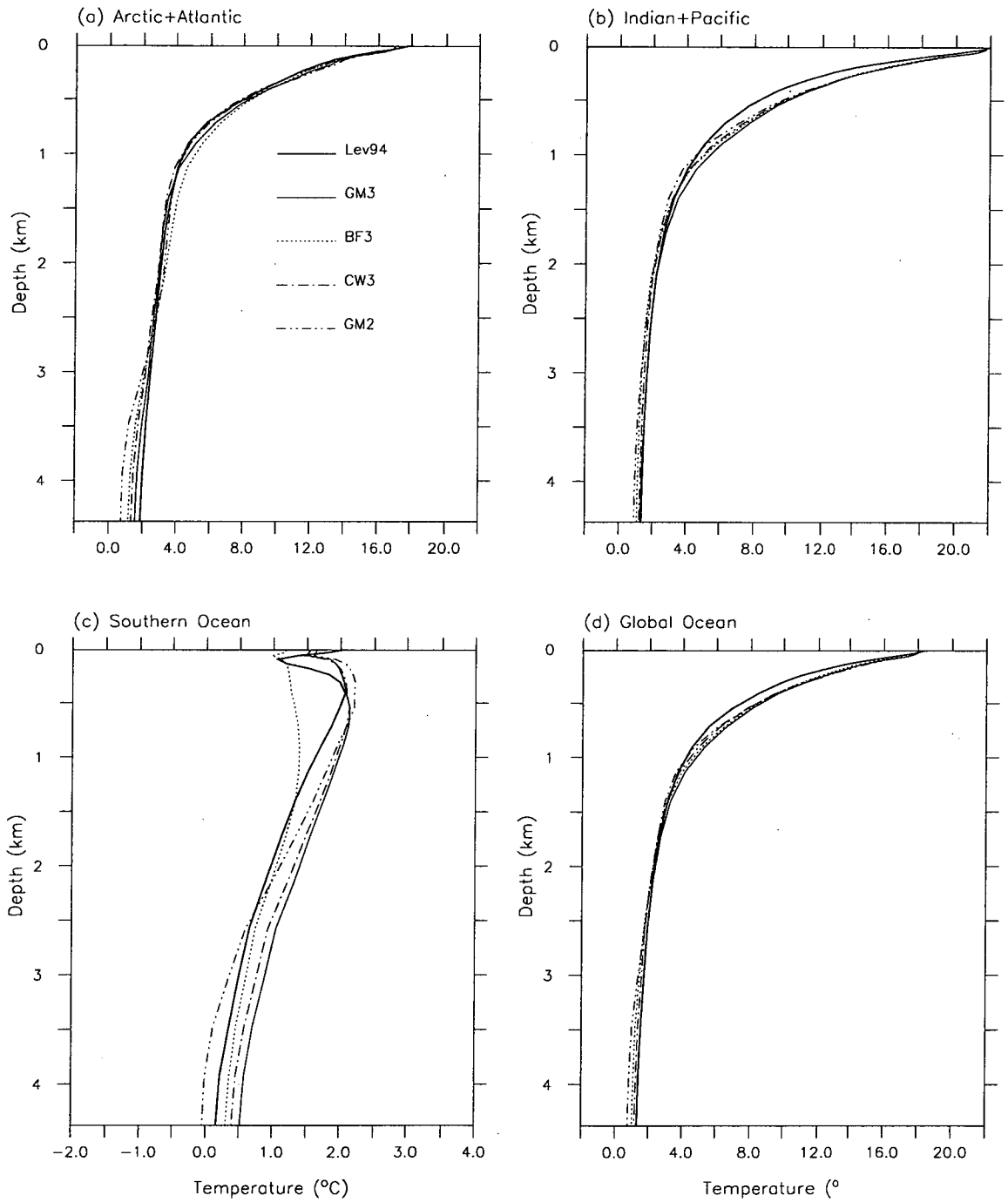

Figure 3.3: Vertical distribution of annual mean temperature in the (a) Atlantic, (b) Indian-Pacific, (c) Southern Ocean, and (d) global ocean.

bias in the thick subsurface layer and thus can not be thought to behave better than the others. GM2 shows a larger warm bias than GM3 in the layer 50–620 m and a marked cold bias below 2500 m, indicating spurious steep vertical temperature gradients in the Southern Ocean. It may be worth mentioning that, in spite of the evident deviations from Levitus, all relaxation spinups produce realistic temperature inversions in the upper 400 m layer in the Southern Ocean.

The RMS differences of the model results from the Levitus data listed in Table 3.1. verify the improvement of GM3 temperature at the abyssal depths in the global ocean, with the overall bias being merely 0.01 °C, in contrast to 0.44 °C for GM2 and 0.28 °C for BF3. However, due to the poor simulations for the upper and mid-depth layers, GM3 shows only slight improvement from GM2 in terms of the global total column mean. CW3 has a smaller RMS error than GM3, suggesting that the CSIRO AGCM windstress may be generally more beneficial to yielding a realistic vertical thermal structure than the NCEP windstress. The BF3 temperature also shows better accordance with Levitus than GM3 in terms of the global total column RMS index. However, it gives a very large cold bias (with RMS difference of 0.55 °C) below 2350 m in the Atlantic, reflecting the spurious feature that too shallow penetration of warm NADW is compensated by too much cold AABW in BF3 for this basin. This confirms the bulk forcing experiment results of Large et al. (1997).

The global ocean zonal and annual mean temperature distributions are shown in Fig.3.4 in comparison with Levitus. CW3 is omitted here because it is very close to GM3. All runs differ from the observations markedly above 1000-1500 m with the largest warm bias occurring near the equator, at around 200 m depth, which is a common feature for coarse-resolution models and is related to weak zonal currents and weak zonal slopes of the isotherms, as addressed by Large et al. (1997). Also evident is the large and noisy biases at around 65°N for all runs, which may result from the model topography error around that latitude in the model North Atlantic, where Iceland is removed and the sub-Arctic Front is displaced due to the coarse resolution. In the vast region from about 45°S to 60°N and from subsurface to around 1000 m depth, all spinups bear similar temperature deviation from Levitus

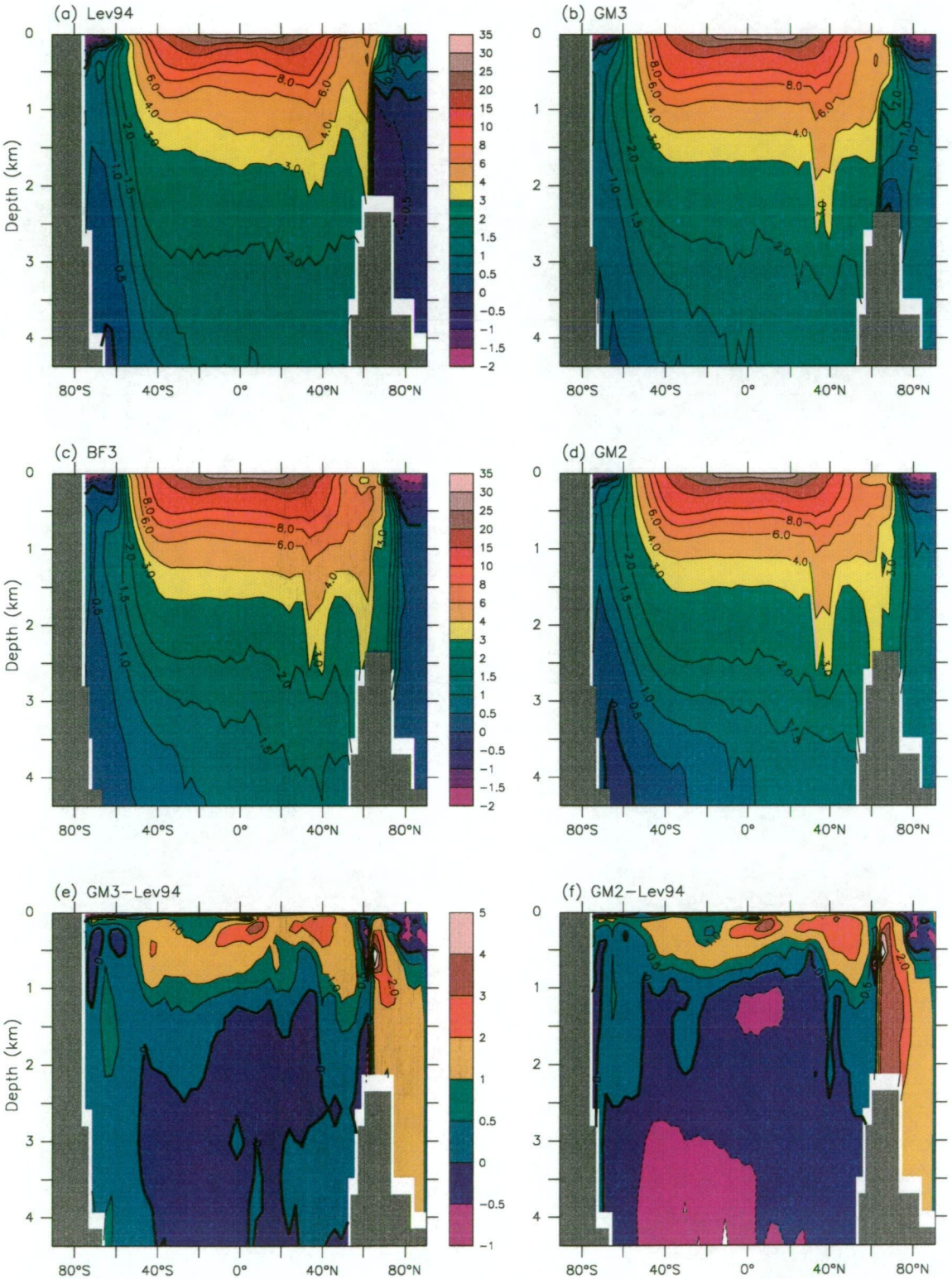

Figure 3.4: Zonally averaged temperature in the global ocean (units: °C). (a) Levitus, (b) GM3, (c) BF3, (d) GM2, (e) GM3 - BF3, and (f) GM3 - GM2.

in both the pattern and magnitude, indicating that the uppermost level relaxation control does not extend much below the surface in the low to mid-latitudes regions. GM3 distorts the temperature structure very little (with less than 0.3 °C cold bias) in mid-depth and deep water between 45°S and 60°N while BF3 and GM2 cause broader departure with over 1 °C cold bias near the bottom.

3.2.3 Salinity Features

Vertical distributions of the horizontally averaged annual mean salinities are presented in Fig.3.5. Unlike temperature, the salinity profiles show a clear distinction between one another, except for the GM3 and CW3 solutions which agree very closely almost everywhere.

At the uppermost level, all relaxation runs give the SSS close to Levitus whilst BF3 suffers extremely large fresh biases in all basins. Below this level, all spinups show clear salt deficiencies in the global ocean subsurface water above 1000 m, and BF3 gives far poorer upper vertical salinity gradients than the other runs. Further down in depth, the GM3 salinity comes close to Levitus, with the bias in the abyssal ocean reduced to nearly zero, owing to the compensation between the opposite errors in the two main basins. In contrast, GM2 drifts away steadily, reaching a large fresh bias up to 0.22 psu in the deep ocean. Clearly, the GM3 configuration has a much better control of the upper layer salinity than BF3, and, as an advantage over GM2, it carries this control down to the abyssal ocean, making the deep water sufficiently salty. This feature assures an evident minimum of global mean salinity at around 800 m and we can therefore see the distinctive characteristics of bottom water and intermediate water formed in the GM3 solution. In contrast, GM2 and BF3 fail to clarify the water mass formations due to their unrealistically weak vertical salinity contrasts.

The overall improvement of model salinity distribution with the GM3 configuration can be further verified by the RMS differences from Levitus, as listed in Table 3.1. Clearly, GM3 performs the best in simulating the vertical structure of salinity in all

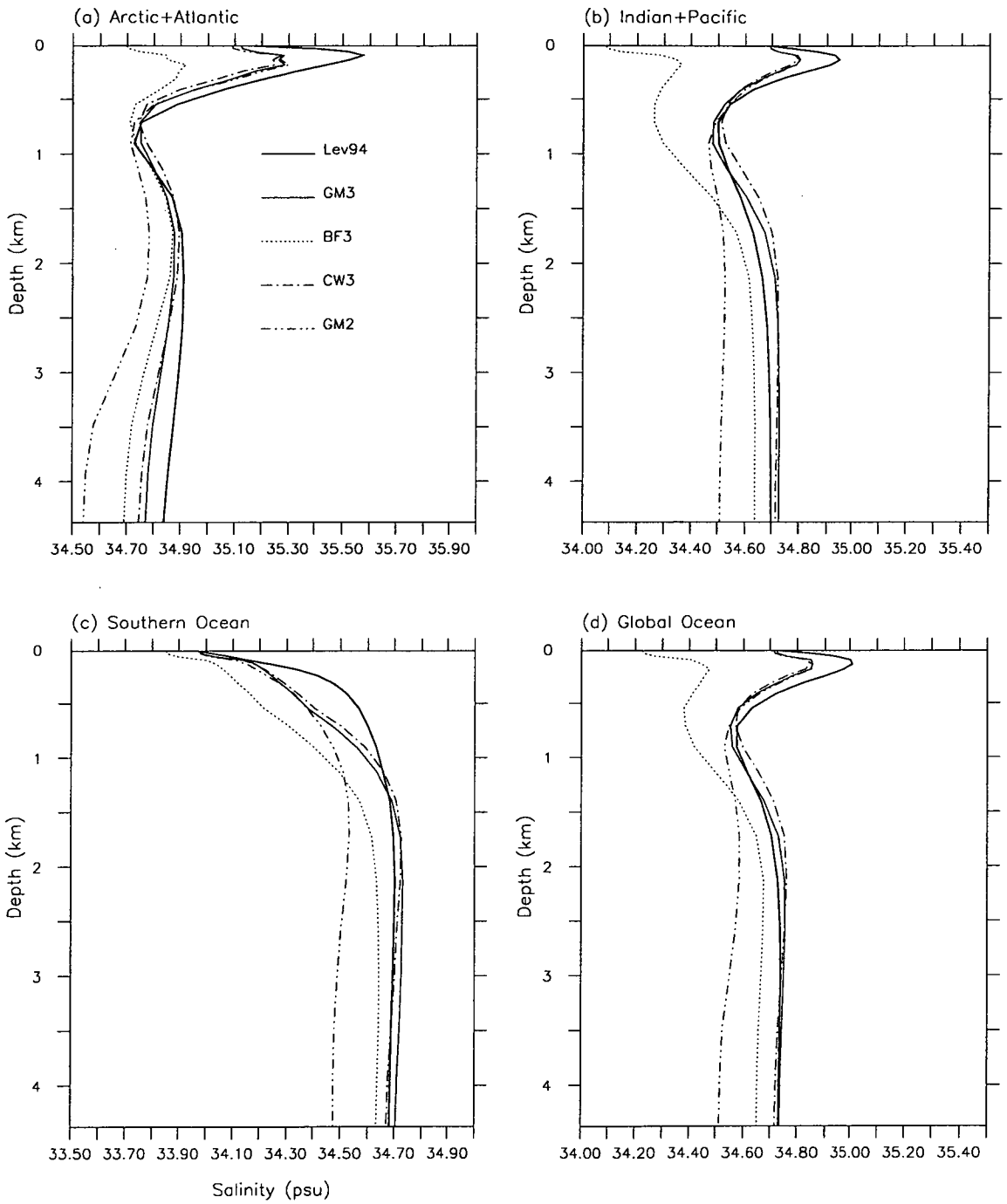

Figure 3.5: Vertical distribution of annual mean salinity in the (a) Atlantic, (b) Indian-Pacific, (c) Southern Ocean, and (d) global ocean.

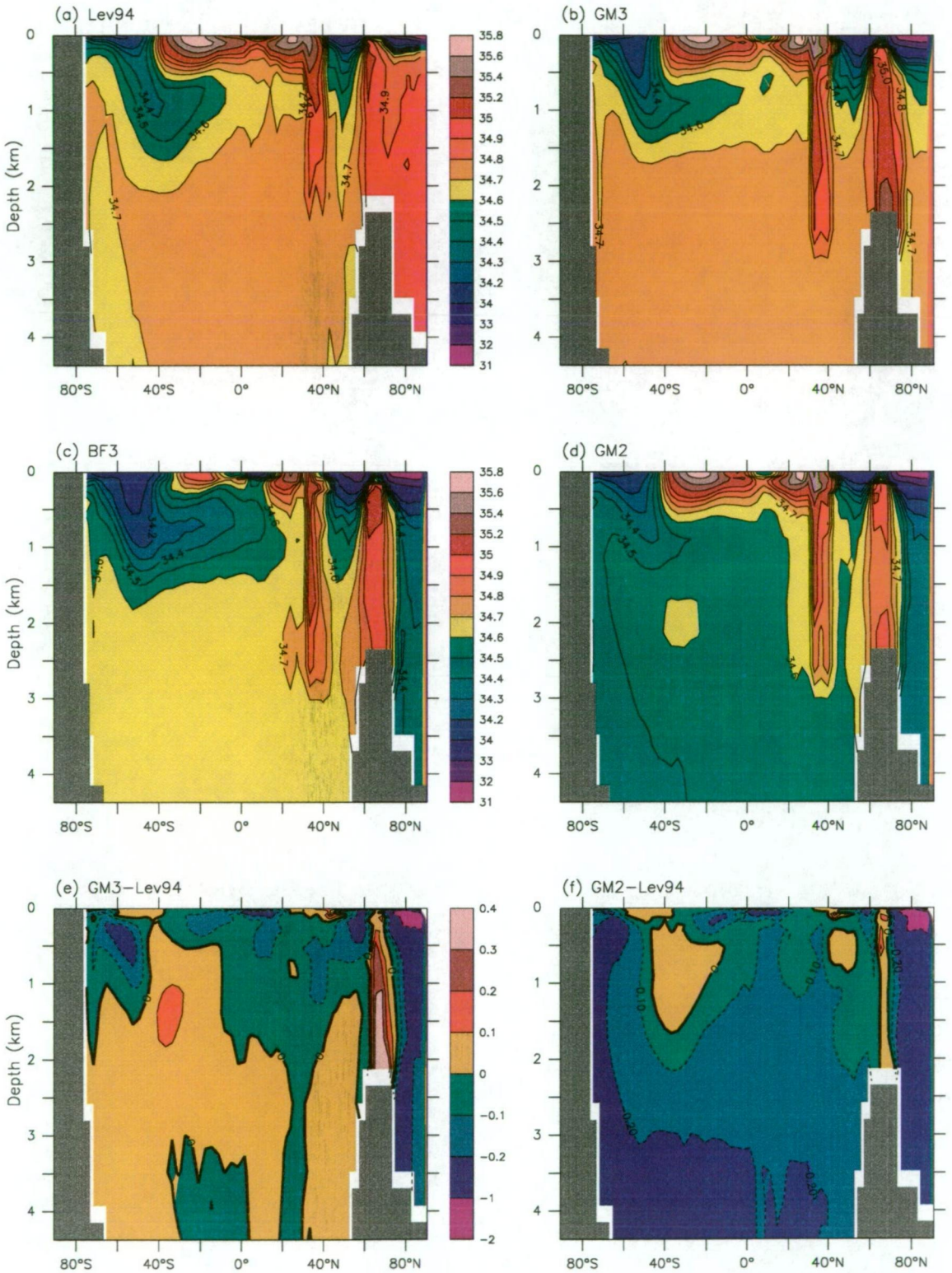

Figure 3.6: Zonally averaged annual mean salinity (in psu). (a) Levitus, (b) GM3, (c) BF3, (d) GM2, (e) GM3 - BF3, and (f) GM3 - GM2.

basins. In the global ocean, for instance, GM3 has 0.09 psu error in the upper layer, and has only 0.02 and 0.01 psu bias in the mid-depth and abyssal ocean, respectively, with the whole column RMS deviation being merely 0.04 psu, contrasting sharply with the GM2 (BF3) errors of 0.09 (0.39), 0.11 (0.09), 0.2 (0.08) and 0.15 (0.19) psu in these columns, respectively.

Fig.3.6 shows the annual and zonal mean salinity features for the global ocean. GM3 produces the most realistic salinity field, with the widely spreading fresh biases in GM2 (over 0.2 psu below 3000 m from the south to 40°N) and BF3 (up to 0.2 psu near the bottom at around 10°S) totally eliminated, owing to the modified salinity forcing in the North Atlantic. The upper ocean sees the most marked deviation (mainly fresh errors) from Levitus in all runs, but GM3 departs the least. The improvement in the salinity vertical structure ensures that GM3 represents realistically the tongue of low salinity Antarctic Intermediate Water (AAIW) as shown in Fig.3.6a from Levitus. This fresh tongue extends from the Southern Ocean surface to about 1500 m depth at around 40°S and reaches 10°S at 1000 m depth, as depicted by the 34.6 psu contour. GM3 simulates this feature very successfully in both the extent and "strength" while GM2 produces a very weak, shallow-penetrating tongue constrained to south of 50°S due to its weak salinity contrast in the upper and lower layers.

The reasonable vertical distribution of salinity for GM3 is central to its realistic stratification shown in Fig.3.2. In the Southern Ocean, for example, the mid-depth and deep water is well stratified due to the sufficiently high salinity which compensates the warm bias efficiently. In contrast, the GM2 solution features a poorly stratified Southern Ocean because of its too large fresh error in the mid-depth and deep water, despite the large cold bias there. It must be mentioned that, although Fig.3.2c shows a quite reasonable density distribution for BF3 below 1500 m in mid-latitudes, such a "near-realistic" feature is, to a large extent, the result of greater compensating temperature and salinity errors in the deep ocean than that for the GM3 case, and the southern high latitudes in BF3 still have a notable low density bias (0.05–0.1 $\mathrm{kg\,m^{-3}}$). In addition, the large fresh error in the upper and mid-depth water causes unrealistic strong stratification in low and mid-latitudes as shown by

Fig.3.2e. The above results show that employing bulk forcing in our model does not improve the water mass production to anywhere near the same extent as it done in GM3. The BF3 solution will thus not be used in the comparisons hereafter, although it does display some other features close to reality. The CW3 result will not be discussed further as well due to its similarity to GM3.

3.3 Surface Fluxes

In the above we have demonstrated that by using the GM3 configuration our ocean model yields a generally more realistic equilibrium climate in terms of the water properties on basin and global scales. This achievement results mainly from the modifications of the surface thermohaline forcing conditions which are expected to affect the implied heat and freshwater fluxes at the air-sea interface. The following analysis will address the question to what degree the GM3 surface fluxes are in agreement with observations. Since previous studies (e.g., Hirst and Cai 1994; Toggweiler and Samuels 1995; England and Hirst 1997) reveal that the attempt to improve the model ocean climate, in particular the deep water formation, by enhancing surface relaxation often causes serious distortion to the surface fluxes, it is important to ensure that such changes in GM3 are within an acceptable range. Mention must be made here that, the global ocean net heat and fresh water flux fields are not well known in detail. The existing climatologies of observation contains large uncertainties from various deficiencies such as instrumental errors, flux parameterizations and sparse observational coverage, particularly for remote regions like the Southern Ocean (Weller and Tayor 1993; Doney et al. 1998). This brings special difficulty to the comparison between our model results and observations.

The model implied heat and salt fluxes are converted from the differences between the model equilibrium surface temperatures and salinities and the surface restoring fields by

$$Q_h = \frac{\rho_0 c_w \Delta z}{\tau_R}(T - T_R) \tag{3.1}$$

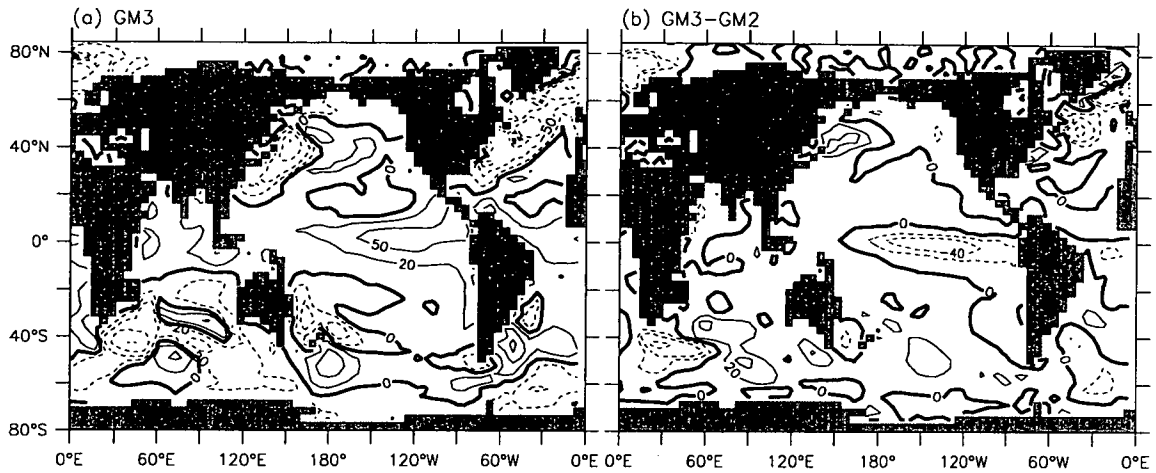

Figure 3.7: Annual mean surface heat fluxes (W m^{-2}) for GM3 and GM3 - GM2. Contours are: (a) 0, ±20, ±50, ±100, ±150, -250; (b) 0, ±20, ±40, ±80, ±120.

$$Q_s = \frac{\rho_0 \Delta z}{\tau_R}(S - S_R) \tag{3.2}$$

and the implied fresh water can be given by

$$Q_{fw} = -\frac{s_y}{\rho_0 S_0} Q_s \tag{3.3}$$

where the constants $c_w = 4000$ JK^{-1}kg^{-1} is the specific heat of sea water; $\rho_0 = 1025$ kg m^{-3} the surface water density; $\Delta z = 25$ m the uppermost layer thickness; $\tau_R = 1.728 \times 10^6$ seconds is the relaxation time scale, i.e, 20 days; $s_y = 3.1536 \times 10^7$ seconds/year is the number of seconds in a year; and finally, S_0 is a constant reference salinity and is taken to be 34.7 psu instead of the local salinity (so that the globally integrated zero net salt flux assures the global zero net freshwater flux). T, S and T_R, S_R are the model first level tracers (temperature and salinity) and the local restoring tracers, respectively, with units of K for T and psu for S. The heat flux Q_h and fresh water flux Q_{fw} have units of W m^{-2} and m yr^{-1}, respectively.

3.3.1 Heat Flux

The annual mean heat fluxes in the global ocean are presented and compared in Fig.3.7 for the GM3 and GM2 solutions. Fig.3.7a shows that the GM3 ocean gains

heat mainly in the equatorial regions and loses heat in mid and high-latitudes. As anticipated, heat flux gets into the ocean mainly in the vast region of the tropical Pacific. The maximum values are over 80 $W\,m^{-2}$ in this heating area and located between 120°W and 150°W on the equator. In contrast, GM2 produces a maximum heating of over 140 $W\,m^{-2}$ in this region, and the Oberhuber (1988) climatology, which is constructed from the COADS data, shows a large heating area centered around 110°E on the equator with a maximum value of over 100 $W\,m^{-2}$. In reality this region has large absorption of solar radiation and receives sensible heat from the air because of the large air-sea temperature difference which results from the local strong upwelling. Over large areas in the subtropics (around 20°S/N) and the polar regions, the heat fluxes are quite small, i.e., generally within ± 50 $W\,m^{-2}$. Both models simulate the maximum heat loss centers off the east coasts of Asia and North America, and also the southwestern Indian Ocean. In the North Atlantic, where in reality the most intense air-sea interaction occurs due to the frequent and lasting strong physical forces, extremes of wind and cold, incursions of icebergs and sea ice, GM3 simulates the largest annual mean heat loss of about 270 $W\,m^{-2}$ in Demark Strait, and a slightly weaker center with the maximum up to 210 $W\,m^{-2}$ just south of the Labrador Sea. Such large annual mean heat loss in the North Atlantic is not found in the GM2 case which shows the largest value of only about 190 $W\,m^{-2}$ in the Demark Strait. The average heat fluxes over region (0–90°W, 30–75°N) for GM3 and GM2 are -42.6 and -36.3 $W\,m^{-2}$, respectively, indicating a slightly larger heat loss in GM3, and the overall impact of the GM3 configuration on the heat budget in the North Atlantic is not very significant.

As regards the observations in the North Atlantic, the Oberhuber (1988, see also Large et al. 1997) map shows a heat loss center with a maximum value over 175 $W\,m^{-2}$ in the region off the east coast of America (between 35 and 40°N), over the western boundary currents, and generally small values in other areas (less than 75 $W\,m^{-2}$. Meanwhile, the NCEP-STR surface flux climatology (Doney et al. 1998), which is constructed using a bulk-flux scheme (e.g., Large et al 1997), a prescribed surface atmosphere state from the NCEP reanalysis and the observed SST climatol-

ogy of Shea et al. (1990), gives larger annual mean heat loss in the North Atlantic, particularly over the western boundary currents (see Fig.2 and Fig.3 of Doney et al. 1998) where the largest annual heat loss reaches over 225 $W\,m^{-2}$. Moreover, the NCAR CSM ocean spinup using bulk forcing gives the largest heat loss of the order of more than 1000 $W\,m^{-2}$ (in fact, up to 1398 $W\,m^{-2}$) over the Denmark Strait and off the southern tip of Greenland (see Fig.14 of Gent et al. 1998). Due to the large uncertainty in observations, our results in the North Atlantic may be taken as reasonable. In the Southern Ocean, both spinups show no spurious large surface heat loss in the whole region (less than 80 $W\,m^{-2}$ south of 50°S and less than 55 $W\,m^{-2}$ near Antarctic). GM3 and GM2 show very similar heat flux patterns in terms of both the magnitude and spatial variability. However, there are still some difference in the overall heat budgets, i.e., the averages over the whole Southern Ocean are -4.5 and -8.5 $W\,m^{-2}$ in GM3 and GM2, respectively, indicating less heat loss in GM3 than GM2, in contrast to that in the North Atlantic mentioned above.

It is of interest to examine the winter heat flux (figures not shown) in the well-known deep water formation regions. The Southern Ocean sees a winter average of heat flux of -31.8 $W\,m^{-2}$ in GM3 and -36.2 $W\,m^{-2}$ in GM2, nearly the same as the annual mean contrast. In the southwestern corners of the Ross and Weddell Seas where the Southern Ocean overturning originates, GM3 also shows very small heat loss changes which cause little impact on the buoyancy fluxes near Antarctica. The small heat fluxes in the Southern Ocean is believed to be realistic according to Jacobs et al. (1985). In the North Atlantic, however, the winter heat fluxes of GM3 and GM2 have large differences in magnitudes, e.g., GM3 shows heat loss as large as 420 $W\,m^{-2}$ in the Demark Strait and 510 $W\,m^{-2}$ south of the Labrador Sea, in contrast with that in GM2 of 265 $W\,m^{-2}$ and 300 $W\,m^{-2}$. As we know, the time integrated heat flux dominates the late winter SST which is of great importance to the North Atlantic overturning. Since the other seasons see quite similar heat flux patterns in GM3 and GM2 (and even generally larger summer heat gain in GM3 than GM2 in the North Atlantic, especially the Denmark Strait), it is the substantially enhanced winter heat loss that triggers the deeper North Atlantic overturning and

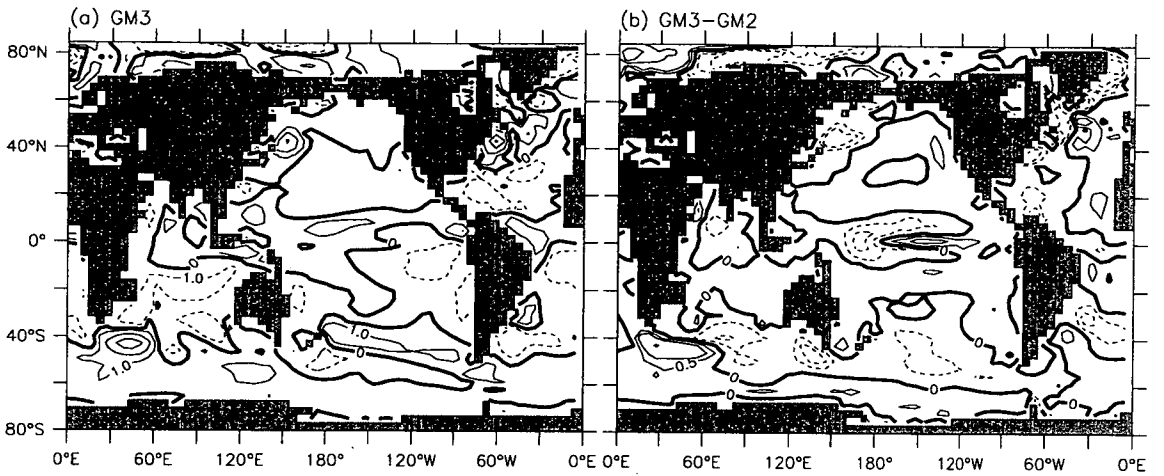

Figure 3.8: Surface freshwater fluxes (mm yr^{-1}) for GM3 and GM3 - GM2. Contours: (a) 0, ±1, ±3, ±6, ±9; (b) 0, ±0.5, ±1, ±3, ±5, ±7.

thus improves the NADW properties in GM3. In addition, the GM3 winter heat flux peak is within the acceptable range, considering the large uncertainty in the observations.

3.3.2 Freshwater Flux

Fig.3.8 presents the annual mean freshwater flux in the global ocean for GM3 and its change from GM2. Compared to heat flux, the fresh water flux distribution in the global ocean is even less well known from observations. Nevertheless, the model implied annual mean fresh water fluxes have a pattern generally consistent with the Oberhuber (1988) and NCEP-STR (Doney et al. 1998) climatologies, except for some small-scale positive and negative concentrations of up to 10–12 m yr^{-1} at locally isolated grid boxes which make the distribution noisy. Fig.3.8a contains net fresh water input in the eastern tropical Indian Ocean, tropical Pacific and Atlantic, South Pacific convergence zones, mid-latitude storm tracks and the Southern Ocean. In addition, large freshwater input is also found in the North Atlantic, which may be too large/extensive compared to the Oberhuber (1988) climatology and thus probably somewhat spurious. The ocean loses fresh water mainly in the subtropical gyres which are the net evaporation zones in reality. Fig.3.8b shows GM3 has larger fresh water gain than GM2 over most of the Pacific Ocean, the eastern part of the

Atlantic and nearly the whole Southern Ocean. But over the western boundary currents, we see less freshwater gain in GM3. In the North Atlantic region (0–90°E, 30–75°N), GM3 sees an overall slightly larger winter freshwater loss than GM2 (0.22 vs 0.16 m yr^{-1}). In the Ross and Weddell Seas (south of 66.9°S), this contrast becomes 0.38 vs 0.42.

Detailed comparison with observations especially in the remote polar regions is hard due to the sparse measurements and rough estimates. In the Ross Sea, for example, Jacobs et al. (1985) estimate a freshwater loss of 0.95 m yr^{-1} due to the formation and removal of sea ice, a freshwater gain of 0.51 m yr^{-1} made up of 0.36 m yr^{-1} glacial meltwater and an amount of 0.15 m yr^{-1} from P - E, which all together make a budget of 0.44 m yr^{-1} net freshwater loss in this region. However, Zwally et al. (1985) estimate much larger sea ice formation rates (4.6 to 7.8 m yr^{-1} for the entire Antarctic shelf) and Wu et al. (1997) reported an intermediate freshwater loss of around 1 m yr^{-1} for both the Ross and Weddell Seas in their coupled ice-atmosphere model. Our spinups give very small annual mean fresh water loss just at the southwestern corners of the Ross and Weddell Seas. In fact, the southernmost row of model grids (73.3–76.5°S band) in the Ross Sea has an average loss of merely 0.12 in GM3, whilst the row nearest Antarctica in the Weddell Sea (70.1–73.3°S band) sees 0.4 m yr^{-1} loss in GM3. Such a weak fresh water loss, together with the weak heat loss discussed above, suggests a weak buoyancy loss as shown below, and is responsible for the relatively weak Southern Ocean overturning, as to be discussed later in this chapter.

3.3.3 Buoyancy Flux

The net fluxes of heat and freshwater (or salinity) at the air-sea interface produce an ocean surface buoyancy flux (or density flux), which acts to convert ocean surface waters from one density class to another, effectively driving a cross-isopycnal mass flux at the surface (Tziperman 1986). Following Curry and Webster (1992), we

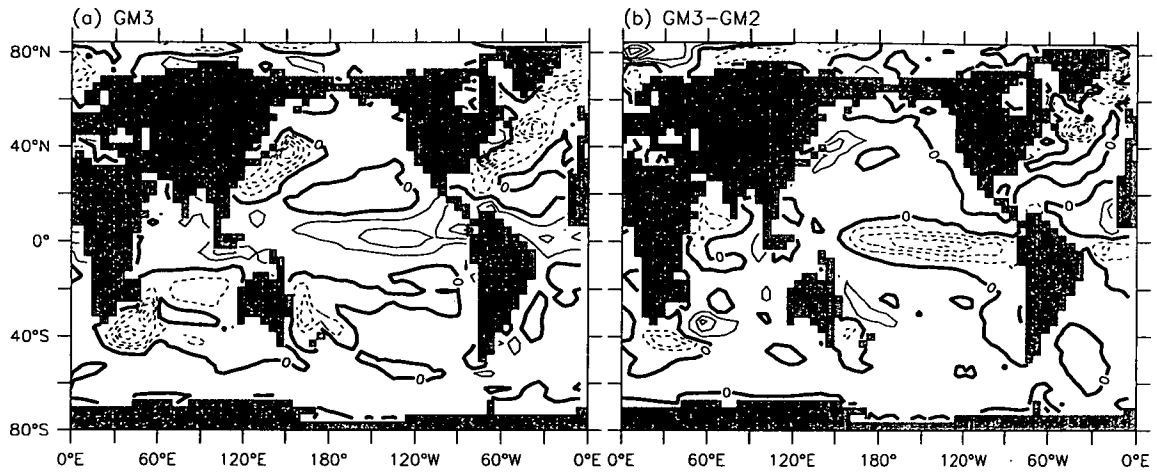

Figure 3.9: Surface buoyancy fluxes (10^{-6} kg $m^{-2}s^{-1}$) for GM3 and GM3 - GM2. Contours: (a) -10 to 8 with interval 2; (b) -6 to 6 with interval 1.

calculate buoyancy flux by

$$\begin{aligned} Q_b &= \frac{\alpha}{c_w} Q_h - \beta Q_s \\ &= \frac{\alpha}{c_w} Q_h + \frac{\rho_0 S_0 \beta}{s_y} Q_{fw} \end{aligned} \tag{3.4}$$

where c_w, ρ_0, S_0, s_y, Q_h, Q_s and Q_{fw} are the same as in equations (3.1) and (3.2). α and β are the thermal expansion and saline contraction coefficients, dependent on sea surface temperature and salinity and can be found in Curry and Webster (1992) (see their Table 1.4). The buoyancy flux obtained above is in units of kg $m^{-2}s^{-1}$. Its negative value meets the instability criterion, and would lead to sinking motion in the ocean surface.

Fig.3.9a and 3.8b display the annual mean buoyancy flux distributions over the global ocean for TGM3 and TGM2 respectively. The features shown here can be readily illustrated by comparison between Fig.3.7 and Fig.3.8. For example, in the GM3 case, the tropical oceans show buoyancy input due to the joint effect of heat and freshwater inputs, indicating the upwelling motions in the tropical ocean surface. The North Atlantic shows extensive buoyancy loss, implying surface sinking over the large area as expected. Obviously, this feature is the result of large heat loss overwhelming the freshwater gain in this region, as shown by Fig.3.7a and

3.8a. In addition, the northwestern Pacific (off the coast of southeastern Asia) and southwestern Indian Ocean see large buoyancy losses due to the overwhelming local heat loss as well. We can also find a notable buoyancy loss off the east coast of Australia, which is the joint effect of the heat and freshwater losses there. The above comparison shows that, in general, heat fluxes dominates freshwater fluxes in determining the buoyancy flux patterns, with the exception of Southern Ocean where the heat fluxes are very small and the effects of heat and freshwater fluxes are therefore comparable. Only in the Ross and Weddell Seas in particularly their southwestern corners, freshwater flux makes the main contribution in determining buoyancy flux. The contrast between the North Atlantic and Southern Ocean reveals the different driving forces for deep water formation in the world ocean, i.e., as is well known, it is the air-sea heat exchange that controls the North Atlantic overturning, and the ice-sea salt exchange (by ice transport, melt and formation) that determines the Southern Ocean overturning.

3.4 Northward Heat and Freshwater Transports

The annual-mean northward oceanic heat and freshwater transports can be readily derived from the implied ocean surface heat and freshwater (or salt) fluxes at equilibrium, that is, their meridional derivatives are equivalent to the zonal integrals of the surface fluxes (Weaver and Hughes 1996; Large et al 1997). Thus, we calculate the transports at latitude φ by integrating the flux zonal integrals from the southernmost point φ_s (of the global ocean) to φ:

$$T_h(\varphi) = \int_{\varphi_s}^{\varphi} \int_{\lambda_w}^{\lambda_e} F_h a_0^2 \cos(\phi) d\lambda d\phi \tag{3.5}$$

$$T_{fw}(\varphi) = -\frac{1}{\rho_0 S_0} \int_{\varphi_s}^{\varphi} \int_{\lambda_w}^{\lambda_e} F_s a_0^2 \cos(\phi) d\lambda d\phi \tag{3.6}$$

where $\rho_0 = 1025$ kg m^{-3}, $S_0 = 34.7$ psu, a_0 is the Earth's radius. λ_e, λ_w are the meridional (eastern and western) boundaries of the basin. F_h and F_s are the surface heat and salt fluxes, respectively.

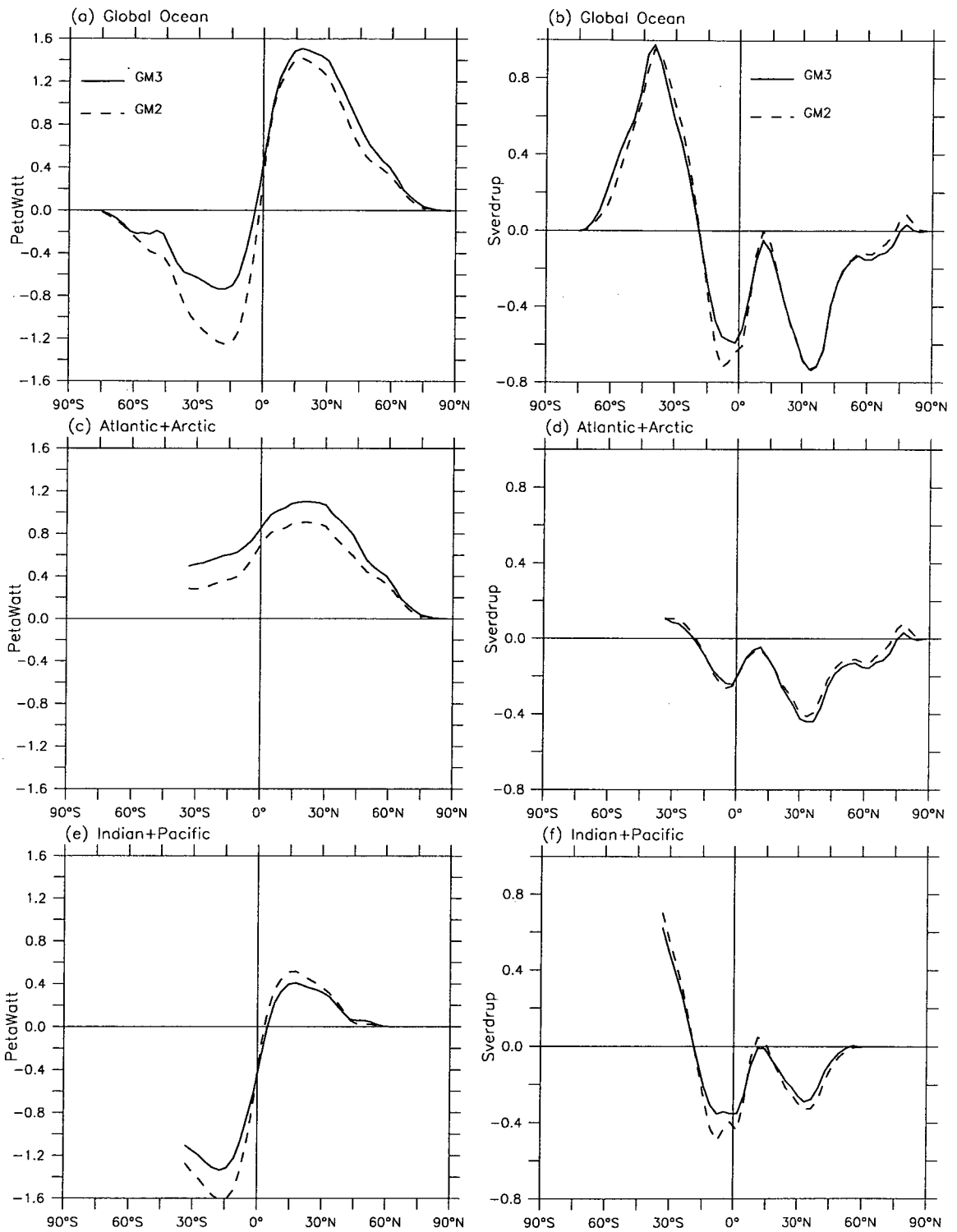

Figure 3.10: Annual mean northward heat (left column) and freshwater (right column) transports: (a)(b) global ocean, (c)(d) Atlantic, and (c)(d) Indian-Pacific.

Fig.3.10 shows the calculated annual mean northward heat and freshwater transports in the global ocean and two individual basins, i.e., Atlantic which includes the Arctic, and Indian-Pacific basins, for the GM3 and GM2 solutions.

GM3 and GM2 bear notable differences in the global northward heat transport as shown in Fig.3.10a, with the largest difference being 0.51 PW (PW $\equiv 10^{15}$ W) at 17.5°S where GM3 and GM2 show peak southward transports of 0.74 and 1.25 PW, respectively. This results jointly from the reduction of southward and enhancement of northward transports in GM3 at that latitude in the Atlantic and the Indian/Pacific Oceans, respectively, as can be seen from Fig.3.10c and 3.10e. The residual estimates from the atmospheric analyses of Trenberth and Solomon (1994) (referred to as the T-S estimate hereinafter) give the largest global southward transport of 1.8 $\pm$ 0.4 PW southward transport at 17.5°S and neither of our results is within their estimated range. At 17.5°N, where both our results and T-S estimates indicate the largest northward transports, GM3 gives 1.51 PW and still stays outside the T-S estimate range (2.1 $\pm$ 0.4 PW). Nevertheless our solutions show a quasi-symmetric pattern about the equator. In addition, our results are in better agreement with the inverse ocean model products of Macdonald and Wunsch (1996) (referred to as M-W), although M-W only gives transport data at a few individual latitudes and is believed to have large uncertainty. For example, M-W estimates the northward transports 1.5 $\pm$ 0.25 PW at 24°N and 0.6 $\pm$ 0.25 PW at 47°N, very close to the 1.47 (1.35) PW and 0.7 (0.5) PW values for GM3 (GM2) at these two latitudes, respectively. At around 30°S, GM3 (GM2) shows southward transport of 0.63 (1.07) PW, also within the M-W estimate range of 0.8 $\pm$ 0.25 PW. In the Atlantic-Arctic basin, our results show that heat is transported northward everywhere. Such a pattern is realistic and in good agreement with both the T-S and M-W estimates. Further south, our results generally lie in between these two estimates, i.e., larger than T-S but smaller than M-W at latitudes south to 20°N, except for the near southernmost latitudes where GM3 is larger than M-W at 23°S and nearly the same as M-W at around 27°S. The systematically larger northward heat transport in GM3 than GM2 is associated with the substantial enhancement of

the North Atlantic thermohaline circulation, as to be shown later, which strengthens the conveyor belt and leads to stronger northward flow in the upper ocean layer, bringing more heat to compensate the larger heat loss in the North Atlantic. Regarding the Indian-Pacific basin, our results show a large discrepancy from T-S at 17.5°N/S, just like the case for the global ocean. However, at 24°N and 30°S, GM3 shows 0.36 PW northward transport and 1.15 PW southward transport, respectively, very close to the M-W estimates (0.45 $\pm$ 0.25 and 1.3 $\pm$ 0.25 PW). The generally weaker southward heat transport south of the equator in GM3 is associated with the smaller heat gain in the mid and east tropical Pacific as shown by Fig.3.8.

As for the freshwater transports, much smaller discrepancy is found between GM3 and GM2. Since few observations are available for the purpose of comparison, it is hard to assess our model performance for freshwater transport. However, Wijffels et al. (1992) calculated the northward freshwater transport from the Baumgartner and Reichel (1975) surface freshwater flux climatology which has large uncertainty due to the poor sampling (see also Large et al. 1997). Given this difficulty, our results are in good agreement with the rough Wijffels et al. estimates in terms of the meridional "fluctuation" pattern and the magnitudes of some maximum values in both the global ocean and individual basins. For instance, GM3 shows the largest global ocean northward freshwater transport of 0.98 Sv (SV $\equiv 10^6$ m^3s^{-1}) at 39.8°S and the largest southward transport of 0.73 Sv at 33.5°N, which contrasts with the observed largest northward transport of 0.91 Sv at 40°S and the second largest southward transport of 0.7 Sv at 40°N. The observed largest southward transport is about 0.72 Sv near the equator, while GM3 shows 0.59 Sv at 1.6°S which is its second largest southward transport. The major discrepancy of both GM2 and GM3 is that the models do not transport freshwater northward in latitudes between 17.5°S and 74.9°N whereas the observed shows a northward transport band from about 7°N to 22°N, with the maximum value being 0.31 Sv at around 14°N. Such a bias occurs mainly in the Atlantic and is a common feature for most OGCMs (e.g., Weaver and Hughes 1996; Large et al. 1997), no matter what kinds of surface forcings are employed.

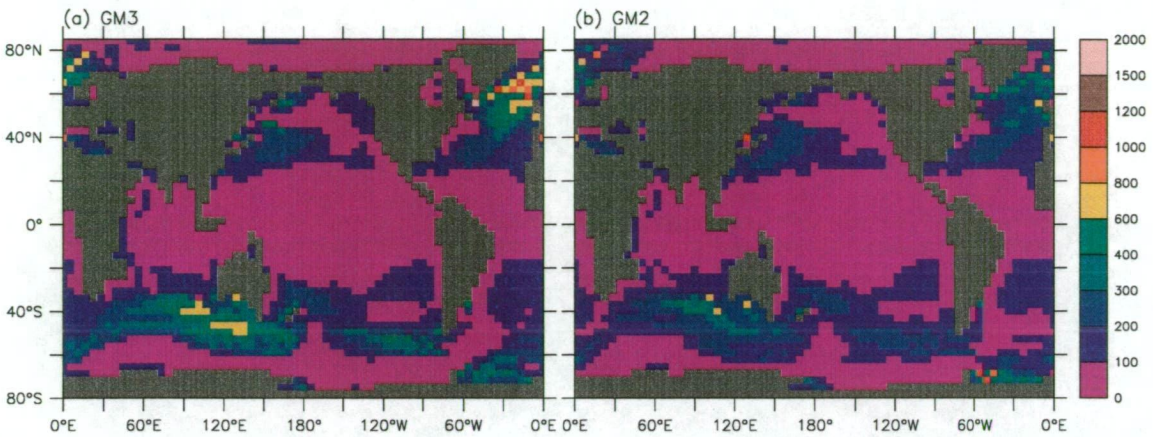

Figure 3.11: Maximum depth of convection in the annual cycle. (units: m)

3.5 Vertical Convection

As demonstrated above, compared to GM2, the GM3 configuration achieves significant improvement in the water column stratification of the world ocean. This change occurs firstly near the surface due to the modifications to thermohaline forcings and has a direct effect on the depth and extent of vertical convective mixing which is driven by buoyancy. In a coupled atmosphere-ocean system, the convective activity in the ocean is very important because it can transport any higher density perturbation at the air-sea interface into the interior water by rapid vertical adjustment. This adjustment, through a simple hydrostatic parameterization in most ocean models, efficiently homogenizes the entire unstable water column within a very short time (actually just one to several model time steps). Then other processes such as diffusion and advection act to operate lateral exchange between the convection site and its surroundings, transferring the water property to other regions. In the real ocean, *the mixed fluid disperses under the influence of gravity and rotation, spreading out at its neutrally buoyant level, leading, on a timescale of weeks (after the cessation of strong forcing at the surface which triggers the convection), to the disintegration of the mixed patch and reoccupation of its site by the stratified fluid of the periphery* (The Lab Sea Group: Marshall et al. 1998). Apparently, convective activity plays an important role in affecting the water mass transformation. Without convection, the vertical motion (or meridional overturning) requires tens of years to take the

surface signal to 1000 m depth and needs hundreds to thousand of years to bring it to abyssal ocean.

Fig.3.11a and 3.11b show the world ocean maximum depth of convection during the course of the annual cycle for the GM3 and GM2 spinups, respectively. This variable is taken as the depth over which the slope of the neutral density surfaces exceeds 1/100 (the maximum slope allowed for isopycnal tracer diffusion), which generates slant-wise vertical buoyancy flux that partly mimics and replaces explicit convective mixing (Hirst and Cai 1994, Gough 1997). It has been proven by previous studies (e.g., Danabasoglu et al. 1994; Hirst and McDougall 1996; England and Hirst 1997) that the GM scheme efficiently reduces the spurious extensive convection which would occur in the case with no GM scheme, especially near Antarctica. Our two solutions, with generally similar global patterns, show no deep convections in the Southern Ocean and Antarctic shelf region. This is in particular the case for GM3, which shows very shallow penetration of convection down to only 400 m depth in the Ross Sea near Antarctica, consistent with the observations (e.g., Olbers et al., 1992) that the ocean between 55°S and 70°S is mostly characterized by upwelling of circumpolar deep water (CDW) from the north and shallow surface mixing layers in high southern latitudes. The GM2 result, however, shows a bit deeper convection in the Ross Sea near Antarctica, which can penetrate to 1000 m depth at a few individual grid points. Such a difference between GM3 and GM2 can be readily verified by Fig.3.2f which shows a clear strengthening in the GM3 surface layer stratification near Antarctica relative to GM2. Accordingly, we can also find an explanation in Fig.3.2f for there being slightly more extensive convection down to 600 m depth in GM3 than GM2 in mid southern latitudes, i.e., the weaker GM3 surface layer stratification in that band aids a deeper convection. In general, the surface convection pattern (in both penetration depth and extent) of the GM3 solution seems to be more realistic than GM2 in the region near Antarctica.

In the North Atlantic, GM3 sees overall more extensive convection and, at some grid points, deep convection can penetrate down to 1000 m and the deepest can reach 1900 m depth at a single point in the Labrador Sea. In reality, such deep

convection in the Labrador Sea is not surprising because this region is characterised by appropriate physical conditions and intense air-sea interactions. The cyclonic atmospheric circulation over the North Atlantic in winter advects cold and dry arctic air over the relatively warm waters of the Labrador Sea and induces large heat export from the sea surface up to many hundreds of watts per square meter which results in large buoyancy loss and triggers active convection. For example, deep convection penetrating down to more than 2200 m depth was observed in the Labrador Sea in the 1993 winter (The Lab Sea Group: Marshall et al. 1998). In contrast, convective overturning is somewhat weaker in GM2 and is limited to a shallower layer above 800 m depth in the whole region. Again, this difference of convection penetration between GM3 and GM2 can be explained using the density distribution change in the band from 40°N to 60°N shown in Fig.3.2f which displays a weakening in the GM3 stratification above 800 m depth. In fact, the zonal mean density difference feature in the Atlantic alone (or the cross section at around 50°N) (not presented here) shows much more substantial weakening in the GM3 stratification between 50°N and 60°N: the densification (relative to GM2) decreases monotonically from over 0.35 $\mathrm{kg\,m^{-3}}$ near the surface to less than 0.05 $\mathrm{kg\,m^{-3}}$ at 2000 m depth. Such a strong stratification weakening favours the generation of convective instability in that water column and the penetration of the local convective overturning to deeper levels. This change in the North Atlantic surface convection of the GM3 solution contributes to the improvement of the NADWF. With the GM3 configuration, the convective mixing transfers (at least part of) the surface properties rapidly to a deeper level and enhances the density (by increasing salinity) of this water column (of larger thickness), which makes the sinking branch of the thermohaline overturning circulation in the North Atlantic ventilate the deep ocean with saltier (and denser) water, therefore resulting in more realistic North Atlantic overturning and thus the NADWF.

3.6 Thermohaline Circulation

The thermohaline circulation (THC) is basically a buoyancy flux-driven diapycnal flow, i.e., overturning, of the ocean in the meridional-vertical plane with global scale cells, in contrast to the quasi-horizontal circulation gyres which are directly driven by the wind and constrained to limited ranges of latitude and depth. So, when referring to THC, we often refer to the motion below the mixed layer because the upper layer THC, which is associated with the horizontal density gradients caused by the geographical distribution of surface heat and salt fluxes, is general weak and of minor importance compared to the wind-driven circulation and, can be altered by the strong mixing, or wind-driven flow, such as tropical upwelling and subtropical downwelling (Ekman pumping). The THC, to a large degree, determines the vertical water mass transport and thus the water mass formation, and dominates the inter-hemispheric water mass exchanges. In a word, it has a critical influence on the distribution of water properties in the intermediate and deep oceans and on the global-scale heat and freshwater transports. It is widely recognised that any model used for climate studies, especially long-term climate change investigations, must be able to represent reasonable large scale features of the world ocean THC which determines the global ocean water mass formations and thermal and hydrological balances in the global climate system.

In models the THC is depicted in the meridional-vertical plane by the meridional overturning streamfunction (ψ), which is well-defined in the global ocean and individual basins bounded by meridional barriers. It denotes the zonally integrated net volume transport rate and is given by

$$\psi(\varphi, z) = -\int_{z_b}^{z} \int_{\lambda_w}^{\lambda_e} v(\lambda, \varphi, z') a_0 \cos(\varphi) d\lambda dz' \tag{3.7}$$

where z_b is the local ocean bottom depth (with negative value) where the streamfunction is defined to be zero, and v is either the Eulerian-mean, eddy-induced transport which arises from the GM isopycnal parameterization, or their sum, i.e, the effective transport in the meridional direction (Hirst and McDougall 1998). φ, λ

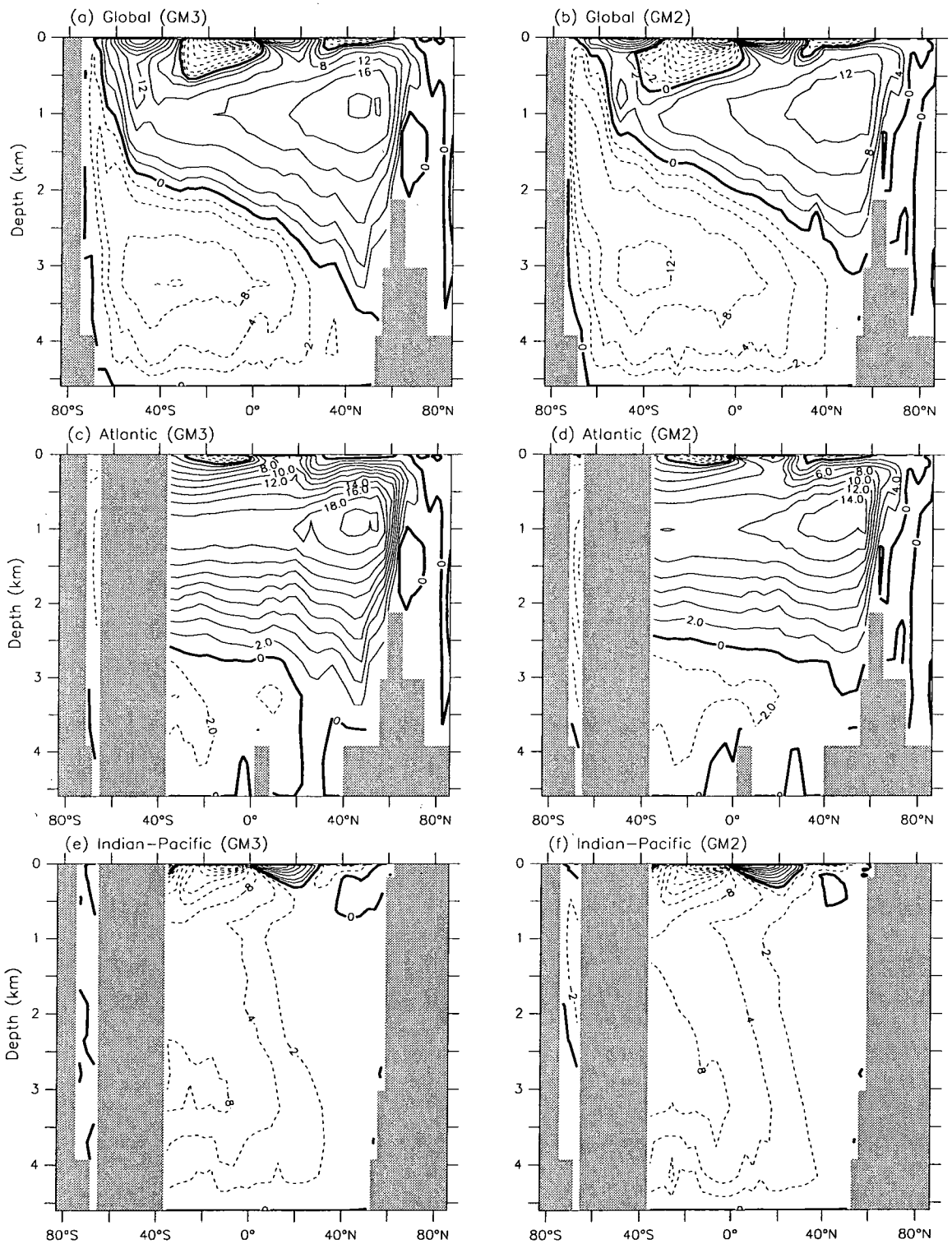

Figure 3.12: Meridional overturning streamfunction in the TGM3 (left column) and TGM2 (right column) solutions. Contours: (a) -40 to 32 with interval 4, plus ±2 lines; (b) -52 to 44 with interval 4, plus ±2; (c) -8 to 22 with interval 2; (d) -10 to 16 with interval 2; (e) -36 to 24 with interval 4, plus ±2; (f) -44 to 36 with interval 4, plus ±2.

and z are the latitude, longitude and depth, respectively, and a_0 the radius of the earth. The zonal definite integral can be conducted either along a whole zonal circle in the global ocean case or starting from the western boundary (λ_w) to the eastern boundary (λ_e) for individual basins.

Fig.3.12 shows the zonally integrated meridional total (effective) overturning streamfunction distributions in the GM3 and GM2 solutions for the global ocean, Atlantic and Indian-Pacific basins. Clearly, after the change of the model configuration in the global ocean, the basic circulation pattern is well maintained in the global ocean, but some significant differences of the overturning intensity between the GM3 result (Fig.3.12a) and GM2 solution (Fig.3.12b) are evident. In the upper layer of each hemisphere, the meridional circulations is dominated by wind-driven Ekman transports, which can be illustrated by the two shallow cells at low latitudes beside the equator in the global patterns. These cells are poleward Ekman transports driven by the tropical easterly trade winds, mostly formed by the upwelling in the broad tropical Pacific. The southward and northward global water mass fluxes in GM3 are 42.8 and 31.7 Sv, respectively, which are markedly weaker than that of 51.7 and 45.6 Sv in GM2, and also the southern cell penetrates shallower in GM3. Such a contrast implies that our use of the NCEP windstress largely reduces the tropical ocean current divergence and thus the upwelling, and is partly responsible for the southward heat transport weakening discussed in section 3.4. In addition, both runs show the near absence of a strong Deacon cell which appears to penetrates deeply, separating the strong Antarctic direct overturning cell from the deep cell in models with no GM scheme (e.g., Manabe et al. 1991; Weaver and Hughes 1996; England and Hirst 1997; Gordon and O'Farrell 1997). Only a remnant of the Eulerian-mean Deacon cell can be seen in our models, at about 50°S, after a cancellation between the mean advection and the eddy-induced advection (see Danabasoglu and McWilliams 1995; Gent and McWilliams 1996; Hirst and McDougall 1998 for details concerning this cancellation). As a result of the cancellation, the direct Antarctic cell is remarkably weakened and is fully merged with the deep cell. The GM3 configuration leads to an even weaker Antarctic overturning and a slightly reduced deep cell compared to

GM2.

In the Indian-Pacific basin north to the ACC, GM3 and GM2 have overall similar overturning patterns, showing northward intrusion of the deep circulation which mostly occurs in the Pacific basin and determines the ventilation of deep North Pacific water. Both runs see weak and broad upwelling below 700 m depth. The Ross Sea shows maximum overturning intensities of 1.9 Sv and 3.5 Sv at 1540 m depth (at 66.9°S for GM3 and GM2, respectively, indicating that the Ross Sea deep water formation is reduced under the GM3 configuration. However, the reduction of the Antarctic deep water formation in GM3 is mostly caused by the change in Weddell Sea where the maximum overturning in GM3 is reduced from 8.4 Sv for GM2 to 3.0 Sv at 1540 m depth, 66.9°S.

The Atlantic basin, where the THC primarily occurs and dominates the meridional circulation, displays the major difference in overturning patterns between GM3 and GM2. In addition to the Weddell Sea feature just discussed, another two important distinctions are evident. Firstly, the GM3 configuration substantially strengthens the NADW formation, yielding a maximum overturning of 20.6 Sv at 1010 m depth 44.6°N in GM3, contrasting that of 15.5 Sv at 800 m depth at the same latitude in GM2. Regarding the factors responsible for this significant enhancement of the NADW formation, besides the apparent effect of the modification to the North Atlantic surface buoyancy forcing fields, the smaller isopycnal thickness diffusion coefficient adopted in GM3 also plays a dynamical role. As addressed by Danabasoglu and McWilliams (1995), smaller isopycnal diffusivity may act to build up larger meridional buoyancy difference in the ocean, which, to some extent, further strengthens the surface forcing enhancement. Consequently, the stronger NADW formation in GM3 strengthens the conveyor belt and results in over 13 Sv southward water transport cross the equator, compared to that of 8 Sv in the GM2 case, as shown by the global patterns in Fig.3.12a and 3.12b. In the GM3 solution, this flow originating from the NADWF is quite realistic as per Roemmich and Wunsch (1985) who estimate a southward transport of 17 $\pm$ 4 Sv at 24°N, compared to the GM3 value of 17.8 Sv at 22.3°N. Secondly, the GM3 North Atlantic overturning

can penetrate to the depth of 3500 m at around 44.6°N and down straight to the bottom north of 47.8°N and in the band 22.3–31.9°N, whilst the deepest penetration in GM2 reaches only around 3000 m. The deeper penetration in broad regions of the GM3 North Atlantic overturning efficiently prevents the extensive northward intrusion of AABW to the abyssal Atlantic Ocean that occurs in GM2, shown clearly in Fig.3.12c and 3.12d.

The differences in the meridional overturning features of GM3 and GM2 provide a straightforward explanation for the differences in water mass properties especially the deep water properties between GM3 and GM2 discussed in section 3.2. As is well known, the global ocean deep water masses are initially formed in either the North Atlantic or the Antarctic shelf regions, distinguished by their T-S characteristics. In the GM3 spinup, for example, the deep water is obviously not the type of fresh and cold surface water near the Antarctic. Instead, it is dominated by the warmer and more saline North Atlantic surface water, i.e., it is formed initially in the North Atlantic and transported to the depth by the sinking branch of North Atlantic overturning near 50°N. This sinking warm and saline water can reach near the bottom and then, carried by the deep circulation and the conveyor belt, spreads throughout the global ocean, gets diluted and cooled by mixing with the fresher and colder water brought by Antarctic overturning from the surface. Due to the weakening of Antarctic overturning, less cold and fresh water is brought down to the deep levels and the deep water, particularly for the Southern Ocean, therefore shows higher salinity but bears a slight warm bias, yielding a more realistic stratification for the GM3 solution. In contrast, the much weaker and shallow-penetrating North Atlantic overturning, together with the stronger Antarctic overturning, is the central factor responsible for the cold and fresh errors in the deep ocean of the GM2 solution, as well as for the BF3 solution.

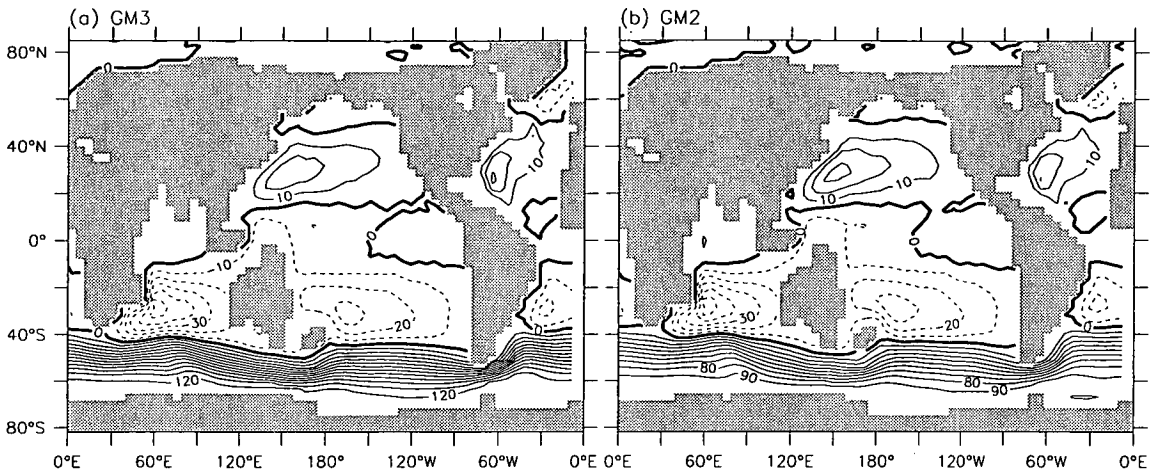

Figure 3.13: Annual mean barotropic streamfunction in: (a) GM3, and (b) GM2. Contour interval is 10 Sv.

3.7 Barotropic Flow

The barotropic streamfunction, i.e., the vertically integrated horizontal mass transport streamfunction is calculated by integrating the depth-integrated zonal component of the horizontal transport from the northernmost grids to the required latitudes:

$$\psi(\lambda,\varphi) = a_0 \int_{\varphi_n}^{\varphi} \int_{-z_b}^{0} u(\lambda,\phi,z)dzd\phi \tag{3.8}$$

where ψ is the barotropic streamfunction in the unit of Sv and the other variables have their conventional meanings as mentioned before.

The annual average barotropic streamfunctions for the equilibrium states of GM3 and GM2 are shown in Fig.3.13a and 3.13b, respectively. Because the horizontal transport is strongly influenced by the wind forcing and the wind stresses have generally similar patterns as shown below, GM3 and GM2 have very similar gyre patterns in the global ocean. For example, in addition to the evident Antarctic Circumpolar Current (ACC), the mid-latitude gyres, i.e., the anticyclonic subtropical gyres, are also clear for both runs in both hemispheres of the Atlantic and the Pacific, and the strongest mid-latitude gyre is seen in the southern Indian Ocean. As to be discussed, the western boundary currents of these subtropical gyres are weak in both runs, reflecting one of the typical spurious features of coarse resolution models. The

cyclonic subpolar gyre in the North Atlantic is clearly displayed for both solutions with the maximum transport larger than 10 Sv, but its counterpart in the North Pacific is too weak to be revealed by the contour interval chosen here. Similarly, the weak tropical cyclonic gyres are also not revealed explicitly in Fig.3.13 except the GM2 tropical Indian Ocean where the gyre is just over 10 Sv. Another common feature for both runs is the Indonesian Throughflow which transports water mass from the Pacific into the Indian Ocean as discussed below. It needs to be mentioned that, due mainly to the coarse resolution of our model, some finer structures of the ocean currents are missing in the solutions. For example, the eastward North Equatorial Countercurrents are not represented in any ocean basin.

Despite the above common features for GM3 and GM2, there are notable differences in the magnitudes of their main currents. Firstly, GM3 gives the ACC transport through Drake Passage of 127 Sv, in good agreemen with the observations of Whitworth (1983), i.e., 118–146 Sv, whereas the counterpart in GM2 is only 97.4 Sv, falling out of the observed range. The result that the GM3 ACC transport is stronger than that in GM2 is mainly attributed to the joint effect of the smaller isopycnal thickness diffusivity in GM3 than that used in GM2, i.e., 0.6×10^7 vs 1.0 $\times10^7$ cm^2s^{-1}, and the stronger NCEP windstress than H-R in the ACC region. For the effect of diffusivity on the ACC transport, Danabasoglu and McWilliams (1995) showed that the ACC transport through Drake Passage diminishes with increased diffusivity due to the isopycnal form stress that gives increased vertical momentum flux with larger diffusivities, thus supporting more drag with weaker flow in the ACC. For the effect of windstress, another example is our experiment CW3 (not shown here), which employs the CSIRO wind forcing with weaker westerly stress than that of the NCEP data over the ACC zone, thus giving an ACC transport through Drake Passage less than 110 Sv. Additionally, the THC conveyor belt strength, which is associated with the NADWF intensity and shows significant difference between the two runs, also plays an important role in setting up the ACC transport in the model by affecting the density structure across ACC. This will be discussed in detail in Chapter 5.

Secondly, the strengths of western boundary currents also differ noticeably between the GM3 and GM2 solutions. Furthermore, these currents in both solutions are more or less weaker than some (crude) estimates from either other model results or observations. In the NH, for example, the maximum Gulf Stream transports are 33.3 and 30.3 Sv in GM3 and GM2, respectively, both being much less than the downstream observations by Hogg (1992), i,e, 150 Sv. Such a large bias is caused mainly by the absence of the larger inertial boundary currents and recirculations in coarse resolution models which use large horizontal eddy viscosity coefficients. Similarly, the maximum Kuroshio transports are 28.3 and 34.4 Sv in GM3 and GM2, lower than some upstream geostrophic transport estimates (e.g., Qiu and Joyce 1992) The Indonesian Throughflow transports are 18.1 and 17 Sv in GM3 and GM2, both within the estimate range of 18.6 $\pm$ 7 Sv by Fieux et al. (1994), although this transport bears large temporal variability in observations. The maximum Agulhas Current transports are 58.2 and 57.5 Sv in GM3 and GM2, respectively, smaller than the observational estimates (around 65 Sv) of Stramma and Lutjeharms (1997). The maximum Brazil Current transports in GM3 and GM2 are 22 and 22.3 Sv, respectively, close to the estimate of Peterson and Stramma (1991).

3.8 Oceanic Horizontal Currents

The annual mean horizontal currents of GM3 in the surface layer (12.5 m), near surface layer (65 m) and at four deep levels (545 m, 1395 m, 2125 m and 3475 m) are shown in Fig.3.14. At the surface, all the major gyres of the global ocean displayed in Fig.3.13 show up here, such as the anticyclonic subtropical gyres in both hemispheres of the Atlantic and Pacific and in the South Indian Ocean, the cyclonic subpolar gyres in the North Atlantic and North Pacific. Also clear are the tropical ocean currents, particularly in the equatorial Pacific, the ACC flow, and the Indonesian Throughflow transport from the Pacific to the Indian Ocean. The maximum annual mean surface velocity of the world ocean in GM3 is 26.6 $\mathrm{cm\,s^{-1}}$, appearing in the equatorial Pacific. In the tropical Atlantic, the strong wind-driven

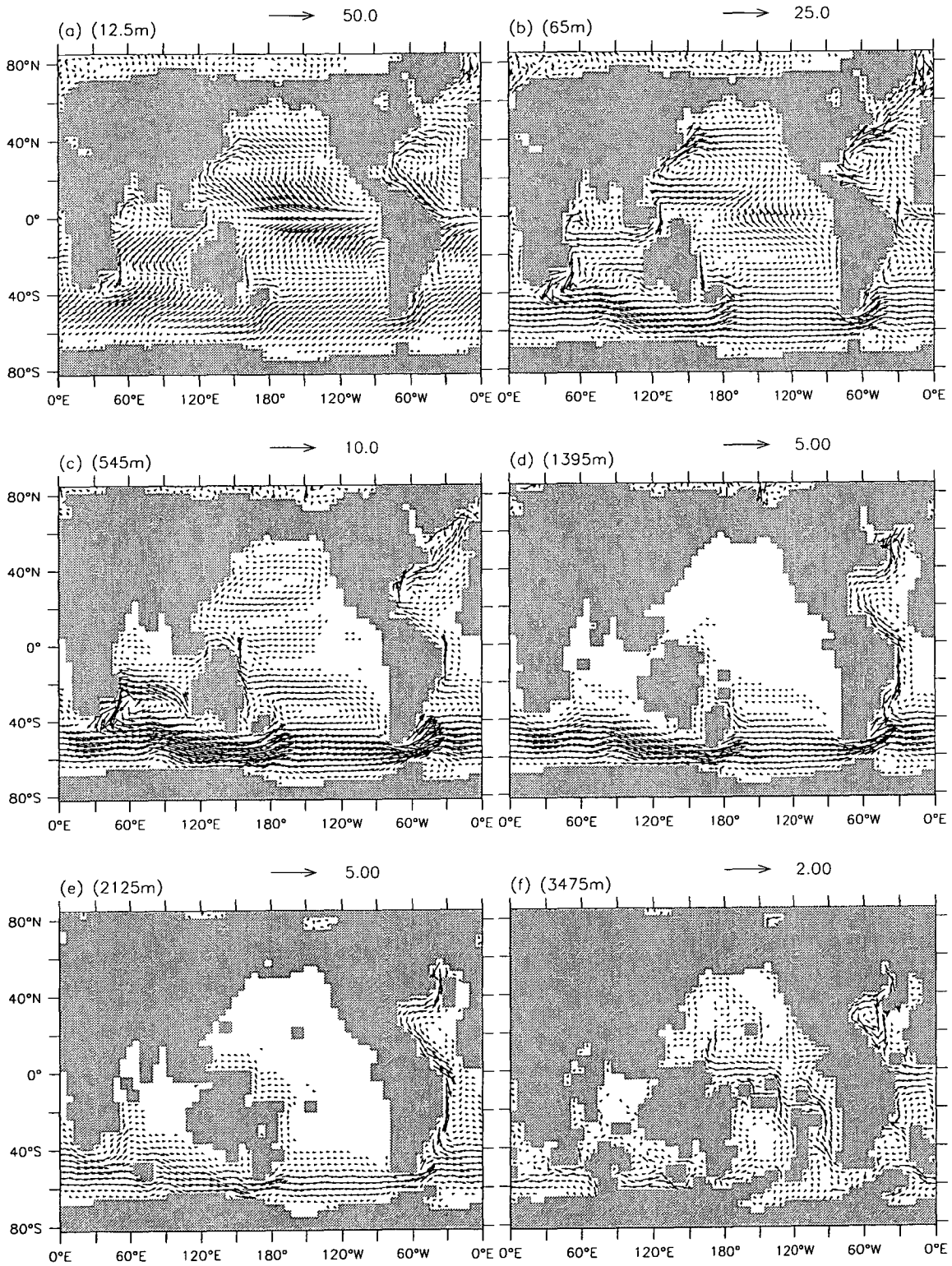

Figure 3.14: Annual mean horizontal currents ($\mathrm{cm\,s^{-1}}$) in GM3: (a) 12.5 m, (b) 65 m, (c) 545 m, (d) 1395 m, (e) 2025 m, and (f) 3475 m.

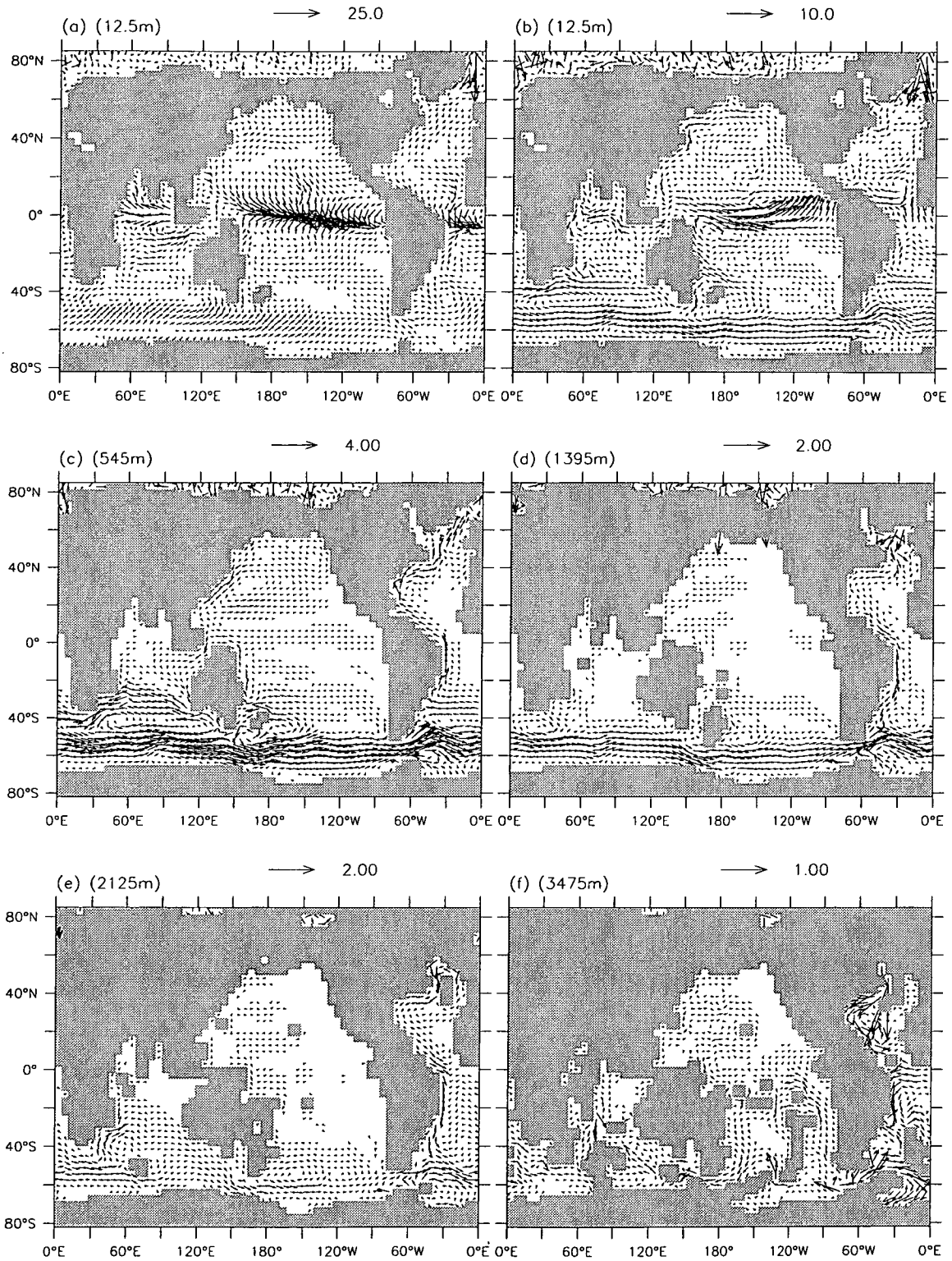

Figure 3.15: Annual mean horizontal currents ($\mathrm{cm\,s^{-1}}$) for GM3 - GM2: (a) 12.5 m, (b) 65 m, (c) 545 m, (d) 1395 m, (e) 2025 m, and (f) 3475 m.

westward current, with the maximum speed of 18.6 cm s^{-1}, separates into two flows at the eastern tip of South America. One branch flows northwestward along the western boundary into the Gulf of Mexico, feeding the Gulf Stream, whilst the other flows southwestward to meet the north-turning ACC, making up part of the Brazil gyre. The broad ACC band (40–60°S) has an average velocity of about 8.3 cm s^{-1} (with the mean zonal velocity of 6.8 cm s^{-1}), and the maximum is 14.5 cm s^{-1} (with a zonal component of 11.9 cm s^{-1}) in the southwestern Indian Ocean. With regard to the surface flow in the Drake Passage, the peak is 14.3 cm s^{-1}, with the corresponding zonal velocity being 11.1 cm s^{-1}. As mentioned before, the coarse resolution of our model prevents the representation of some details of the ocean current system such as the narrower jets and the Equatorial Counter Currents. Furthermore, the current velocity magnitudes are largely reduced by the coarse resolution and the related large horizontal viscosity. This leads to much too weak and too broad main currents such as the ACC, the western boundary currents and the equatorial currents, compared to the observed values. However, the associated mass transports are in much better agreement with the observational estimates due to the compensating errors in the (low) flow speed and the (broad) lateral scale, such as the case of ACC transport in GM3.

The near surface current system shown in Fig.3.14b is under much smaller impact of the surface winds, and Ekman drift diminishes in both the tropical and southern high latitude regions. As a result, the ACC flow in this layer is much closer to a quasi-geostrophic balance, whereas the Pacific Ocean sees a clear convergence towards the equator, which compensates for the wind-driven surface upwelling. All the subtropical gyres and the western boundary currents are more evident at this level than that in the surface layer. At the subsurface depth (545 m), shown in Fig.3.14c, all the wind-driven upper gyres are largely reduced but can still been discerned in the mid latitude Pacific (both hemispheres) and in most parts of the Indian ocean in particular. At the mid-depth level (1395 m), the above gyres completely disappear, but the Atlantic western boundary currents and the the ACC flow are evident. The maximum speed reaches 2.18 cm s^{-1} in the NADW formation region, and the largest

ACC flow velocity also reaches as high as 2.16 $cm\,s^{-1}$ in the Drake Passage. Note that the Atlantic western boundary currents flow in the direction opposite to that of its upper layer counterpart, transporting the deep water formed in the North Atlantic southward into the Southern Ocean. This flow joins the ACC in the South Atlantic and, while circulating around Antarctica, acts with the deep THC cell, ventilating the other ocean basins. The large blank areas in the Pacific and Indian Oceans indicate that there exist extensive almost 'horizontally motionless' regions at this level, with very weak velocity (less than 0.1 $cm\,s^{-1}$). The 2125 m depth (Fig.3.14e) sees generally similar flow pattern to that at the 1395 m level, i.e., the NADW flows out of the North Atlantic basin into the Southern Ocean where it joins the ACC and then flows around Antarctica.

The horizontal currents at 3475 m depth (Fig.3.14f) show significant difference from that displayed in the mid-depth figure. We see quite strong currents in both the central Atlantic and Pacific Oceans at this deep level. A few topography-related deep gyres are evident, in particular the one in the Gulf of Mexico, which obviously originates from the NADW formation region and the water mass can only flow out of the basin with the North Atlantic deep overturning. Some other features related to the deep water formation and deep ocean ventilation in our model ocean are also evident in this figure. The deep water formed off Antarctica spreads northward in both the Pacific and Atlantic Oceans, but the flows in the two basins bear clear differences. The flow originating from the Weddell Sea is very (perhaps unrealistically) weak and seems constrained to the South Atlantic, while the flow originating from the Ross Sea is far more north-reaching (into the North Pacific). Such a contrast can also be seen in Fig.3.12c and 3.12e, implying that the northward flow of the global ocean thermohaline circulation deep cell is dominated by the Pacific component in our model.

The GM2 solution shows basically similar patterns of the horizontal currents but the flow intensities are significantly different at all depths. Fig.3.15 shows the deviation of the GM3 solution to the GM2 result, i.e., GM3 - GM2, at the above discussed five levels. In the surface layer, corresponding to the stronger tropical easterly H-R

windstress, GM2 shows faster and broader equatorial currents and much stronger divergence in the tropical Pacific due to poleward Ekman drift. This is reflected by the strong 'convergence' towards the equator in the Pacific and the Atlantic Oceans. In addition, the H-R data gives weaker westerlies over the Circumpolar Ocean, leading to a slower surface zonal (ACC) flow and weaker northward meridional transport (i.e., Ekman drift) in GM2. In contrast to those surface velocity values in GM3 mentioned above, GM2 presents the largest velocity of 40.2 $cm\,s^{-1}$ (in the equatorial Pacific), and the average velocity in the ACC zone is below 7 $cm\,s^{-1}$ with a zonal component of 5.6 $cm\,s^{-1}$. The near surface depth (65 m) in the GM2 solution shows a clearly weaker ACC flow and, as expected, much stronger convergence towards the equator in the Pacific Ocean induced by the much stronger divergence in the surface layer. At the subsurface level (545 m), we see much stronger ACC and northward flow in the western boundary region of the Atlantic in GM3. At mid-depth levels, GM3 shows somewhat faster outflow from the NADW formation region, and the ACC is stronger as well. For example, at the 1395 m depth, the average ACC flow around Antarctic (40–60°S) is 0.7 $cm\,s^{-1}$, compared to 0.6 $cm\,s^{-1}$ for GM2. In the Atlantic Ocean, the stronger northward flow in the subsurface layer and southward flow in the mid-depth layer for the GM3 solution is naturally a result of the enhanced NAWDF (compare Fig.3.12c and 3.12d). Such an enhancement in the NADWF is also partly responsible for the strengthening of the ACC flow in the upper to mid-depth level due to its impact on the ocean interior thermal structure across the ACC. This will be discussed further in later chapters. In the deep ocean, the two solutions show clear differences in the water formation regions. Firstly, contrasting with the evident southward outflow of NADW for GM3, GM2 shows no such flow there at all, consistent with the features displayed in Fig.3.12b and 3.12d which indicate that the North Atlantic overturning can not reach down to the depth below 3000 m and therefore no deep water forms in the abyssal ocean for GM2. Secondly, the deep water formation off Antarctic is more evident in GM2 than GM3. This is true for both the Pacific and the Atlantic and the latter shows the substantial difference, i.e., the flow originating from the Weddell Sea is much stronger in the GM2 case and it spreads farther north. This means more Antarctic

deep water formation and more northward invasion from the southern abyssal ocean in GM2, corresponding with the features shown in Fig.3.12.

3.9 Wind-driven Circulations

The atmosphere exerts its dynamical influence on the ocean through the momentum flux (i.e., windstress) on the air-sea interface. This momentum flux is the most important forcing for the upper ocean circulation especially in open water away from coastal regions. It is of interest to reveal the association of the depth-integrated oceanic flow with the windstress forcing.

3.9.1 Surface wind stresses

Fig.3.16 shows the annual mean distributions of the surface wind stresses from the NCEP and H-R climatologies used for GM3 and GM2, respectively. These two climatologies have overall similar patterns in both zonal and meridional distributions. The zonal components are characterised simply by extensive tropical and subtropical westward stresses and strong eastward stresses in middle to high latitudes, whilst the meridional components show more complex structures featured mainly by two southward stress bands, i.e., the 20–40°S band and the one centered at 20°N; and northward stresses in tropical oceans centered at around 10°S and over northern oceans, with nearly all the maxima of the meridional stresses being near the eastern coasts. However, further examination reveals significant differences between these climatologies.

Firstly, the NCEP wind gives stronger zonal (eastward) stress in the southern Indian Ocean with the maximum being over 0.22 $\mathrm{N\,m^{-2}}$, compared to the maxima of less than 0.20 $\mathrm{N\,m^{-2}}$ for the H-R data in that region. In the North Pacific, both datasets have similar eastward stress maxima of around 0.1 $\mathrm{N\,m^{-2}}$ but in the North Atlantic a large difference occurs in the zonal stress maxima which are 0.11 and 0.15 $\mathrm{N\,m^{-2}}$

Figure 3.16: Annual mean windstresses from the NCEP and H-R climatologies for (a) NCEP zonal, (b) NCEP meridional, (c) H-R zonal, and (d) H-R meridional. Contour interval is 0.04 for (a)(b) and 0.02 for (c)(d). (units: $\mathrm{N\,m^{-2}}$)

for the NCEP and H-R winds, respectively. Also notable is the difference in the extensive westward stress band, i.e., the tropical and subtropical Pacific and Atlantic Oceans and the low latitudes of southern Indian Ocean where H-R gives larger maxima than NCEP. For example, the Indian Ocean and Pacific Ocean see 0.11 and 0.1 $\mathrm{N\,m^{-2}}$ westward stress maxima, respectively, in NCEP, contrasting with 0.13 and 0.12 $\mathrm{N\,m^{-2}}$ in H-R. This means stronger easterly trade winds in the tropical oceans for GM2 and this leads to stronger divergence of the ocean currents in the GM2 solution, which is partly responsible for the larger poleward heat and water mass transports discussed above.

It is now widely recognized that the H-R windstress is a bit too strong for the tropical oceans, primarily because of their use of a systematically too large drag coefficient (e.g., Chelton et al. 1990). In addition, the most remarkable difference in zonal stresses occurs off the Antarctic coast. NCEP shows quite strong westward stress (near 0.08 $\mathrm{N\,m^{-2}}$ between 0–150°E and up to over 0.09 at the southeastern corner of Ross Sea) along the coast, but the H-R data shows no such westward stress around Antarctica. Thus, the NCEP windstress seems more realistic than the H-R data near the Antarctic due to its successful representation of the presence of Polar Easterlies along the coast. Tomczak and Godfrey (1994) show that the dominant westerly winds over the circumpolar currents turns into easterly at around 65°S along the Antarctic coast according to their calculation on the basis of merchant ship data for the period 1980-1986. With regard to the meridional stresses, due to the same reason, the H-R data also give larger northward stresses in the southern tropical and subtropical oceans and larger southward stresses in the eastern Pacific and Atlantic Oceans at around 20°N, indicating a bit too strong intertropical convergence compared to NCEP. In addition, the H-R wind shows no notable northward stresses off the Antarctic coast. In contrast, NCEP gives large northward wind stresses off Antarctica especially at the southwestern corners of Ross and Weddell Seas where the offshore stresses are over 0.07 and 0.03 $\mathrm{N\,m^{-2}}$, respectively. These northward offshore stresses along the Antarctic coast are also evident in the calculations of Tomczak and Godfrey (1994).

3.9.2 Sverdrup estimate of the barotropic flow

As mentioned above, wind forcing is the primary and major factor driving the barotropic flow in our model. However, there are other factors which may have significant influence on this depth-integrated transport. For example, the bottom stress acts to drag the ocean flow in continental shelf regions such as the western boundary currents, and thermohaline circulation in some regions such as the North Atlantic interacts with the bottom topography, producing bottom pressure torque and driving the horizontal mass transport. Nevertheless, it is worthwhile to examine to what degree the windstress alone determines the barotropic flow in our model. The Sverdrup model which only includes the surface windstress effect on the barotropic flow is widely used for this purpose through the comparison between the actual depth-integrated transport and the Sverdrup estimate.

According to Godfrey (1989), the transport streamfunction of the Sverdrup circulation can be obtained by integrating the curl of surface windstress westward along latitude lines from the eastern boundary of ocean basins, namely

$$\begin{aligned} \psi_S(\lambda,\varphi) &= -\int_{\lambda_E}^{\lambda} \frac{1}{\rho_0\beta}\mathbf{k}\cdot(\nabla\times\tau)a_0\cos(\varphi)d\lambda' \\ &= -\frac{a_0^2}{2\Omega\rho_0}\int_{\lambda_E}^{\lambda}\mathbf{k}\cdot(\nabla\times\tau)d\lambda' \end{aligned} \tag{3.9}$$

Here $\beta = df/dy = 2\Omega\cos(\varphi)/a_0$, and $\Omega = 7.29\times10^{-5}/s$ is the angular velocity of the earth; $\mathbf{k}\cdot(\nabla\times\tau)$ is the curl of the windstress vector τ and the other variables have their conventional meanings. At the eastern boundary λ_E, the Sverdrup streamfunction is defined to be zero except for two islands in our model, i.e., Australia and New Zealand. For these two islands, a circulation around each of them is allowed for and should be computed using the island rule of Godfrey (1989), i.e., $\psi_I = \frac{1}{\rho_0\Delta f}\oint\tau\cdot d\mathbf{l}$, where the path of the integral is counterclockwise and along the nearest boundary, $\Delta f = f_N - f_S$ is the difference of the Coriolis parameter between the northernmost and southernmost points of the island. The resultant transports around the

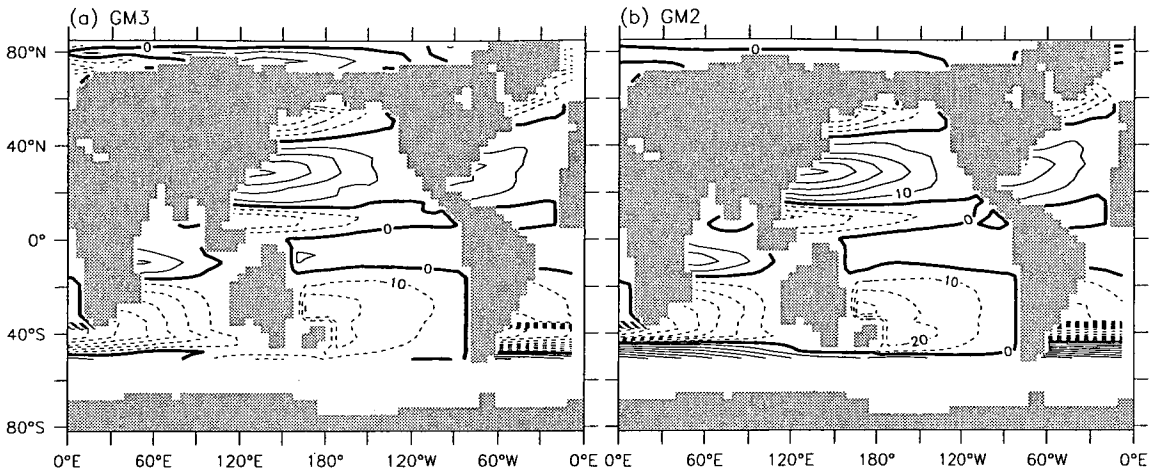

Figure 3.17: Annual mean wind-driven barotropic flow from the Sverdrup model (units: Sv). Contour interval is 10 Sv.

given islands are then used as the eastern boundary conditions for calculating the transports in basins west of the islands. Obviously, the Sverdrup transport is not defined in the ACC region and the Arctic Ocean due to the absence of eastern land boundaries. In addition, the region south of the ACC is omitted in our calculation.

Fig.3.17a and 3.17b present the Sverdrup estimates of the barotropic transports for GM3 and GM2, respectively. Comparisons between Fig.3.17a and 3.13a, Fig.3.17b and 3.13b show that the Sverdrup model can to some extent describe the model real barotropic transports and capture the main features of the real flows in both runs. For example, the basic structures of the subtropical and subpolar gyres shown in Fig.3.13 are well represented in Fig.3.17. However, the model transports of the western boundary currents in particular, are not in good agreement with the Sverdrup estimates or, in other words, in Sverdrup balance. In fact, all the western boundary currents, to various degrees, are either underestimated or overestimated by the Sverdrup model. In the GM3 solution, for example, the Sverdrup model estimates the maximum Gulf Stream transport 12 Sv less than the real model calculation and overestimated the maximum Kuroshio transport by more than 13 Sv. The northern hemispheric subpolar gyres see even larger differences between the real transports and the Sverdrup estimates, which is especially the case for the North Pacific where the subpolar gyre transport is over 30 Sv in the Sverdrup estimate but only around 5 Sv in the real model calculation. The gyres in tropical oceans such as the one

centered around 15°N in the Pacific and that centered at 10°S in the Indian Ocean are both exaggerated largely by the Sverdrup model. The Agulhas current, the east Australian current and the Brazil gyre are in somewhat better Sverdrup balance in terms of the maximum transports but the locations are obviously displaced in the Sverdrup estimates. In addition, the Indonesian Throughflow is evidently underestimated in the Sverdrup model, i.e., less than 10 Sv, resulting from the inadequate transport around Australia, which is also partly responsible for the too large estimate of the tropical Indian ocean gyre mentioned above. The GM2 solution shows a similar deviation between the Sverdrup estimate of the global transport pattern and the real model result.

We further examine the western boundary currents in the full model and the Sverdrup estimates. The Kuroshio transports in both full solutions are much weaker than their wind-driven counterparts, indicating that the bottom stress plays a significant role in affecting the barotropic flow, i.e., slowing it down in this region. In contrast, the Gulf Stream transports are stronger than their wind-driven estimates, indicating that the North Atlantic overturning circulation is very important in driving the barotropic flow there. This is even more evident when we compare the situations for the Gulf Stream and the Kuroshio. For the Kuroshio, with no significant effect of overturning, the transport is wind-driven and largely reduced by the bottom friction drag; however, the Gulf Stream transport is considerably stronger than the wind-driven estimate, due only to the contribution of the THC which strongly interacts with the bottom topography (as mentioned above), compensating the bottom stress drag and strengthening the total barotropic flow. The difference between GM3 and GM2 also verifies the importance of thermohaline circulation in driving the Gulf Stream transport, i.e., the stronger and deeper-penetrating North Atlantic overturning leads to a stronger Gulf Stream transport in GM3 (bear in mind that the wind-driven transport is weaker in GM3 than that in GM2 as indicated by Fig.3.17).

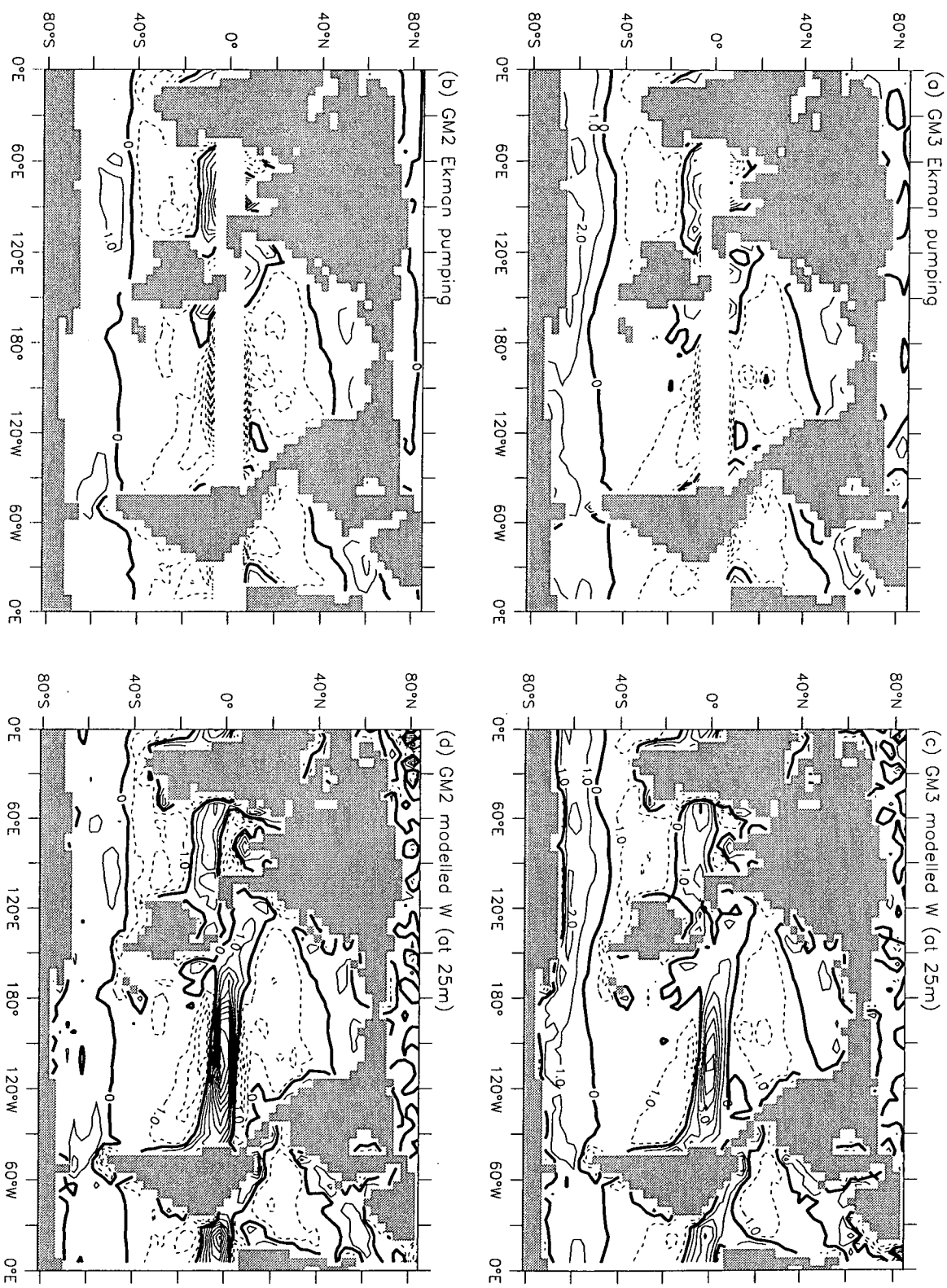

Figure 3.18: Ekman pumping velocity (w_E) and the model vertical velocity at 25 m depth for: (a)(c) GM3, (b)(d) GM2. Contour interval is 1. (units: 10^{-4} cm s^{-1})

3.9.3 Ekman pumping and the modelled vertical velocity

The oceanic upwelling and downwelling are of no doubt very important for the distribution of hydrographic properties below the surface layer. The divergence of the wind-generated, depth-integrated Ekman transport, known as the Ekman pumping, is the major contributor to the vertical movement into or out of the surface layer, and is determined jointly by the surface windstress and the planetary vorticity, i.e.,

$$w_E = \nabla \cdot \mathbf{V}_E = \frac{1}{\rho_o} \mathbf{k} \cdot \nabla \times (\tau / f) \tag{3.10}$$

where $\mid \mathbf{V}_E \mid = \mid \tau / \rho_0 f \mid$ is the Ekman layer (depth-integrated) transport.

Fig.3.18a and 3.18b show the calculated annual mean Ekman pumping velocity for GM3 and GM2, respectively. Note w_E is not defined near the equator and not well defined along boundaries. Obviously, most of the ocean is characterised by Ekman transport convergence (downwelling) from tropical to subtropical regions, whereas the divergence of Ekman transport (upwelling) is found in subpolar regions. This is the case in both hemispheres and for both runs. A distinctive difference between GM3 and GM2 can be seen in the Southern Ocean (for the poleward side of the core of the Westerlies) where the upwelling in GM3 is much stronger than that in GM2, due to the much larger curl of the NCEP windstress. This contrast is reflected in the difference of the meridional overturning streamfunctions between GM3 and GM2, shown in Fig.3.12a and 3.12b, where the wind-driven mid-latitude upwelling in the Southern Ocean is stronger and penetrates deeper in GM3 than in GM2.

The model vertical velocity distributions just below the first layer are presented in Fig.3.18c and 3.18d for GM3 and GM2, respectively. This is the real velocity required to compensate the upper layer divergence, mainly the wind-driven Ekman transport divergence. All the major features in the Ekman pumping velocity fields can be found in the modelled, in fact, diagnosed, vertical velocity distributions, such as the extensive downwelling in the subtropics and the upwelling in the subpolar regions. Furthermore, we can see that strong upwelling occurs in the tropical region

along the equator in all the ocean basins. As is well known, near the equator the windstress is easterly and does not change much, but the Coriolis parameter f is very small and changes sign across the equator. This results in a large poleward Ekman transport on the two sides of the equator and strong upwelling (divergence) occurs. Along most eastern ocean boundaries we see evidence for upwelling as well. This is because the wind blows equatorward along the coast (see Fig.3.16), resulting in offshore Ekman transport which can only be compensated for by upwelling. In addition, we can also see upwelling in the western boundary regions particularly the Gulf Stream region. However, it is not governed only by the windstress via Ekman dynamics any more but determined largely by the strong western boundary currents. To put it simply, the upwelling is required to compensate for the strong poleward currents there.

Some differences between Fig.3.18c and 3.18d are evident. For example, both the upwelling in the equatorial Pacific and Atlantic Oceans and the neighbouring downwelling motions on the two sides to the north and south are stronger in GM2 than GM3, caused by the stronger easterly wind of H-R than NCEP along the equator. As a result, the stronger easterly wind along the equator strengthens the poleward Ekman transports on both sides of the equator in GM2, which on one hand causes larger divergence in the equatorial region, and on the other hand enhances the neighbouring convergences. As expected (but not shown), the stronger H-R wind near the equator also exerts its impact deeper into the ocean than does the NCEP wind. Consequently, the wind-induced tropical upwelling in the eastern Pacific can be traced down to 210 m in GM2, compared with 160 m in GM3. In addition, the stronger equatorial upwelling in GM2 is responsible for its larger net heat gain there, especially in the eastern Pacific, as already discussed. Another different feature occurs along the coast of Antarctica, i.e., GM3 shows somewhat more evident downwelling than GM2 in a very narrow zone just off Antarctica. This happens because the northeasterly windstress off Antarctic in NCEP (see Fig.3.16) leads to Ekman transport convergence along the Antarctic coast but this is entirely missing under the H-R wind forcing. Thus, the NCEP windstress tends to strengthen the

downwelling near Antarctica. However, such a strengthening in the surface layer is more than offset by the weakening of thermohaline circulation due to the enhancement of vertical stratification with the GM3 configuration and consequently the GM3 Antarctic overturning is even weaker than that of GM2. As we know, at deeper levels of the model ocean, the control of the wind-driven Ekman transport divergence on the vertical motion becomes weaker and is gradually taken over by the thermohaline circulation, particularly in the water mass formation regions where the sinking of dense water primarily determines the vertical velocity.

Chapter 4

Coupled Model Control Runs

In recent years, fully coupled models have been widely used to study climate changes occurring in the past century and at the present time. With no doubt they are the most powerful tool available for us to assess/predict future climate and the possible changes induced by anthropogenic forcing. Clearly, a stable control solution with realistic representation of both the atmospheric and oceanic components is an essential prerequisite for a coupled model used to simulate climate change and climate variability. This chapter documents results from two coupled control runs using the CSIRO coupled climate model (mark2) with the GM3 and GM2 oceans. These two runs are referred to as CGM3 and CGM2, respectively.

4.1 The CSIRO Coupled Model

The CSIRO fully coupled model is a comprehensive global general circulation model which consists of atmospheric, oceanic, sea-ice and biospheric components with full annual and diurnal cycles. A detailed description of the CSIRO fully coupled model is given by Gordon and O'Farrell (1997) and here we only provide a brief introduction to the sub-models excepting the oceanic component which has already been discussed in detail in Chapter 2.

The atmospheric sub-model is spectral with the spherical harmonic series rhomboidally truncated at wavenumber 21 and the physical processes are calculated on a Gaussian grid with resolution roughly 5.625^o longitude by 3.18^o latitude (McGregor et al. 1993, Watterson et al. 1995). It has nine levels in the vertical on a σ-coordinate system and contains parameterization for gravity wave drag, a moist convective adjustment scheme, semi-Lagrangian moisture vapour transport and a relative humidity based cloud parameterization.

The sea-ice component is fully described by O'Farrell (1998). It is dynamic and includes the cavitating fluid rheology of Flato and Hibler (1990). Its thermodynamic part employs the three-level form of Semtner (1976) which allows for internal heat capacity in the ice. Advection and divergence of ice can result from both wind stress and stress from the relative motion of the ocean currents. The ice concentration and the percentage of open ocean are determined from the energy budget of the mixed layer adjacent to the ice in a partially covered grid box. The salt content in sea ice is assumed to be 10 psu and, when sea ice forms and melts, the salinity difference between the ice and local water is converted to an equivalent salt flux which applies to the ocean uppermost level as a part of the surface salinity forcing.

Land surface interactions are parameterized using a soil-canopy model (Kowalczyk et al. 1991, 1994). The scheme allow of a range of land surface and soil processes, including the rainfall runoff which occurs after saturation of the surface soil and follows a path of steepest descent to reach the sea with no time lag. Since the sea-ice model and biospheric model have been developed in conjunction with the atmospheric model, hereinafter we refer to the "atmospheric-ice-biospheric model" as the "atmospheric model". It uses a time step of 30 minutes in both stand-alone mode and coupled mode.

The CSIRO coupled model is flux adjusted and runs in a synchronous time-stepping mode, with one ocean time step (i.e., 1 hour for all prognostic variables) being followed by two atmospheric steps. The atmospheric fluxes are averaged over these two steps, "corrected" by a constant (but with annual cycle) amount of "adjustments"

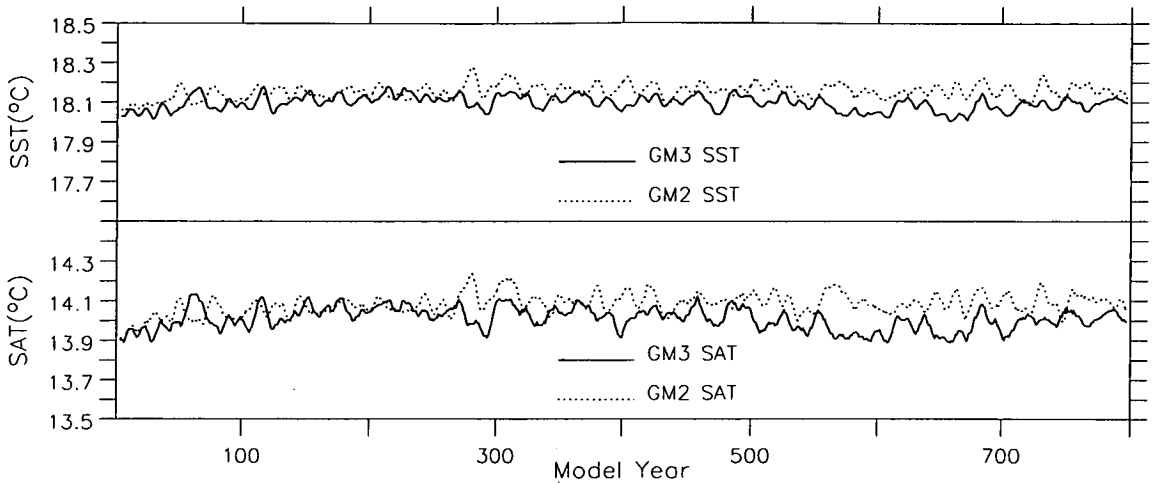

Figure 4.1: Time series of global average SST/SAT in the course of the CGM3 and CGM2 runs. A 7-year running run filter is applied.

and then passed to the ocean model. The method of adjusting fluxes follows the principle of Sausen et al. (1988) and is described in Gordon and O'Farrell (1997). Appendix A details the surface adjustments for the coupled runs CGM3 and CGM2 discussed here.

CGM3 and CGM2 differ from each other only in their oceanic components. They are initialized with the final states of an identical atmospheric spinup and the ocean spinups GM3 and GM2, respectively, and then both integrated forward for a duration of 800 years with surface adjustments applied, featuring a constant (equivalent) CO_2 concentration of 330 ppm in the atmosphere, which is the same as that set in the atmospheric model spinup.

4.2 Surface Climate and Residual Drift

After establishing the coupling between the atmosphere and the ocean, constraints for the model ocean surface variables, particularly the temperature and salinity, are removed and all quantities are able to evolve 'freely' in response to the air-sea interaction, including exchanges and various complicated feedbacks, and the evolution of the oceanic circulation. The first concern is whether or not the surface can maintain a reasonably realistic climate under the 'control' condition, which is

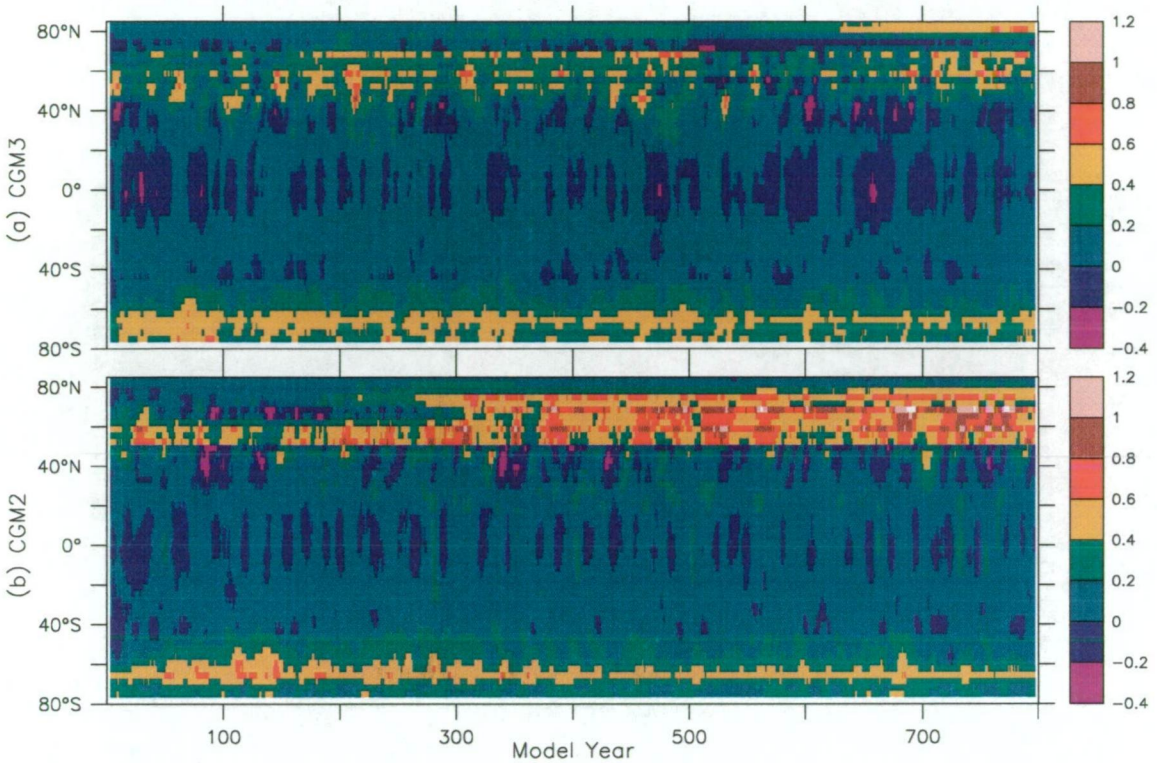

Figure 4.2: Changes of zonal mean SST (relative to year 1-50 mean). (a) CGM3, (b) CGM2). (units: °C). A 7-year running run filter is applied

not ensured at all in many models despite the use of surface adjustments.

4.2.1 Temperature (SST and SAT)

The SST and the surface air temperature (SAT), especially their evolutions during the course of integration, may be the most commonly used indices to show the climate stability and, to a large degree, the reliability of a coupled model. In our study, the SAT is the so-called "screen temperature": air temperature calculated at 2 m above the surface, taking into account the boundary layer structure of the atmospheric model (Gordon and O'Farrell 1997). Our results show that the CSIRO mark2-GM version coupled models perform extremely well in terms of the ability to produce very stable global mean SST and SAT, as revealed by the curves in Fig.4.1.

Over the whole 800-year integration, both runs display nearly no trends, with negligible drift in either SST or SAT. Taking SST as the example, we see a warming less

than 0.1 °C in the whole course of both runs and most of this drift occurs in the first few decades after coupling. In general, during the whole period of integration, the CGM2 ocean shows slightly higher global mean SST than CGM3, which is in accordance with the difference between the corresponding ocean spinups, and the variabilities are of similar magnitudes and frequencies (after the interannual signals are removed by the smoothing filter applied). As anticipated, the SAT variations follow the corresponding pattern, especially the frequency and phase, of the SST evolution but with a noticeably larger magnitude of variability. The SAT drift is very minor as well but slightly larger than the related SST drift, e.g., CGM3 and CGM2 see increases in SAT of about 0.1 °C and 0.15 °C, respectively, by the end of the integrations. The SAT warming is larger in CGM2 than CGM3 because the relatively higher SST in CGM2 leads to a larger adjustment of the SAT. As is understood, the ocean thermal state largely determines that of the overlying air.

Although CGM2 and CGM3 show similar and very small drift in terms of the globally averaged SST, there are notable differences of the latitudinal SST responses to the coupling between the two runs, particularly in the northern high latitudes. Fig.4.2a and 4.2b show the time series of zonally averaged SST change from the corresponding ocean spinups for CGM3 and CGM2, respectively. Both runs experience large warming in the band centered just south of the Circumpolar Ocean. This change occurs (reaching over 0.4 °C) almost immediately after coupling and thereafter the SST remains nearly unchanged. However, the most remarkable drift is found in CGM2 in the band centered around 60°N, where warming reaches order 0.8 °C towards the end of the run. In contrast, CGM3 sees no such strong warming in the same band but it suffers a warming of over 0.4 °C in the Arctic during the last 200 years of the integration. In the tropical oceans, warming and cooling epochs occur alternatively in both runs but these signals are very weak and should not be mistaken as ENSO events. [The ENSO variability in the model has been discussed in detail in Walland et al. (2000) and Vimont et at. (2001).] The result that the variation in the tropical oceans is weak is related to the coarse resolution of our ocean model and our use of a smoothing filter as well. The subtropical oceans

centered around 20°N/S see generally mild warming for both runs.

Fig.4.3a shows the geographical distribution of the difference of annual mean SST climate between CGM3 and CGM2 at the end of the integrations (last 50 year mean), and Fig.4.2b exhibits its counterpart in the ocean spinups (i.e., GM3 - GM2). It is evident that the SST contrast between GM3 and GM2 is preserved very well in the coupled runs in most of the oceans. However, we note that in some regions such as the northern North Atlantic both control runs suffer large drift from their initial states, as displayed by Fig.4.3cd, leading to a remarkable change of the SST contrast there, in particular in the Barents Sea where the largest SST difference reaches 6 °C, resulting jointly from the local warming in CGM2 and cooling in CGM3. In addition, we see that in both runs the persistent warming bias near Antarctica mentioned above occurs mainly in the Ross Sea, and the northern high latitudes strong warming bias occurs in both the North Atlantic and the North Pacific. The large cooling bias found over the Barents Sea in CGM3 mentioned above is over 3 °C, which, in the zonal mean, 'compensates for' the large warming bias in the eastern coastal region of Greenland and results in much weaker warming in that band for CGM3, as already shown.

4.2.2 Sea Surface Salinity

Both runs maintain very stable annual mean SSS in terms of the globally averaged value, with only small fluctuations within ±0.02 psu (not shown). However, the zonal mean evolutions displayed in Fig.4.4 reveals that the SSS behaves differently at different latitudes. The common feature shown in Fig.4.4a for CGM3 and 4.4b for CGM2 is that, while it remains nearly unchanged in most parts of the world ocean, especially the SH oceans, the SSS changes considerably in the mid to high latitude NH oceans. The most striking drift of SSS occurs in the northern North Atlantic and the Arctic (north of 70°N) where the SSS increases immediately after coupling and keeps increasing during the whole course of integration for CGM3 but becomes stable in the last 300yr period for CGM2. The final increase is over 1.2

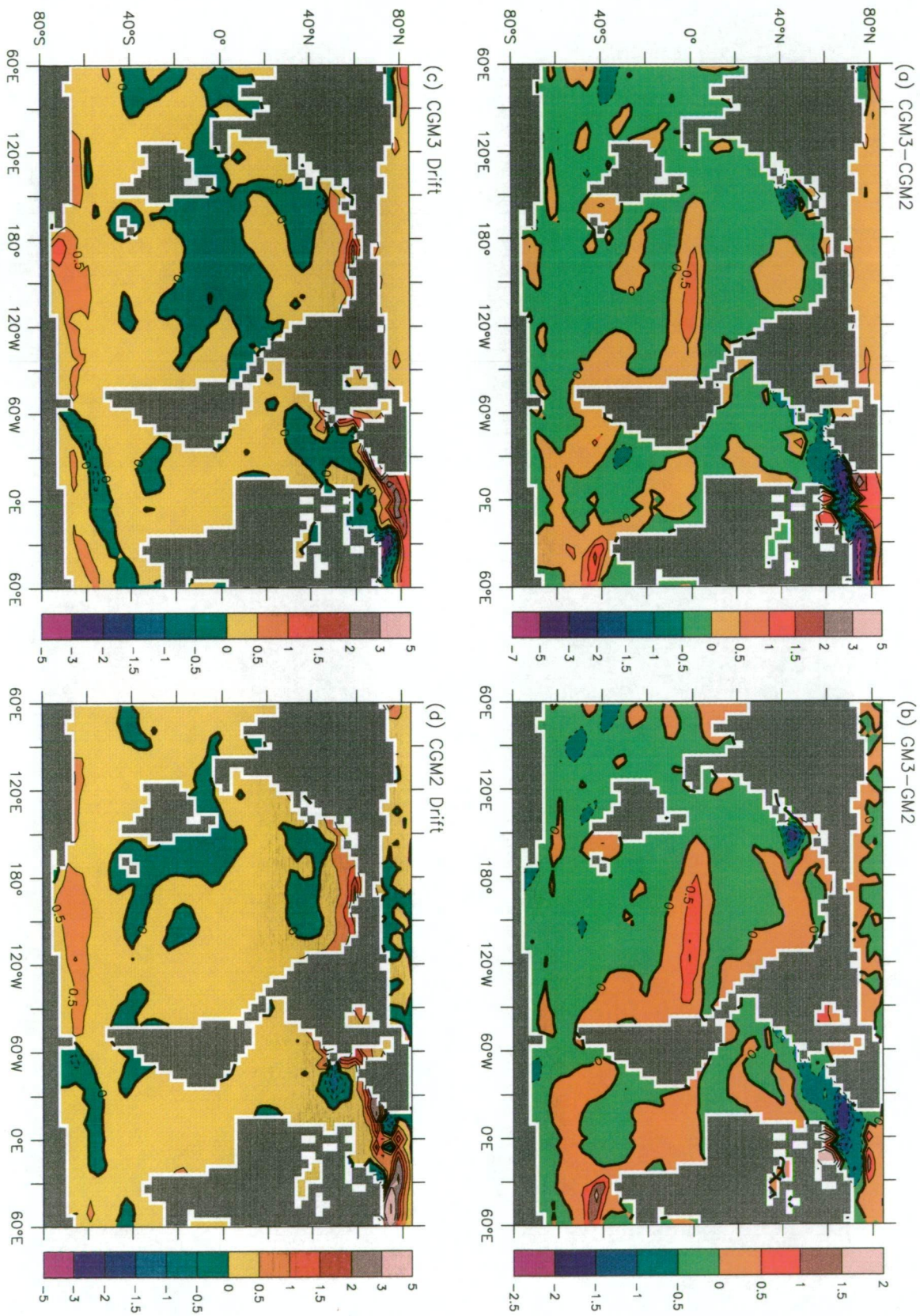

Figure 4.3: Distributions of SST (°C): (a) contrast between CGM3 and CGM2 by the end of the runs; (b) contrast between GM3 and GM2, (c) drift in CGM3, (d) drift in CGM2.

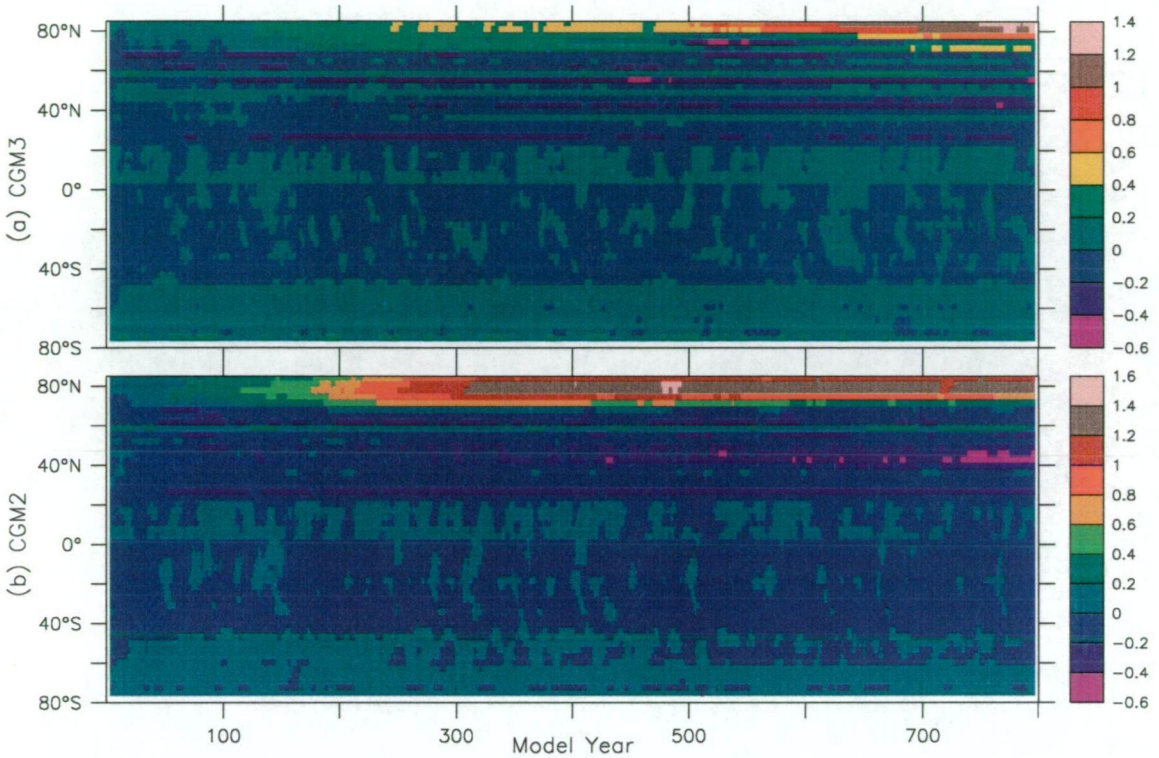

Figure 4.4: Changes of annual and zonal mean SSS (relative to year 1-50 mean) for: (a) CGM3, (b) CGM2). A 7-year running run filter is applied. (units: psu)

psu in the Arctic for both runs. In contrast, the mid-latitudes experience continuing freshening in CGM2 in particular, with the largest drift reaching near 0.6 psu just north of 40°N by the end of the integration. Such a freshening is found in CGM3 as well but with smaller magnitude.

The geographical distributions of the final SSS changes (relative to spinup climates) are shown in Fig.4.5c and 4.5d for CGM3 and CGM2, respectively. The bias of SSS increase is evident in (nearly) the whole Arctic for both runs. Such a bias is most likely attributable to the the change of surface forcing. In the spinup stage the restoring condition keeps the model SSS close to the low relaxation field (Levitus data) in the Arctic region, which leads to strong local gradients in both the horizontal and vertical directions. In the coupled mode, the removal of the surface constraint allows the model SSS to be able to evolve freely and local physical processes such as the advection, diffusion and convection operate to redistribute the salinity fields. As a consequence, significant SSS increase occurs in the Arctic and, accordingly, noticeable salinity reduction occurs in other regions, either at the surface or at

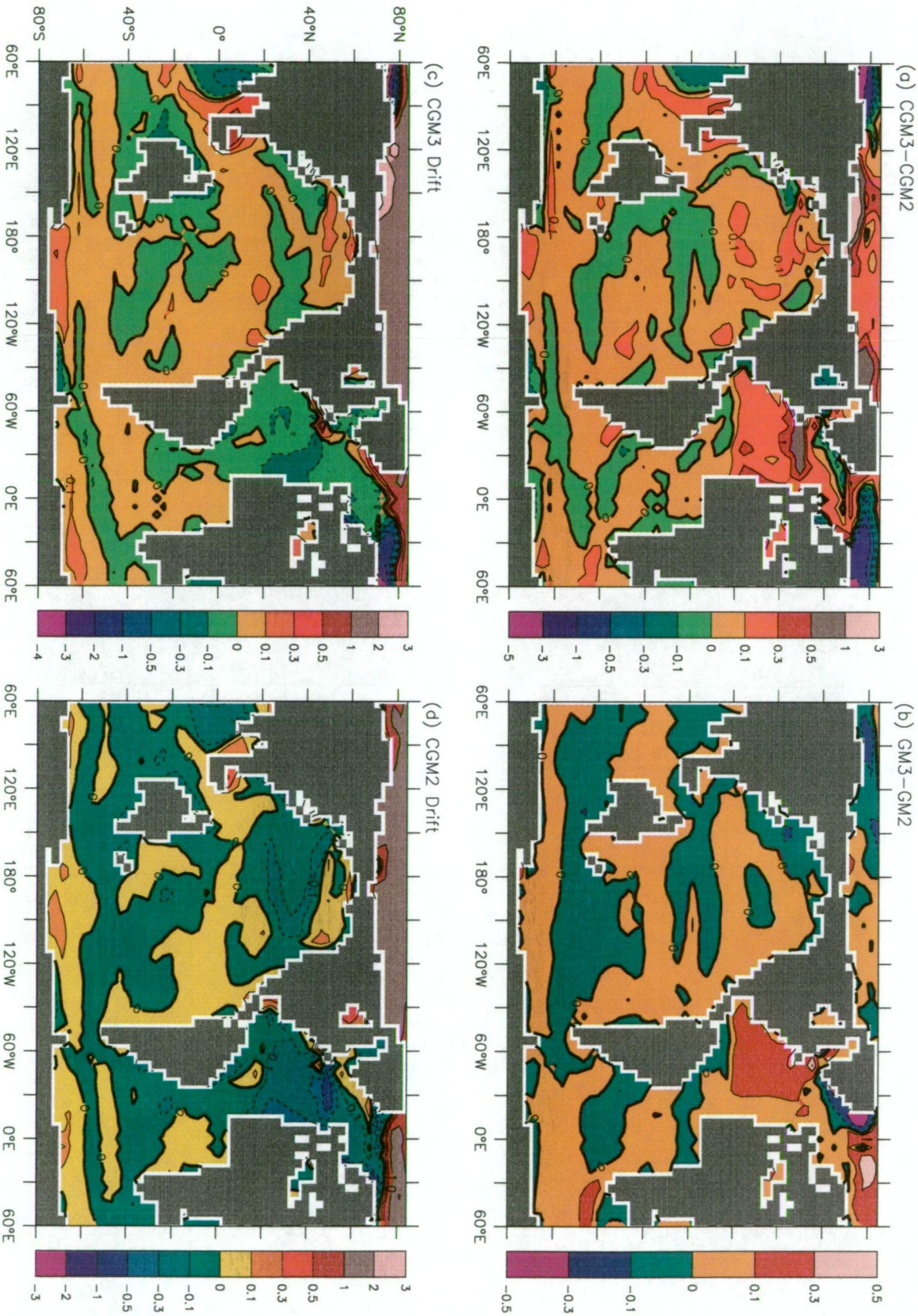

Figure 4.5: Same as Fig.4.3 but for sea surface salinity (psu).

depth. CGM3 sees the largest SSS increase (over 3 psu) in the East Siberian Sea and, meanwhile, the Barents Sea is freshened by as much as 5 psu. CGM2 suffers a little smaller drift over these regions but noticeable change is also found in coastal regions of the Barents Sea in particular. Such a large and local change in SSS may be attributable to both the removal of surface restoration of salinity and numerical noise, which is often found in ocean models based on the Cox-Bryan code.

The numerical noise, suppressed at the surface in ocean-alone mode due to the relaxation, can result from various model deficiencies or limitations such as coarse resolution, truncation errors associated with irregular vertical spacing and the Cox isopycnal mixing scheme at boundaries, and inappropriate diffusivity and/or viscosity (for details, see Weaver and Sarachik 1990; Gerdes et al. 1991; Gough and Welch 1994; Hirst and Cai 1994; Hirst and McDougall 1996). Although this problem may be very model- and topography-dependent, the noise typically appears as isolated grid values of tracer variables, such as salinity seen here, that are extreme relative to surrounding grid values and, if severe and spreading out, may contaminate the model solution by providing sources for spurious water masses. Hirst and McDougall (1996) found that either a lower isopycnal slope limit (e.g., 1:1000) or a smaller diffusivity of neutral density thickness κ_e (e.g., 0.40×10^7 cm^{2}s^{-1}) could result in numerical water mass contamination in their model. They concluded that all solutions using eddy-induced transport and no horizontal diffusivity should be carefully checked for numerical contamination. Note our models use a weak (and depth-dependent) background horizontal diffusivity to replace the isopycnal thickness diffusivity in the high northern latitude region (beginning from 74.9°N) to avoid spurious temperature and salinity, and the noise is found just south of this region and/or at the 'boundary'. The smaller drift in CGM2 than that in CGM3 is probably the result of its use of a larger κ_e (1×10^7 cm^{2}s^{-1}) in the ocean interior, contrasting to the value of 0.6×10^7 cm^{2}s^{-1} in CGM3, as already mentioned.

In addition, considerable drift in the northern North Atlantic is evident in both runs, but CGM3 sees large increases of salinity over the Gulf Stream region and the Labrador Sea (due probably to the removal of S relaxation and numerical noise

discussed above) and relatively weak freshening over other region, whilst CGM2 experiences marked freshening in most part of the northern North Atlantic. Such a large area freshening is also clearly seen over the North Pacific in CGM2. In the SH oceans, the two runs show SSS drift of very small and similar magnitudes. Fig.4.5a and 4.5b show the inter-version differences in the SSS distribution for the coupled runs and ocean spinups, respectively. The basic features of the differences between spinups are generally well maintained between the coupled runs in most basins. However, large changes occur in the Arctic and the northern North Atlantic, particularly from the Greenland Sea to the Barents Sea, owing to the different trends of drift there in the coupled integrations.

4.2.3 Sea ice

Fig.4.6 shows the time series of the annual mean sea ice extents and volumes for both hemispheres in the two coupled runs. Coinciding with the overall sea surface warming bias in the Arctic shown in Fig.4.2, the NH ice evolution has an apparent trend of reduction in both the extent and volume. By the end of the integration, CGM3 has lost about 5% of the ice cover area in NH, i.e., from 11.4×10^6 km^2 for the first 50 year average down to 10.84×10^6 km^2 for the last 50 year mean, and the loss of ice cover in CGM2 is about 7%. Both runs suffer much larger NH ice drift in the ice volume. For CGM3, in addition to the large interdecadal variability, the NH ice volume decrease from 19.3×10^3 km^3 to 12×10^3 km^3, indicating a loss up to 37.8% in the course of the run, with over 90% of this drift occurring in the last 300 years. The ice mass loss in CGM2 is slightly smaller but still reaches 17.6%. In the SH, the sea ice simulation is shown to be much more stable in both runs even though a dramatic decrease is evident in the first few decades for the ice cover in particular. After the initial drift, the ice extent evolves with a weak tendency to increase, and the last 10 year average reaches the level close to the first decade mean, with a decrease of only 3% and 15% for CGM3 and CGM2, respectively. It is interesting to note that, compared to the extremely stable ice volume, the SH

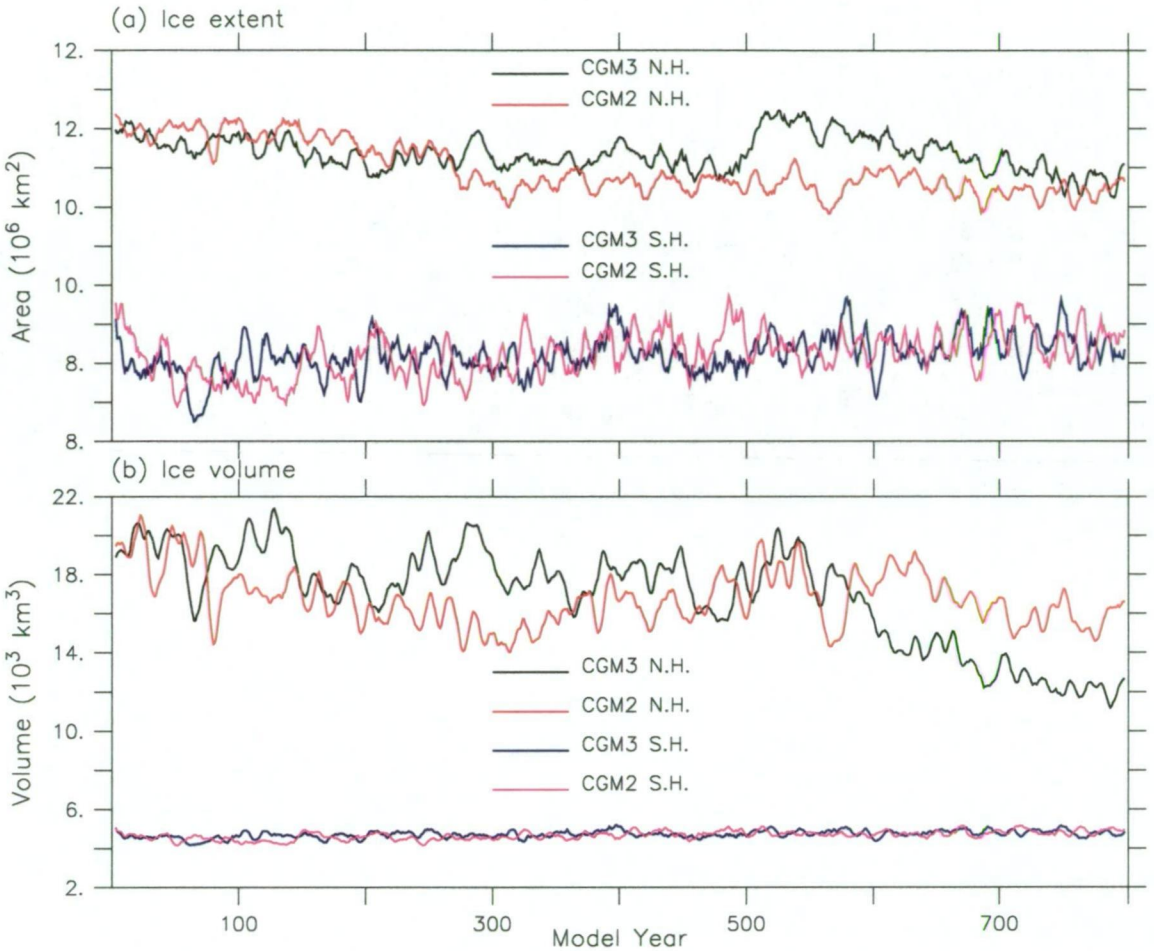

Figure 4.6: Time series of sea ice area and volume in both hemispheres for CGM3 and CGM2: (a) area, (b) volume.

ice cover area shows large interdecadal variability, which contrasts sharply with the situation of the NH where the ice volume shows larger variability than the ice cover.

Mention needs be made that, although the simulated SH ice falls within the observed range in the annual cycle, i.e, 2–15$\times 10^6$ km^2 (von Storch et al. 1997), and shows little drift, the annual mean model SH ice volume of less than 5×10^3 km^3 is somewhat too small compared to the accepted values, i.e., 10–16$\times 10^3$ km^3 (Parkinson and Bindschadler 1984; Stossel et al. 1990).

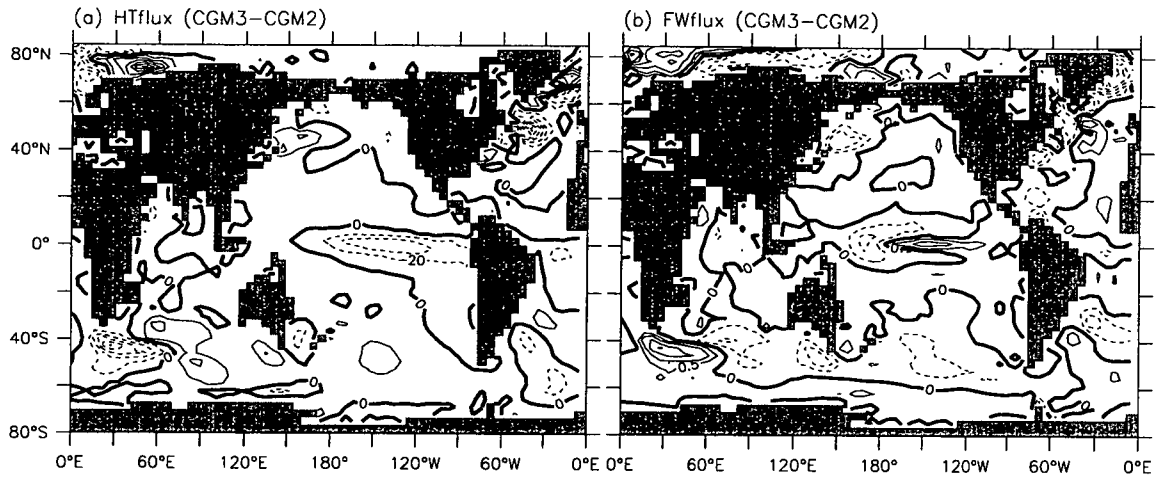

Figure 4.7: Differences of surface fluxes between CGM3 and CGM2 for period yr751-800: (a) heat, (b) freshwater. Contour interval is 20 $W\,m^{-2}$ for (a), and 1 m/yr for (b).

4.2.4 Surface Fluxes

In the coupled mode, the heat flux is computed at the interface between the ocean and air or ice above. For the ice free areas, the heat flux consists of solar heating, longwave warming or cooling, and heat exchange due to evaporation and sensible heat flux. For ice-covered ocean, there is a heat flux through the ice as well as the above components operating through leads. Regarding the freshwater flux in the coupled mode, it comprises precipitation less evaporation, runoff in coastal regions and the part due to ice melting and formation in the ice-covered ocean. Although these flux components may experience more or less drift and/or variation during the integration (not shown), the compounded fluxes show little drift in both runs, and the resultant inter-version differences, including that of the buoyancy flux (not shown), are preserved very well. This can be clearly seen by comparing Fig.4.7a and 4.7b to their counterparts for ocean spinups, i.e., Fig.3.7b and 3.8b. The only exception may be found in the Barents Sea region for heat flux in particular. This region, due to the negative SST drift shown in Fig.4.2, turns into a weak net heat gain area in CGM3 from a weak net heat loss area in GM3 and, in contrast, it loses more heat in CGM2 due to the positive SST drift there. Consequently, we see a marked heat flux difference between CGM3 and CGM2 in this area which is absent in the difference between GM3 and GM2.

4.3 Water Properties in the Ocean Interior

It is important for a coupled model to be able to keep a stable climate in the ocean interior in terms of the thermohaline state, especially the stratification. As is understood, large trends in the ocean interior will contaminate long-term responses of the ocean to surface perturbations in climate change studies.

Fig.4.8 shows the annual and basin mean vertical distributions of ocean water properties, including density, temperature and salinity, at the beginning (the first 50 year mean) and the end (the last 50 year mean) for the Southern Ocean and the global ocean in CGM3 and CGM2. The Atlantic and the Indian-Pacific basins are not shown separately here because they show results generally close to the spinup climates, with a little drift in a manner similar to that of the global ocean. Clearly, as illustrated by Fig.4.8a and 4.8b, both runs are subject to negligible drift in the water column stratification during the 800 year long integrations, and the contrast between the spinups GM3 and GM2 are thus nearly perfectly maintained for the global ocean in particular.

Examination of Fig.4.8c–f reveals that the temperature and salinity vertical structures do experience some noticeable changes, but the difference between the two runs are kept very well through the whole course of the integration. Furthermore, the drift in temperature and salinity develops in such a "reverse and compensating" way, i.e., the water is getting colder but fresher especially in the deep ocean, that the resultant density structures stay nearly unchanged in both runs, as shown in Fig.4.8a and 4.8b.

The global ocean zonal mean patterns of the water properties at the end of integrations are displayed in Fig.4.9, 4.10 and 4.11, for the density, temperature and salinity, respectively. Included are the corresponding drifts from their initial states, the difference between CGM3 and CGM2, and the Levitus climatology. Very clearly, all these variables are maintained close to their spinup climates shown in Fig.3.2, 3.4 and 3.6 for most latitudes of the global ocean. In the region south of 50°N,

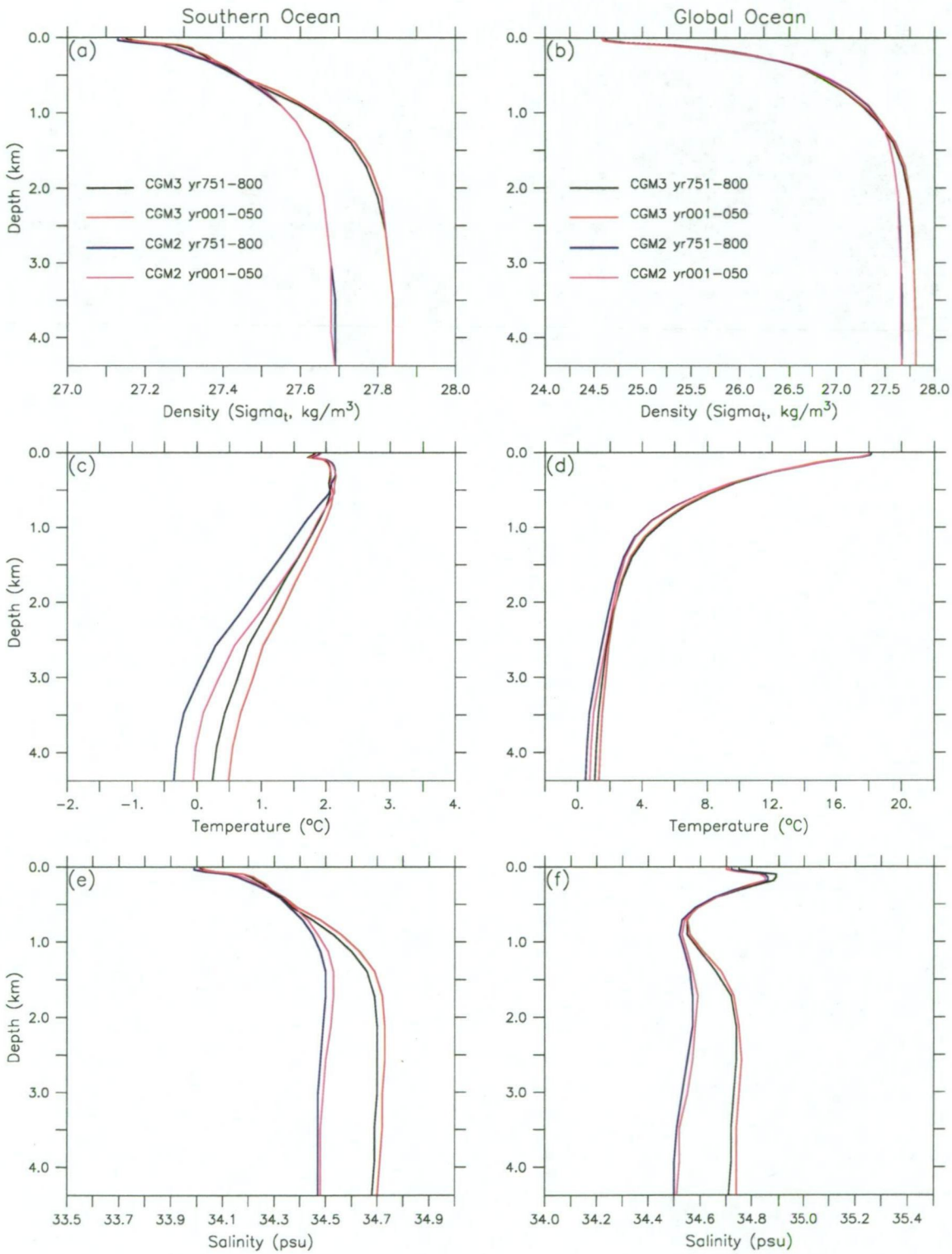

Figure 4.8: Vertical profiles of density (σ_t), temperature and salinity in CGM3 and CGM2 for the Southern Ocean (left column) and global basin (right column): (a)(b) density, (c)(d) temperature, (e)(f) salinity.

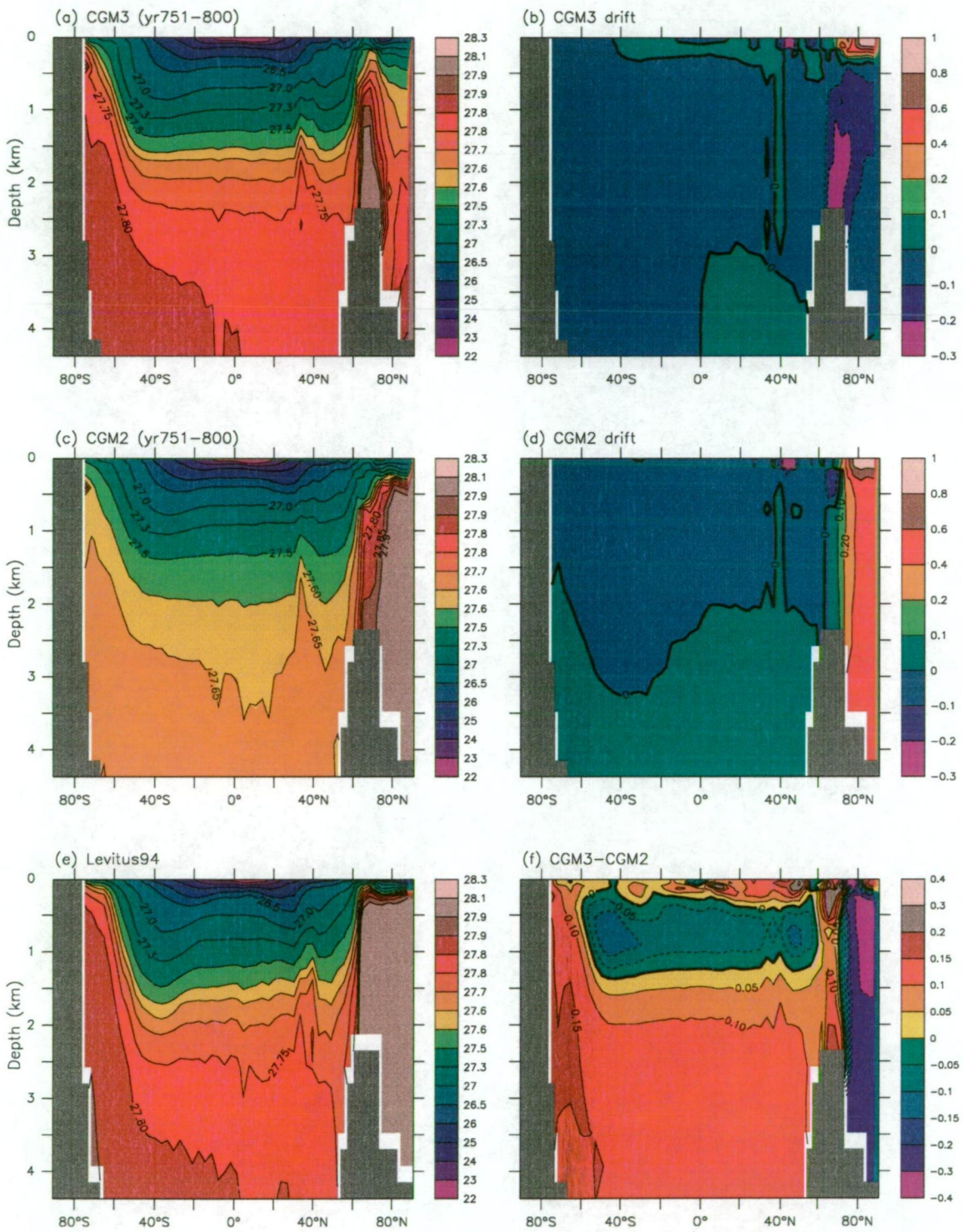

Figure 4.9: Zonal mean density (σ_t) structure for the global basin: (a)(b) are for the last 50-year mean in CGM3 and CGM2, (c) Levitus climatology; (d)(e) the final drift in CGM3 and CGM2, (f) difference of final state between CGM3 and CGM2. (units: $\mathrm{kg\,m^{-3}}$)

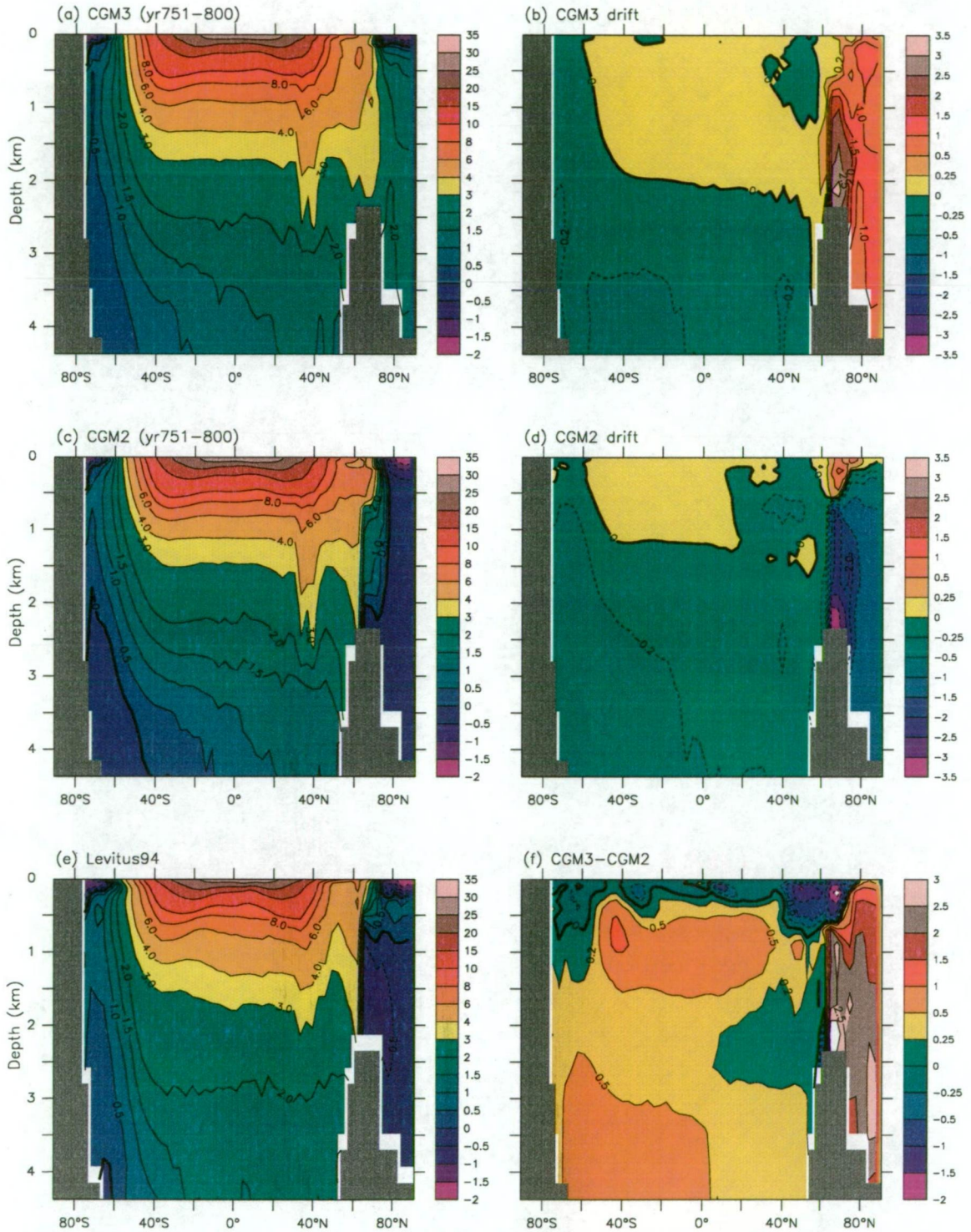

Figure 4.10: Same as Fig.4.9 but for temperature.

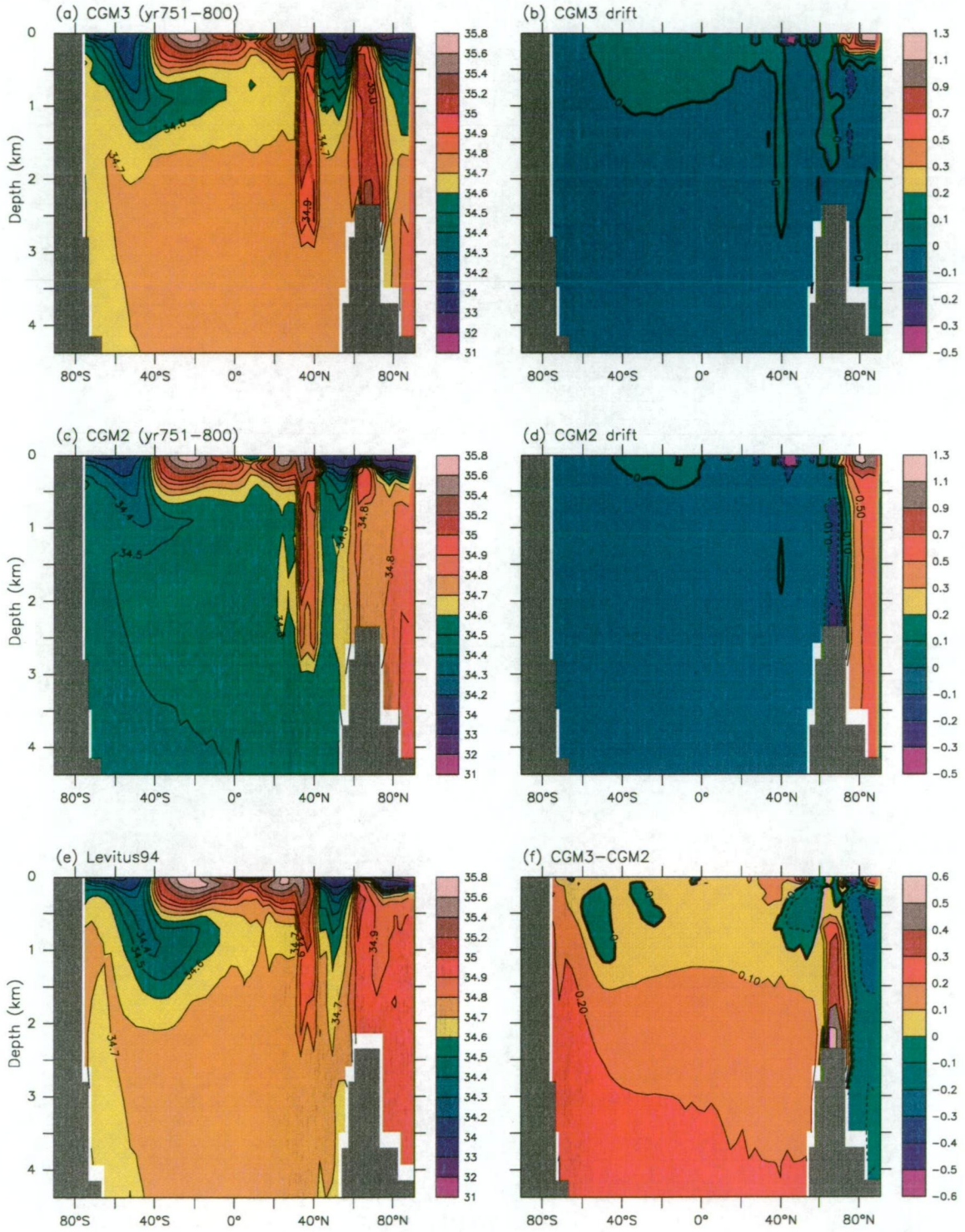

Figure 4.11: Same as Fig.4.9 but for salinity.

the water column stratification shows the least and negligible change due mainly to the above-mentioned small and compensating drifts in temperature and salinity, and, unsurprisingly, the stratification contrast between the ocean spinups shown is preserved in the coupled control runs.

However, significant drift occurs in the ocean north of 60°N, and the two runs behave quite differently there. First, CGM3 experiences considerable warming in the northern high latitudes, with the largest warming being more than 3 °C just over the Greenland-Scotland sill, whereas CGM2 suffers a similar magnitude of cooling in the same region. Accordingly, CGM3 sees more extensive (but very weak) warming in the "conveyor belt" region because the sinking branch of the North Atlantic overturning circulation transports some of the warming over the Greenland-Scotland sill down to greater depths and then brings it to the southern region with the circulation. Second, both runs exhibit marked salinity increase in the upper layer of the North Pole region, with the largest change being over 1.2 psu near the surface as already shown in the SSS change pattern. While CGM3 salinity stays little changed beneath 500 m, CGM2 sees penetration of such a positive anomaly down through the whole column to the north of 70°N, and, as a sharp contrast, the neighbouring Norwegian Sea column sees evident freshening with the largest negative anomaly being over 0.4 psu. Consequently, the northern high latitude ocean stratification is largely reduced in CGM3, whereas it changes little in CGM2 because the density gradient changes a lot horizontally rather than vertically, and the vertical stratification contrast between CGM3 and CGM2 reverses that between their spinups in the Arctic, as shown by Fig.3.2f and Fig.4.9f.

It may deserve special mention that the drift of temperature and salinity in CGM2 results in much more realistic northern high latitude ocean water properties than that produced in GM2. The marked deviation of the GM2 climate from the observations (Levitus 1994) in the Arctic Ocean, i.e., too warm and too fresh and therefore too light at depth as indicated by Fig.3.4 and Fig.3.6, is "corrected" to a large extent in the CGM2 solution. As a contrast, tracer drift in CGM3 further degrades the closeness of the water properties to the observations in the Arctic, and

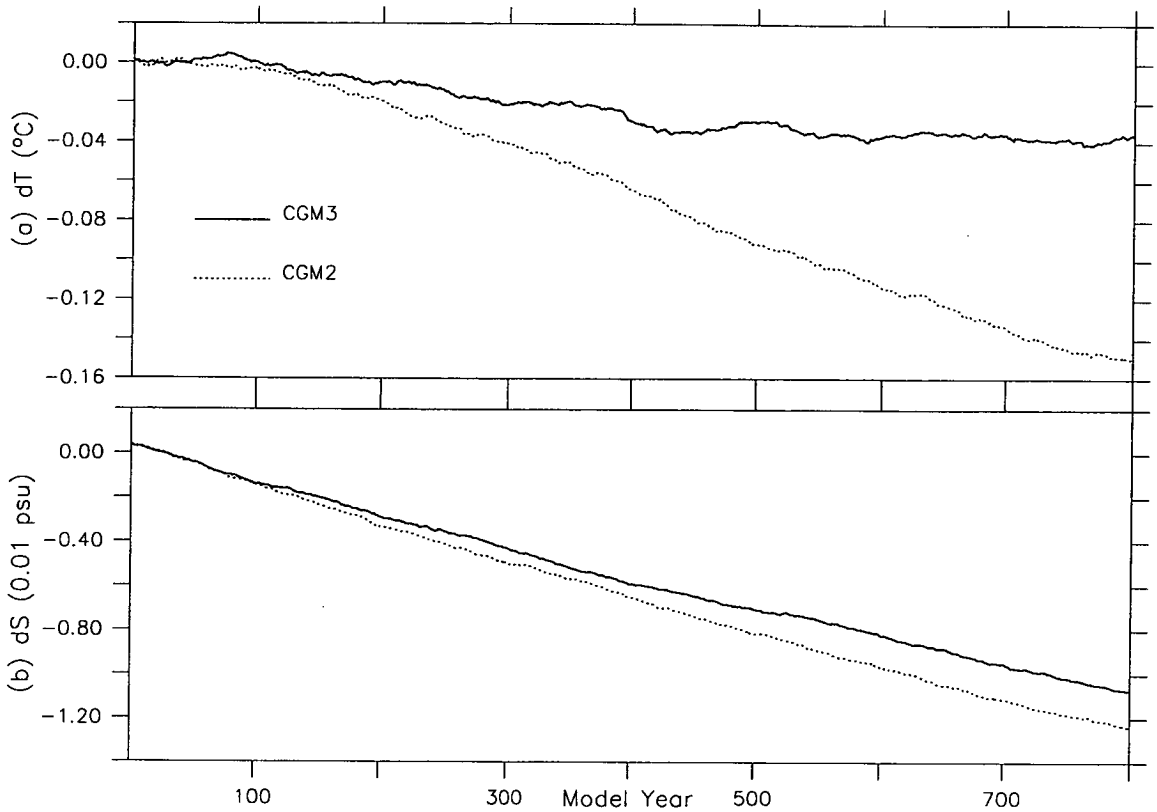

Figure 4.12: Changes for the entire ocean: (a) temperature, (b) salinity.

the evident weakening in the vertical stratification in the ocean north of 60°N is directly responsible for the generation of a local thermohaline circulation as to be shown later, which is absent in the GM3 solution.

Fig.4.12 illustrates the evolution of the global ocean volume-weighted changes in temperature and salinity (relative to the first 50 year mean) for CGM3 and CGM2. As shown in Fig.4.12a, both runs have a trend of cooling for the entire ocean and CGM3 reaches its (quasi-)equilibrium much more quickly than CGM2 due mainly to its stronger overturning circulation in the north which transports the surface perturbation signals down to the deep ocean more efficiently. The final drift of the temperature for the entire water column is within 0.04 °C in the CGM3 run while its counterpart in CGM2 is about 0.13 °C by the end of the integration. Hirst et al. (2000) showed that the employment of the GM scheme in the ocean greatly suppresses the convection, especially at southern high latitudes, and thus reduces the coupled model climate drift substantially. Compared to their results, i.e., a

cooling of about 0.38 °C in the global ocean temperature (volume-weighted mean) in a 1000 year control run with a tendency of further cooling by the end of integration (see their Fig.18), our simulations with more recent GM version ocean models show further reduction in the climate drift and quicker convergence, especially in the case of the CGM3 integration. This is largely brought about by the more realistic initial oceanic state obtained with the modified surface forcing fields. With respect to the vertical character of the temperature changes (not shown), CGM3 sees warming bias in a layer from the surface down to near 2 km depth in the course of the run, while the warmed layer in CGM2 shoals from 1.3 km to 0.5 km depth along with the progression of the integration. The deep ocean in both runs is subject to a noticeable cooling bias (up to 0.25 °C) by the end of the runs, and it converges somewhat more quickly in CGM3.

It is also evident that, as shown in Fig.4.12b, the global ocean experiences a very weak freshening during the integrations. CGM3 suffers a salinity reduction of about 0.011 psu by the end of the run while CGM2 is subject to a slightly larger one, i.e., near 0.013 psu. This drift in salinity, although very small, indicates a kind of deficiency of the model that breaks the salinity closure constraint. It appears to become larger under global warming forcing and is discussed in Appendix B. Examination of the depth-dependent changes (not shown) reveals that CGM3 suffers freshening in the deep ocean and an increase of salinity in the upper layer water (above 600 m depth), whereas CGM2 sees freshening in the entire water column by the end of the integration.

4.4 Convection and Overturning Circulation

Due to the general persistence of stratification in most parts of the world ocean, particularly in those convectively active regions, the major features of convective mixing simulated in ocean-alone mode are thus generally well maintained in the coupled runs (not shown). However, there still are some evident changes. For CGM3,

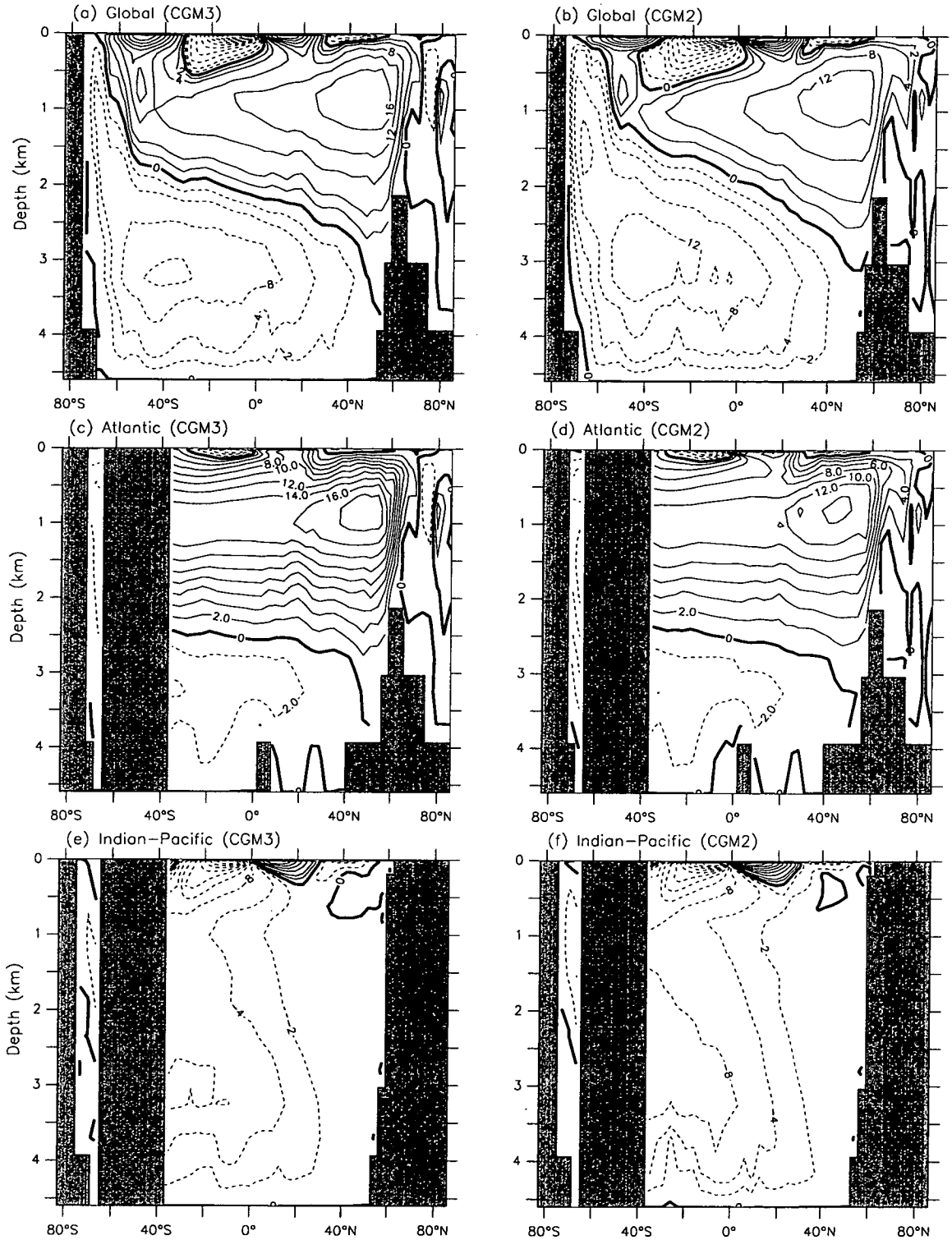

Figure 4.13: Overturning streamfunction (Sv) for the last 50 year period of the CGM3 (left column) and CGM2 (right column). Contours: (a) -40 to 32 with interval 4, plus ±2 lines; (b) -52 to 44 with interval 4, plus ±2; (c) -8 to 22 with interval 2; (d) -10 to 16 with interval 2; (e) -36 to 24 with interval 4, plus ±2; (f) -44 to 36 with interval 4, plus ±2.

the maximum depth of convection in the Labrador Sea has shoaled from 1900 m in GM3 to no more than 1550 m. Such a shoaling is associated with the intensification of the subsurface layer stratification there, which is clearly shown in Fig.4.9b (0–500 m, 50–60°N sector), due mainly to the surface freshening bias following the removal of SSS relaxation. It has an immediate impact on the downward penetration of the North Atlantic overturning. In the Southern Ocean, the maximum depth of convection also changes a little. For example, in the Weddell Sea shelf region and the southwestern corner of the Ross Sea, the deepest convection can penetrate about 100 m deeper in the CGM3 final solution than in GM3, which may contribute to somewhat stronger local overturning circulation in the coupled mode as shown below. In CGM2, the most notable change in the convection occurs in the Weddell Sea: the deepest penetration can reach down to 1200 m depth, in contrast to 1000 m in the spinup solution, which also leads to a slightly stronger overturning in the Southern Ocean as discussed below.

Fig.4.13 shows the last 50 year mean meridional overturning streamfunctions for the coupled runs in the global ocean and individual basins. Compared to their counterparts in the ocean spinup solution (Fig.3.12), the fundamental pattern of the world ocean THC in both versions are clearly preserved. However, drift in the circulation intensity can be seen in the northern North Atlantic and in the Southern Ocean, although the changes are very small. For instance, as shown by the global ocean circulations, the Antarctic direct downwelling cell (AABWF) and the merged deep overturning cell (outflow of the AABW) become slightly more intense in the coupled runs, while the strength of the North Atlantic overturning (NADWF) becomes somewhat weaker. In addition, due to the substantial weakening of the vertical stratification in the Arctic as shown in Fig.4.9b, CGM3 sees a pair of local overturning circulations in this region which are absent in the GM3 spinup. However, these "new born" weak cells have no direct connection to the outside and thus can impose little effect on the global ocean.

Fig.4.14 presents the time series of overturning streamfunction peak values in the North Atlantic (44.6°N, 800 m depth) and the Southern Ocean (66.9°S, 1540 m

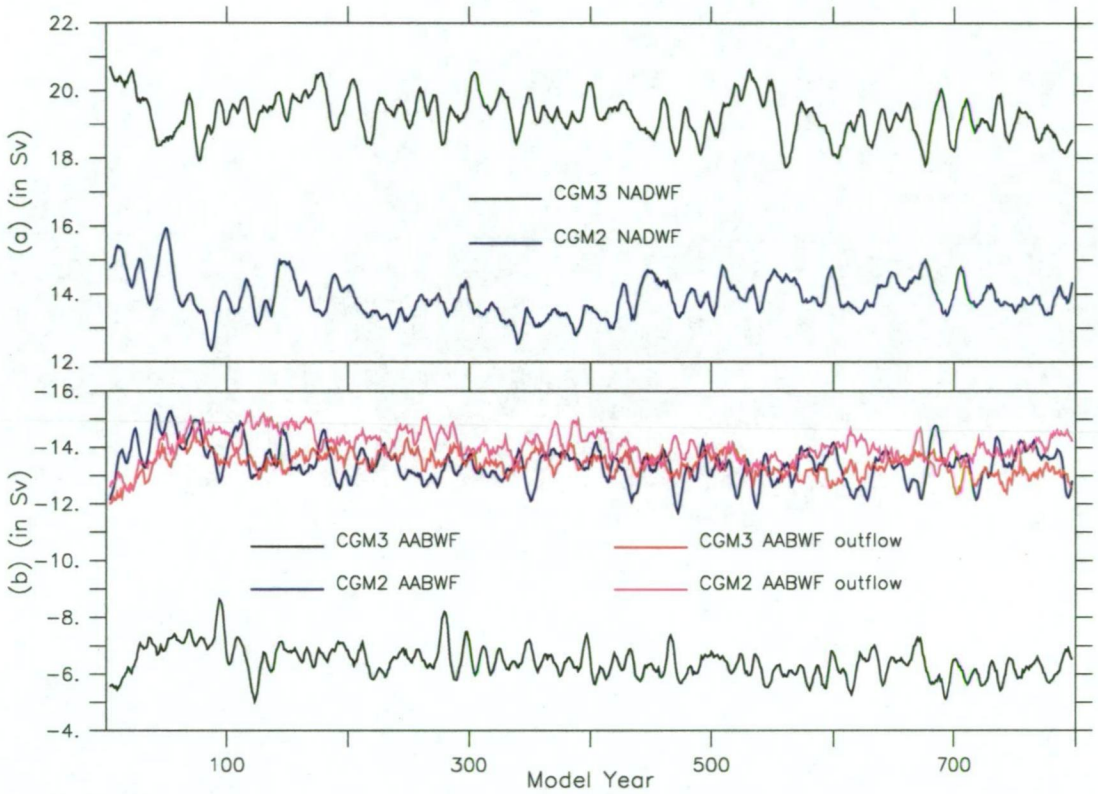

Figure 4.14: Time series of global ocean overturning intensities in CGM3 and CGM2: (a) NADWF; (b) AABWF and AABW outflow.

depth) for both runs. We see that both the weakening of the NADWF and the strengthening of the AABWF occur in the first few decades following coupling, and after that the overturning circulations stay quite stable, but with considerable interdecadal variability. The depth of the NADWF penetration becomes slightly shallower following coupling, corresponding to the shoaling of convection and weakening of overturning in the northern North Atlantic.

4.5 Antarctic Circumpolar Current

It is of great interest to examine the behaviour of the global ocean barotropic flow in our coupled runs, since some previous studies have shown that this vertically integrated horizontal mass transport, particularly in the southern high latitudes, is rather sensitive to the coupling. For example, the CSIRO model mark2-HB version

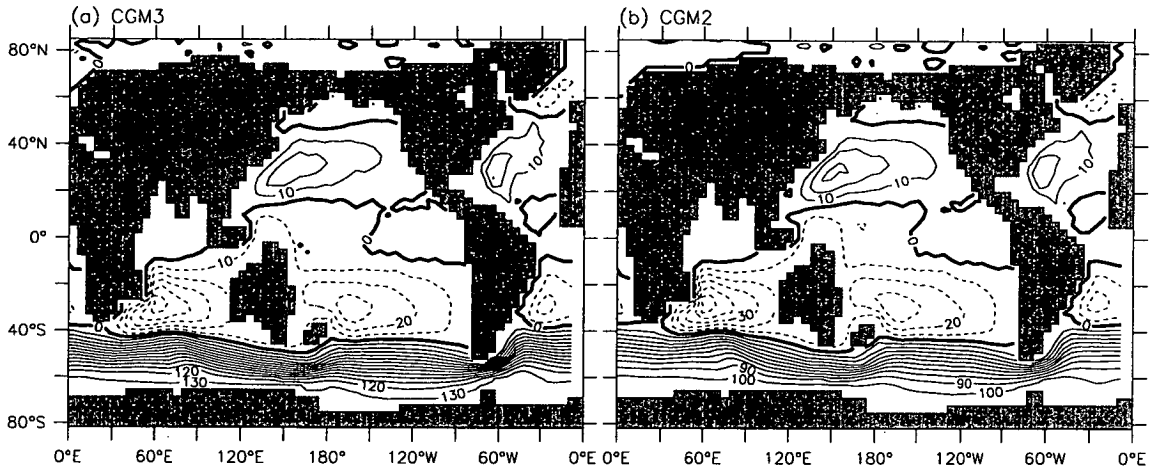

Figure 4.15: Barotropic streamfunctions for the last 50 year mean for: (a) CGM3, and (b) CGM2. Contour interval is 10 Sv.

(Gordon and O'Farrell 1997) suffered dramatic climate drift in the ACC transport. In a control integration, the ACC intensified by about 30 Sv within 100 years following coupling (Cai and Gordon 1999), despite the use of flux adjustments. The NCAR CSM, which is configured with no flux adjustments, suffered substantial drift in the barotropic flow of all main currents, especially the ACC which increased from around 120 Sv of the uncoupled ocean equilibrium to 280 Sv within the first few decades (centuries of deep water integration) of the ice-ocean spinup, and remained at a level more than twice its initial value throughout a 300-year coupled control integration (e.g., Danabasoglu 1998, Bryan 1998).

Our coupled runs, as a contrast, show very little drift in the barotropic flow following the coupling and during the course of 800-year integrations. The annual mean barotropic streamfunctions for CGM3 and CGM2 shown in Fig.4.15 are very close to their ocean spinup counterparts in terms of the pattern of all the major gyres and their intensities, with no noticeable change in those main current transports. The only exception may be found in the ACC, which experiences minor but "visible" change in both runs, with the transport through Drake Passage increasing from about 127 Sv (100 Sv) to 134 Sv (108 Sv) in the CGM3 (CGM2) integration. It is noted that nearly all this drift occurs within the first century following coupling in both runs, and the total drift rates of 5.5% for CGM3 and 8% for CGM2 in the

800-year integration are obviously very small compared to that occurring in some other models such as those mentioned above.

An interesting question arises as to what causes the big difference of the ACC response to coupling between our models and the others. The work of Bryan (1998) revealed that the substantial drift of ACC transport in the NCAR CSM coupled model results initially from the Southern Ocean ice-covered region SSS drift due to the removal of restoring upon coupling. In the coupled mode, the sea-ice and ocean models interact and the SSS shift begins because of the deficiency in the ice model, i.e., far too much offshore transport of sea ice. This large offshore ice mass transport must be supported by excessive new ice formation which leads to large amounts of brine rejection over the Antarctic shelf and upsets the freshwater balance. As a result, the surface density increases, which causes deeper convective mixing and thus intensifies the overturning off Antarctica as shown in the Fig.8 of Bryan (1998). As is well known, the ACC is primarily driven by the prevailing westerly winds and its speed and transport are thought to be a balance between the surface zonal windstress and the bottom and lateral frictional retardation, i.e., the topographic form drag. Bryan (1998) pointed out that the westward-directed form drag is proportional to the strength of the southward flow below the depth of the shallowest sills in the circumpolar channel. The intensification of deep convection and overturning enhances the northward flux of AABW and thus diminishes the strength of the westward drag, allowing the ACC to strengthen until the retarding bottom and lateral friction and the driving stresses can reestablish a balance.

Cai and Baines (1996) showed that the ACC is also driven by a kind of "bottom form stress", which is actually the zonal pressure force pointing eastward, associated with the northward outflow of AABW. The strengthened overturning off Antarctica, or say the AABWF, naturally enhances this flow in the Antarctic bottom ocean, in effect accelerating the ACC. For the CSIRO coupled model mark2-HB version, a similar mechanism is in operation and the direct cause of the ACC strengthening is the joint effect of SST and SSS drift (i.e., cooling and salinity increase) in the Southern Ocean (see Gordon and O'Farrell 1997, Cai and Gordon 1999), which is

associated with the Antarctic ice growth. Gordon and O'Farrell (1997) showed that the SH ice volume increased by about 20% during their first hundred year integration, and, as per Hirst et. al (2000), the corresponding ice cover extended more than 30% by the end of the 300-year integration for the same run. The ice growth and the other related drift in the southern high latitudes, as addressed by Cai and Gordon (1999), is primarily caused by the instability of oceanic convection of the spinup climate which is obtained by applying large artificial horizontal diffusion in the ocean model for numerical reasons. Hirst et al. (2000) showed that their GM1 version ocean model, which is very similar to the GM2 version used in this study, yields stronger upper ocean stratification, cooler, saltier and thus denser deep water which reduces the deep convection in the southern high latitude ocean. Such improvements strengthen the model convective stability considerably and therefore largely reduce the coupled model oceanic drift in the Southern Ocean. This conclusion is confirmed by our control experiment results, which, in addition to a stable westerly windstress (not shown) providing the primary zonal momentum to drive the ACC flow, shows very small drift in sea ice, SSS, SST, overturning circulation and convection in the Southern Ocean, and thus very small drift in the ACC transport. This small ACC drift (enhancement), according to the above discussion, is largely associated with the intensification of the overturning off Antarctica following coupling and the accordant strengthening of the deep ocean northward flow. This issue will be further addressed in Chapter 5, where we examine the change of ACC under global warming and discuss the relevant mechanisms.

4.6 Climate Variability

Here we examine and compare climate variabilities in our coupled runs, using SST/SAT as the indicators and focusing on the interannual and interdecadal scale variations over the globe and some important ocean regions in particular.

Fig.4.16 presents the standard deviations for the modelled annual and decadal mean

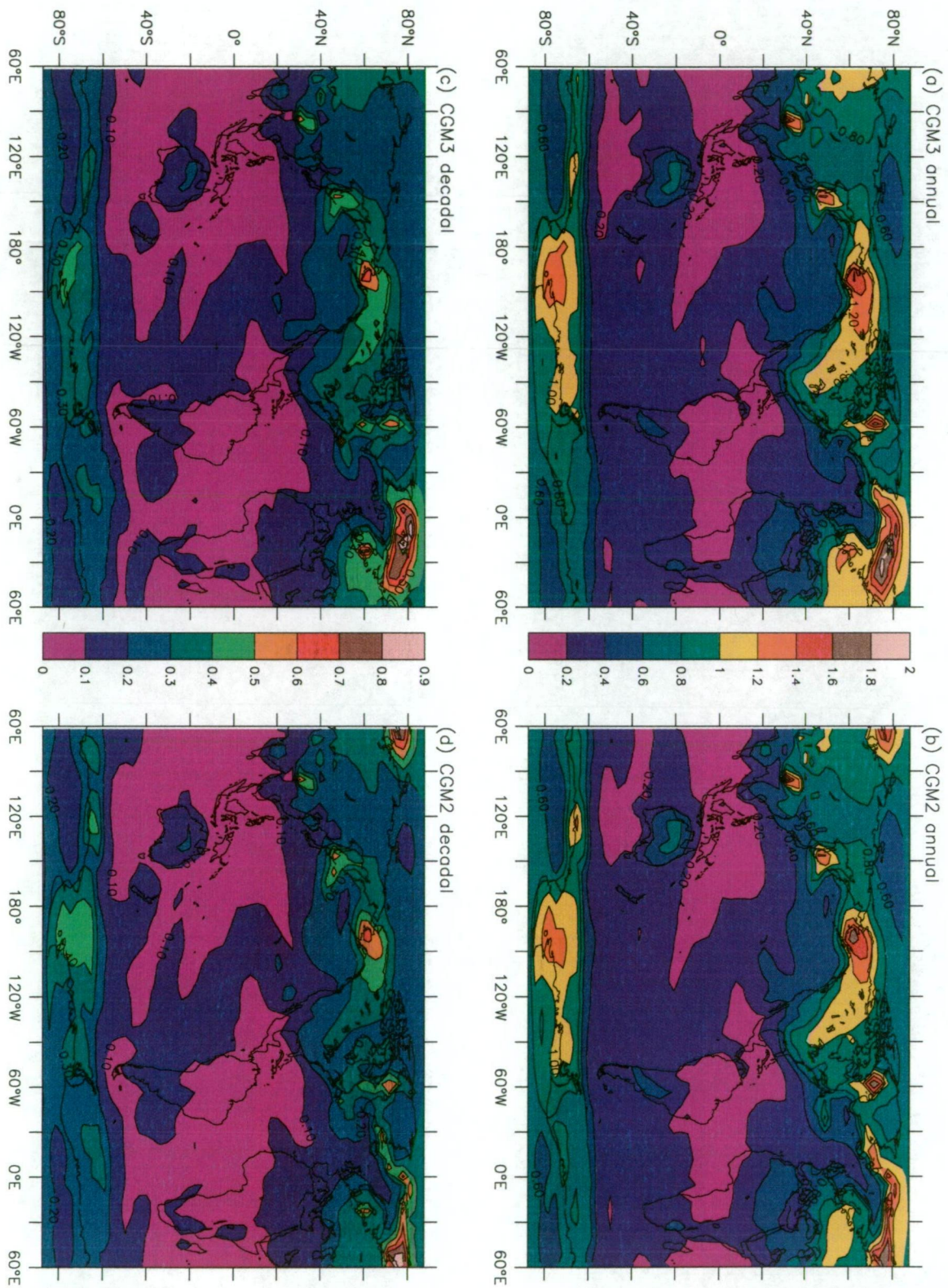

Figure 4.16: Standard deviation of annual and decadal mean SAT over the globe for: (a) CGM3 annual, (b) CGM2 annual, (c) CGM3 decadal, (d) CGM2 decadal. Contour interval is 0.2 for (a)(b), and 0.1 for (c)(d). (units: °C)

SAT over the globe. To account for the long-term drift of the system, the SAT time series for all gridpoints have been detrended. We define the long-term trend lines for each gridpoint by using a centennial smoothing filter (i.e., 99-year running mean) on the respective 800-year long time series, and calculate the deviations of either annual or decadal means about these trend lines. Clearly these two runs bear large similarity in the "natural" (internal) variabilities on both the interannual and interdecadal scales in terms of the magnitude and geographical distribution pattern in nearly all regions (over both the land and oceans), with only some noticeable differences existing over the North Atlantic, especially the Barents Sea, where both runs suffer significant drift in SST, as already shown above. In addition, the variabilities of the two different time scales have very similar global pattern except for the distinctive magnitudes. Namely, all those regions subject to significant interannual variability see large interdecadal variation as well. For the case of interannual time scale, large variability say, over 1.2 °C, is found mainly in high latitudes in both hemispheres, especially those regions with season-dependent ice- or snow-cover such as the Ross Sea in the Southern Ocean, Hudson Bay and the Barents Sea in the North Atlantic and Arctic, Alaska in North America, the Sea of Okhotsk in the northwestern Pacific, and the Himalayas-"the roof of the world".

As is well known, in these ice- or snow-covered regions, the "normal" natural interannual variation of the ice/snow extent can trigger sensitive and large responses from the local overlying air temperature due to the positive ice/snow-albedo-temperature feedback. This feedback process operates in the following way: as sea-ice/snow cover increases(decrease), surface and planetary albedos increase (decrease), which leads to the increase (decrease) in outgoing shortwave radiation and therefore reduces (increases) the absorption of solar energy by the coupled system, causing the SST or surface air temperature to decrease (increase), and thereby resulting in further increase (decrease) in sea ice or snow cover. Apparently, this feedback firstly enhances climate drift in the coupled model once it operates in one direction until other complicated processes such as those negative feedback mechanisms work to turn it back in another way. No matter which way the ice/snow develops, the local

temperature always keeps changing in response and thus has a large variability. As a contrast, tropical and sub-tropical oceans in the model see small variations, i.e., typically less than 0.4 °C. It is interesting to note that, except for the largely reduced magnitude (which is still relatively large), the global SAT interdecadal variability has a distribution pattern coinciding with its interannual scale counterpart very well, especially in the above-mentioned ice/snow covered regions. This indicates that in these regions the SAT persists with evolution trends for periods up to the centennial scale.

Hirst et al. (2000) have shown that, although the GM scheme leads to substantial improvement in the ocean water properties, especially much more realistic vertical stratification and thus much reduced convection, its employment in the ocean component only results in some regional increases or decreases in the magnitude of interannual variability of SAT, giving rise to no systematic overall change from that produced in the HB version model. As expected, our runs with the two more recent GM versions show no significant difference as well in the SAT variability distributions over the globe.

Table 4.1 lists the interannual and interdecadal variabilities of SST and SAT in terms of the standard deviations (S.D.) for some important basins. These regions are the global ocean, the Southern Ocean (south of 50°S), the North Atlantic (40–75°N, 60°W–0°E), the western tropical Pacific (10°S–10°N, 120–160°E), and the eastern tropical Pacific (10°S–10°N, 80–120°W). The S.D. values are calculated about their respective centennial mean time series, i.e., long-term trend line (as a way to detrend).

Although Fig.4.15 shows large variability in many regions such as the high latitude Southern Ocean around Antarctica, the variabilities obtained in terms of area-averaged time series for a region as a whole give much reduced magnitudes, just due to the cancellation of reverse changes at different gridpoints. Unsurprisingly, CGM3 and CGM2 show quite similar SST (SAT) variabilities on both the interannual and interdecadal time scales in all basins. However, it may be worth noting that the

Table 4.1: Standard deviations of annual and decadal mean SAT and SST in CGM3 (C3) and CGM2 (C2) for the specified regions (units: °C). The S.D. is calculated about the corresponding trend lines based on a centennial mean smoothing filter (therefore the S.D are actually taken over the period of model year 50-751).

		Globe		N. Atlantic		S. Ocean		E. Pacific		W. Pacific	
		C3	C2	C3	C2	C3	C2	C3	C2	C3	C2
SST	Annual	.042	.045	.158	.163	.074	.083	.207	.221	.130	.121
	Decadal	.027	.027	.102	.109	.042	.051	.108	.105	.039	.032
SAT	Annual	.055	.060	.200	.203	.149	.162	.193	.209	.089	.088
	Decadal	.035	.035	.115	.126	.073	.090	.101	.099	.038	.035

CGM3 variabilities are generally slightly smaller than their CGM2 counterparts in all basins except for the western tropical Pacific. The largest differences are found in the Southern Ocean, where the SST (SAT) interannual variability in CGM3 is 12.2% (8.7%) smaller than that in CGM2 while the SST (SAT) interdecadal variability in CGM3 is 21.4% (23.3%) smaller than that in CGM2. It is a common deficiency for all models with coarse resolution in tropical oceans in particular, that they are not adequate for simulating ENSO behaviour. In the eastern tropical Pacific basin which is roughly located in the NINO3 region, the SST interannual variability being smaller in CGM3 than CGM2 may suggest that the CGM3 version has even less ability to simulate the ENSO like events than CGM2. For the global ocean, our results show SAT interannual variabilities of 0.055 °C and 0.060 °C in CGM3 and CGM2, respectively, both being much smaller than the estimation of Santer et al. (1995), i.e., about 0.10 °C, and also smaller than the simulated value of 0.076 °C of Hirst et al. (2000) using the GM1 version model.

Chapter 5

Transient Climate Change: $3\times CO_2$ Experiments

Results from two parallel transient climate change experiments using the CSIRO coupled model are documented in this chapter. Our focus is on the oceanic responses to CO_2 forcing, especially the changes of THC, but evolution of the surface condition is also presented due to its strong relevance to the ocean interior change. Comparisons have been made to examine the difference in climate change between the two runs.

5.1 Experiment Description

The two transient global warming integrations are initialized with the control solutions of CGM3 and CGM2 at the end of model year 100 and are referred to as TGM3 and TGM2, respectively. The atmospheric CO_2 equivalent of total greenhouse gases (referred simply to as CO_2) concentration follows the (extended) IPCC/IS92a radiative forcing scenario for the period 1880 to 2082 (Shine et al., 1990; Kattenberg et al., 1996), i.e., $C = C_0 e^{\Delta Q/6.3}$ where C is the changing equivalent CO_2 concentration, C_0 (330 ppm, notional 1880 level) the initial CO_2 amount used in the control

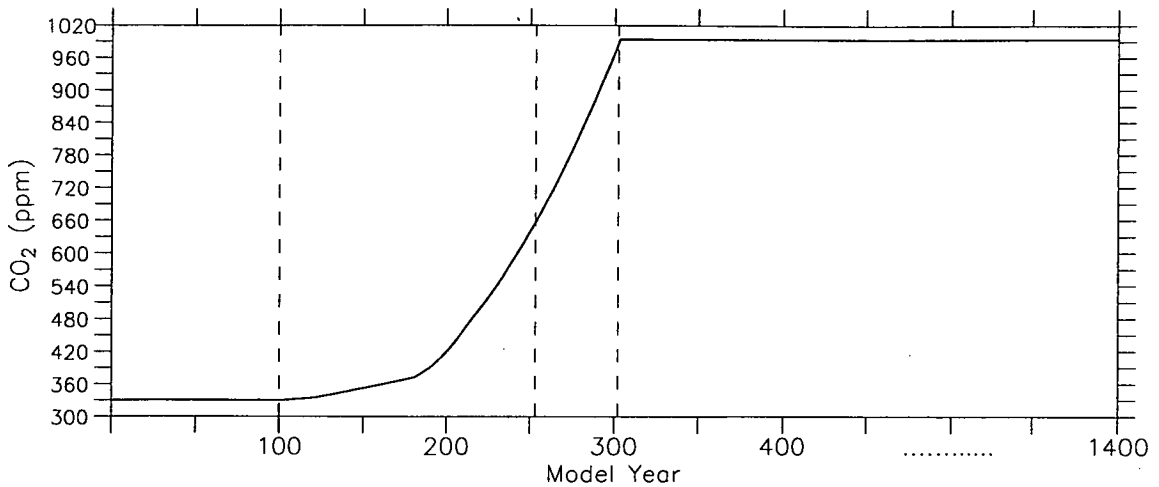

Figure 5.1: Equivalent CO_2 forcing scenario (IPCC/IS92a) for transient experiments TGM3 and TGM2.

run, and ΔQ is a specified radiative forcing change, taken to be that for CO_2 and all other trace gases except for aerosols. For the period from 1880 to 1990, ΔQ is taken to be that given by IPCC 1990 (their Fig.2.2) and scaled upward by a factor of 1.07 as per the reanalysis of IPCC 1995. For the period from 1990 to 2082, ΔQ is taken to be that given under the IS92a emission scenario according to IPCC 1995 (their Fig.6.19). CO_2 reaches three times the 1880 level in 2082, and henceforth is set unchanged at that elevated value. The $3\times CO_2$ stabilization integrations last for about 1100 years (i.e., until 3180) in TGM3 and 650 years (until 2730) in TGM2, respectively. For simplicity and uniformity, in our discussions hereinafter the model year count will be referenced to the start of the control runs instead of the calendar year. Therefore TGM3/TGM2 has a total integration length of 1400/950 years, comprising three periods: 100 year control simulation, 202 year integration with CO_2 increase during which CO_2 doubles in year 253 and trebles in year 302, and an extended CO_2 stabilized period of about 1100/650 years, as shown by Fig.5.1.

The following discussions are mainly based on the results from TGM3, and the TGM2 results are presented where appropriate for comparison, aimed at examining the dependence of climate change, especially the oceanic change, on the basic state of the ocean. In addition, for simplicity we define the transient responses of all variables under examination as the changes relative to their corresponding initial

control climates (i.e., year 51 to 100 mean). As discussed in Chapter 4, the oceanic variables in the control runs are subject to very small residual drifts in terms of the average state on basin to global scales. However, considerable drift occurs in limited regions, e.g., SST and SSS over the Arctic Ocean. This kind of local drift will to some extent contaminate the local response to the warming forcing and are addressed in our discussions.

5.2 Surface Responses

Naturally, the effect of the atmospheric CO_2 anomaly forcing is firstly reflected by the surface changes. Here we examine the evolution of surface thermal and hydrological states at the sea surface in response to the transient CO_2 increase and the subsequent stabilization.

5.2.1 Surface Air Temperature

Fig.5.2 presents the temporal variation of the annual mean surface (screen) air temperature change in response to the CO_2 anomaly forcing in TGM3. Also included is the difference in response between TGM3 and TGM2. Fig.5.2a shows a global average warming of about 6.6 °C by the end of the TGM3 integration. During the period of increasing CO_2, SAT response follows the thermal forcing nearly linearly, in a manner similar to that found by Manabe and Stouffer (1994) and very close to the change rate obtained by Hirst (1999) in the CSIRO model GM1 version with a similar increase/stabilization scenario. By the time of CO_2 tripling, the globally averaged warming reaches up to 3.8 °C. During this period, average warming over the continents is 4.9 °C, significantly larger than that over the oceans (3.4 °C). As is well recognized, this land-sea contrast of response of surface warming is due to the large difference in the effective heat capacity (vertical heat transfer rate) between the oceans and land. After CO_2 tripling, the global average SAT still keeps increasing at a fairly large rate (about 0.57 °C/century) for 400 years, leading to an additional

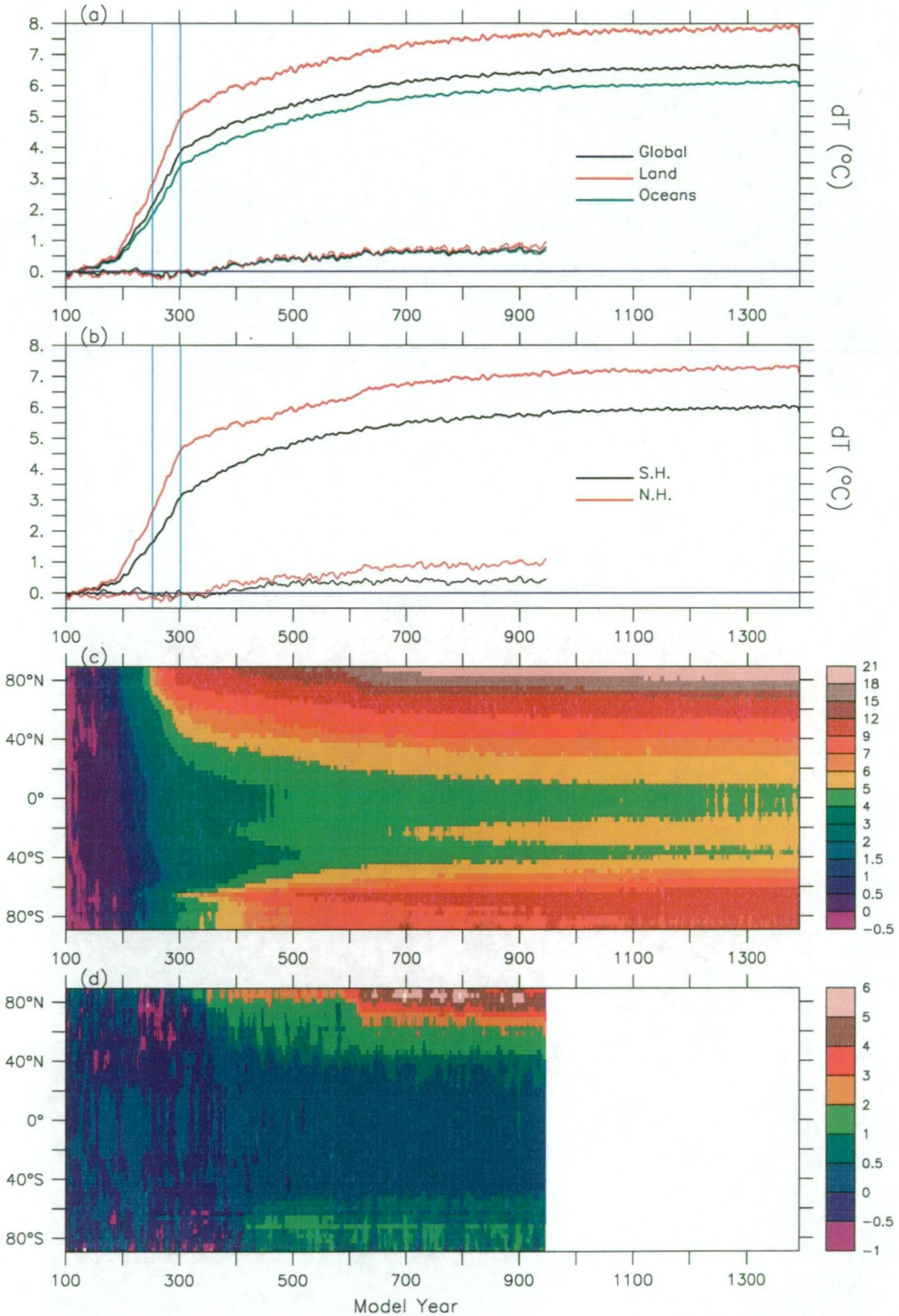

Figure 5.2: Time series of SAT changes: (a) over globe, land and oceans for TGM3 (thick curves) and for TGM3 - TGM2 (thin curves), (b) same as (a) but over NH and SH, (c) and (d) are zonal mean for TGM3 and TGM3 - TGM2, respectively. (units: °C)

warming of 2.3 °C by year 700, with the corresponding changes over ocean and land being 2.4 and 2.2 °C, respectively. During the last 700 years of the run, the rate of warming is substantially reduced (to only 0.07 °C/century over both the oceans and the continents), with the additional change being less than 0.5 °C, indicating that the SAT is approaching towards its equilibrium state. Fig.5.2b shows the evolution of SAT anomalies over the two hemispheres. The inter-hemispheric contrast, i.e., warming in the SH lagging behind the NH, is also attributable to the difference of thermal inertia between the ocean and land, as the SH has the larger part of the world ocean and thus has larger effective heat capacity than the NH. However, the model exaggerates to a great extent the inter-hemispheric asymmetry of SAT response. For example, TGM3 estimates an average warming of 1.3 and 0.8 °C in the Northern and Southern Hemispheres, respectively, by the last decade of 20th century, in contrast with the observed estimate of around 0.55 and 0.5 °C (IPCC 1996). This discrepancy is partly due to the model not taking into account the effect of changes in the sulfate aerosol loading, which is believed to offset the CO_2 induced warming and primarily affects the NH (Mitchell and Johns 1997). The above results suggest that our model may have overestimated the climate sensitivity of the global system to the imposed CO_2 forcing, but other factors such as the effects of aerosols and solar forcing need also to be considered.

Fig.5.2c shows the time series of zonally averaged annual mean SAT change in TGM3. During the first century of CO_2 forcing, the SAT change is within 1 °C in most latitudes except for the northern polar region. In the second century, the response begins to increase rapidly in all latitudes, with the northern high latitudes being warmed significantly more than the other regions. In the NH, the response increases poleward and has a minimum near the equator. In the SH, however, the response is quite uniform in low latitudes but decreases from 20°S to around 55°S and then increases poleward. The response is smaller in the Tropics and the southern mid latitudes because, as we shall see, a greater proportion of the surface radiative heating is used to increase evaporation rather than to raise the temperature, and the increased evaporative cooling reduces the surface warming in these regions compared

to higher latitudes. Regarding the large warming in high latitudes, particularly the Arctic, it is associated with the retreat of sea ice cover under CO_2 forcing. After CO_2 stabilization, the rate of warming in low latitudes is reduced appreciably whilst the high latitudes still undergo rapid warming due to the continuing retreat of the ice cover. By the end of the TGM3 run, the Arctic and Antarctic see a warming over 20 °C and 9 °C respectively, much larger than the warming of 5 °C in the Tropics, greatly reducing the meridional gradient of temperature and exerting significant influence on the atmospheric circulation in the North Hemisphere in particular.

The TGM2 run shows a trend of warming qualitatively similar to that of TGM3 in terms of global, hemispheric and zonal mean. However, there exist noticeable difference in magnitude of the rate of warming between these two runs. As illustrated by the contrast of the SAT responses shown in Fig.5.2a, 5.2b and 5.2d, TGM2 simulates a slightly more rapid SAT increase before CO_2 tripling, but the warming is reduced faster immediately after CO_2 stabilization and the global mean response over both the ocean and land is 0.6~0.8 °C lower than the TGM3 results by the end of the TGM2 integration. It is also noted that, during the period of CO_2 increase, the inter-hemispheric asymmetry of warming is slightly greater in TGM2 than GM3, but it weakens gradually in the CO_2 stabilization period, with the reduction being over 0.5 °C by year 950 as shown in Fig.5.2b. Fig.5.2d reveals that the difference of zonal mean warming between TGM3 and TGM2 occurs mainly in high latitudes, particularly the Arctic Ocean where the ice cover retreats much faster in TGM3 than TGM2, as will be shown later.

Fig.5.3 shows the geographical variations of the response of annual mean SAT in TGM3 and TGM2. By the time of CO_2 tripling (5.3ab), a poleward amplification of warming, and the contrast of warming between land and ocean are evident, with the largest warming being more than 14 °C and 12 °C for TGM3 and TGM2, respectively, over the Barents Sea. However, we see a marked delay of warming in the northern North Atlantic and the Ross and Weddell Seas where the SAT changes significantly less than the surrounding regions because the local oceanic deep convective mixing and overturning transmit the surface warming down to the depth of the

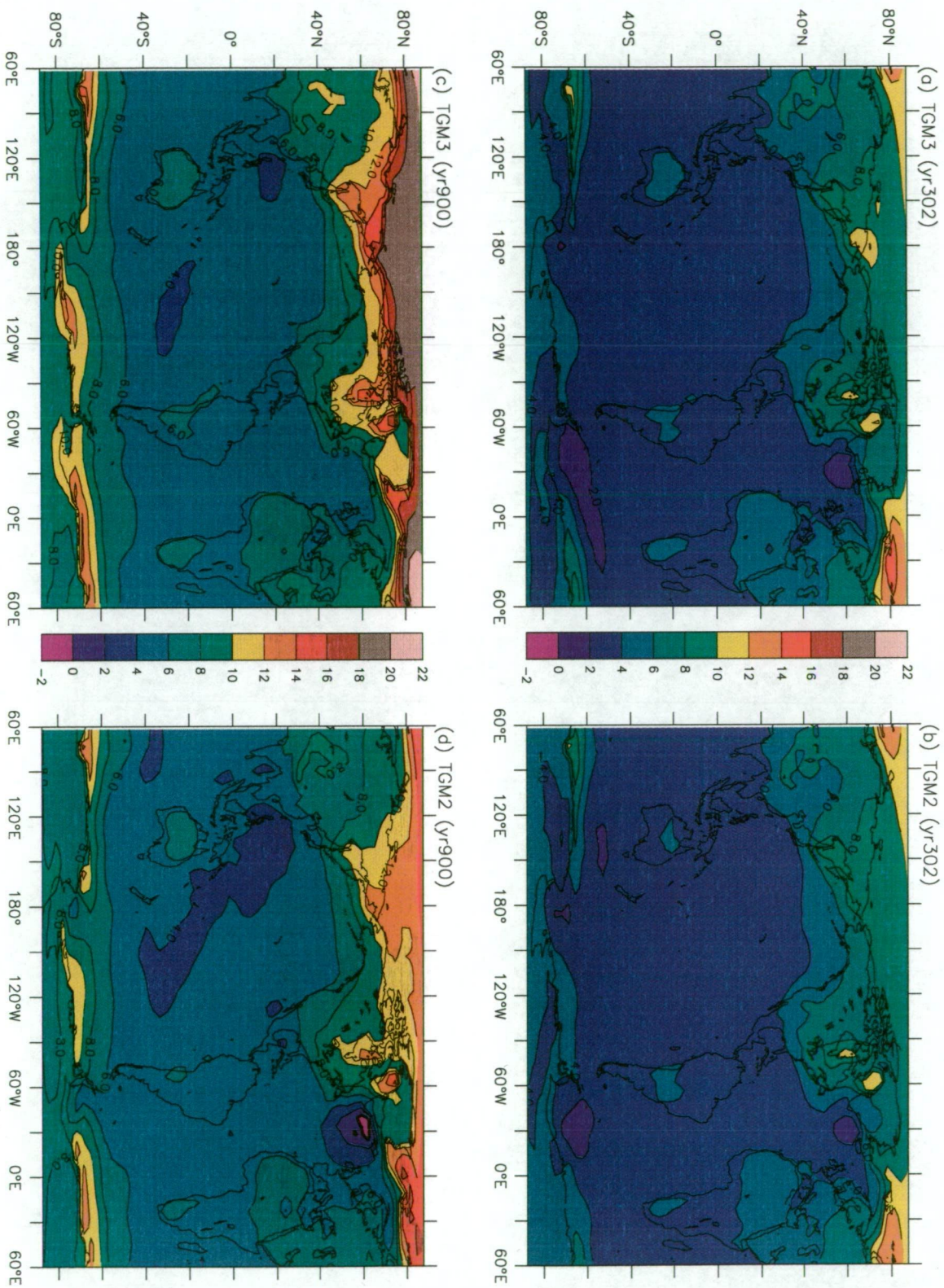

Figure 5.3: Geographical distributions of SAT changes (decadal mean centered on yr302 and yr900) relative to yr51-100 mean: (a) TGM3 yr302, (b) TGM2 yr302, (c) TGM3 yr900, (d) TGM2 yr900.

ocean interior, which causes very large effective oceanic thermal inertia and slows down the surface warming. As we will see, the deep convection and overturning in the above regions is either largely reduced (in the NADWF region) or completely suppressed (in the AABWF region) as CO_2 increases, leading to a substantial reduction of the effective oceanic thermal inertia by the time of CO_2 tripling. Thereafter, the Southern Ocean deep convection and overturning remain inactive and warming over the Circumpolar Ocean gradually catches up and eventually exceeds the northern neighbouring ocean, as shown by Fig.5.3c and 5.3d which present the warming pattern of year 900 for TGM3 and TGM2, respectively. However, the delay of warming over the northern North Atlantic is still noticeable particularly in the TGM2 run. In the following 500-year TGM3 integration, the SAT changes little (not shown), indicating that the surface has reached a near-stable thermal state which is characterised by a warming as high as 21 °C over the Arctic, up to 16 °C in the immediate vicinity of the Antarctic continents, and around 5 °C over the vast region of low to mid latitude ocean.

5.2.2 Sea Surface Temperature

Fig.5.4 shows the time series of the response of SST to CO_2 forcing in TGM3 and the difference in change of SST between TGM3 and TGM2. As is understood, the SST largely determines the thermal state of the overlying atmosphere, thus we see very similar trends of sea surface warming (Fig.5.4a) and the increase of SAT (Fig.5.2a) over oceans in particular. Due mainly to the larger oceanic thermal inertia, SST increases less than SAT. By the end of the TGM3 integration, the globally averaged SST change is about 5.4 °C, 0.7 °C less than SAT change over the oceans. Such a difference in the rate of warming between SST and SAT is more evident in high latitudes, as can be seen by comparing the zonally averaged evolution of changes in SST (Fig.5.4b) and SAT (Fig.5.2b). In the period of CO_2 increase, SST changes very slowly in high latitudes in both hemispheres compared to the overlying SAT increase because the net heat received by the sea surface is mainly used to melt the sea ice.

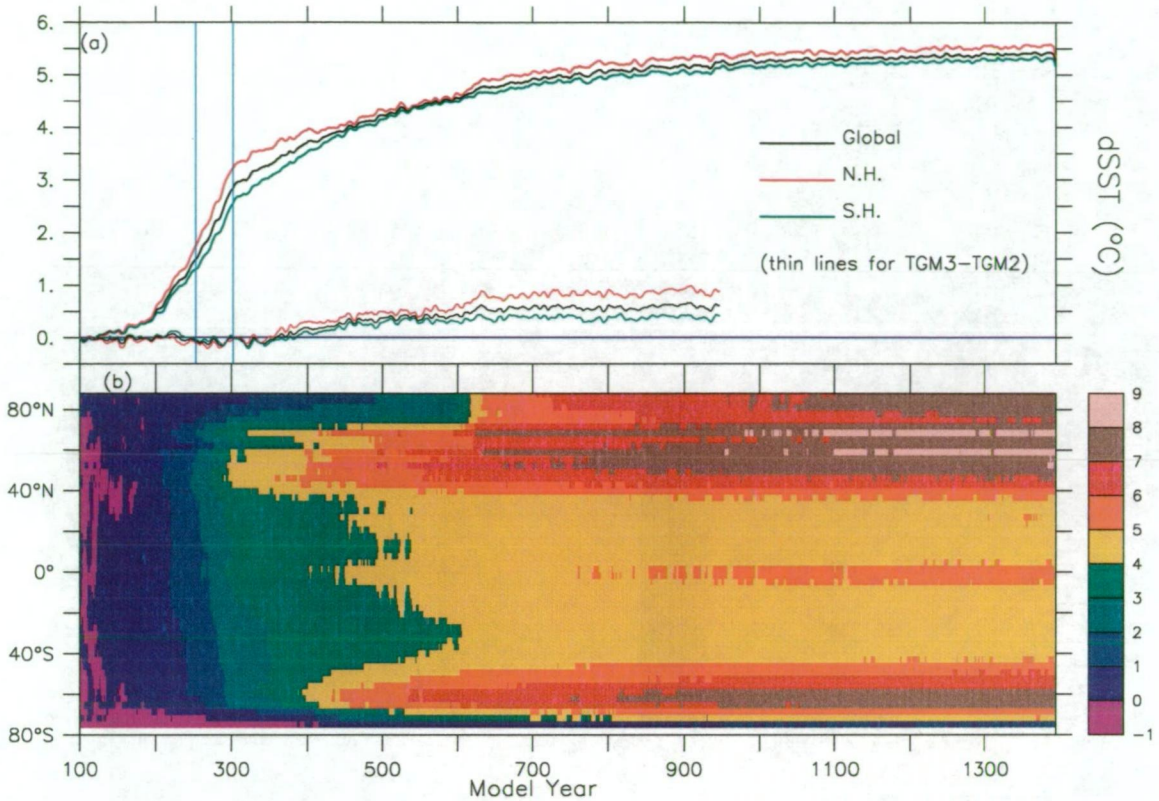

Figure 5.4: SST changes: (a) TGM3 (thick) and TGM3-TGM2 (thin), (b) TGM3.

This situation continues for a few more hundred years after CO_2 stabilization, during which the existence of sea ice prevents the SST from deviating far from the freezing point, leading to a relatively small response of SST in the Arctic Ocean, and the region immediately adjacent to Antarctica, to the CO_2 induced warming forcing. On the other hand, the thinned ice (due to the melt) allows more heat to escape upwards from the ocean than would otherwise be the case, which also slows down the warming in the surface water.

Also evident in Fig.5.4b is that, from around year 600, SST begins to increase significantly faster in the northern high latitudes. This is because the Arctic sea ice cover has disappeared nearly completely by year 600, and thus the constraints to the SST evolution has then been eliminated (see Fig.5.6). However, as mentioned above, the large oceanic heat capacity slows down the SST change. Consequently, by the end of the TGM3 run, the SST increase is just above 7 °C in the Arctic Ocean, in sharp contrast to the SAT change of 21 °C there. In the Southern Ocean, ice cover

exists at the southwestern corner of the Ross Sea for the whole course of the TGM3 run (Fig.5.6), therefore the response of the SST in the southernmost ocean region is restricted within 2 °C, and the largest warming of over 7 °C occurs in the zone immediately south of the Circumpolar Ocean due to the retreat of sea ice. Compared to the latitudinal distribution of SAT anomaly, the poleward amplification of SST change in the North Hemisphere is much smaller and thus the response of SST shows a rough inter-hemispheric symmetry. Similar to the contrast of response in SAT between TGM3 and TGM2, after sharing very close warming rates for about two and half centuries, the response of SST in TGM3 becomes noticeably larger than that in TGM2 in terms of the global, hemispheric and zonal mean. The largest difference is found in the high latitudes, especially in the Arctic Ocean, due mainly to the difference in the rate of sea ice retreat in these two runs.

Fig.5.5 illustrates the geographical distributions of decadal mean response of SST for periods centred on years 302 and 900 for TGM3 and TGM2. The variation of the warming patterns and the contrast between TGM3 and TGM2 is qualitatively similar to that described above for SAT. More evident is the delay in warming over the NADWF region and the Ross and Weddell seas in the whole course of the TGM3 and TGM2 integrations. As already discussed, the existence of sea ice restricts the development of the SST anomaly, such as the situation of the Arctic Ocean in TGM2 and the Ross Sea in both runs, and the deep convection and overturning cause larger effective thermal inertia which reduces the warming rate as well, such as for the case of the northern North Atlantic. However, we note that, in the NADWF region, the sea surface warming is extremely slow in TGM2 compared to that in TGM3. In fact, a cooling is found off the southern coast of Greenland in year 900. This is because, as we will see, in the course of the TGM2 run the North Atlantic thermohaline circulation is greatly reduced, which on the one hand greatly reduces the northward transport of warm surface water from lower latitudes, causing local cooling, and on the other hand reduces the penetration of the surface temperature anomaly (i.e., cooling) into the deep ocean, thereby enhancing the surface cooling. This represents a positive feedback process under CO_2 forcing. Another important reason for this

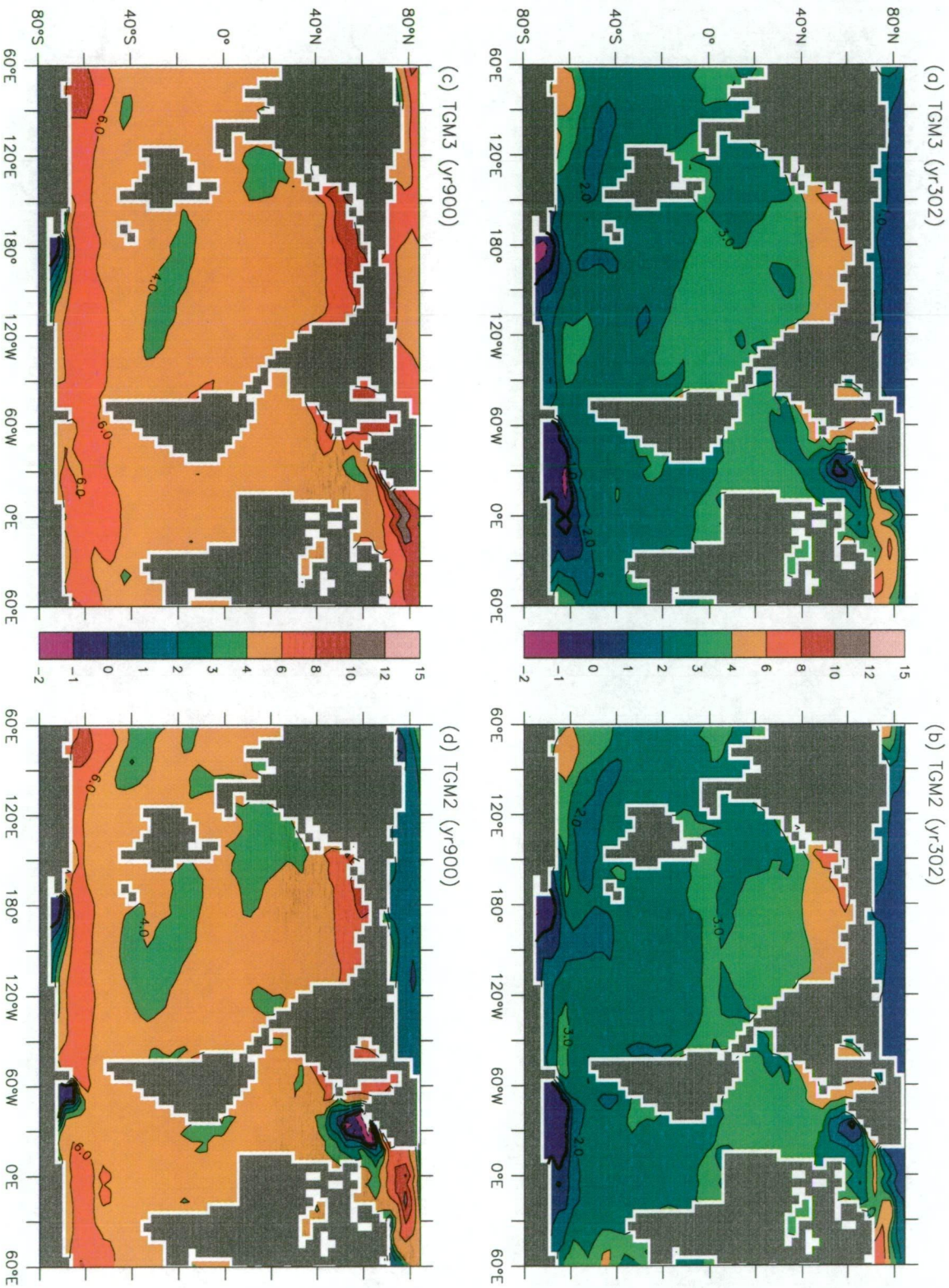

Figure 5.5: Same as Fig.5.3 but for SST changes.

cooling is the suppression of deep convection caused by the P - E induced surface freshening as will be shown later. With less convection, less relatively warm water is brought up from below and thus the surface cools down. Such a high latitude cooling associated with a CO_2 increase is also found in other coupled models (Manabe and Stouffer, 1994; Murphy and Mitchell, 1995; Russell and Rind, 1999). In addition, the surface flow along the eastern coast of Greenland is slightly strengthened due to the windstress in response to CO_2 forcing and brings more relatively cold water from the Arctic to the region off southeastern Greenland, together with the cooling described above, causing ice formation to occur there (not shown), which also constrains the evolution of SST.

With respect to the difference in the rate of warming between TGM3 and TGM2 found in the northern North Atlantic, this results mainly from the difference in change of the thermohaline circulation there. In TGM3, as shown later, the North Atlantic overturning is reduced to a much less extent and recovers relatively more rapidly after CO_2 tripling, causing much less reduction in the transport of warm water from lower latitudes, thereby leading to relatively rapid warming in the northern North Atlantic. In the high latitude Southern Ocean, a similar cooling is found around Antarctica, especially in the Ross Sea and Weddell Seas, which is also attributable to the suppression of deep convection associated with the CO_2 induced freshening. This cooling, especially in the period before CO_2 tripling, largely constrains the Southern Ocean sea ice melt from the bottom in the early stage of global warming, which in turn acts to maintain the SST at near the freezing point, as already addressed above. In fact, the Weddell Sea ice volume increases slightly in the first 200 years (not shown), resulting from the increase of snowfall over the sea ice which forms snowice and compensates for the ice-melt due to the surface air temperature increase. In addition, the reduction in upward heat flux due to the enhanced stratification probably also contributes to the surface cooling off Antarctica.

In the last 500 years of the integration, TGM3 shows a small change in SST mainly occurring in the Arctic Ocean (not shown), implying that the sea surface is nearing a quasi-equilibrium in terms of the thermal adjustment in response to stabilized

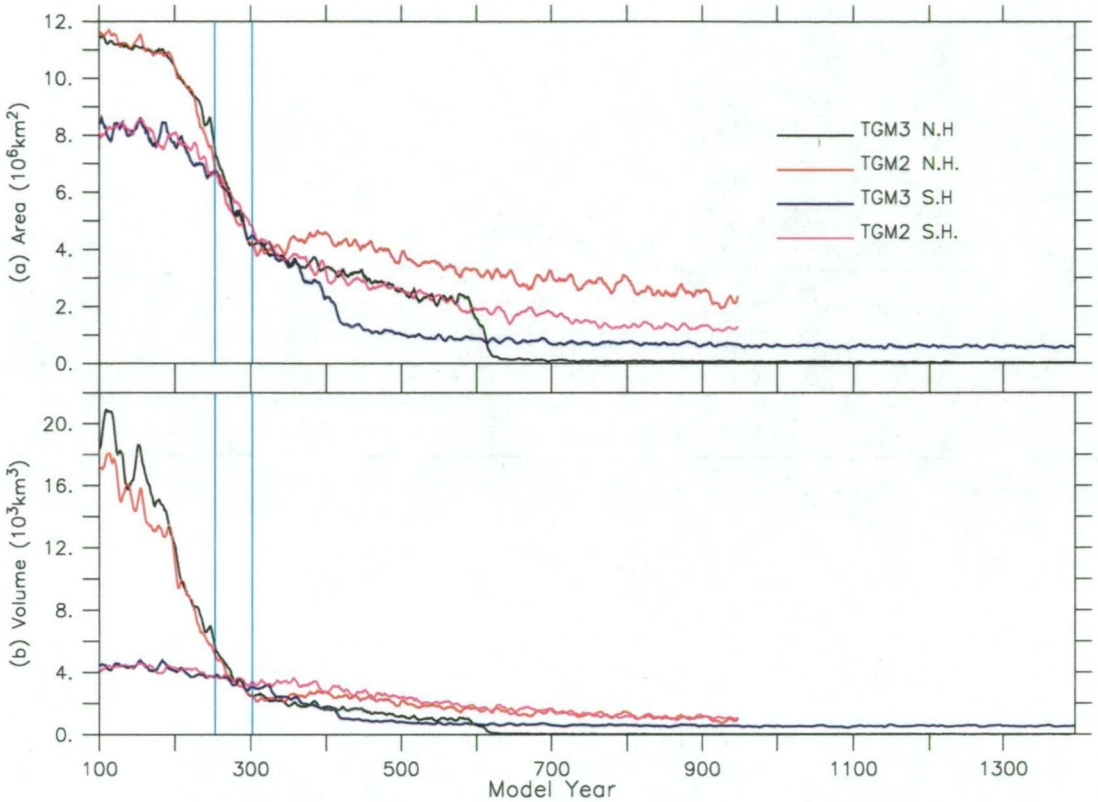

Figure 5.6: Time series of sea ice in TGM3 and TGM2: (a) NH and SH ice area, (b) NH and SH ice volume. A 7-yr running mean filter is applied.

$3\times CO_2$ forcing. However, we will show that this is only a temporary "near-stable" state at the surface associated with a close-down of the deep ocean ventilation.

5.2.3 Surface Heat Balance

The change of the surface thermal state in response to global warming forcing on the one hand is a result of the adjustment of the surface heat flux budget during the evolution of the climate system and, on the other hand, is one of the determinants of the changes in the surface heat flux budget. Despite the complexity of a series of feedbacks involved in the change of surface thermal state, examination of the surface heat budget in the course of the transient experiments can directly help us in understanding the features of surface warming and the mechanisms responsible for the difference of warming between regions such as land and ocean, and between models, i.e., TGM3 and TGM2.

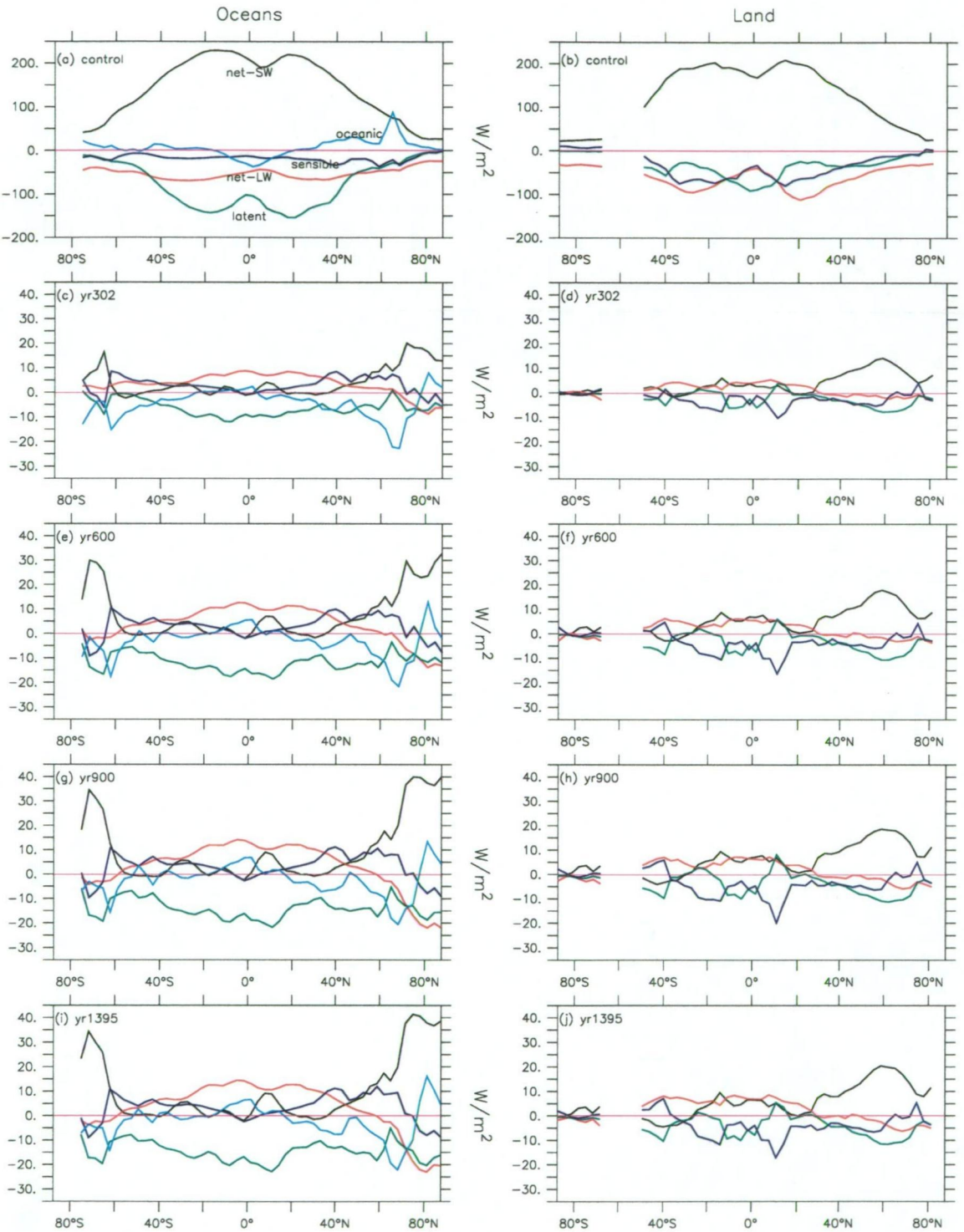

Figure 5.7: Latitudinal distributions of surface heat fluxes over the ocean (left) and land (right) in TGM3. (a) and (b) are initial states, and panels (c)–(j) show the decadal mean changes centered on years 302, 600, 900, and 1395.

Fig.5.7 presents changes (relative to the initial distributions) of the zonally averaged annual mean surface fluxes of net solar radiation, net long-wave radiation, latent heat and sensible heat over the oceans (left panels) and land (right panels) for decadal epochs centred at years 302, 600, 900 and 1395 in TGM3. It also shows the control climate (initial state) of the above heat budget components for reference: 5.7a for the oceans and 5.7b for the continents. For the oceans, oceanic heat flux is also included. In all figures positive values indicate surface heat gain and negative values imply heat loss.

We can see that, by the time of CO_2 tripling, noticeable changes occur in all heat flux budget components over high latitude oceans in particular. Globally averaged surface temperature increases due mainly to the reduction in long-wave radiative heat loss over low to middle latitudes and the increase in absorption of solar radiation over middle to high latitudes. In the period before CO_2 tripling, both CO_2 and water vapour increase in the model atmosphere, which increases the downward long-wave radiation, more than compensating for the increase in outgoing long-wave radiation due to the surface warming over low to middle latitudes, thereby reducing the terrestrial radiative heat loss there. In contrast, over high latitudes, especially the Arctic Ocean, the large increase in surface air temperature causes a net increase in long-wave radiation heat loss. Solar energy absorbed by land surfaces increases substantially in the northern middle to high latitudes due to the poleward retreat of snow cover. Similarly, the absorption of solar radiation over the high latitude ocean regions, especially polar oceans, increases because of the poleward retreat of the sea ice cover. The low latitude continents absorb more solar energy as well due primarily to the reduction in cloud cover there. Over high latitude oceanic surfaces, much of the additional heat is used to melt sea ice, and even in areas where sea ice disappears completely, the large heat capacity of the oceanic mixed layer prevents a large warming.

The above change over the ocean is in contrast to that over land where the small heat capacity of the soil leads to a more rapid temperature increase in response to the warming. This difference is partly responsible for the land-sea contrast in the

response of the surface air temperature to the increase of CO_2. Another important factor associated with such a contrast is the difference in evaporation between land and sea. The latent heat flux increases significantly over the oceanic surface, especially from 40°S to 60°N, whereas it changes relatively little over the continents, and therefore we see larger evaporative cooling over oceanic surfaces than land surfaces. As can be understood, along with the increase of SST, saturation vapour pressure over ocean surfaces increases and thus enhances the evaporation. However, although the land surface temperature increases even more than the SST, the evaporation over land surface is less because soil is often not saturated with water and thus can only support an evaporation much less than the potential rate. The sensible heat flux changes in a generally opposite sense over land and oceans: it warms the oceanic surface and cools the land surface in all latitudes except for polar region, acting to weaken the land-sea contrast in temperature change. This is because the land surface is warmed more than the overlying air and the sea surface is relatively less warmed than the overlying air.

With regard to the oceanic heat flux which supplies heat from the interior of the ocean to the surface in the northern middle to high latitudes (Fig.5.7a), we see that it is largely reduced under CO_2 forcing, making a negative contribution to the heat balance over the oceanic surface from 30°N to 80°N, particularly the band between 50°N and 75°N. As we know, the thermohaline circulation transports warm (and salty) water from low latitudes to the northern North Atlantic where some of the heat is released to the overlying atmosphere whilst some is transported into the deep ocean by the deep convective mixing and the sinking branch of the overturning. Under CO_2 forcing, as we shall see later, the THC is largely weakened and the northward heat transport is thus significantly reduced. Due to the large reduction in heat supply from tropical oceans, the upward heat flux from the surface of the northern North Atlantic is naturally reduced.

Following the CO_2 stabilization, changes in the above surface heat budget components begin to slow down, but noticeable evolution is still found in terrestrial radiation, evaporation and the absorption of solar energy over the oceanic surface

in particular, due to the continuing change of surface temperature and atmospheric moisture. 300 years after CO_2 tripling, as revealed by comparison between Fig.5.7e and 5.7c, terrestrial radiative cooling is further reduced over low latitude oceans, whilst the evaporative cooling is increased there. In the polar oceans, the further reduction of sea ice results in more absorption of solar radiation, leading to a marked increase in evaporation there. By year 900, the Arctic sea ice disappears completely and the absorption of solar energy reaches a maximum which is kept nearly unchanged during the rest of the TGM3 integration. In contrast, sea ice over the high latitude Southern Ocean is reduced rapidly to a very small amount in the first few centuries and remains relatively stable from year 400, causing little change in the absorption of solar energy near Antarctica thereafter. Evaporation, sensible heat and oceanic heat fluxes are all seen to change slightly from year 600 to year 900 and then remain quite stable thereafter, indicating that a near-steady state is reached in terms of the surface heat balance.

Evolution of the surface heat budget components in the TGM2 integration (not shown) bear general similarity to those in TGM3 discussed above. However, difference between TGM3 and TGM2 is evident in the absorption of solar energy over high latitude oceans, particularly the Arctic Ocean, and the oceanic heat flux over the northern North Atlantic. Unlike TGM3, TGM2 shows the existence of sea ice over some regions in the Arctic Ocean for the whole course of integration, thus the absorption of solar energy by the Arctic oceanic surface is considerably less than that in TGM3 after CO_2 tripling, leading to smaller increase in surface temperature and less evaporation, and thus the evolution of the surface heat flux budget is slower, suggesting that a longer time is needed for the northern high latitudes to reach a quasi-steady state.

5.2.4 Oceanic Surface Heat Flux and Heat Transport

In the above we have shown the zonal mean feature of changes in various surface heat budget components under CO_2 forcing. Now we turn to examine some details

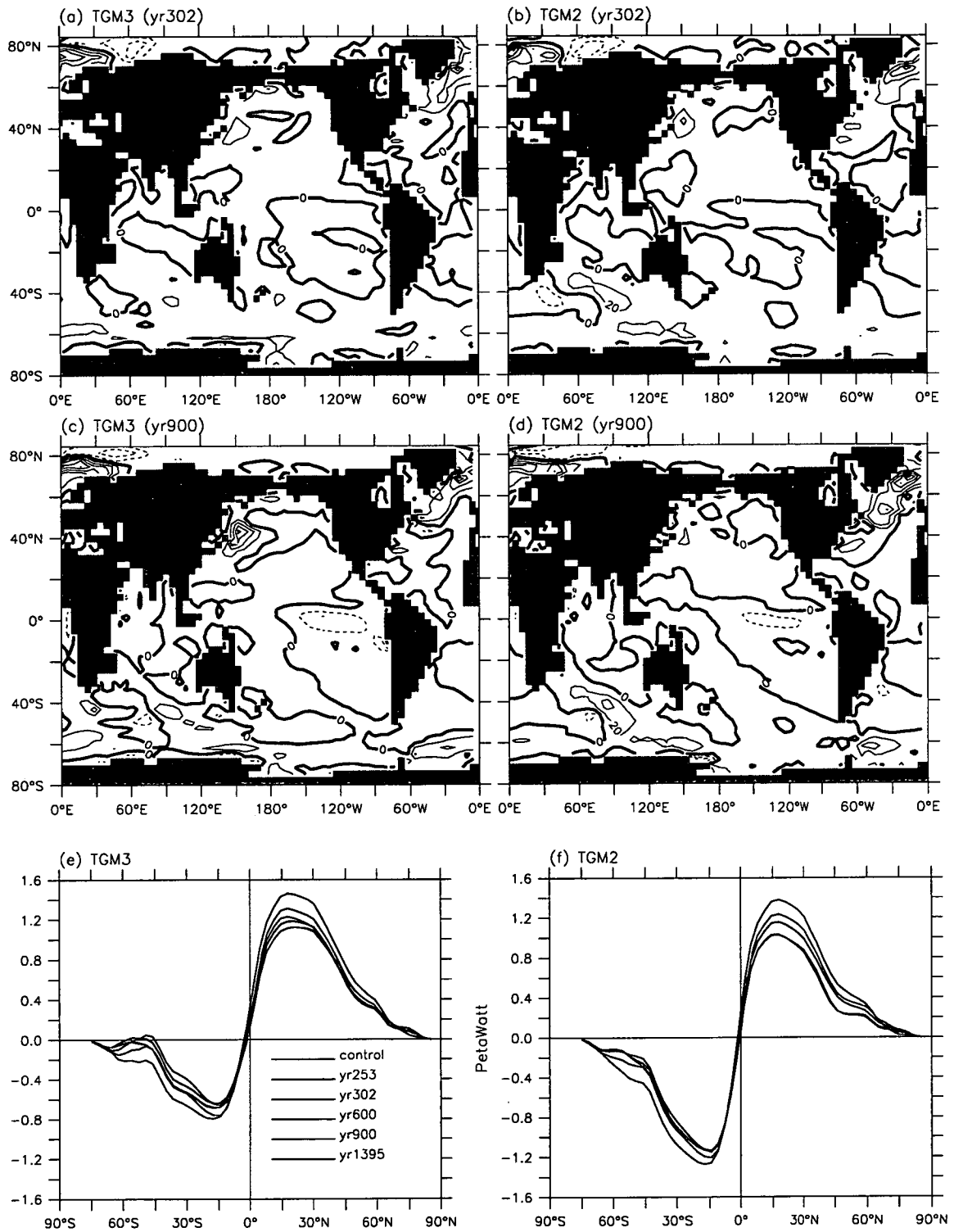

Figure 5.8: Changes of sea surface heat flux and oceanic northward heat transport in TGM3 (left) and TGM2 (right). (a)–(d): geographical distributions of heat flux changes (contour interval is 20 $W\,m^{-2}$); (e)(f) heat transports. Shown are decadal mean centered on indicated years.

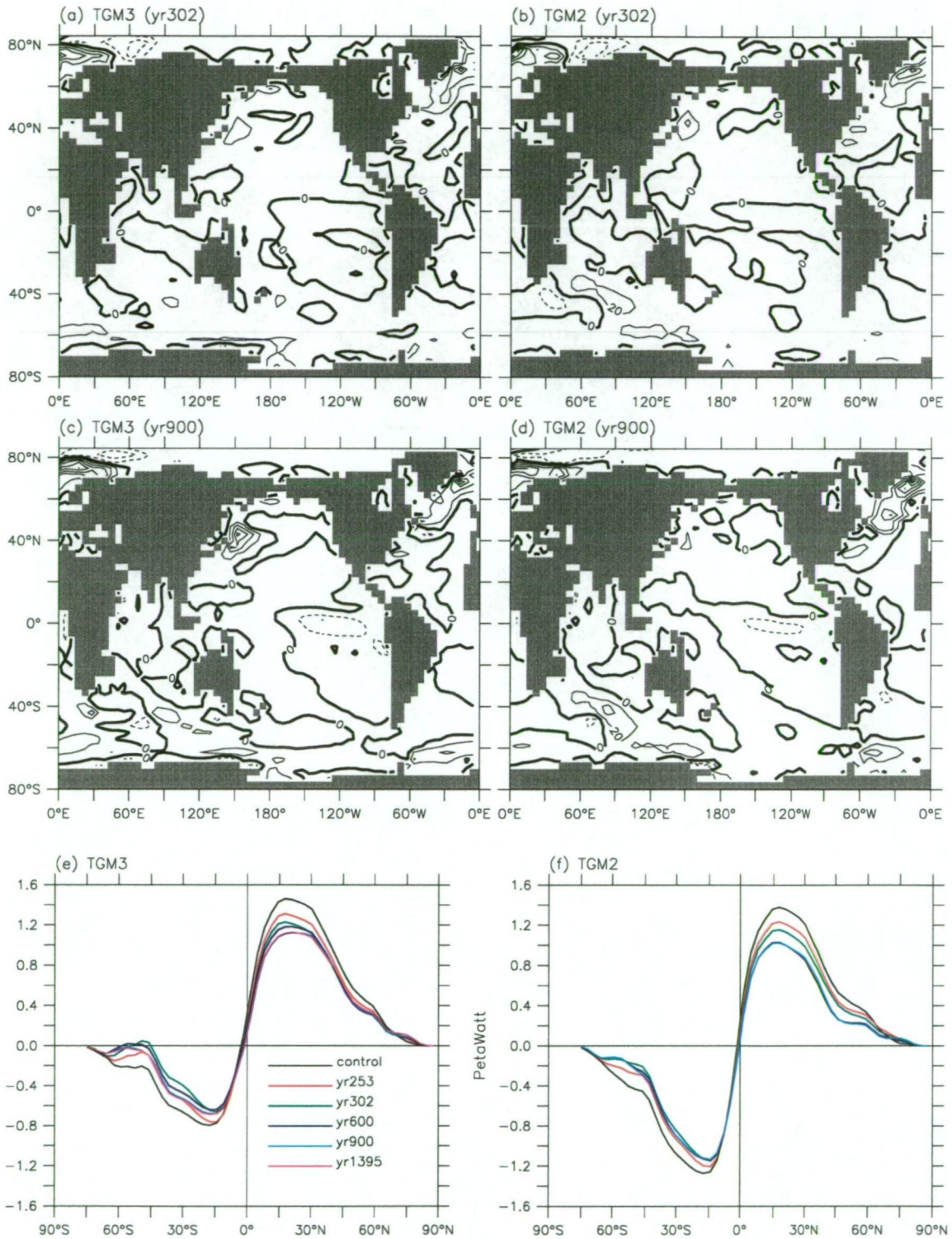

Figure 5.8: Changes of sea surface heat flux and oceanic northward heat transport in TGM3 (left) and TGM2 (right). (a)–(d): geographical distributions of heat flux changes (contour interval is 20 $\mathrm{W\,m^{-2}}$); (e)(f) heat transports. Shown are decadal mean centered on indicated years.

of the geographical pattern of changes in the oceanic surface heat fluxes, as shown in Fig.5.8a–d, and evolution of the oceanic northward heat transports, shown in Fig.5.8ef. Note, in Fig.5.8a–d, positive (negative) values stands for heat gain (loss) of the ocean surface layer. It can be seen that the two runs show qualitatively similar CO_2 induced changes in the oceanic surface heat budget in terms of geographical distribution.

By the time of CO_2 tripling, the surfaces of Circumpolar Ocean and the Weddell and Ross Seas absorb more solar radiation due to the reduction in clouds and/or poleward retreat of sea ice, which compensates for the increase in evaporative heat loss due to surface warming over the Weddell and Ross Seas in particular, resulting in net heat gain from the atmosphere. Over the equatorial and southern tropical oceans, the warming induced increase in evaporative heat loss overrides heat gain from other components, causing slight net heat flux out of the ocean. In the Northern Hemisphere, large change occurs in the northern North Atlantic where the evaporation is largely reduced due to the reduction in northward heat transport, as already discussed above. A similar but much weaker change is also found over the region north of the Kuroshio Current in the northwestern Pacific due to the reduction in evaporation. As can be seen in 5.9 which illustrates evolution of the latitudinal profiles of the annual mean zonal windstresses in both runs for the epochs examined, the northern low latitude easterlies become weaker under CO_2 forcing, accordingly the wind-driven poleward Ekman drift in the northern Indian-Pacific is reduced, which results in less poleward heat transport to middle latitudes, leading to a reduction in evaporative heat loss over the northwestern Pacific. Examining Fig.5.8e, we see an evident weakening of poleward heat transports in both hemispheres for both runs by the time of CO_2 stabilization. In the NH, this weakening is associated with the decline of the thermohaline circulation (such as that in North Atlantic) and of the poleward Ekman drift (such as that in the North Pacific). In the SH, the equatorward Ekman drift is enhanced due to the intensification of westerly wind stress in the middle latitudes, which plays an important role in reducing the poleward heat transport.

By year 900, change in the oceanic heat flux over the tropical eastern Pacific has developed southward for both runs. This is because, on the one hand, the continued warming leads to more evaporative heat loss and, on the other hand, the southern low latitude easterly windstress declines slightly as shown in Fig.5.9, weakening the poleward Ekman currents and therefore reducing the poleward heat transport, which enhances the local warming, causing more evaporation. In the high latitude Southern Ocean, due to the CO_2 induced shutdown of deep convection and overturning (as will be shown later in this chapter), the vertical mixing and thus the transport of heat sequestrated in the surface layer into the deep ocean are largely reduced, leading to the Circumpolar Ocean surface being warmed more than that of the lower latitudes as shown in Fig.5.8c and 5.8d, despite the weakening of poleward heat transport from low latitudes mentioned above. The North Atlantic sees further reduction in evaporative heat loss in TGM2 because the THC which transports heat from low latitudes is further weakened. This is not the case for TGM3 because, as we shall see later, the thermohaline circulation is reintensified slightly after CO_2 tripling. However, in the region north of the Kuroshio Current, TGM3 sees a further reduction in evaporation because of the continuing decline in the poleward heat transport by the wind-driven currents as mentioned above.

For the TGM3 integration, the last period from year 900 to year 1400 sees very little change in the geographical distribution of the oceanic surface heat flux and thus quite stable meridional heat transports, partly attributable to a relatively steady state of the zonal windstresses.

5.2.5 Precipitation, Evaporation and Runoff

Atmospheric CO_2 increase results in enhancement of the globally averaged rates of both precipitation (P) and evaporation (E) over oceanic regions in particular, and, as found in many previous studies (e.g., Manabe et al. 1991), the change of precipitation in response to global warming is highly diverse in terms of the geographical distribution.

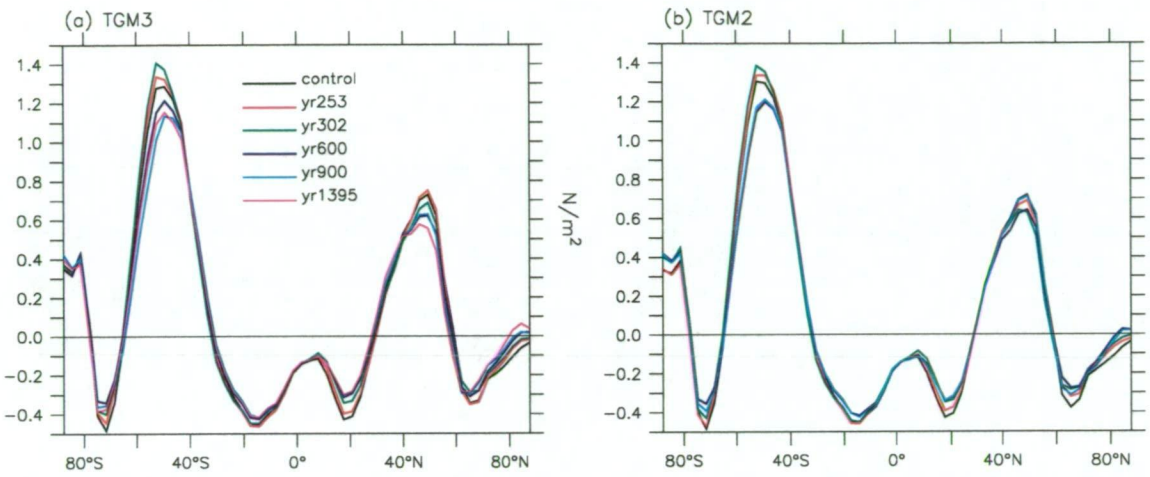

Figure 5.9: Evolution of zonally averaged decadal mean zonal windstress.

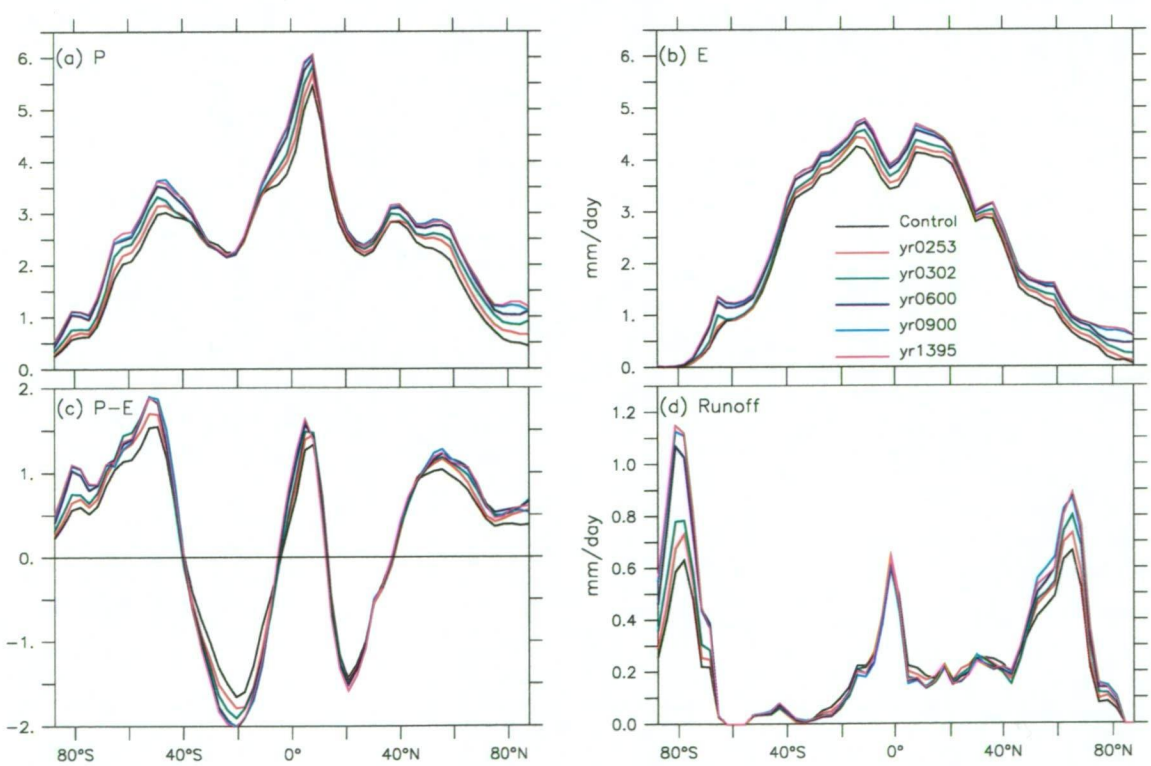

Figure 5.10: Evolution of zonally averaged annual mean hydrological budget in TGM3: (a) P, (b) E, (c) P - E, and (d) runoff.

Fig.5.10a illustrates the evolution of zonally averaged annual mean precipitation from the control climate to transient decadal epochs centered on years 253, 302, 600, 900 and 1395 in TGM3. Fig.5.10b shows the corresponding evolution of zonal and annual mean evaporation. The TGM2 integration presents very similar responses of P and E to that in TGM3 and thus is not included here. It deserves mention that, despite the coarse resolution of the model, the simulated control climate of precipitation is very close to the estimates from observations in terms of zonal mean distributions. For example, our model simulates rainfall peaks in the middle latitude westerly wind belts and the Inter-Tropical Convergence Zone (ITCZ), giving a maximum annual mean rainfall of 5.46 mm day^{-1} in the ITCZ, in strikingly good agreement with the estimated maximum rainfall of 5.34 mm day^{-1} near the equator as per Budyko (1963) and 5.53 mm day^{-1} in the ITCZ according to Baumgartner and Reichel (1975). In both polar regions, our model gives very small precipitation, i.e., less than 0.2 mm day^{-1} over Antarctica and no more than 0.5 mm day^{-1} over the Arctic Ocean, consistent with the observations as well. The simulated evaporation is also generally within the range of estimates, especially the pair of peaks occurring in the subtropical high pressure belts are nicely reproduced, very close to the estimate of Budyko (1963) in terms of both the locations and amplitudes. As a contrast, the GFDL model (Manabe et al. 1991) simulates a peak rainfall of only about 4.05 mm day^{-1} over the tropical region, and largely overestimates the precipitation over both polar regions, i.e., 1.37 mm day^{-1} over Antarctica and 1.64 mm day^{-1} over the Arctic Ocean. Our model's capability to capture the basic features of meridional distributions of both the precipitation and evaporation provides us with the confidence that the global hydrological cycle is represented realistically and its response to CO_2 induced global warming may therefore be reasonably well simulated.

Fig.5.10a and 5.10b show notable difference in changes of the latitudinal profiles of P and E. For precipitation, the response is a bit more latitude-dependent than that of evaporation. Namely, the most significant increase of precipitation occurs in latitudinal zones where the precipitation is initially large except for high latitudes, whilst

evaporation changes more evenly from 40°S northward. This is because precipitation itself and its changes are largely determined by the atmospheric circulation, especially vertical motions and convection which are generally maintained in pattern but changed in strength under global warming conditions, and the change of evaporation is mainly attributed to the change in thermal state of the oceanic surface in particular, which is relatively less diverse in terms of latitudinal distribution. The difference in changes of precipitation and evaporation implies a global hydrological redistribution and has a profound effect on oceanic circulations, particularly the THC as discussed later. Fig.5.10c shows the latitudinal profiles of P - E. It is evident that the oceans lose fresh water by largely enhanced excess of evaporation over rainfall in the southern low latitudes between 5°S and 40°S, which is compensated for by the net fresh water gain over mid to high latitudes, particularly in the Southern Ocean. With regard to the evolution of runoff shown in Fig.5.10d, changes occur mainly over northern mid to high latitude continents and Antarctica, which are discussed further below.

Warming at the surface and in the troposphere on the one hand leads to an increase in evaporation from the surface, particularly the oceanic surface as already shown, and on the other hand enriches the water vapour content in the troposphere and thus enhances the poleward moisture transport, thereby increasing the precipitation in middle to high latitudes. For southern high latitudes, the existence of sea ice, deep convection and overturning in the early stage of CO_2 forcing, as well as the permanent snow cover over Antarctica slow down the local warming significantly, leading to small changes in evaporation and thus larger and larger P - E. The increase in P - E on the one hand contributes directly to an increase in the supply of fresh water over the oceans, and on the other hand freshens the oceans surrounding Antarctica indirectly through enhanced runoff from the Antarctic continent. Note the increase in Antarctic runoff results mainly from the assumption in the model that mass of the Antarctic ice sheet and ice shelves is maintained constant in the course of both control and transient integrations [1]. Such an assumption is certainly quite

[1]For simplicity, the present model assumes a constant mass for the Antarctic ice sheet plus

crude but to some extent reasonable given the uncertainty of current estimates of the Antarctic ice sheet and ice shelves' response to climate change, including basal melt rates and increased ice flow. Without this assumption, much of the increase in P - E over Antarctica would have been maintained on the continent instead, contributing to the accumulation of snow/ice over the Antarctica ice sheet. In contrast, the increase of runoff over north middle to high latitudes is attributable to both the snow melt in the first couple of centuries of CO_2 forcing and the P - E increase over land.

5.2.6 Oceanic Surface Freshwater Budget and SSS

Fig.5.11 shows the evolution of surface freshwater flux change induced by CO_2 forcing in TGM3. The counterparts in TGM2 are omitted again due to the close similarity. The freshwater budget shown here is mainly attributable to the combined effect of changes in P - E over oceans and runoff from the continents discussed above, and advection and diffusion in the ocean interior. Another important factor contributing to the freshwater budget over the high latitude oceans is associated with the sea ice, as discussed below.

The sea ice affects the sea surface freshwater budget via two processes. One is the sea ice removal from the formation regions. Continuously, Ekman drift and ocean advection take sea ice away (equatorward) from where sea ice forms, e.g., the coastal region around Antarctica and the Arctic Ocean adjourning the high latitude North Atlantic, to lower latitudes where it finally melts. This causes a freshwater loss to the polar surface ocean, acting to increase surface salinity there. However, under global warming, such an equatorward transport of sea ice is reduced due to the reduction of sea ice formation over the warmed high latitude oceans and to the weakening of

ice shelves during the course of the integrations. In effect, enhanced P - E over Antarctica is assumed to be balanced by enhanced melt around the edges. Long-term projections of Antarctic ice-sheet/shelf volume change resulting from global warming are poorly constrained at present, with the sign being sensitive on centennial and longer time scales to assumptions about changes in ice-shelf basal melting rates (Huybrechts and de Wolde 1999, see also Warner and Budd 1998 and O'Farrell et al. 1997).

Figure 5.11: Geographical distributions of the sea surface freshwater flux changes in TGM3 for decadal epochs centered on indicated years. Contour interval is 0.5. (units: m yr^{-1})

high latitude easterly windstresses in both hemispheres (see Fig.5.9), implying an effective freshening over the high latitude oceans and, accordingly, a net freshwater loss to the adjacent lower latitude oceans. The other process is the local passive melt of sea ice due to the warming, which freshens the ice covered oceanic surface but this freshening is very small compared to other factors. For example, the Southern Ocean loses ice volume of about 3000 km^3 in the first 300 years with CO_2 forcing, equivalent to a freshening less than 0.001 m yr^{-1} over oceans to the south of 65°S. As a contrast, the reduction of sea ice export through 65°S totals about 26220 km^3 in the same period, indicating an average freshening of about 0.0087 m yr^{-1} over the same region. In fact, by the end of this period, the freshening implied by the decline in ice export is 0.038 m yr^{-1} and can finally reach 0.055 m yr^{-1} 100 years later.

One of the most evident features in Fig.5.11 is the freshening in the tropical Pacific Ocean. At the early stage of global warming this freshening occurs over all tropical oceans, but gradually this broad coverage shrinks to a narrow zone in the tropical Pacific Ocean while its intensity is enhanced after CO_2 stabilization. This is because the warming induced increase in evaporation gradually catches up with and finally exceeds the increase of rainfall over the tropical Atlantic Ocean in particular. As shown below, the weakening of thermohaline circulation in the North Atlantic reduces the poleward transport of the low latitude warm and saline surface water, which on the one hand reduces the poleward heat transport, causing a rapid increase of SST in the low latitudes and thus largely increasing evaporation and, on the other hand, reduces the poleward salt transport, implying a loss of surface freshwater as well. Over the tropical Pacific, however, rainfall in the ITCZ increases more quickly than evaporation, continually enhancing the local freshening. Adversely, the subtropical Pacific regions experience more and more evaporation and relatively stable rainfall, and thereby show a considerably net loss of freshwater. Such a contrast of freshwater budget between the tropical and subtropical Pacific leads to a change of the meridional density gradient, which resists the divergent (poleward) flows and suppresses the upwelling of the tropical Pacific Ocean.

Also evident is the development of freshening over the Arctic Ocean and high latitude Southern Ocean, especially the Ross and Weddell Seas, due to the continual enhancement of P - E, runoff, decline in sea ice formation and export, and sea ice melt. It is the freshening over the Ross and Weddell Seas that reduces the surface density, intensifies the water column stratification, and thereby suppresses the deep convection, which shuts down the Southern Ocean overturning and the bottom water ventilation of the world ocean. These processes will be discussed in detail later. Over the Circumpolar Ocean, especially its southern side centered on 60°S, we see a notable narrow zone with net freshwater loss to the north of the Ross Sea in particular, developing gradually along with the integration. While the enhancement of evaporation is found to be smaller than the precipitation increase over this latitude band, except for a few very limited local regions, such a freshwater loss can be largely explained by the decrease of sea ice transport from the high latitude Southern Ocean as mentioned above. In the northern Greenland Sea and Barents Sea (between 65^o and 80°N), a marked freshwater loss is located as well. This results mainly from the different changes in equatorward ice transport at the north and south boundaries of this region, i.e., more output to the south side than input from the north. In addition, the excess of evaporation over precipitation also makes a contribution to this freshwater loss in the Barents Sea shortly after CO_2 increases, and in the northern Greenland Sea during the last few centuries of the run. As for the freshening evident in the middle to high latitude North Atlantic, this is the result of an increase in P - E and it plays a crucial role in stabilizing the water column and thus substantially reducing the NADWF as shown in detail later.

Fig.5.12 presents the time series of globally averaged annual mean SSS and the evolution of the latitudinal distribution of annual mean SSS change under CO_2 forcing in TGM3 (and TGM2). While the SST responds to the global warming very soon after CO_2 starts increasing (Fig.5.4a), the world ocean SSS changes relatively slowly. The global ocean surface is generally freshened from the second century of warming forcing when the sea ice and land snow/ice begin to melt rapidly (e.g., see Fig.5.6). For the case of TGM3, by the time of CO_2 tripling, both hemispheres see

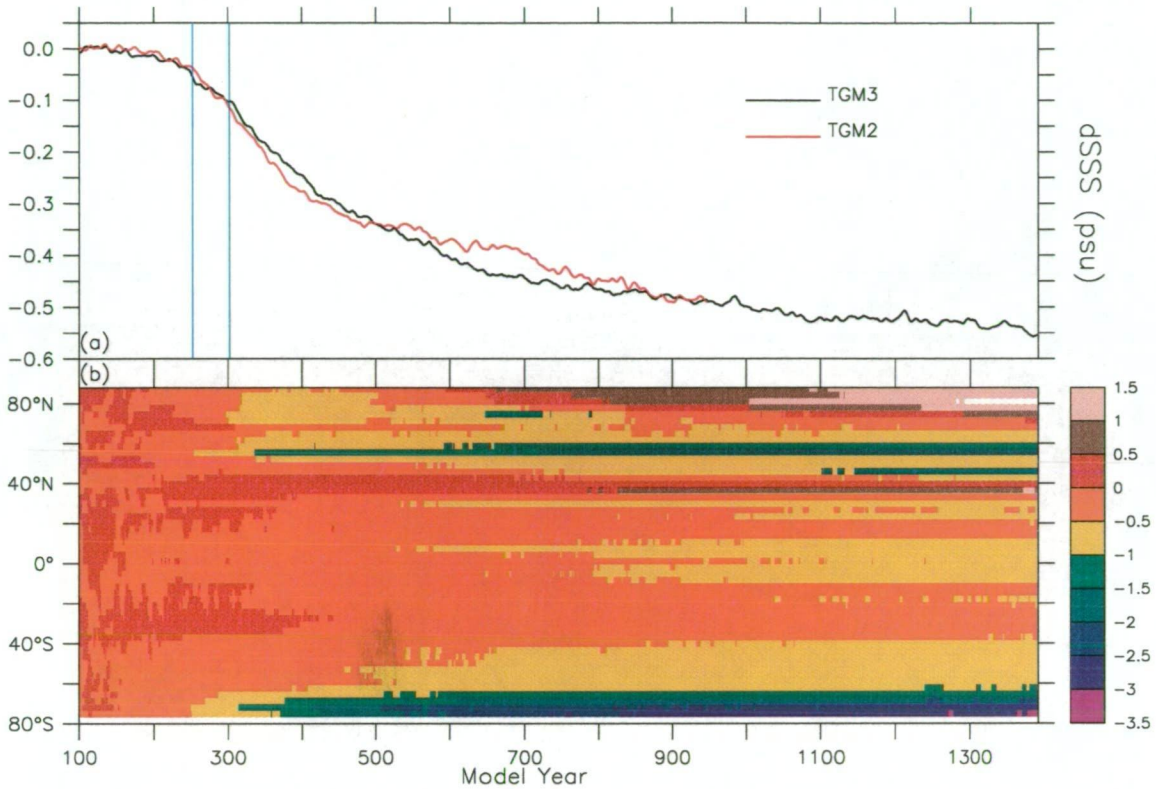

Figure 5.12: Time series of SSS changes: (a) over globe ocean for TGM3 and TGM2, and (b) zonal mean for TGM3. (units: psu).

a surface freshening of about 0.1 psu. More rapid freshening occurs during the first two centuries of CO_2 stabilization and, within this period, the global ocean surface becomes 0.24 psu fresher. During the following 400 years, i.e., year 500–900, global mean SSS decreases by 0.14 psu, while the last 500 years sees a further freshening of only 0.07 psu. By the end of TGM3, the world ocean surface is freshened by about 0.55 psu, with changes in the NH and SH being 0.41 psu and 0.65 psu, respectively. TGM2 shows a generally similar trend of freshening at the global ocean surface. Fig.5.12b shows that, in TGM3, the zonal mean SSS decreases rapidly in mid to high latitudes of both hemispheres due to the large freshening caused by the increasing P - E, runoff and sea ice change as discussed above. This freshening is the determinative factor acting to shut off the Southern Ocean overturning and plays an important role in reducing the North Atlantic THC. However, the Arctic Ocean sees an abnormal SSS increase after year 600. This is probably the consequence of climate drift and/or the numerical contamination of SSS there, in particular the

Barents Sea, as discussed in Chapter 4.

5.3 Responses in the Ocean Interior

As has been shown, the oceanic changes under CO_2 forcing firstly occur at the surface where the physical interaction between air and sea enable them to exchange energy and matter directly. This change is then transported into the ocean interior by the oceanic convection, diffusion and circulation in particular, changing the ocean interior water properties and thermohaline structure and, most importantly, the stratification, which in turn exerts influence on changes at the surface and the entire climate system.

5.3.1 Temperature

Fig.5.13a illustrates time series of changes in annual mean global ocean temperature for the upper layer (0–800 m), mid-depth layer (800–2350 m), abyssal layer (2300–4600 m), and the whole water column, in the two runs. It should be noted that the climates of the thermal states for the above layers are notably different between the corresponding control runs: CGM3 gives temperatures in these layers warmer than that of CGM2 by 0.15, 0.33, 0.42 and 0.33 °C, respectively. In spite of this difference in initial state, the rates of warming are very close in TGM3 and TGM2 in the upper and abyssal layers. However, significant difference of response between the two runs is found in the mid-depth layer where TGM3 shows a warming larger than TGM2 by 0.13 °C at the time of CO_2 tripling, and this difference is further enlarged to 0.32 °C by year 900, which causes a slightly quicker warming in TGM3 than TGM2 for the entire ocean column, e.g., by 0.04 °C and 0.12 °C at year 302 and year 900, respectively.

The above inter-version difference of mid-depth layer warming is associated with the difference of THC, in particular the North Atlantic overturning, and its re-

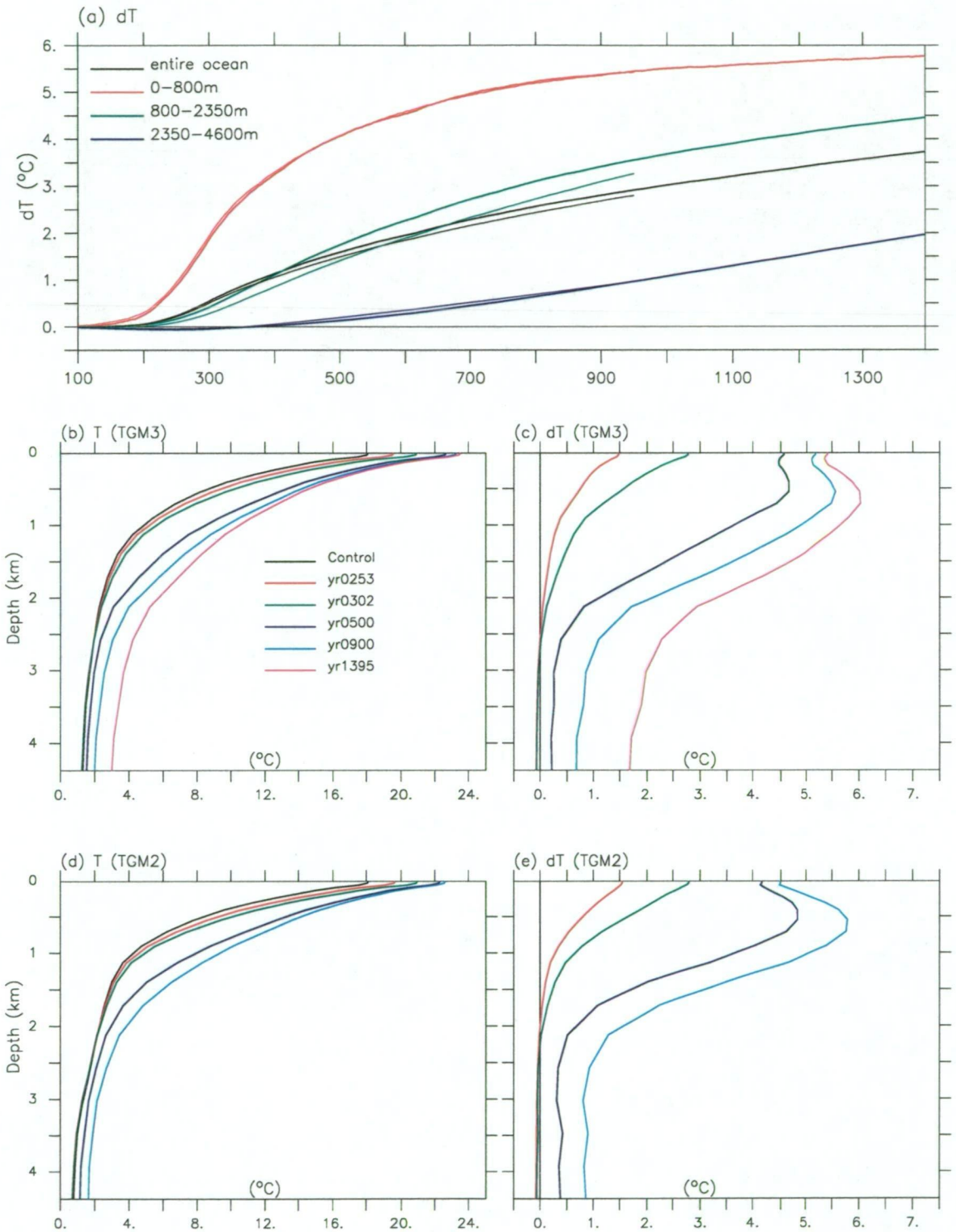

Figure 5.13: (a) Time series of temperature change for the entire ocean and sub-layers in TGM3 (thick) and TGM2 (thin); (b)–(e) vertical profiles of T and ΔT for 10-yr epochs centered on indicated years.

sponse to the warming in these runs. We have already shown in Chapter 4 that the initial NADWF of TGM3 is appreciably larger than that of TGM2, and we will see that, under CO_2 forcing, the penetration depth of the North Atlantic overturning is shoaled and the associated NADWF is reduced and constrained in the layer above 2500 m in both runs. Because the intensity of the remaining NADWF and the associated global ocean conveyor belt is considerably stronger in TGM3 than in TGM2, surface warming is transported into the mid-depth layer more effectively in TGM3 which therefore sees larger warming in the mid-depth ocean than TGM2.

Also evident in Fig.5.13a is that the warming trends for the three sub-layers vary differently in the course of, say, the TGM3 integration. Table 5.1 lists the warming rates for these layers during different periods of this run.

Table 5.1: Rates of warming (°C/century) for three sub-layers (upper, mid-depth and abyssal) in the TGM3 integration.

	yr100-302	yr302-600	yr600-900	yr900-1200	yr1200-1400
0–800m	**0.9546**	0.8917	0.2757	0.09470	0.05795
800–2350m	0.2156	**0.6151**	0.3822	0.2356	0.1748
2350–4600m	-0.01628	0.1031	0.1924	0.2241	**0.2250**

Clearly the upper layer is warmed most rapidly during the CO_2 increase period, i.e., 1.9 °C by the time of CO_2 tripling, and thereafter the warming rate decreases gradually, with the temperature being increased by about 0.12 °C in the last two centuries of the run. The mid-depth layer sees a maximum rate of warming in the three centuries following CO_2 tripling, and then the warming gradually declines as well. In contrast, the abyssal layer experiences a steadily increasing warming and sees a temperature increase of 0.45 °C in the last 200 years of the run. The fact that the deep ocean warming rate gradually catches up and finally exceeds that of the overlying layers is of great importance to the evolution and adjustment of the oceanic circulation. It gives rise to the anticipation that, once the deep ocean becomes warm enough after thousands of years under the continual $3\times CO_2$ forcing, the water column will be destabilized substantially, which may possibly lead to the

recovery or reoperation of the reduced or collapsed overturning in the high latitude oceans.

The above contrast of warming rate between different layers in the TGM3 integration can also be seen clearly in Fig.5.13b and 5.13c which show the vertical profiles of the global ocean temperature for some 10-year periods and the changes relative to the control climate, respectively. During the last 500 years of the integration, the surface is warmed by a mere 0.25 °C, whilst the bottom ocean temperature increases by as much as 1.0 °C, with intermediate varying warming rates at other interior levels. Another feature shown in Fig.5.14c, and also in Table 5.1, is the slight cooling occurring in the bottom ocean during the CO_2 increase period. This is associated with the reduction of the North Atlantic overturning, i.e., the shoaling of the NADWF penetration allows further northward intrusion of the cold Southern Ocean bottom water, which results in a significant cooling in the North Atlantic bottom water. The profiles shown in Fig.5.13d and 5.13e for TGM2 are generally similar to their counterparts in TGM3, but the rate of warming near the surface seems to decline more quickly.

Fig.5.14 shows the evolution of the latitude-depth distribution of zonally averaged annual mean warming in the global ocean for the two runs. Due to the effect of wind induced vertical mixing, warming is found in the near surface layer at the early stage of CO_2 forcing in all latitudes, except for the polar oceans where the existence of sea ice causes very small warming (or even slight cooling) at the surface and thus no noticeable warming is found beneath. As expected, the northern mid to high latitudes see more rapid downward penetration of the warming signal due to the transport by the sinking branch of the North Atlantic overturning and, unsurprisingly, the stronger overturning in TGM3 results in more rapid downward penetration of heat in the North Atlantic than that in TGM2. The cooling of the bottom ocean discussed above is found in the NH during the period of CO_2 increase. Near the polar oceans, especially the Circumpolar Ocean, the removal of sea ice allows surface warming to develop rapidly and penetrate downwards due to the wind-driven vertical mixing, as can be seen from Fig.5.14e and 5.14f for the

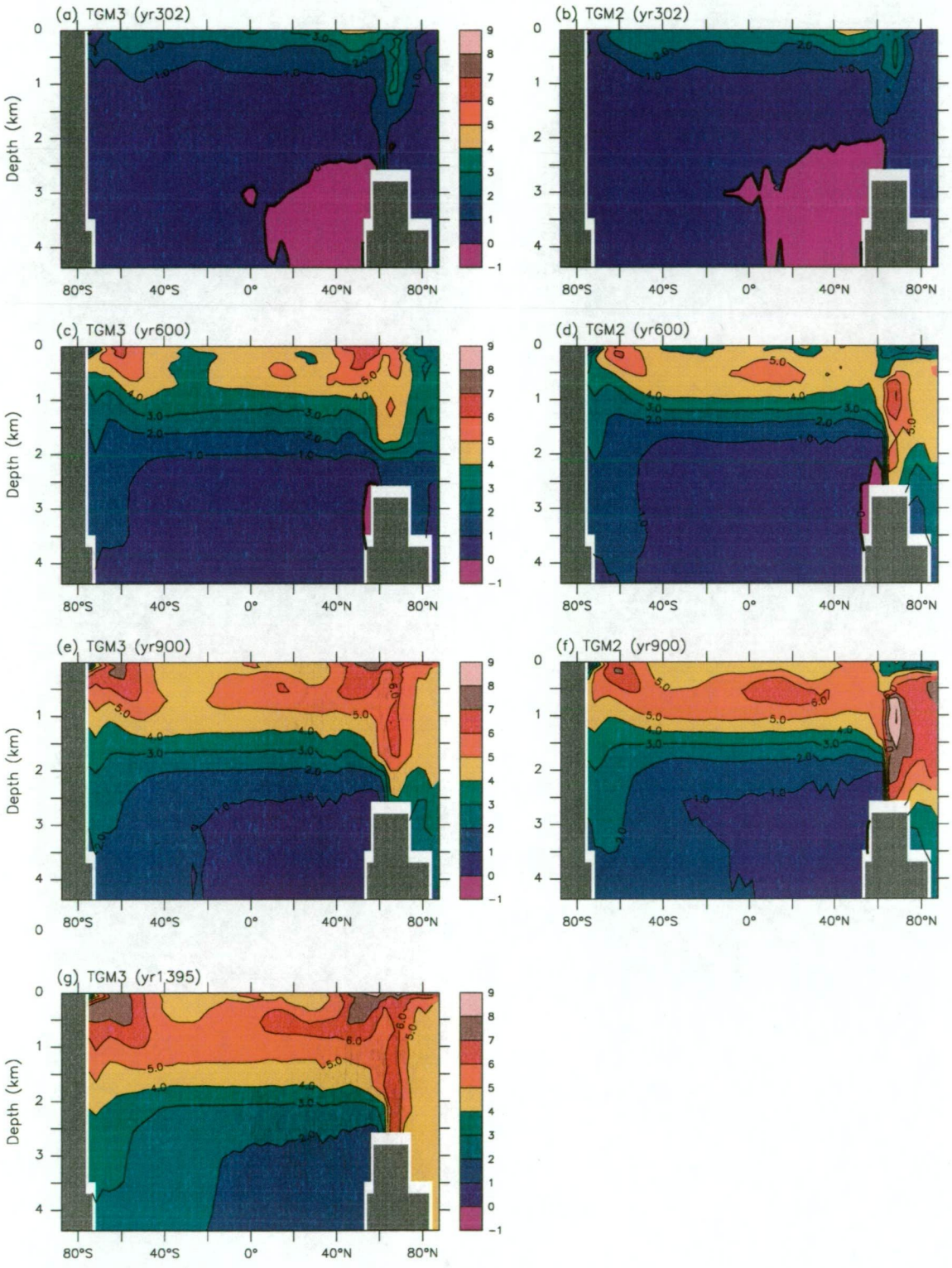

Figure 5.14: Zonally averaged global ocean temperature changes in TGM3 (left) and and TGM2 (right) – decadal mean centered on indicated years. Contour interval is 1 °C.

decade centered on year 900.

The notable deep penetration of warming near Antarctica, however, is attributed to the remains of the deep cell which, originating from the AABWF and dying away gradually under CO_2 forcing, brings the warming signal in the northern mid-depth ocean (mainly the North Atlantic) into the southern high latitudes where it sinks and thus takes the warmed water downwards. This process, although largely weakened following the shut-off of Southern Ocean overturning, still operates and is responsible for the bottom ocean ventilation. We see that, in the deep/bottom ocean, warming spreads northward (that is to say the warming in the northern bottom ocean is the smallest all the time). This spreading of the bottom warming is because the North Atlantic overturning can not penetrate down into the abyssal ocean any more, and the deep water is warmed only by the northward penetration of the Southern Ocean bottom water which gradually replaces the cold northern bottom water due to the transport by the weak but ongoing deep meridional circulation. Regarding the extremely large warming found in the North Atlantic intermediate water between 65°N and 70°N in the TGM2 run, it seems to be the result of numerical noise in temperature (similar to that found in the surface salinity field over the Arctic Ocean in TGM3 as addressed above), which spreads northward by the spurious background horizontal diffusion in the high latitudes and causes an anomalously large warming in the Arctic Ocean interior.

5.3.2 Salinity

Analyses similar to the above are made to examine salinity changes in the ocean interior, as shown in Fig.5.15. From 5.15a we see that the upper layer freshening becomes evident in the second century of warming and thereafter increases steadily due to the sea ice melt and snow melt runoff from the continents, which result in a slight salinity decrease in the entire ocean. Note that the surface freshening is notably larger in TGM3 because of its larger surface warming leading to more melt of ice and snow. As for the slight enhancement of salinity in the mid-depth

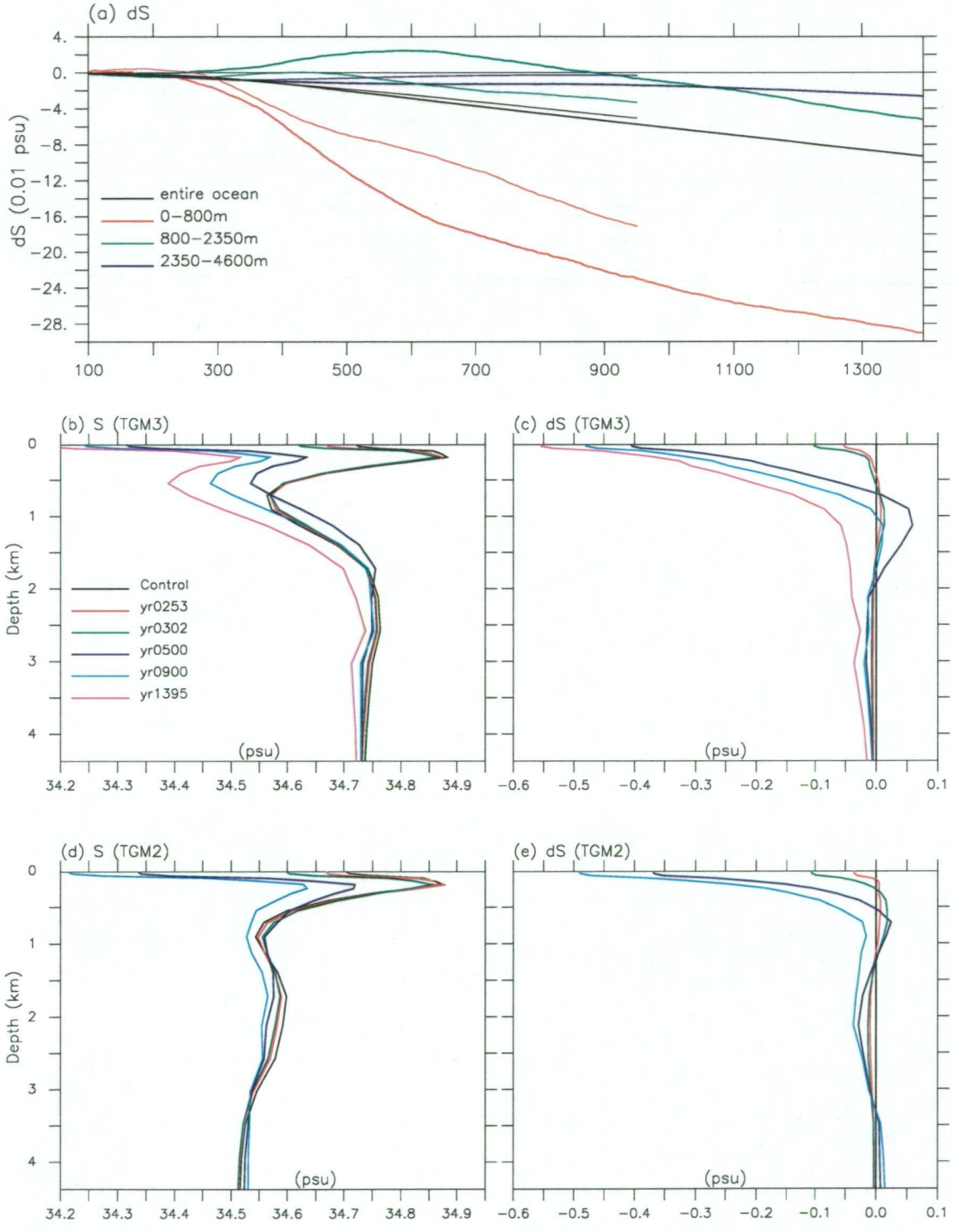

Figure 5.15: Same as 5.13 but for salinity.

layer during the 500 years after CO_2 tripling, it results mainly from the shutoff of AABWF and the shoaling of NADWF penetration as shown below. With the cessation of Southern Ocean overturning and deep convection, the strong (advective and convective) vertical mixing stops, and therefore the exchange between the fresh surface/sub-surface water and the underlying saline mid-depth water is substantially reduced, causing a further freshening in the upper layer and accordingly an increase of salinity in the mid-depth water. More importantly, the shoaling of NADWF leads to an intensification of ventilation into the mid-depth layer with the saline North Atlantic surface water through the world ocean conveyor belt, resulting in an increase of salinity in the mid-depth layer. Another possible contributing factor is the excess of evaporation over precipitation in the middle latitude Indo-Pacific Oceans and low to mid latitude Atlantic Ocean, where the resultant salinity increase is transported into the mid-depth layer (initially) by the wind-driven vertical mixing. Fig.5.15b and 5.15c show the development of surface freshening and its downward transport into deeper levels. By the end of the TGM3 run, freshening near the surface is as large as 0.55 psu while the change at the bottom is less than 0.02 psu, with the entire ocean freshened by nearly 0.1 psu. Such a large freshening for the entire ocean is not a 'natural' result of the warming forcing in our model. It is a kind of drift due to some (unclear) reason that breaches the numerical salinity closure in the model as mentioned in Chapter 4. It is further examined in Appendix B.

Examining changes of the salinity vertical structure such as the depth-latitude feature for the global ocean (not shown), we see that the two runs bear general similarity in the change of pattern in most latitudes, except for the Arctic Ocean where TGM3 suffers a numerical noise problem at the surface after about year 600 as already discussed. Surface freshening is evident over mid to high latitudes in both hemispheres during the period of CO_2 increase. We have previously mentioned that this freshening weakens the NADWF and shuts off the AABWF. This change in the world ocean THC in turn has a notable impact on the distribution of salinity in the ocean interior. For the Southern Ocean, the shutoff of AABWF largely reduces the exchange of salinity between the fresher near-surface water around Antarctica

and the underlying saltier water, directly causing an increase of salinity in the interior ocean beneath. Similarly, the change of NADWF, including the reduction in intensity and the shoaling of penetration depth, results in less transport of saltier northern North Atlantic surface water into the deep ocean, which, together with the further northward intrusion of fresher Southern Ocean bottom water associated with the 'retreat' of NADWF penetration, freshens the deep and bottom water in the North Atlantic in particular.

5.3.3 Density

The changes in the salinity and temperature fields shown above indicate a reorganization of the density structure in the world ocean under global warming from greenhouse forcing. Fig.5.16a presents time series of changes in annual and global mean density for three sub-layers and the entire ocean. Very soon after CO_2 begins to increase, the upper layer density starts decreasing in response, due mainly to the surface warming because SST responds to the radiative forcing directly and thus more quickly than SSS, as already shown. From the second century of CO_2 forcing, the upper layer density decreases rapidly for a few hundred years during which the rate of change reaches a maximum by the time of CO_2 tripling and then declines quickly. In the meanwhile, the mid-depth layer starts responding and the rate of density change gradually catches up and finally exceeds its overlying counterpart at around year 800, by then the contrast of density between the upper and mid-depth reaches the maximum and, because the abyssal ocean stays nearly undisturbed until then, vertical stratification has been intensified to the greatest extent. After that, densities of all levels still keep decreasing, with the change in the mid-depth being slightly quicker than that in the upper layer, and, after over 1000 years, the rate of change in the bottom ocean eventually catches up with that of the mid-depth in the last century of the TGM3 run.

Fig.5.16b–e show evolution of the vertical profiles of globally averaged annual mean density and the changes relative to the control climate for both runs. The enhance-

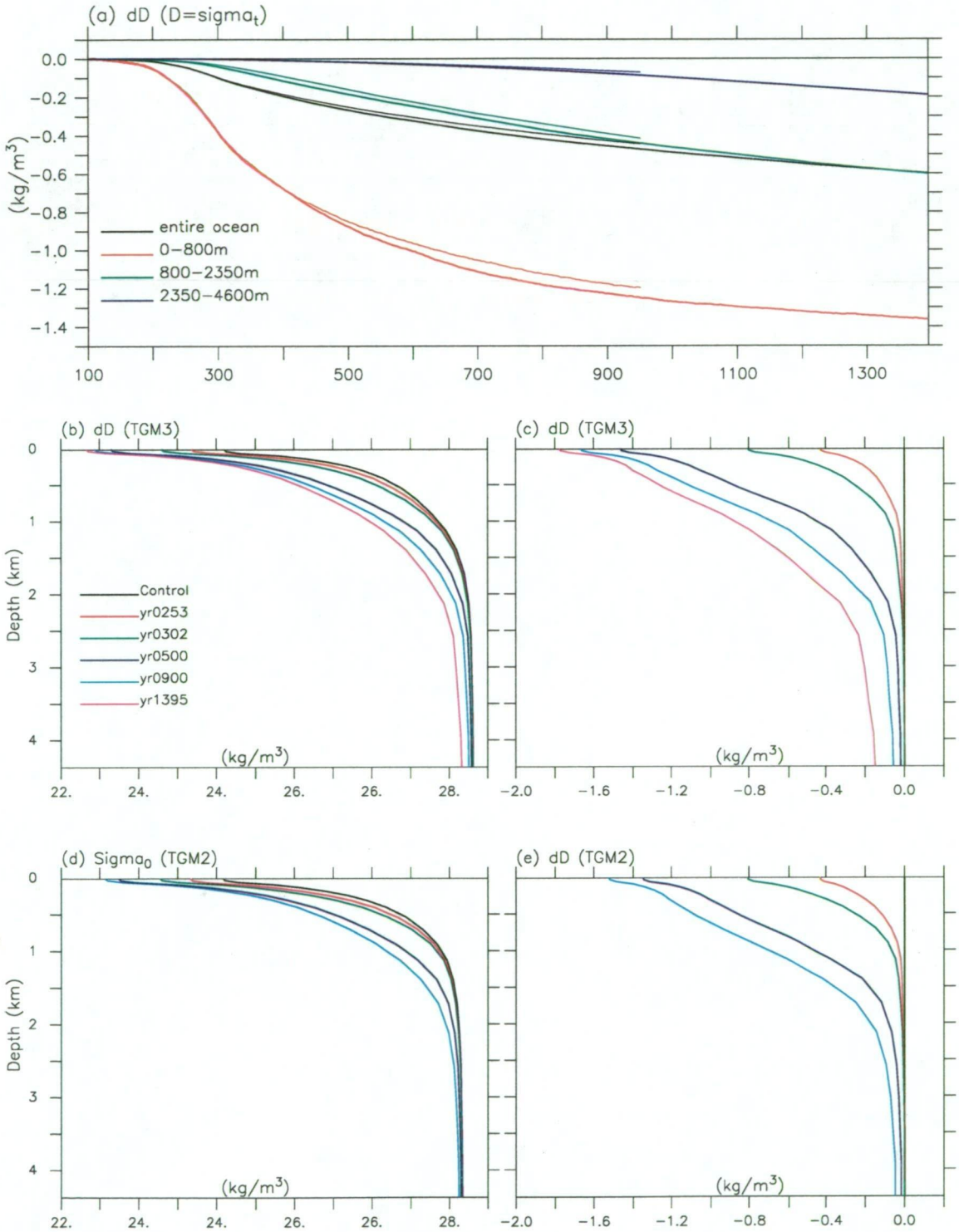

Figure 5.16: Same as 5.13 but for density (σ_t).

ment of stratification discussed above is clearly seen in these panels. Evident is the relatively 'uniform' change of density at all levels during the last 500 years of the TGM3 integration, indicating that the stratification strengthening is nearing its end, and the reverse evolution, i.e., stratification weakening, may occur thereafter. This highlights the possibility that the continual warming in the deep ocean may eventually adjust the vertical density contrast towards a pattern more similar to its initial state and thus allow a resumption of the world ocean thermohaline circulation. Comparison between Fig.5.13 and Fig.5.16 shows a general 'reverse' similarity between the trends of temperature and density, showing the dominance of temperature change in adjusting global ocean stratification under CO_2 forcing. The drift of salinity in the ocean interior only causes a minor change in the density structure, as will be further discussed in Appendix B. However, at the stage of CO_2 increase, surface freshening in the southern polar ocean and the northern North Atlantic, does play a crucial role in stopping the AABWF and substantially weakening the NADWF, as will be shown in detail later.

5.3.4 Sea Level–Thermal Expansion

Global warming results in an average temperature increase of about 3.75 °C for the entire ocean by the end of the TGM3 integration and, as an important consequence, the global ocean density (referenced to the surface) is reduced by as much as 0.6 $kg\,m^{-3}$. This indicates a considerable expansion of the world ocean water volume, implying a rise of the sea level. Since in our model the melting of glaciers or the Antarctic and Greenland ice sheets and shelves which in reality can contribute to the sea level rise is not included, as already addressed, and the effect of changes in P - E and runoff is very small, we discuss here only the global ocean sea level rise due to the thermal expansion of sea water.

Our calculation of the global mean sea level rise is based on the local change of specific volume for the entire world ocean and on an assumption of water mass conservation in all model layers. To consider only the effect of thermal expansion, we

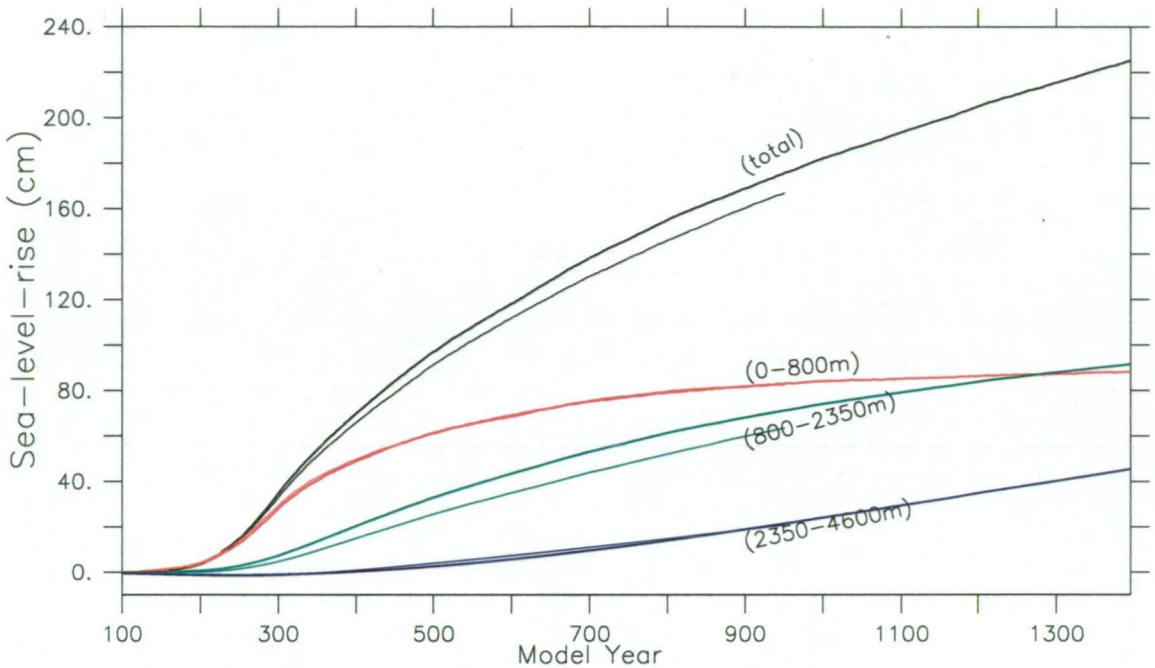

Figure 5.17: Global mean sea level changes caused by thermal expansion during the integrations of TGM3 (thick) and TGM2 (thin). Also included are the contributions of three sub-layers. (units: cm).

define a locally referenced density $\rho_T = \rho(S(0), T(t), p)$, where $S(0)$ is the initial value (control climate) of salinity, $T(t)$ the transient temperature and p the local pressure. Thus ρ_T is only temperature dependent at a specified level, with the 'contamination' of the salinity anomaly (i.e., freshening) to the specific volume change being removed.

Fig.5.17 illustrates the temporal variation of the global mean sea level rise due to the thermal expansion of sea water in both runs. Also included are the contributions from three sub-layers, as indicated by the colour curves. TGM3 estimates a rate of sea level rise of only a few tenths of centmeters per decade in the first century of CO_2 forcing, but this rate increases rapidly to 5 cm per decade by the time of CO_2 tripling. By that time the mean sea level rise reaches about 35.6 cm, to which the upper, mid-depth and bottom layers contribute 28.8 cm, 7.6 cm and -0.8 cm, respectively. Obviously, in the period of CO_2 increase, the sea level rise is attributed mainly to warming in the near surface layer. The mid-depth ocean begins to contribute from the second century whereas the abyssal ocean experiences a thermal contraction due to the cooling resulting from less transport of water warmer than AABW downward

into the deep ocean interior by the reduced world ocean THC, especially the North Atlantic overturning as mentioned above. After CO_2 stabilization, the rate of sea level rise drops quickly down to 2.0 cm per decade in the next 200 years and further decreases to about 1.25 cm per decade by year 900, and down to below 1.0 cm per decade by the end of the run. The mid-depth layer water expands quickly after CO_2 trebling as the expansion of the upper layer slows down dramatically, and the bottom ocean starts expanding as well and the rate of expansion gradually catches up, consistent with the warming trends for these layers shown in Fig.5.13a. By the end of the TGM3 run, thermal expansion leads to a global mean sea level rise of about 225 cm, with the contributions from the three sub-layers being 88 cm, 91.6 cm and 45.4 cm, respectively.

Our estimate of the long-term global mean sea level rise due to thermal expansion is both qualitatively and quantitatively close to that found by Manabe and Stouffer (1994). In their doubling and quadrupling CO_2 experiments, Manabe and Stouffer obtained global mean sea level rises of 200 cm and 100 cm (see their Fig.3), respectively, by the end of the two runs, i.e., year 500. Our tripling CO_2 run TGM3 gives a value of about 118 cm at around year 600 (i.e., the 500th year of CO_2 forcing), comfortably lying between their $4\times$ and $2\times$ CO_2 results. It should be noted that our result is much nearer to their $2\times$ CO_2 side instead of lying clearly in the middle. This is probably because they employed the "Business-as-Usual" scenario for CO_2 increase (1% yr^{-1} compounded) under which CO_2 doubles at year 70 and quadruples at year 140, in contrast to the IS92a scenario used in our experiments under which CO_2 needs 153 years to double and 302 years to treble, indicating their stronger radiative forcing and thus effectively a more intensive warming period or more rapid penetration of heat into the deep ocean in their experiments than ours. Recently, Voss and Mikolajewicz (2001) estimated a global mean sea level rise of about 150 cm induced by thermal expansion in their 850-year CO_2 quadrupling integration using the ECHAM3/LSG model with the IPCC scenario A (Houghton et al. 1990) under which CO_2 quadruples after 120 years. This result is much lower than the estimate of 175 cm in our tripling CO_2 experiments by year 950 (i.e., the 850th year

of forcing), despite their quicker and stronger radiative forcing, indicating a larger climate sensitivity of our model to global warming.

It may merit mention that our model gives a global mean sea level rise due to thermal expansion of about 5.2 cm for the period 1880 to 1990 (model years 100 to 210), in reasonable agreement with the report of IPCC 1995 (Warrick et al., 1996) which gave an estimated range of 2 to 7 cm attributable to thermal expansion. As for the projection of global sea level rise over the period 1990 to 2100, TGM3 shows a value of about 37.7 cm by thermal expansion, which is quite close to the "best estimate" of 49 cm for the IS92a scenario in IPCC 1995, given that the contribution of changes in the hydrological cycle associated with the oceanic water budget is much smaller for this period. In fact, it can be expected that thermal expansion of sea water will be the dominant contributor to global mean sea level rise during the next century. For example, based on the CO_2 scenario integrations with the Hadley Centre coupled model (Johns et al. 1997) and with a separate glacier model, Gregory and Oerlemans (1998) estimated a thermal expansion induced sea level rise of 30 cm and a contribution of glacier melting of 13.2 cm for the period 1990 to 2100. In the long run, however, the potential changes in the land ice masses (e.g., ice-shelf basal melting with increased ice flow, and surface accumulation changes) caused by global warming are substantial, and the sea level rise will be largely influenced by the land ice melting (Warner and Budd 1998; Huybrechts and Wolde 1999). Manabe and Stouffer (1994) estimated an additional sea level rise ranging from 3.5 m to 7 m due to the ice sheet melting in their 500-year quadrupling CO_2 integration, much more than the contribution of thermal expansion, i.e., 2 m, as mentioned above.

As for the situation of TGM2, Fig.5.17 shows nearly the same rate of change in the world ocean mean sea level due to thermal expansion as that in TGM3 during the period of CO_2 increase. After CO_2 tripling the rate of rise in TGM2 decreases slightly faster and, by year 950, the sea level rise is about 166.8 cm, 9 cm less than that in TGM3. Such a deviation is attributable totally to the difference of warming in the mid-depth layer as shown in Fig.5.13a. We see strikingly close thermal expansions for the two runs in both the upper and abyssal layers, again in close accordance with

the warming trends displayed in Fig.5.13a.

5.4 Changes of the Thermohaline Circulation

We have shown that global warming induced by increasing CO_2 forcing substantially changes the ocean water density structure, especially in the high latitudes of both hemispheres. As a direct consequence, the density-driven global ocean THC changes remarkably in response. Because the THC plays a crucial role in adjusting the global thermal and hydrological budgets in the coupled atmosphere-ocean system, its change is very important to the global climatic environment, especially for the long-term evolution of the climate system. This section documents the transient and long-term behaviours of the overturning circulation in individual basins and the world ocean for TGM3 and TGM2.

Fig.5.18–5.20 show the evolution of the THC for the global ocean, the Atlantic sector and the Indian-Pacific sector, respectively, for both runs. In all figures, the top row displays the initial state (i.e., yr51-100 mean) and the others are snapshots of decadal means centered on indicated years. As can be seen from the left panels of Fig.5.18 and Fig.5.19, in the course of the TGM3 integration, the North Atlantic overturning or say the NADWF is substantially reduced during the period of increasing CO_2 and, accordingly, the downward penetration of its sinking branch shoals markedly. After CO_2 tripling, the overturning intensity shows a tendency to come back but never fully recovers, and the penetration is constrained above the depth of 2000 m all the time since it shoals up to that level. In the Southern Ocean, the downwelling off Antarctica collapses completely before CO_2 tripling, meaning a shutdown of the AABWF, but the associated deep circulation cell remains quite strong at that time, keeping the bottom ocean ventilated by transporting the AABW northward into the NH through both the Atlantic and Indian-Pacific basins as shown in Fig.5.19 and Fig.5.20. However, this deep cell gradually dies away due to the disappearance of its direct driving force, i.e., the AABWF, and the deep ocean becomes relatively

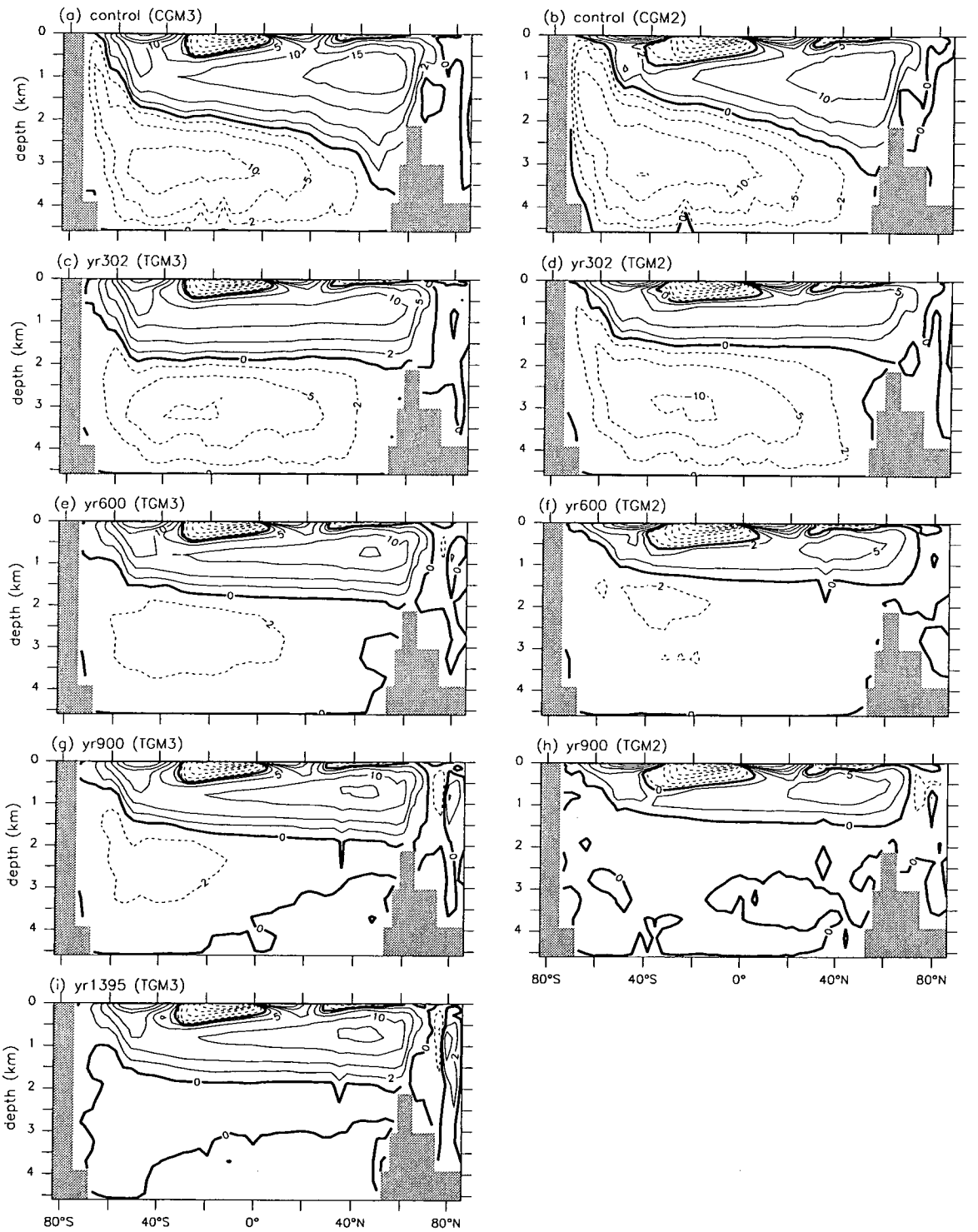

Figure 5.18: Global ocean overturning streamfunctions (Sv) in TGM3 (left) and TGM2 (right) – (a)(b) initial state, and (c)–(i) decadal mean centered on indicated years. Contours: 0, ±2, ±5, ±10, ±15, ±20, ±30, ±40.

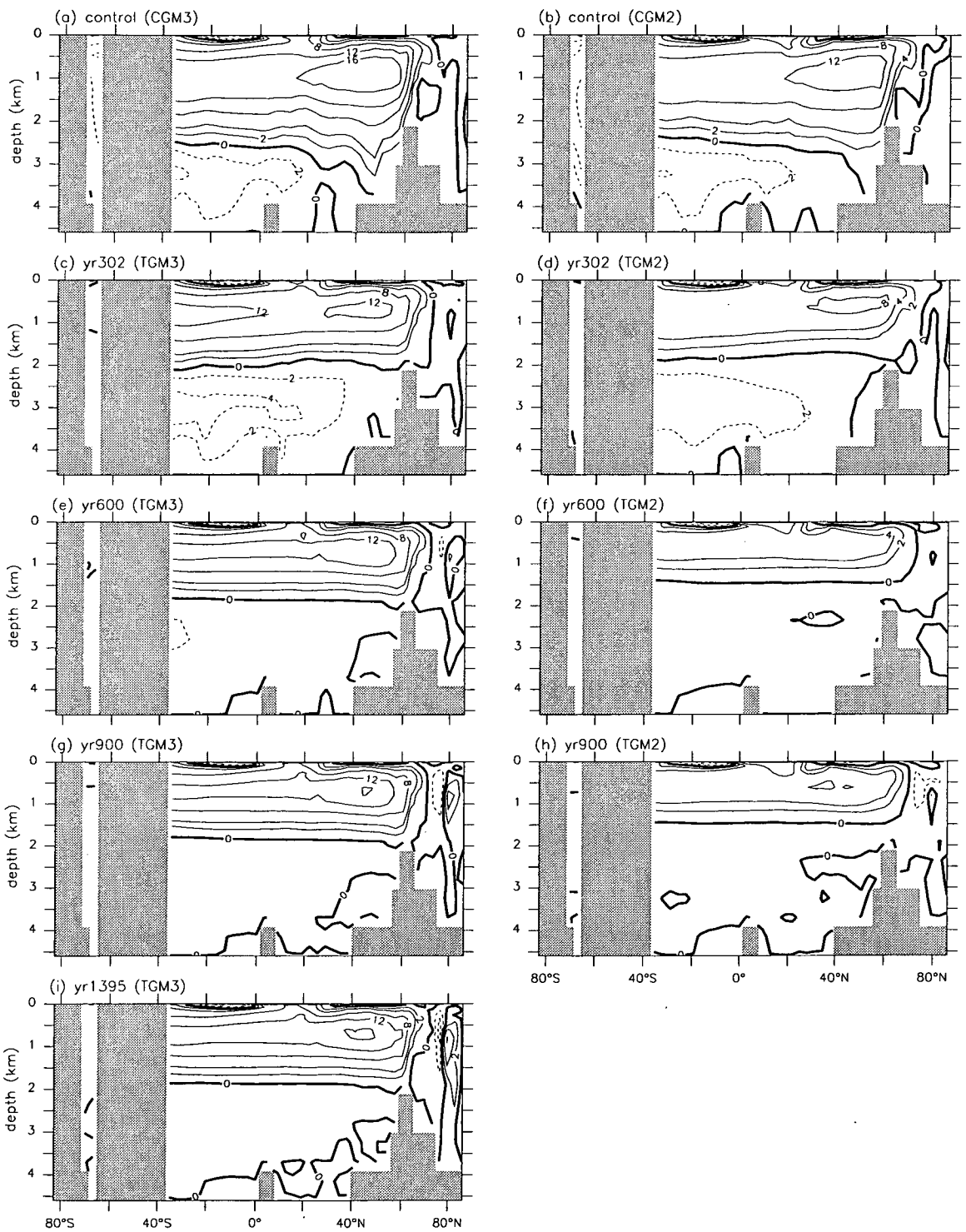

Figure 5.19: Same as 5.18 but for the Atlantic Ocean. Contours: 0, ±2, ±4, ±8, ±12, 16.

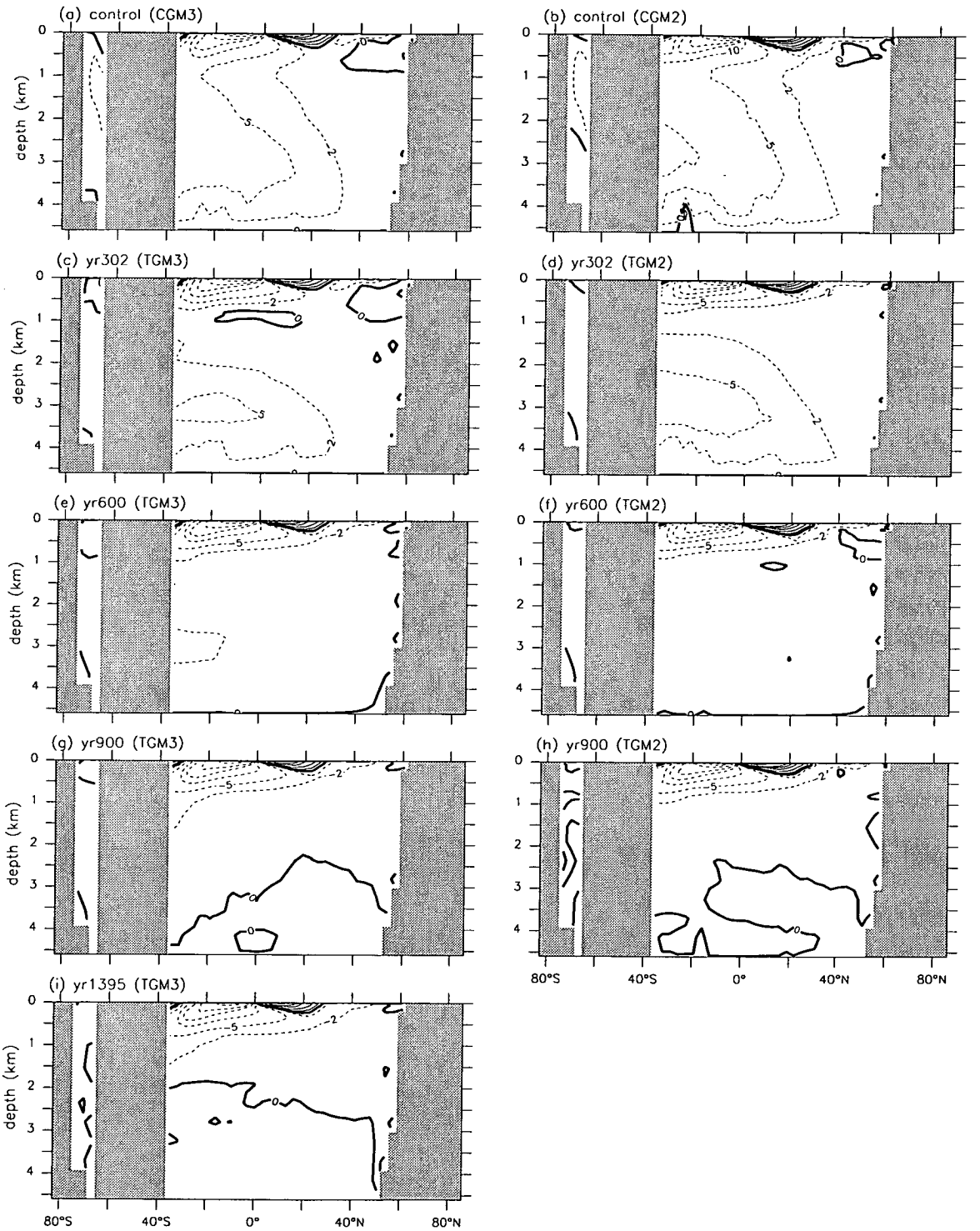

Figure 5.20: Same as 5.18 but for the Indian-Pacific basin. Contours: 0, ±2, ±5, ±10, ±15, ±20, ±30, -40.

isolated in the last few centuries of the run. For the TGM2 integration, the global ocean THC evolves in a manner similar to that of TGM3 described above, but with notable differences in the magnitude of the changes. For example, the NADWF is reduced to a larger extent and its penetration is shoaled to a level above 1500 m; the AABWF collapses somewhat more slowly but the deep cell dies away faster after the shutoff of AABWF. Fig.5.20 also shows that, in both runs, the upwelling from the deep ocean into the low latitude intermediate water in the Indian-Pacific basin stops along with the retreat of the northward intrusion of the AABW, indicating a cutoff of the direct exchange between the deep ocean and subsurface layer.

To illustrate the transient response of the world ocean THC more explicitly, we choose the streamfunction maximum intensities of NADWF (located at 44.6°N, 800 m depth), AABWF (66.9°S, 1250 m depth) and the northward outflow of the AABW (35°S, 3250 m depth) as the main indicators of the world ocean THC and show their time series under CO_2 forcing in Fig.5.25a, 5.25b and 5.25c, respectively. The THC evolution and the difference of change between the two runs described above are clear in these plots, with more details revealed.

For the NADWF, we see that it weakens quickly from the second century of global warming forcing in both runs. In TGM3, it reaches a minimum only 30 years after CO_2 tripling and then shows a noticeable increase during the following 300 years. As a contrast, in TGM2 it continues to decrease slowly after the rapid decline in the CO_2 ramp-up period until it reaches a minimum at around year 500. Moreover, the largest reduction of the NADWF in TGM3 is only about 37% (i.e., from 19.6 to 12.3 Sv), while the counterpart in TGM2 is up to 67.9% (from 14.3 to 4.6 Sv). In an earlier study using a version of the CSIRO climate model very close to that for TGM2 and under a similar CO_2 increase/stabilization scenario, Hirst (1999) found a trend of the NADWF evolution (see his Fig.12) very similar to our TGM2 result.

Two factors may be responsible for the difference of the NADWF changes in response to CO_2 forcing between TGM3 and TGM2 (or Hirst's result): the NADWF itself and the associated conveyor belt. In TGM3, the initial intensity of the NADWF

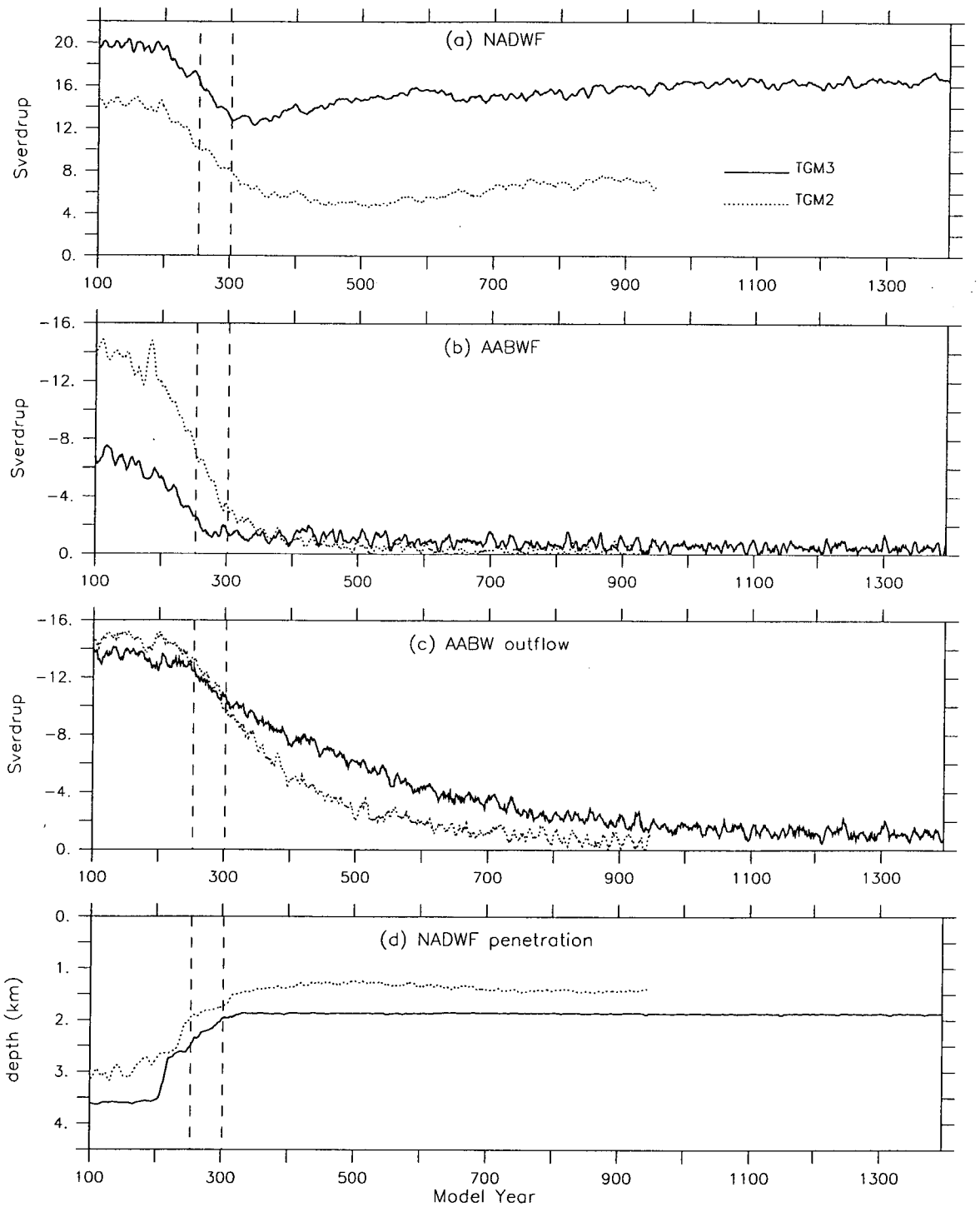

Figure 5.21: Time series of the maximum overturning streamfunction values for TGM3 and TGM2: (a) NADWF, (b) AABWF, (c) outflow of the AABW, and (d) penetration depth of the NADWF.

is about 19.6 Sv and and the conveyor belt accordingly transports over 13 Sv of water mass across the equator, much stronger and thus more realistic than their counterparts in TGM2 or Hirst's run (around 15 Sv and 7 Sv, respectively). Such a stronger circulation in TGM3 is more efficient in transporting the warm water from low latitudes to the NADWF region at the early stage of CO_2 increase, resulting in a larger buoyancy gain at the surface and therefore a more rapid reduction in the overturning intensity. On the other hand, although the NADWF is reduced quickly to a minimum (about 12.3 Sv, as shown above) and its penetration largely shoals, it is still very strong compared to the minimum of 6.5 Sv in Hirst's case and 4.6 Sv in TGM2. The sinking branch of this overturning circulation transports the warmed and freshened surface water to the mid-depth quite efficiently, destabilizing the water column above and partly resulting in the relatively quick restoration in a short period following CO_2 tripling. In addition, Fig.5.21d shows significant shoaling of the overturning penetration depth in both runs. Accompanying the spindown of the NADWF intensity, the penetration depth in TGM3 is reduced quickly from the second century of CO_2 forcing and reaches a level just above 2000 m by the time when the NADWF is reduced to a minimum. After that this penetration depth remains unchanged, although the NADWF begins to reintensify clearly. Similarly, TGM2 sees a shoaling of the penetration consistent with the NADWF variation, which lasts until around year 500 when the NADWF intensity reaches a minimum and then shows a slight recovery. In general, the difference of the penetration depth between the two runs is maintained through the course of the integrations under CO_2 forcing.

As shown in Fig.5.21b, the AABWF is more sensitive to the surface perturbation than the NADWF and begins to respond from the beginning of CO_2 forcing. It collapses before CO_2 tripling in TGM3 but lasts for one more century in TGM2 before being shut off nearly completely, showing no sign of recovery in the following integrations of both runs, confirming the finding of Hirst (1999). One notes that, although the remaining residual direct downwelling cell off Antarctica is very weak in both runs, it is still noticeably stronger in TGM3 than in TGM2 after year

400. Further examination of the AABWF components (not shown) reveals that, for TGM3, the downwelling in the Weddell Sea, which initially takes up about two thirds of the total AABWF in our model, breaks down completely by the time of CO_2 doubling, while the other large contributor, downwelling in the Ross Sea, lasts for a longer duration and is responsible for the persistence of the weak residual overturning off Antarctica mentioned above. In TGM2, the Weddell Sea downwelling is initially much stronger than the counterpart in TGM3 and thus takes a bit longer time to shut off (i.e., soon after CO_2 tripling).

Northward outflow of the AABW illustrated in Fig.5.21c shows much lower sensitivity to the surface warming forcing than the AABWF but weakens steadily throughout the integrations but never breaks down completely. This is not unexpected since the deep circulation, although initially driven by the downwelling off Antarctica, can be maintained by the meridional pressure gradient in the deep ocean, which, once established, will take a long time to disappear. Moreover, in this process, the gradually weakened circulation slows down the weakening of the meridional pressure gradient, which in turn damps the weakening of the circulation itself. TGM2 sees a more rapid decline of the deep cell than TGM3, indicating a stronger dependence of the operation of the deep ocean THC on the AABWF in TGM2. As has been shown before, TGM3 has a remarkably stronger (and thus more realistic) stratification in the high latitude Southern Ocean, which on the one hand means a more stable water column and thus results in a weaker overturning adjacent to Antarctica and, on the other hand, favours the persistence of the deep cell by providing a stronger meridional pressure gradient in the deep ocean. In addition, for TGM3, the weak residual overturning (but stronger than that in TGM2 as mentioned above) may also help the deep circulation last longer.

5.5 Mechanism for the THC Changes

Manabe and Stouffer (1994) found that the main reason for the THC breakdown in their CO_2 quadrupling experiment was the capping of the high-latitude oceans by relatively fresh low-density water. Using a simplified coupled model, Schmittner and Stocker (1999) confirmed the finding of Manabe and Stouffer by showing that the increased poleward freshwater transport in a warmer atmosphere is mainly responsible for the cessation of the NADWF, although they noted that at the early stage (i.e., the first 70 years) of CO_2 forcing, both the surface warming and freshening contribute to lower densities in the northern North Atlantic. However, Mikolajewicz and Voss (2000) found that the heating from above has a much more important effect than the changes in freshwater forcing on the THC weakening in the ECHAM3/LSG model. In our CO_2 tripling experiment, surface freshening is responsible for the shut-off of the Southern Ocean overturning whereas the surface warming also plays an important role in weakening the North Atlantic overturning.

5.5.1 Surface Warming and Freshening

We have discussed the CO_2 induced oceanic warming and freshening in terms of global or zonal means. Here we examine this issue again but focus more closely on the regions where the model deep/bottom water formation occurs. In the following presentation, we start from the evolution of the hydrological cycle, then the surface water properties and finally the stratification, generally in a sense of regionally averaged features.

The freshening of surface waters adjacent to Antarctica is partly a result of changes in the hydrological cycle. As already pointed out, the CO_2 increase firstly warms the atmosphere, enhancing the poleward atmospheric moisture transport, leading to an increase of P - E in high latitudes. Fig.5.22a shows the change of annual mean P - E averaged over the oceans southward from 60°S, including the contribution of runoff, i.e., meltwater input from the Antarctic ice sheet and ice shelves, in the

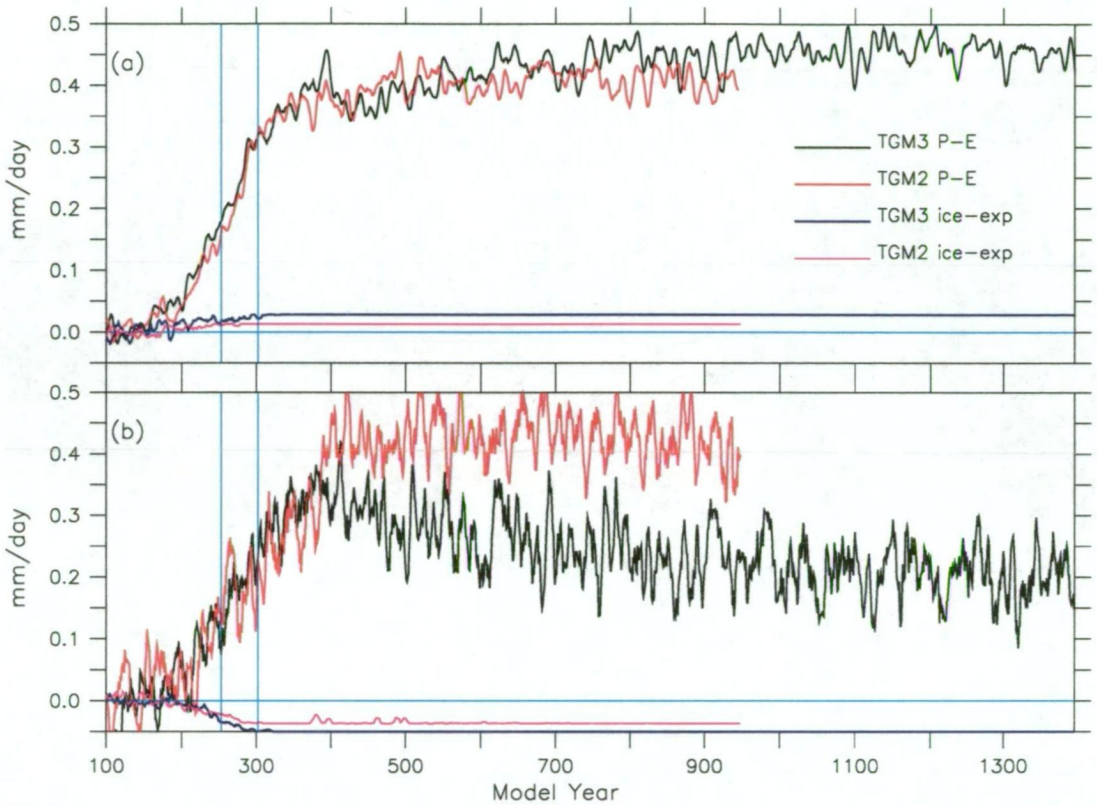

Figure 5.22: Time series for changes in freshwater fluxes contributed by P - E and sea ice transport for TGM3 and TGM2 in : (a) Southern Ocean (south of 60°S), (b) North Atlantic (90°W– 30°E, 50 – 65°N).

TGM3 integration. P - E generally increases around Antarctica during the period of increasing CO_2 and for about a century thereafter, but then fluctuates about a fairly constant mean value for the remainder of the run. This plateauing in southern high latitude P - E in the latter TGM3 integrations implies general constancy in the poleward atmospheric moisture transport, and is associated with relatively small atmospheric warming in the tropics and southern mid-latitudes during this period (e.g., Hirst 1999), while enhanced high latitude evaporation associated with the major ongoing SST increases and sea ice decreases (Fig.5.4b) is roughly balanced by enhanced regional precipitation.

Another factor contributing to the freshening of surface water adjacent to the Antarctic coast in the global warming experiments is the reduction in net northward sea ice export. Under global warming conditions, less ice forms near the Antarctic coast, and the northward transport of sea ice is accordingly reduced, thereby

resulting in a reduction in freshwater loss and hence freshening around Antarctica. The overall Southern Ocean sea ice volume (Fig.5.6b) shows little change during the first 120 years of the TGM3 integration, but then shows a fairly steady decline over the next two centuries to a low residual level of roughly 20 percent of the original volume, which then persists for the latter part of the run. The decline in net northward transport of ice volume across 60°S is shown in Fig.5.22a as a small positive contribution to the regional surface freshwater flux change, which of course assumes a constant value soon after about CO_2 tripling as sea ice no longer reaches that latitude. However, much of the northward drifting sea ice melts prior to reaching the 60°S latitude, even in the control integration. The relative contribution of sea ice change to the surface freshwater flux is much larger than that seen here if oceanic areas closer to the Antarctic coast are considered (e.g., the region to the south of 65°S), where net northward ice transport is much larger in the control.

For the case of TGM2, Fig.5.22a shows that the hydrological cycle over the high latitude Southern Ocean evolves in a similar way, but P - E keeps increasing for one more century and then settles around a level notably lower than that in TGM3 for the last couple of centuries. This difference indicates a smaller poleward transport of the atmospheric moisture in TGM2 than TGM3 in the Southern Hemisphere due partly to the slight less surface warming over the southern low latitude oceans in TGM2 as already shown. It can also be seen that the freshening due to change of ice export in TGM2 is only about half that in TGM3.

In the North Atlantic region (50°~65°N), the surface freshening is mainly attributable to changes of P - E, runoff from the continents and the southward transport of sea ice across the south and north boundaries of the region. Fig.5.22b shows the time series of changes in the hydrological cycle [2], (i.e., P - E, and the ice inflow) over our target region. Although fluctuating greatly, P - E increases a few decades after

[2]The contribution of runoff is not included here due to the difficulty in specifying the runoff inflow from the continents into our target region. However, an integration of runoff recorded over the continents in region 50°~65°N, 90°W and 30°E~60°E gives a rough estimate that the runoff inflow increases at a rate comparable to the P - E change in the first century of CO_2 forcing and can cause a freshening of 0.1~0.2 mm day^{-1} over the target ocean region after year 400. The case for TGM2 is similar.

CO_2 begins to increase. It reaches a maximum by about year 400 and thereafter declines generally, with a gradually decreasing rate of change. The large fluctuation of P - E over the North Atlantic ocean in the course of the integration reflects a strong variability of the atmospheric meridional circulation in the NH. As for the freshening caused by the change of ice input, we simply assume that the excess of sea ice inflow from the north over the outgoing ice amount through the southern boundary melts in our target region as a net freshwater gain. It is seen that such a freshwater gain begins to decrease from the second century of CO_2 forcing and declines to a minimum of -0.05 mm day^{-1} soon after CO_2 tripling and thereafter stays at this level thereafter, because no more sea ice is transported into or out of this region in the latter part of the run. This kind of freshwater loss somewhat cancels the P - E induced freshening.

In the TGM2 run, P - E shows an increase generally similar to that in TGM3 by around year 350, but with clearly larger fluctuations. The change keeps increasing strongly to a maximum of about 0.5 mm day^{-1} soon after year 400 and thereafter fluctuates between 0.35 and 0.5 mm day^{-1}, showing no marked trend of decline as we see in the TGM3 run, indicating that a near constancy of hydrological cycle is reached. The difference in P - E increase over our target region of the North Atlantic between TGM3 and TGM2 is mainly caused by the difference of change in evaporation. As we have already shown above, SST increase is significantly larger in TGM3 than in TGM2 from around year 400, leading to much more freshwater loss by evaporation and thus largely reducing the P - E in TGM3. The freshwater loss due to the change of sea ice transport is a somewhat smaller than its TGM3 counterpart, but changes can still be seen a few centuries after CO_2 tripling. In fact, such a small change is attributable to the ice formation and transport off southeastern Greenland where strong cooling occurs in the latter part of the TGM2 run, as shown in Fig.5.05d.

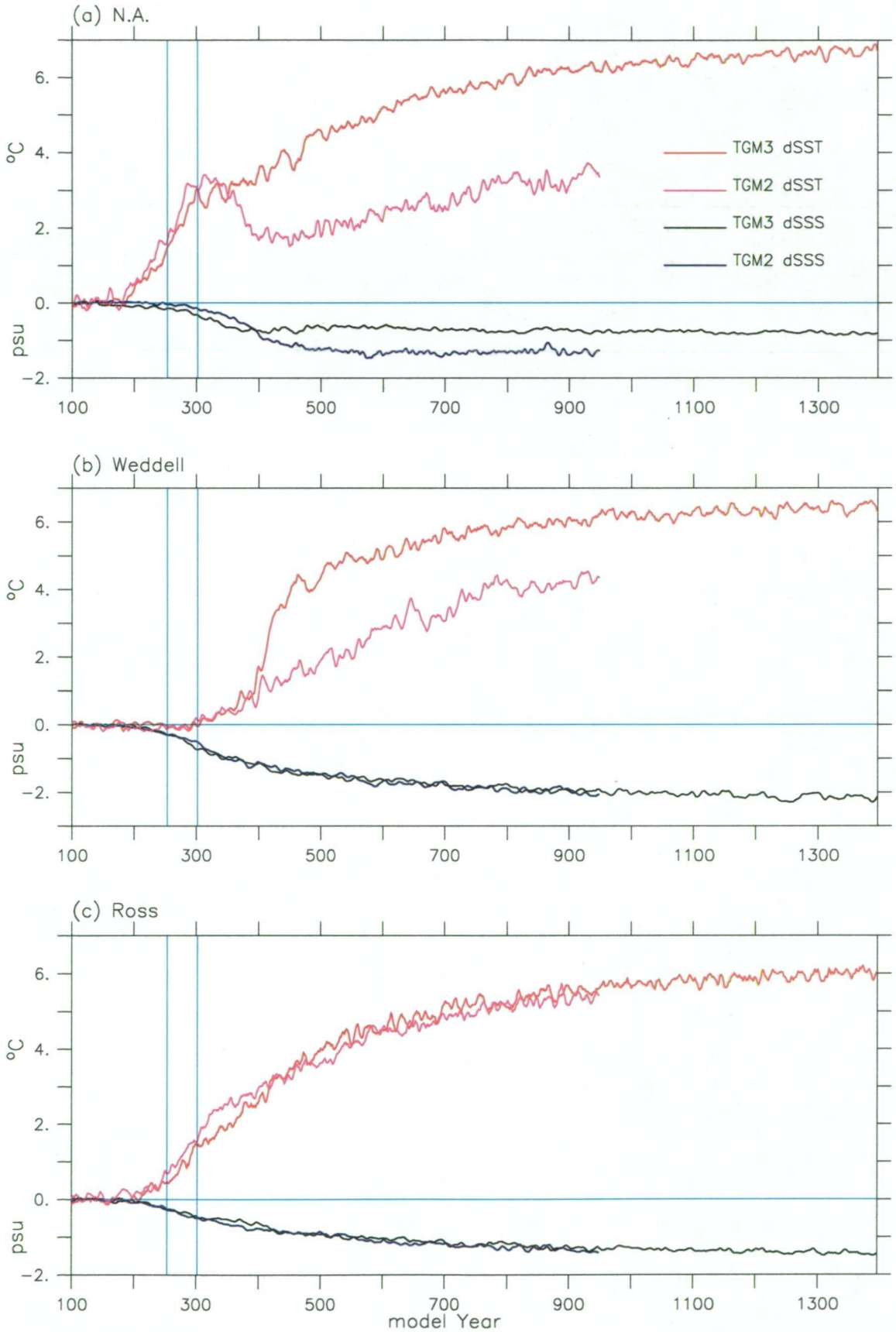

Figure 5.23: Time series for changes in annual mean SST and SSS for TGM3 and TGM2 over the: (a) North Atlantic (50 – 65°N), (b) Weddell Sea (south of 60°S), and (c) Ross Sea (60°S poleward).

5.5.2 Changes in SST and SSS

Fig.5.23 shows the time series of changes in the annual mean SST and SSS averaged over our target regions for both the TGM3 and TGM2 integrations. Note the Southern Ocean is now separated into the Weddell Sea (south to 60°S) and the Ross Sea/Bellingshausen Sea (south to 60°S) to examine the inter-regional difference of changes in the thermohaline conditions. The freshening due to the change in P - E discussed above causes a substantial decrease of SSS. Also evident is the difference of SSS change in the North Atlantic between the two runs, namely, the decrease of SSS in TGM2 is much larger than that in TGM3 after year 400, due to the remarkable difference of change in freshwater input shown above. In the Southern Ocean, the two runs bear close similarity of SSS change over both the Weddell Sea and Ross/Bellingshausen Seas in spite of a notable difference in P - E increase. This may be because the freshening from above is somewhat cancelled by the weak upmixing of salty deep water associated with the residual overturning off Antarctica which, as already revealed, is slightly stronger in TGM3. However, the Weddell Sea experiences a markedly larger loss of salinity than the Ross/Bellingshausen Seas in both runs, due mainly to the effect of Antarctic catchment which leads to different flow of runoff into the two regions. With respect to the surface warming, we see a rapid and nearly linear increase of SST over the North Atlantic region from the last decade of the first century with CO_2 forcing until the time of CO_2 stabilization. In contrast, the Southern Ocean, especially the Weddell Sea sees a much slower response of SST due mainly to the existence of sea ice. After CO_2 stabilization, the two runs see quite different SST changes over both the the North Atlantic and the Weddell Sea regions after year 400. It is the above differences of warming/freshening between regions and/or between the two runs that cause the different responses of surface densities and thus the water column stratification, resulting in different behaviours of the THC in our target regions in the course of the TGM3 and TGM2 integrations.

5.5.3 Changes in SSD and Stratification

To discriminate between the effects of warming and freshening in changing the density structure of the world ocean, especially the northern North Atlantic and the Southern Ocean, we follow Manabe and Stouffer (1994) and Schmittner and Stocker (1999) to calculate the density changes induced by temperature change only ($\Delta_T\sigma_t$) and by salinity change only ($\Delta_S\sigma_t$), namely,

$$\Delta_T\sigma_t = \sigma_t(T, S_0) - \sigma_t(T_0, S_0) \tag{5.1}$$

$$\Delta_S\sigma_t = \sigma_t(T_0, S) - \sigma_t(T_0, S_0) \tag{5.2}$$

where T and S are the transient temperature and salinity, and T_0 and S_0 are their initial values (year51-100 mean).

Fig.5.24 illustrates evolutions of the surface density changes $\Delta\sigma_t$, $\Delta_S\sigma_t$ and $\Delta_T\sigma_t$ over the three target regions for both the TGM3 and TGM2 runs.

For the North Atlantic region, it can be seen from Fig.5.24a that the SSD decrease is alternately dominated by the contributions of surface warming and surface freshening during the period of increasing CO_2. In TGM3, for example, the slight decrease of SSD in the first century is attributed to the freshening but thereafter the warming takes over until around year 350. Obviously the NADWF reduction shown in Fig.5.21a is the joint effect of surface warming and freshening, with the former making somewhat more contribution since the weakening of NADWF occurs mainly in the period when warming dominates. During the following century or so the surface freshening resumes the dominance but thereafter the warming overrides the freshening effect more and more for the rest of the run. In TGM2, the situation is much simpler: SSD is reduced nearly completely by the surface warming prior to CO_2 tripling, but, from around year 380, the freshening rapidly replaces the warming to become the more important factor to weaken the SSD. Generally speaking, surface warming is the main reason for the reduction of the North Atlantic overturning in

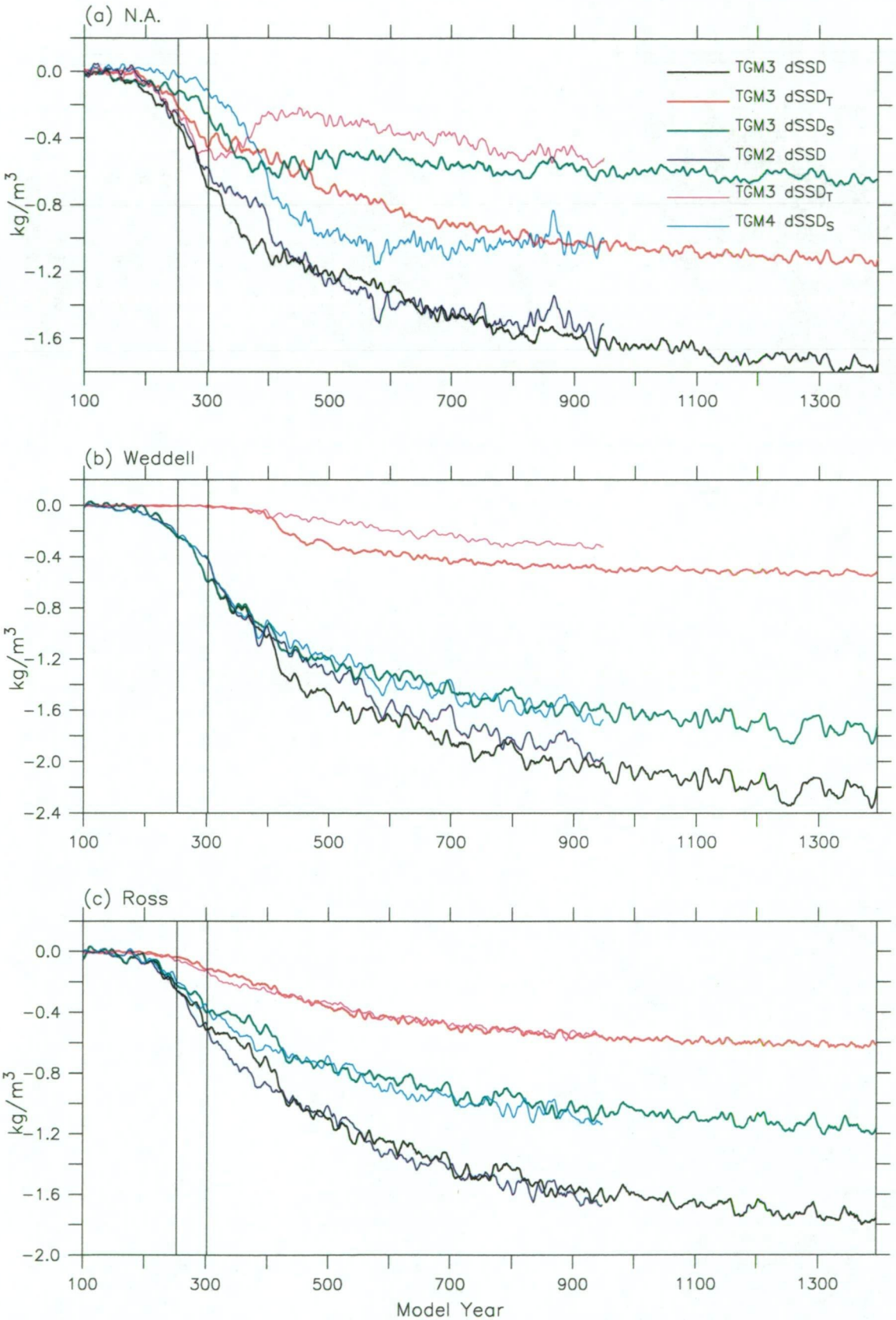

Figure 5.24: Time series for changes in annual mean SSD (σ_t) for TGM3 and TGM2 over the: (a) North Atlantic (50 – 65°N), (b) Weddell Sea (south of 60°S), and (c) Ross Sea (60°Spoleward). Also included are the SSD changes induced by SST change alone and by SSS change alone.

our experiments, in contrast to the finding of Manabe and Stouffer (1991, 1994), but confirming the result of Mikolajewicz and Voss (2000). In addition, when the deep levels are warmed enough to destabilize the water column stratification, the lasting surface warming is still the main factor resisting the recovery of NADWF in TGM3, but, in TGM2, it is the continual freshening from above that plays the main role.

In the high latitude Southern Ocean around Antarctica, however, surface freshening overwhelms the warming in reducing the SSD through the whole course of the integrations. Over the Weddell Sea, as shown in Fig.5.24b, the SSD anomaly $\Delta_T\sigma_t$ follows the SSS-induced change $\Delta_S\sigma_t$ closely until year 400, and thereafter the surface warming begins to contribute more or less in both runs. Similarly for the case of the Ross/Bellingshausen Seas in the period of increasing CO_2 but the SST changes begin to make a notable contribution much earlier, i.e., before CO_2 doubling, and this contribution gradually increases up to one third of the total SSD reduction from year 500. Comparing Fig.5.24b with 5.24c, we see a much larger reduction of SSD over the Weddell Sea than the Ross Sea by the end of the runs due to the much larger surface freshening (mainly from the runoff inflow), indicating that a much stronger stratification is established in the Weddell Sea (not shown) which is much harder to destabilize for a resumption of the downwelling there as will be shown later.

The evolution of annual mean SSD change shown above gives some indications of the reduction/shutdown of the world ocean THC. However, a more specific examination of the surface and subsurface density field is needed to establish the circumstances of the related processes. In this context, it is useful to examine the relationship between peak (wintertime) surface density attained in our target regions and the deeper ocean densities. As is recognized (Hirst 1999), a key feature of the deep water formation process is that the later winter SSD in at least some locations in the deep water formation regions substantially exceeds the general ambient density of the deep water.

Fig.5.28a–c show the maximum winter (Feb.–Apr. for the North Atlantic region and Aug.–Oct. for the Southern Ocean) surface density attained at any oceanic point of the target regions in each year, together with the annual and area mean densities at two deep levels over the same region for the TGM3 run. Note the deep levels are taken as the 710 m and 1130 m depths in the North Atlantic, and the 1130 m and 2125 m depths in the Southern Ocean, respectively, considering the depths where the maximum streamfunction values, i.e., the NADWF AABWF, are located. The density variable used here is σ_2, or potential density referred to 2000 db, as this is more relevant to deep overturning and convection than the surface-referenced density (σ_t)[3]. The contrast between the winter peak SSD and the interior ocean densities simply implies the largest possible instability of the water column which supports the overturning and the direct convection.

For the North Atlantic region, the winter peak SSD is initially larger than the ambient densities at the two deeper levels. Under CO_2 forcing, it gradually declines towards the average densities beneath and drops below the density at the 1130 m depth before CO_2 doubling because of the quicker warming and freshening at the surface than in the ocean interior, meaning a strengthening of the upper layer stratification, leading to a reduction of the overturning. By the time of a few decades after CO_2 tripling, this winter peak SSD 'rises' a little relative to the ocean interior densities (up to the value of the 1130 m depth), indicating that a 'rebound' may be occurring to the overturning. Note the winter peak SSD never falls below the density at the 710 m depth, indicating that the NADWF reduction is limited and the associated overturning can operate all the time in the upper layer. The deep convection shoals noticeably after CO_2 tripling but still reaches below 1000 m depth, as shown by Fig.5.25d.

In the Southern Ocean, however, due to the rapid freshening at the surface and the much slower deep ventilation and adjustment, the winter peak SSD near Antarctica

[3]A reference level at around 1000 db may be more relevant for our purpose here in the North Atlantic region, but calculation shows that, except for the different density values, no large difference is evident in the evolution trend or the contrast of the densities used here

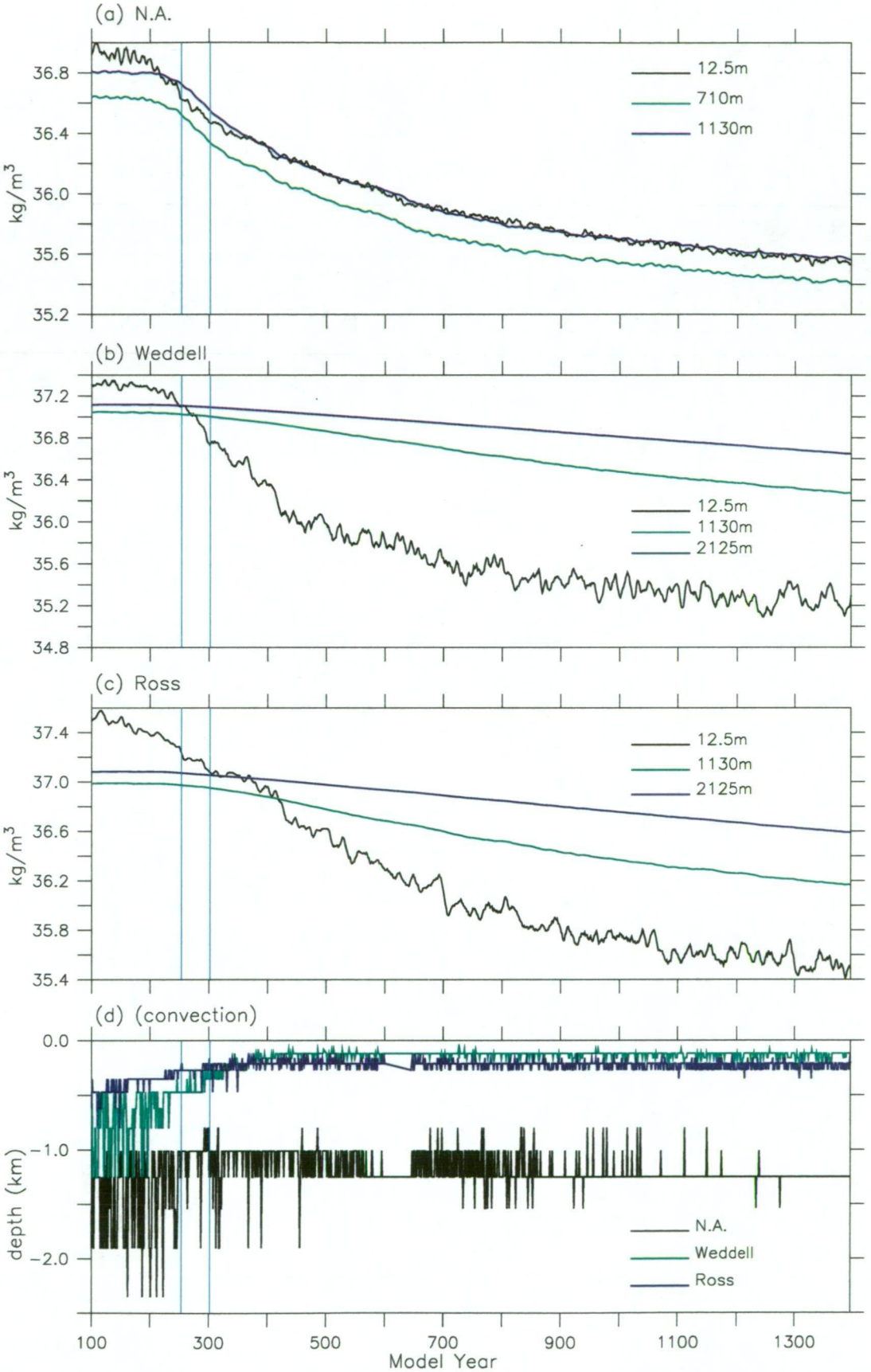

Figure 5.25: Changes of the winter peak SSD (σ_2) and densities at two deep levels in TGM3 over the: (a) North Atlantic (50 – 65°N), (b) Weddell Sea (south of 60°S), and (c) Ross Sea (60°S poleward). (d) shows the maximum convection depths in the course of the annual cycle for these three regions.

declines drastically and falls below the ambient densities at the two deeper levels before or soon after CO_2 tripling, and remains so through the rest of the integration, as similarly found by Hirst (1999). With the decline of surface densities to values well below those found at depth, and the stratification being continuously intensified, the density driven overturning and direct convection naturally shut down around Antarctica. Comparison between Fig.5.25b and 5.25c shows that the Weddell Sea winter peak SSD is initially much closer to the ambient interior densities than that of the Ross Sea. Such a small density contrast (largest instability) is relatively easier to be demolished and reversed by a small perturbation of freshening at the surface. Consequently, the overturning is much more sensitive to the surface freshening and thus collapses very quickly in the Weddell Sea, as discussed above. Fig.5.25d shows that the deepest convection in the Weddell Sea is reduced largely from the second century of CO_2 forcing and, after CO_2 doubling, there is no deep convection reaching below 500 m depth in the oceans south of 60°S around Antarctica.

The same analysis for the TGM2 run reveals generally similar trends of the winter peak SSD and the ambient interior densities (not shown). A significant difference worth mentioning is found in the North Atlantic where the winter peak SSD in TGM2 is reduced more than that in TGM3. It declines to a level of the density at the 710 m depth by the time of CO_2 doubling and stays close to this level until around year 650 and then shows a 'rise' relative to the densities at deeper levels, but with remarkably larger fluctuation, clearly indicating a larger reduction and a slower recovery of the NADWF in the TGM2 integration. In addition, the decline of the Southern Ocean winter peak SSD is slower, supporting a longer persistence of the AABWF in TGM2.

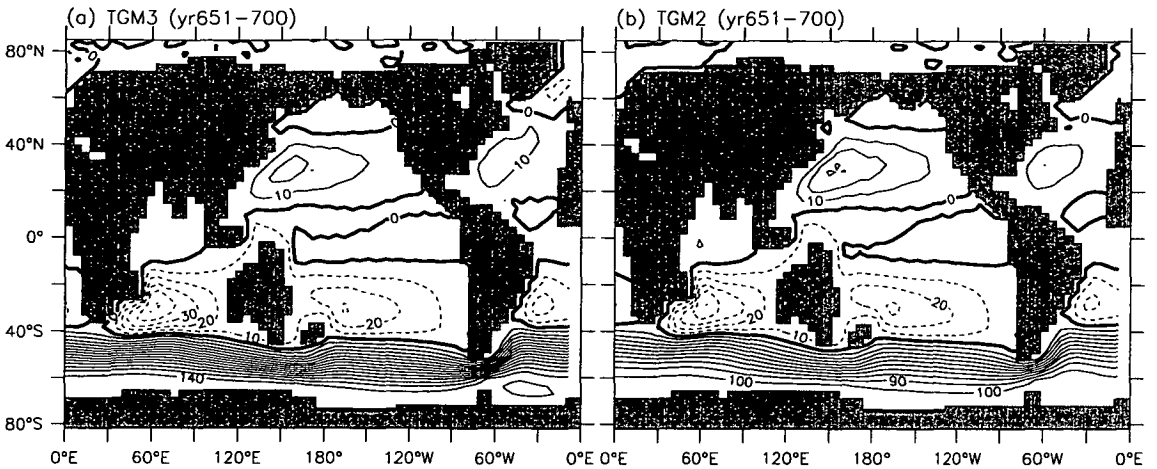

Figure 5.26: Barotropic streamfunction for year651-700 mean. Contour interval is 10 Sv.

5.6 Barotropic Flow–Changes in the World Ocean Major Currents

Under CO_2 forcing, the oceanic barotropic flow undergoes noticeable variations, accompanying the changes of surface windstresses, the THC and the world ocean water mass properties.

Fig.5.26 shows a snapshot of the annual mean barotropic streamfunctions in TGM3 and TGM2 averaged over period of yr651-700. Although the basic flow pattern is well maintained in terms of all the major gyres, the intensities of these gyres are changed to different extents, as can be seen from the comparison with their respective control climates shown in Fig.4.15. What is in common for these two runs is the weakening of all the anticyclonic subtropical gyres, i.e., the western boundary currents, especially the Gulf Stream, but a significant difference of the ACC change is also found between the two runs, i.e., a substantial intensification occurs in TGM3 while a much smaller change occurs in TGM2.

Fig.5.27 reveals the temporal evolution of the maximum barotropic flow streamfunction values for the ACC transport through Drake Passage, the Gulf Stream and the Kuroshio Current. It is evident that, in TGM3, the ACC transport increases steadily during the first three centuries of CO_2 forcing and reaches a maximum of

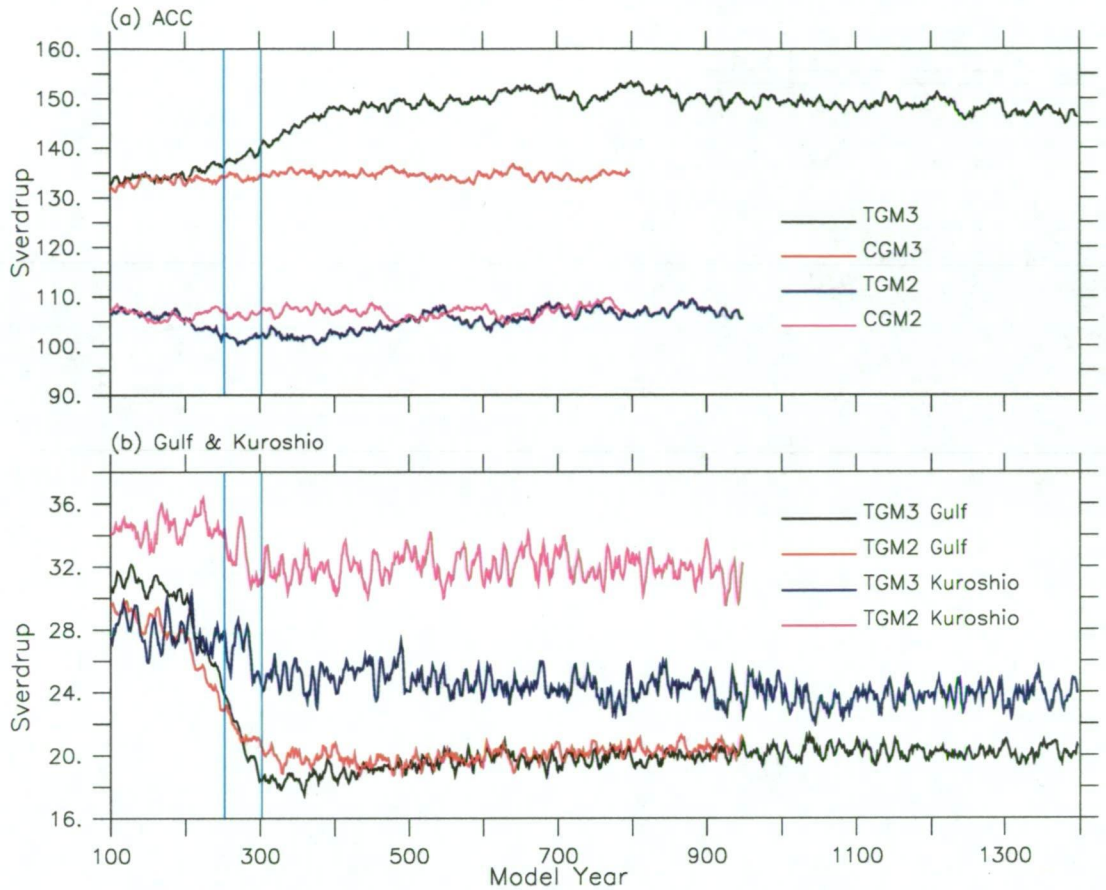

Figure 5.27: Time series for the western boundary flows and ACC transports: (a) ACC transport, (b) Gulf Stream and Kuroshio Current.

about 153 Sv by around year 700, about 14% larger than the initial flow intensity, i.e., 134 Sv for the 100th year. From year 800 the TGM3 ACC flow ramps down slowly but by the end of the run it is still considerably stronger than its control status. In contrast, TGM2 sees a general decline in the ACC transport during the period of increasing CO_2 and the maximum reduction (less than 7%) is reached before CO_2 tripling. Thereafter the ACC flow shows a general gradual recovery, reaches a maximum slightly higher than its initial intensity by year 540, then settles around a level of the initial magnitude. For the Gulf Stream, TGM3 sees a reduction up to 47% while TGM2 experiences a weakening of about 40% by the time soon after CO_2 tripling and henceafter changes little, especially in the case of the TGM2 run. With much larger fluctuation, the Kuroshio Current changes relatively little under CO_2 forcing in both runs. The Agulhas Current (not shown) experiences some weakening and the final change is about 14%, with most reduction occurring

in the period of increasing CO_2. As for the Indonesian throughflow (not shown), which plays an important role in water mass and heat exchange between the tropical Pacific Ocean and Indian Ocean, it steadily weakens in both runs. For TGM3, it ramps down from around 18 Sv to 13 Sv or so within the first three centuries of CO_2 forcing and then is maintained at that level throughout the rest of the run. In TGM2, despite a slightly smaller initial value of about 17.1 Sv and a slower change in the first 100 years, from the second century this flow is subject to a rate of decrease similar to that seen in TGM3, and the two runs have a very close 'final' state for the Indonesian throughflow.

In Chapter 3 we have already seen that the North Atlantic region is subject to easterly trades in the tropics to subtropics and westerlies at higher latitudes (see Fig.3.16a). It is this shear of windstress that primarily drives the Gulf Stream by providing negative vorticity to the surface layer of the water body in the basin. The North Atlantic overturning, apart from the surface windstress, also plays an important role in driving the Gulf Stream. Under CO_2 forcing, substantial changes occur in both the wind field and the overturning circulation, which jointly cause the reduction of the Gulf Stream transport. Taking the TGM3 run as the example, the NADWF is reduced and its downward penetration shoals greatly, and, in the meantime, both the low latitude easterly trades and the mid latitude westerlies and thus the shear of windstress mentioned above is reduced (see Fig.5.9a), due to the warming-caused changes of the surface pressure field (not shown). These changes naturally diminish the Gulf Stream. Following the stabilization of CO_2, however, the Gulf Stream shows a weak but steady tendency to recover, obviously resulting from the gradual recovery of NADWF. For the TGM2 run, the NADWF is reduced to a much larger extent and shows much slower recovery, and the Gulf Stream thus shows nearly no tendency of returning. Similar changes of shear of the wind occur in the North Pacific and the South Indian Ocean, leading to the reduction of transports of the Kuroshio Current and the Agulhas Current in both runs.

5.7 Changes of the ACC Transport

The above shown striking difference of ACC behaviour between TGM3 and TGM2 (Fig.5.27a) under CO_2 forcing indicates a complicated mechanism responsible for setting and adjusting the ACC flow. This merits our further exploration.

5.7.1 Factors Controlling the ACC

As we have already discussed in Chapter 4, the ACC is driven by the westerly winds and the "bottom form stress" (Cai and Bains 1996), which are balanced by bottom and lateral frictional drag. Recently, Gent et al. (2001) analyzed a hierarchy of coarse resolution ocean model experiments using the ocean component of the NCAR CSM with a variety of surface forcings to address the question of what sets the mean transport through Drake Passage. Following Olbers (1998), they examined the zonally averaged zonal momentum balance of the ACC for three different depth regions in their coarse resolution ocean model which is basically similar to our ocean model. The three depth regions are the Ekman (0–150 m), intermediate (150–2000 m) and deep (below 2000 m) layers. They showed that the dominant balance in the Ekman layer is between the westward Coriolis force (due to the northward Ekman drift) and the vertical divergence of the frictional stress (resulting from the surface windstress), while the balance in the intermediate layer is the lateral Reynolds stress divergence and the eastward Coriolis force (due to a small residual southward flow), and the deep layer is subject to a balance between the eastward Coriolis force (resulting from an overall strong meridional flow to the south) and the topography-related pressure term.

It can be understood that stronger westerly wind over the ACC leads to larger northward Ekman transport and the return southward transport below the Ekman layer is thus expected to be stronger. Similarly, stronger overturning circulation off Antarctica causes stronger northward outflow of the AABW, leading to stronger return southward transport in the overlying intermediate layer as well. An

enhanced southward flow in the intermediate layer must be balanced by a larger lateral Reynolds stress divergence, which is provided by a stronger zonal velocity (i.e. the lateral Reynolds stress divergence is roughly proportional to the velocity), thereby increasing the ACC transport. Gent et al. (2001) concluded that, with fixed model formulation and physical parameter values, the ACC transport through Drake Passage is determined by two external forcing factors: the strength of the meridional Ekman transport at the latitude of Drake Passage and the strength of the thermohaline circulation off the Antarctic shelf. In addition, they suggest that the meridional Ekman transport drives about 100 Sv of Drake Passage transport while the Southern Ocean overturning drives the remaining flow of about 30 Sv in their model based on an estimate that an increase in the AABWF of 1 Sv produces about 7 Sv increase in Drake Passage transport.

We have also found that different zonal windstress over the ACC does result in ACC transports of different magnitudes. In Chapter 3 we described an ocean spinup experiment CW3 which is identical to the GM3 spinup except for its use of the CSIRO AGCM wind forcing. It is noted that CW3 yields an ACC transport less than 110 Sv, in contrast to 127 SV for GM3 which is forced by a stronger windstress (i.e., the NCEP winds, see Fig.A.2 for comparison between these two winds), indicating that increased westerly forcing over the ACC latitude band enhances the ACC transport in our ocean-alone model. However, this direct dependence of the ACC transport on zonal wind seems not so clear in the coupled model. In the control runs CGM3 and CGM2, for example, within (and only within) the first century following coupling the ACC flow is intensified by about 7 Sv and 8 Sv (see Chapter 4), respectively, whereas the zonal wind shows no evident drift at all. We attributed this drift to the intensification of the AABWF off Antarctica. Similarly, Bryan (1998) attributed the large drift of the ACC in the NCAR CSM (see also Chapter 4) to the disturbance to the ocean freshwater balance associated with the introduction of unreasonably large meridional transports of sea ice by the ice model, rather than the windstress change. He carried out several short experiments with the ocean-alone model and ocean-sea ice coupled model using different atmospheric forcing to discriminate the

effects of windstress and ice transport on the ACC. He found that, with the absence of sea ice, an increase of zonal wind does not accelerate the ACC directly, unless an ice model is included and thus providing a northward ice transport off Antarctica. Note this is in sharp contrast with the results of our ocean spinups mentioned above, bringing some ambiguity into our understanding of the relationship between wind forcing and the ACC transport.

5.7.2 Windstress over the ACC and Overturning off Antarctica

Nevertheless, in our exploration of the ACC change under CO_2 forcing, a first thought is that the change of zonal wind over the ACC induced by the uneven meridional distribution of surface warming as mentioned above may be an important factor in accelerating or slowing down the ACC flow. Fig.5.28a shows the time series of zonal windstress averaged over the ACC around the globe for TGM3 and TGM2. In response to the zonal wind changes, Ekman drift towards the north in the upper layer changes following the wind variation very closely (not shown). We see an evident increase of the eastward surface driving force for the ACC in both runs during the period of increasing CO_2. After CO_2 stabilization, this force drops steadily throughout the rest of the runs, despite large fluctuations. Such a variation obviously deviates from the change of ACC transport shown in Fig.5.27a, except for the TGM3 run which shows an accordant increase of ACC flow in the first 2 centuries. It appears that the change of zonal wind does not necessarily cause a synchronous response of the ACC transport in our model under global warming condition. This may be somewhat unexpected but is not so surprising in light of the above discussion.

Thus a second natural thought is that the change of Southern Ocean overturning and the associated northward outflow of the AABW may be responsible for the change of the ACC transport. However, this seems not to be very indicative because the AABWF is shown (in Fig.5.21b) to decrease rapidly and collapses nearly completely

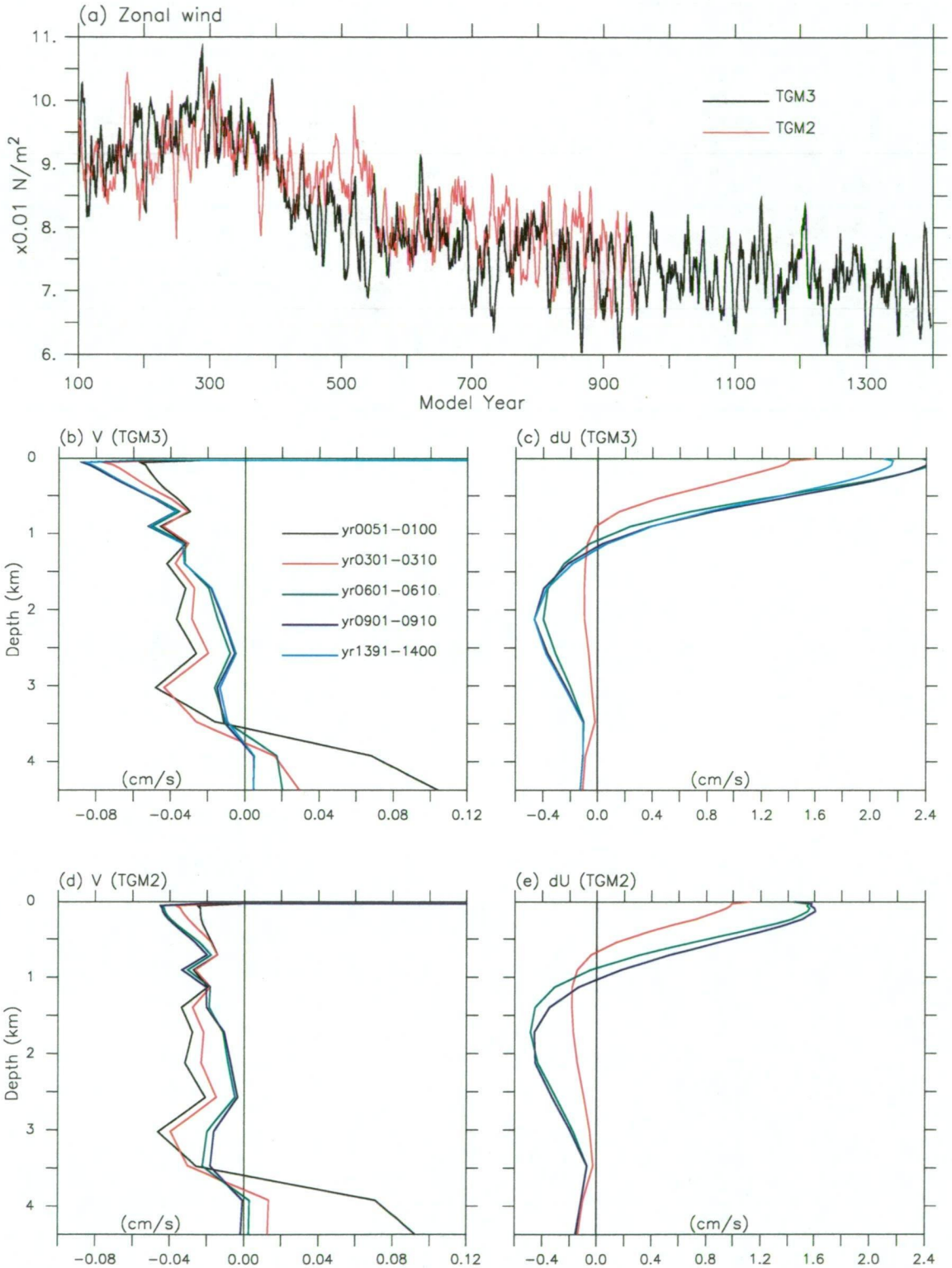

Figure 5.28: Average zonal wind and vertical structure of horizontal velocities in the ACC zone (around 51 – 63.7°S).

before or soon after CO_2 tripling in both runs, and the AABW northward outflow weakens accordingly (Fig.5.21c). Only the TGM2 run sees a qualitative agreement between the changes of the AABWF and the ACC transport in the period before year 170 or so when both of these quantities show a trend of decrease.

Examination of the velocity structure around the ACC region and/or its change in the course of the integrations sheds some light on the relationship between the meridional and zonal motions, and thus reveals the effects of changes in zonal windstress and the AABWF on the ACC transport. Fig.5.28b and 5.28c illustrate the vertical profiles of the meridional velocity and the change of zonal velocity, respectively, averaged around the ACC band for several epochs from the TGM3 run. Note the Ekman drift velocity, which varies between 2.5 and 5.2 cm s^{-1}, is truncated in 5.28b for economy. While the surface layer northward Ekman drift is intensified during the first 200 years with increasing CO_2, the underlying subsurface layer (above 800 m) sees a strengthened southward return flow. This enhancement of the southward transport may be partly attributable to the strengthening of surface zonal windstress because an increased northward flow in the surface layer must be compensated by a stronger southward transport beneath. However, the strengthening of this southward transport continues and develops downwards after CO_2 tripling while the zonal wind weakens considerably, indicating that there must be some other factors responsible for the subsurface layer meridional velocity change. In response to the strengthening of the southward flow, the eastward transport increases substantially in this layer due to the increased driving force, i.e., the Coriolis force. Of course, in the near surface layer, the zonal wind acts directly as a driving force and enhances the zonal flow in the period of increasing CO_2, but its effect seems to be secondary because the zonal flow continues to increase while the wind force drops after CO_2 tripling. At other depths, we see evident, continuing weakening of the northward outflow of AABW below 3250 m due to the shutoff of AABWF, which leads to a substantial reduction in the southward return flow in the overlying layer between 1100 m and 3250 m. Accordingly, the reduced Coriolis force is balanced by a weaker Reynolds stress drag, requiring a slower zonal flow in this layer.

For the case of the TGM2 run shown in Fig.5.28d and 5.28e, we see changes in meridional and zonal velocities at all depths qualitatively similar to that in TGM3 discussed above. However, quantitative differences are evident at upper and mid depths between these two runs. In the layer above 1250 m depth, southward flow through the ACC 'wall' is clearly stronger and is enhanced to greater extent in TGM3 than in TGM2, resulting in a much larger increase in the zonal flow. At the same time, the mid depths, from 800 m to 2000 m, for example, see a smaller decrease in the southward flow and thus a smaller reduction in the zonal flow in TGM3 than in TGM2. Such a contrast between the two runs is especially clear for the snapshot at the time of CO_2 tripling indicated by epoch yr301-310. In TGM3, a large increase of zonal velocity in the upper layer overrides the small reduction below, resulting in an enhanced integrated ACC transport, but the reverse is the case for TGM2. This indicates the different behaviours of the ACC transport in the first few centuries between the two runs, namely, the ACC keeps increasing in TGM3 but ramps down in TGM2. It is clear that the overturning off Antarctica plays a central role in causing such a difference, at least for that in the subsurface to mid-depth water where the reduction of southward flow across the ACC is larger in TGM2. As per Gent et al. (2001), the contribution of the AABWF to the ACC transport is proportional to the AABWF intensity. We note that the initial AABWF in TGM2 is about 14 Sv, more than twice that in TGM3 (see Fig.5.21b), indicating that the AABWF is much more important to the ACC transport in TGM2 than in TGM3. Therefore, it is easy to understand that the collapse of AABWF under CO_2 forcing has a much larger impact on the ACC transport in TGM2. Such an impact is reflected by the larger reductions of the southward velocities and (then) the eastward flow in the layer below around 800 m depth.

5.7.3 Thermohaline Structure Across the ACC

So far, we have examined the two 'external' forcing factors, i.e., zonal windstress and the overturning off Antarctica, which are believed to set the ACC transport,

and have only found some limited explanation for the changes of ACC flow in the two runs. What is responsible for the major change (i.e., the change in the upper layer) remains unknown. Is it possible that, under global warming conditions, the ocean interior change, especially the change in the thermohaline structure, plays a key role in resetting the ACC transport? That the southward flow in the upper layer increases despite the reduction of zonal wind after CO_2 stabilization is the clue to what happens in the water mass properties which exerts influences on the meridional momentum balance such that the circulation flow velocity is changed accordingly. That is, there must be a change in the meridional pressure gradient occurring in the course of the runs. As we know, the ACC flow, to a first order approximation, is a geostrophic flow which, once established by a zonal momentum balance, is maintained by a meridional momentum balance between the Coriolis force pointing to the north and pressure gradient force to the south, i.e., $fu = -\frac{1}{\rho}\frac{\partial p}{\partial y}$. The pressure force is deduced by the implied sea surface slope, or say the meridional variation of the dynamic height (down to the Antarctic coast), which is determined by the meridional distribution of density. It can be understood that any disturbance to the meridional density contrast across the ACC will naturally cause a geostrophic deviation, which acts to adjust the flow and force terms involved until a new balance is reached again. This process is known as the geostrophic adjustment. Under the global warming condition, as we have already shown, the global ocean interior undergoes lasting and uneven changes in water properties, especially in regions sensitive to surface thermohaline perturbations. These changes in the ACC region upset the geostrophic balance and lead to a continuing adjustment and development of the ACC flow as long as the anomaly forcing is maintained.

To reveal the association between changes of the ACC transport and the thermohaline structure, we present in Fig.5.29a time series of the difference between oceanic density zonally averaged around the ACC band and over 0-2350 m depth at 65.3°S and that at 52.6°S for both transient integrations, together with that from their control runs. 5.29b–e show the meridional cross section of the density change south of 35°S for two snapshots (yr301-310 and yr901-910) in the two runs, giving an

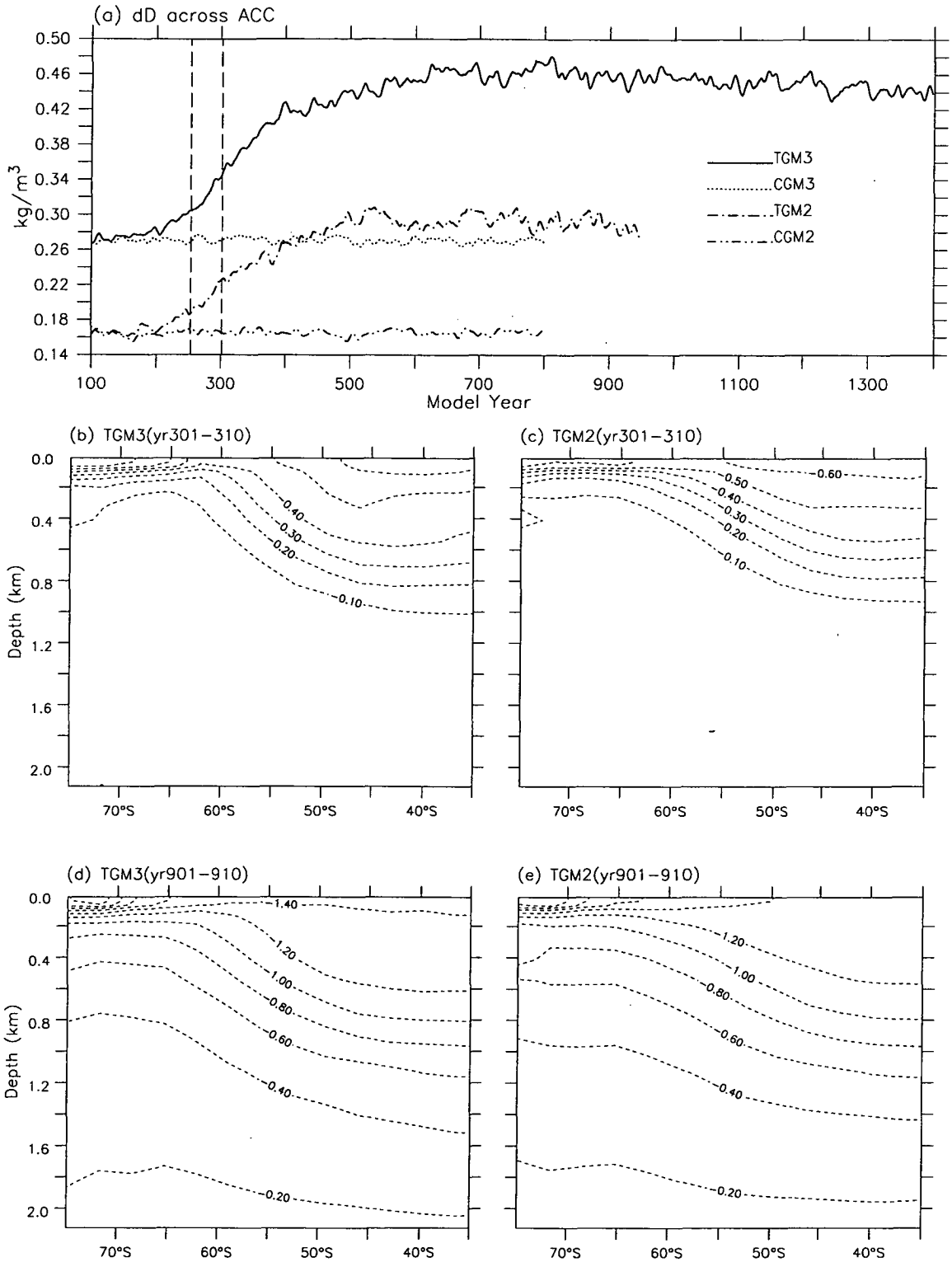

Figure 5.29: (a) Time series of meridional density (σ_t) contrast across ACC, averaged over 0–2250 m layer around globe, (b)–(e) zonal mean density changes (kg m^{-3}) for periods yr301–310 and yr901–910 in the Southern Ocean.

indication to the continuous tilting of isopycnals down to the north, namely, the isobars sloping down to the south across the ACC. For TGM3, the meridional density contrast across the ACC, i.e., the dynamic height difference between the north and south sides of the ACC, increases substantially in the first three centuries under CO_2 forcing, and continues to increase until year 700 when a maximum is reached. Thereafter it ramps down very slowly, with considerable fluctuation. Comparing this evolution with that for the ACC transport shown in Fig.5.27a, we find a strikingly strong resemblance. In fact, when these two variables are detrended, correlation between them is as large as 0.574 for a reconstructed 1200 year period. This is no doubt a highly significant correlation although the number of 'effective' degrees of freedom would be much less than 1200 because of the persistence and autocorrelation in the time series. We note that, in the control run CGM3, these two quantities show nearly no long term trend from year 101 to 800, and their correlation coefficient for this period is over 0.37. The much closer relationship between these two variables in the transient integration than in the control run seems to indicate that CO_2 induced change in the ocean interior thermohaline structure plays a critical role in resetting the ACC flow. Similarly, TGM2 gives a correlation between the ACC transport and the density contrast of 0.502 for a detrended and reconstructed period of 850 years and the last 700 years of CGM2 shows a value of 0.48 for this correlation.

The continuous strengthening of the upper layer southward flow across the ACC after CO_2 stabilization, shown in Fig.5.28b and 5.28d for TGM3 and TGM2, respectively, is apparently attributable to the continuous increase in the north-south pressure force induced by the density change in the subsurface layer rather than due to the change of Ekman drift associated with the surface windstress. Fig.5.29a indicates that, by around year 700, the zonal and vertical mean meridional density contrast across the ACC over the upper layer (0–2250 m) is enhanced by about 0.20 $kg\,m^{-3}$ in TGM3, whereas such a enhancement is only 0.12 $kg\,m^{-3}$ in TGM2. The larger increase of the density contrast leads to larger steric (pressure surface) height differences across the ACC in this layer and thus results in a larger zonal

geostrophic transport for TGM3 than TGM2. The associated increase in lateral Reynolds stresses then facilitate a stronger southward flow in TGM3. We note that, as the density change to the north of the ACC deepens, the strengthening of the upper layer zonal (geostrophic) flow develops downwards, and so does the enhancement of southward flow. This is the case for both runs. Consequently, in TGM3 the ACC transport increases steadily (until year 700) and in TGM2 it begins to increase after the surface layer strengthening starts overriding the mid-depth layer weakening.

Regarding the question as to what causes the change of the meridional density contrast across the ACC and why TGM3 is subject to a larger change than TGM2, it may be readily explained by changes in the surface thermohaline conditions, the global THC and the wind forcing. At the south side of our target region, i.e., the ACC latitude band, we have shown that the deep convection and overturning off Antarctica is largely suppressed or completely shut down rapidly due to CO_2 induced surface freshening, which decouples the ocean interior and the surface layer, leading to relatively small changes of temperature and salinity in the ocean interior. To the north of the ACC, however, convection and wind-driven subduction is little changed (see, e.g., Fig.5.18) and thus still effective in transporting the surface thermal anomaly (warming) into the subsurface layer, resulting in relatively large warming and therefore less dense water mass in the ocean interior there. Further, the world ocean THC conveyor belt, although weakened due to the large reduction of NADWF, can still transport heat southward to this latitude (see also Fig.5.18), warming the interior water north of the ACC. It is the difference of the conveyor belt transport reaching the north side of the ACC between the two runs that is the main factor responsible for the reduction of density being larger in TGM3 than in TGM2 there. This is evident in Fig.5.18 which shows that the conveyor belt is much stronger in TGM3 all the time.

In conclusion, we attribute the changes of ACC transport under global warming forcing to both the change of meridional density structure in the ocean interior, especially the upper layer (from the surface to 1000–2000 m depth), and the change

of overturning off Antarctica. The enhancement of north-south density contrast largely increases the upper layer zonal flow whilst the shutoff of AABWF depresses the deeper zonal flow significantly. TGM3 shows a steady increase of the ACC transport in the course of the first half of the run because the upper intensification overwhelms the deeper reduction. In contrast, TGM2 suffers some decrease in the ACC transport during the period of increasing CO_2 because the collapse of overturning off Antarctica decelerates the subsurface to mid-depth zonal flow to a degree too large to be compensated by the upper layer acceleration. In an environment with largely changed thermohaline circulations and ocean interior climate, the change of zonal windstress over the ACC region has only a minor effect on the ACC transport.

5.8 Global Ocean Horizontal Currents

Fig.5.30 shows a snapshot (decadal mean centered on year 900) of the changes of global ocean horizontal currents at six selected levels in TGM3. All the changes of thermohaline circulation, barotropic flow and the surface windstress discussed above are at least partly reflected in these pictures. We note that some changes occurring at the early stage of CO_2 forcing is different from what is shown here, and this snapshot may be thought of as the long term or quasi-equilibrium response, especially for the upper levels above 2125 m depth.

For the change of surface horizontal currents shown in Fig.5.30a, the most evident feature is the strong convergence occurring in the equatorial Pacific Ocean, which means a suppression of the upwelling in this region and it is associated with the weakening of the poleward Ekman drift caused by the reduction of Trade Wind forcing. Such a change is also found in the tropical Atlantic Ocean due to the same reason. However, the case of the Indian Ocean is different where we see considerable strengthening in the westward flow along the equator and a divergence (upwelling) which is absent in the control climate. In NH, the strengthening of the Arctic surface water outflow through the Greenland-Norwegian Basin into the northern

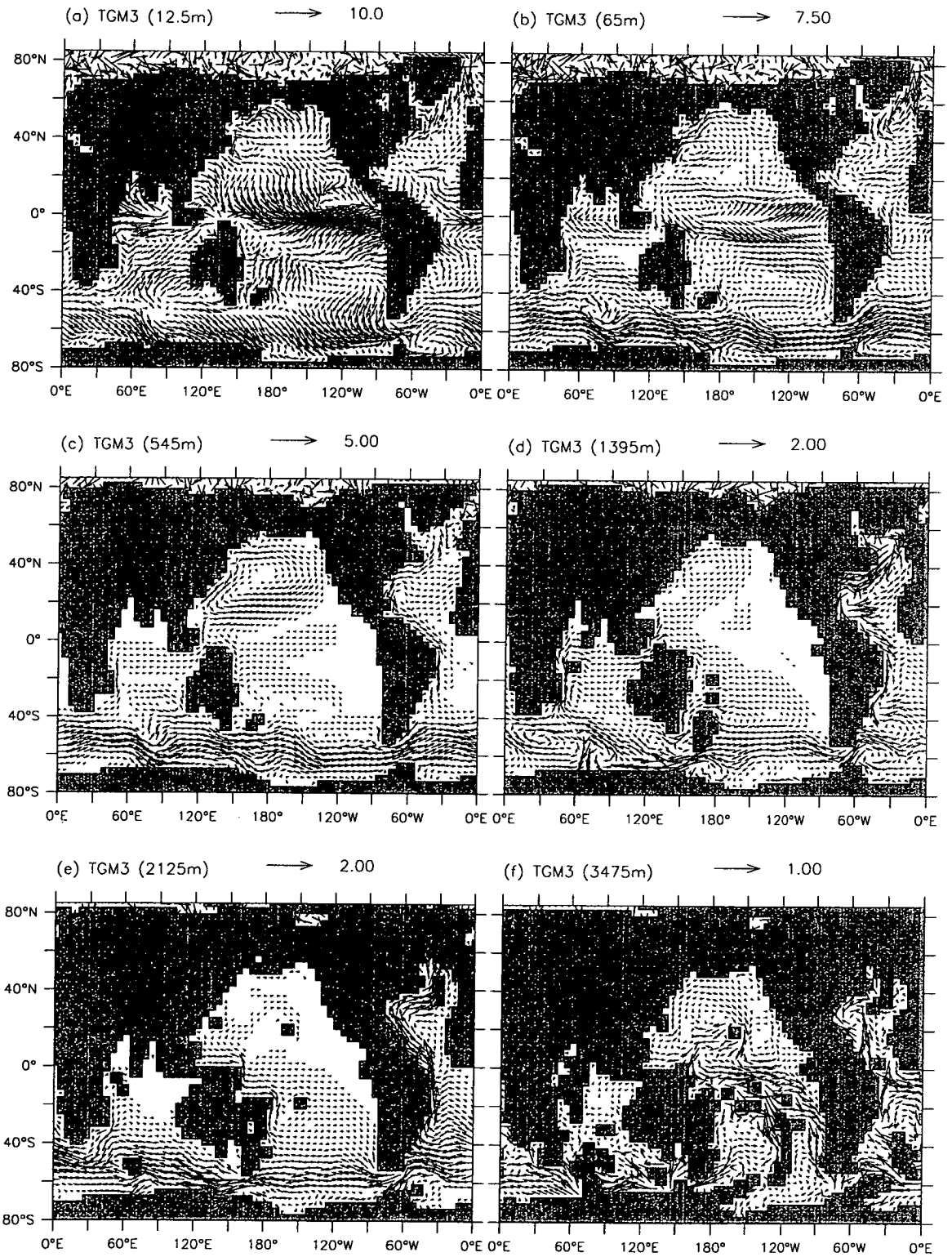

Figure 5.30: Changes of horizontal currents ($cm\,s^{-1}$) at six levels for period yr896–905 in TGM3: (a) 12.5 m, (b) 65 m, (c) 545 m, (d) 1395 m, (e) 2125 m, and (f) 3475 m.

North Atlantic is evident. This extra flow brings more cold water southward and plays an important role in delaying the warming in the region off southeastern Greenland as discussed in section 5.2. All the western boundary currents associated with the wind-driven subtropical gyres undergo noticeable weakening in the surface layer. In SH, the most remarkable change occurs in the ACC zone where the surface flow is largely intensified, as shown in Fig.5.28c. However, the northward Ekman drift in the high latitude Southern Ocean is clearly reduced due to the diminution of the easterly wind forcing (see Fig.5.28a). Note that Ekman drift over the southern high latitudes is strengthened in the first 300 years of CO_2 forcing when the zonal wind is stronger. The Indonesian throughflow in the surface layer is strengthened, due mainly to the wind change.

At the near surface depth shown in Fig.5.30b, major changes occur in the ACC zone, tropical Pacific and the Arctic outflow region (i.e., Greenland-Norwegian Basin). As we have already seen in Fig.5.28c, the ACC flow is significantly strengthened in the upper layer, especially near the surface, due mainly to the change of meridional density structure across the ACC. A wide divergence zone in the equatorial Pacific region shown in this figure indicates that the initial (compensating) convergence towards the equator at this level is largely reduced due to the weakening of upwelling in the surface layer shown in Fig.5.30a. Also evident is the weakening of the Pacific subtropical gyres. At the subsurface level of 545 m depth, the changes in the Kuroshio Current, the Gulf Stream and the ACC flow are even more evident due to the disappearance of the 'chaotic' influence of the surface wind. We see a strong anticlockwise gyre induced by CO_2 forcing in the subtropical and mid-latitude Pacific Ocean, which largely cancels the initial clockwise circulation (shown in Fig.3.14c) and reduces the intensity of the Kuroshio Current. A clear reverse current is also found in the Gulf Stream at this level, indicating that the return flow of the Atlantic Ocean conveyor belt associated with the NADWF is weakened. The ACC is strengthened at this level due to the change of meridional density gradient discussed above. The Indonesian throughflow current begins to slow down from this level and gradually reverses, i.e., flows from the Indian Ocean into the Pacific Ocean near the

bottom, which is evident at the 1395 m level shown in Fig.5.30d (see Fig.3.14d for reference). Such changes in the deeper levels are responsible for the reduction of the integrated throughflow and are believed to be associated with the CO_2 induced difference of deep ocean thermal state between the two basins near the equator.

At the two mid-depth levels, however, we see different changes in the Atlantic western boundary currents, including the Gulf Stream. Namely, the southward NADWF outflow is intensified markedly at the 1395 m depth but is nearly stopped at the 2125 m depth (see Fig.3.14e for comparison). As is shown in Fig.5.19a–e, the North Atlantic overturning does not penetrate down into the deep ocean below 2000 m after CO_2 stabilization, and thus there is no more outflow of the NADW at the deep levels. Note that the NADWF intensity is recovered up to more than 15 Sv by year 900 but its penetration is still limited above the 2000 m depth, naturally resulting in an enhancement of the outflow at the 1395 m level as a compensation. For the ACC, these two levels see similar changes, i.e., remarkable weakening, due to the reduction in the southward flow induced by the shutoff of the AABWF, as already discussed. At the abyssal depths, the horizontal circulations become very weak due to the closedown of the deep ocean ventilation. Fig.5.30f shows a change pattern at the 3475 m level that is generally the reverse of currents shown in Fig.3.14f, indicating a nearly stagnant state of the bottom ocean.

In the TGM2 run, all the above changes of the horizontal currents occurring in TGM3 are also evident except for the Atlantic western boundary currents at the 1395 m depth where, due to the much larger reduction and slower recovery of the NADWF, the outflow of NADW shows no strengthening in TGM2 by the end of the run. In addition, the Arctic surface water outflow is strengthened noticeably more than that in TGM3, and is partly responsible for the stronger and longer-lasted cooling in the high latitude North Atlantic ocean surface for TGM2, as discussed in section 5.2.

Chapter 6

Ocean Equilibrium under $3\times CO_2$ Conditions

We have seen that, after 1100 years' integration under $3\times CO_2$ stabilization forcing, the ocean interior, especially the deep ocean is still far from a final equilibrium solution in terms of the thermal structure. However, the deep ocean warming rate gradually catches up and finally exceeds that of the overlying layers in the last few hundred years. This evolving trend of temperature raises the speculation that the continuation of this long-term warming of the ocean interior may eventually reactivate the Southern Ocean overturning (after thousands of years), when the water column, which is largely stabilized at the early stage of global warming forcing, is destabilized to such a degree that an environment favouring the operation of deep convection and overturning off Antarctica in particular, is re-established.

To verify this possibility, normally an extension to the TGM3 run of at least several thousand years is needed. Wu and Budd (2001) performed a similar long-term $3\times CO_2$ stabilization run towards equilibrium using an earlier version of the CSIRO coupled model and found only very limited recovery of the AABWF after integrating for over 2500 years. By examining the warming rate of the ocean interior near the end of the run, they estimated that it needs more than 3000 years for the bottom ocean temperature change to catch up with that in the surface layer. Therefore, as

can be understood, some even longer time is required for the entire ocean to further adjust and reach an 'expected' equilibrium. Obviously, such a normal approach of straightforward continued time-integration would be too lengthy to be feasible for a PhD program duration in particular. Therefore we need to seek a 'shortcut' to reach this objective, namely, to bring the system to its 'final' state, hopefully a stable equilibrium. For this purpose, we conduct an additional integration which, under stabilized 3×CO_2 forcing, employs the Bryan (1984) technique in the ocean component to accelerate the convergence of deep ocean to equilibrium. After this acceleration, the integration is continued in the normal mode (with the acceleration switched off) for a period of a few hundred years to examine the stability of the accelerated solution. This integration is referred to as ATGM3 and is described in detail below.

6.1 Accelerating the Deep Ocean Convergence

The Bryan (1984) method is based on modifying the time scales of the ocean system to reduce the bandwidth of natural frequencies of the model by distorting the physics. The distortion of physics involves decreasing speed of gravity waves and Rossby waves to eliminate the very high frequencies and, at the same time, shrinking the local time scale of the deep sea relative to the upper ocean to reduce the very long time scales. It '*may also be interpreted as decreasing the local heat and salt capacity of the deep ocean without altering the advective or diffusive fluxes of these quantities. Since only local derivatives with respect to time are changed, equilibrium solutions with distorted physics should correspond exactly to equilibriums for the prototype model*' (Bryan 1984). As this approach enlarges the time step of the lower ocean so that, in effect, the deep ocean runs equivalently longer than the upper ocean, it has been widely used in ocean climate studies as an efficient strategy for ocean model spinup. It is also used in coupled models to achieve an equilibrium climate for climate change studies (e.g., Bryan 1982).

Following Bryan (1984), ATGM3 implements the above technique by using depth-dependent time steps for the ocean sub-model. All the accelerating scales are listed in the last column of Table 2.1, ranging from 1.0 for the 8 upper layers (above 360 m) to 27.4 for the deepest layer (level 21, 4375 m). ATGM3 is initialized with the TGM3 solution at the end of model year 700 (i.e., about 400 years after CO_2 tripling). The accelerated integration lasts for 400 years (referenced to the upper ocean and the other submodels with normal time step, referred to as 'surface years'), implying nearly 11000 years 'effective' integration for the deepest level with intermediate varying times for other deep levels. Thereafter, the integration is continued but in a synchronous mode (as for TGM3) for 500 years such that the system has enough time to overcome the impact of physics distortion. This is also aimed at examining whether or not the world ocean can finally settle down to a 'normal', stable equilibrium after a further adjustment. In summary, ATGM3 starts from year 700, running in accelerating mode for 400 surface years, and then is switched into normal integration from year 1100, lasting until year 1600. It is subject to a constant 3×CO_2 level throughout. The reason why we start the ATGM3 integration from the middle of TGM3 instead of following TGM3 from the end of the run (year 1400) is that, by doing so, we have an 'overlapping' period which can be used for comparison as a way to assess the effect of acceleration.

Although the acceleration of deep ocean convergence is known to work at the price of distorting the physics en route, as per the argument of Bryan (1984) (also see above), the warming transport processes should be maintained to be approximately realistic as that of the normal run through the course of the integration. This seems to be true for the ATGM3 run as the deep ocean warming rate is comparable for the overlapping period between TGM3 and ATGM3. For example, at the deepest level TGM3 shows a global mean warming of about 1.3 °C from year 700 to 1400 whilst ATGM3 gives a warming of 1.1 °C in an equivalent period (from year 700 to 726); at the 1720 m depth where the accelerating factor is 12.9, ATGM3 estimates a warming of 1.9 °C from year 700 to 755, very close to the TGM3 warming of 1.8 °C in the last 700 years; and the other deep levels show similar accordance of

temperature change between the two modes over equivalent times. This suggests that the acceleration does not cause abrupt change in terms of the warming tendency. More importantly, when the same acceleration method is applied to the control run CGM3 (and CGM2) from year 801 to 1000, no significant change in the intensity of the THC climate is evident for all the major indicators such as the NADWF, AABWF and the outflow of AABW, except for some notable changes in variability (not shown). Therefore, in this study, the acceleration scheme seems unlikely to cause any significant artificial 'acceleration shocks' which might contaminate the deep ocean warming or the response of world ocean THC to the equilibrium long term CO_2 forcing.

To examine the robustness of the ATGM3 solution, especially the effect of acceleration, a parallel integration ATGM2, which originates from the TGM2 run, is also performed based on the same strategy and procedure as that described above for ATGM3. The following sections document the result of ATGM3, and compare it with that of ATGM2 where appropriate. For completeness, all time series are made to include the first 600 year transient integration of the TGM3 (TGM2) run and the following total 900 year integration of ATGM3 (ATGM2). A few epochs are selected to show snapshots of the ocean climate (or its change) in the course of integration, amongst which the last 'decade' of acceleration (yr1091-1100) and the last century of the normal extension (yr1501-1600) are used to demonstrate the evolution during the normal mode adjustment period and compare the accelerated solution and the final settled 'equilibrium' in terms of various quantities examined.

6.2 Surface Changes

Although all the climate variables at the sea-air interface are shown to converge much more rapidly than inthe ocean interior for the TGM3 integration, changes are still evident after year 700, i.e., in the acceleration phase. It is of interest to examine if the surface change is consistent with that observed in the later period of

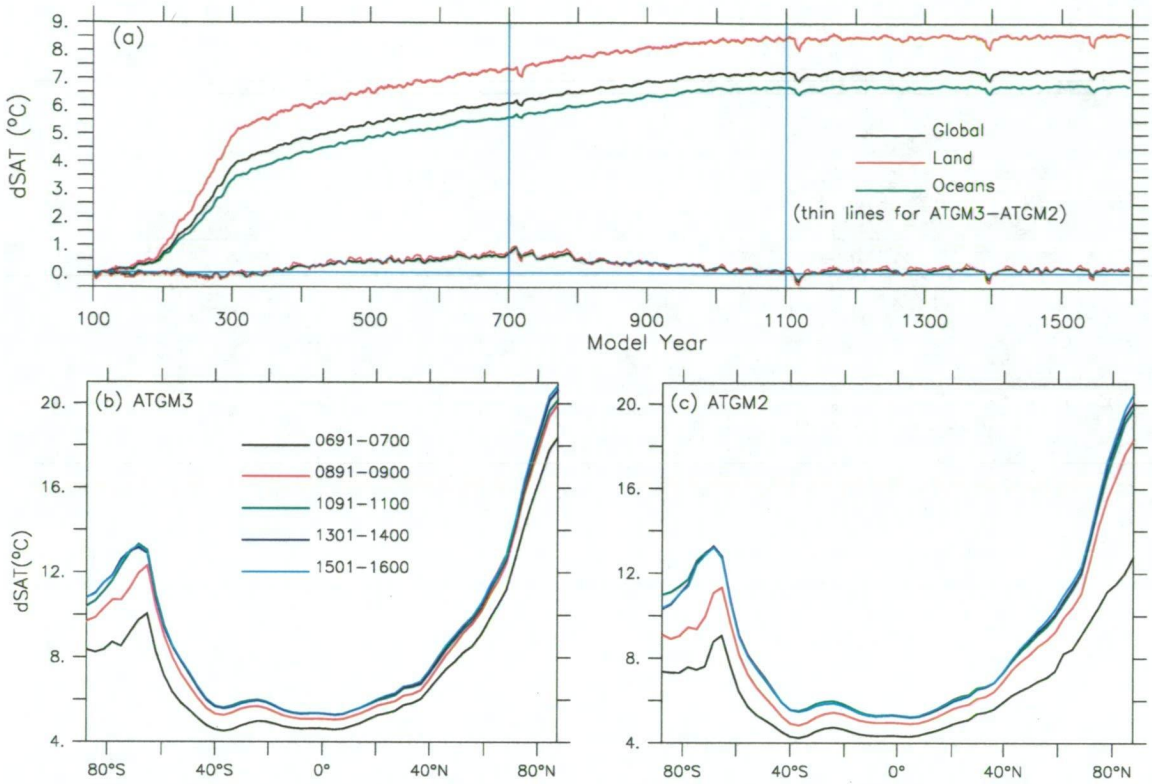

Figure 6.1: (a) Time series of SAT changes from ATGM3 and ATGM3 - ATGM2 over the globe, land and oceans; (b)(c) evolution of zonal mean SAT changes.

the TGM3 run. It is expected that the final solution may be quite different in some regions such as the Southern Ocean due to the re-arrangement of the ocean climate there.

6.2.1 SAT and SST

Fig.6.1a shows the time series of annual mean SAT changes (relative to the yr51-100 mean) over the globe, continents and oceans in the course of the ATGM3 integration. Also shown are the corresponding differences of SAT change between ATGM3 and ATGM2. We see that, during the 400 year acceleration period, the global mean SAT is increased by about 1.07 °C. While no difference of SAT change is found between the land and oceans, it can be seen that more warming occurs over the SH than the NH (1.31 verse 0.85 °C). Clearly the last 100 year of acceleration causes very little SAT change, indicating an equilibrium is reached at the surface in terms

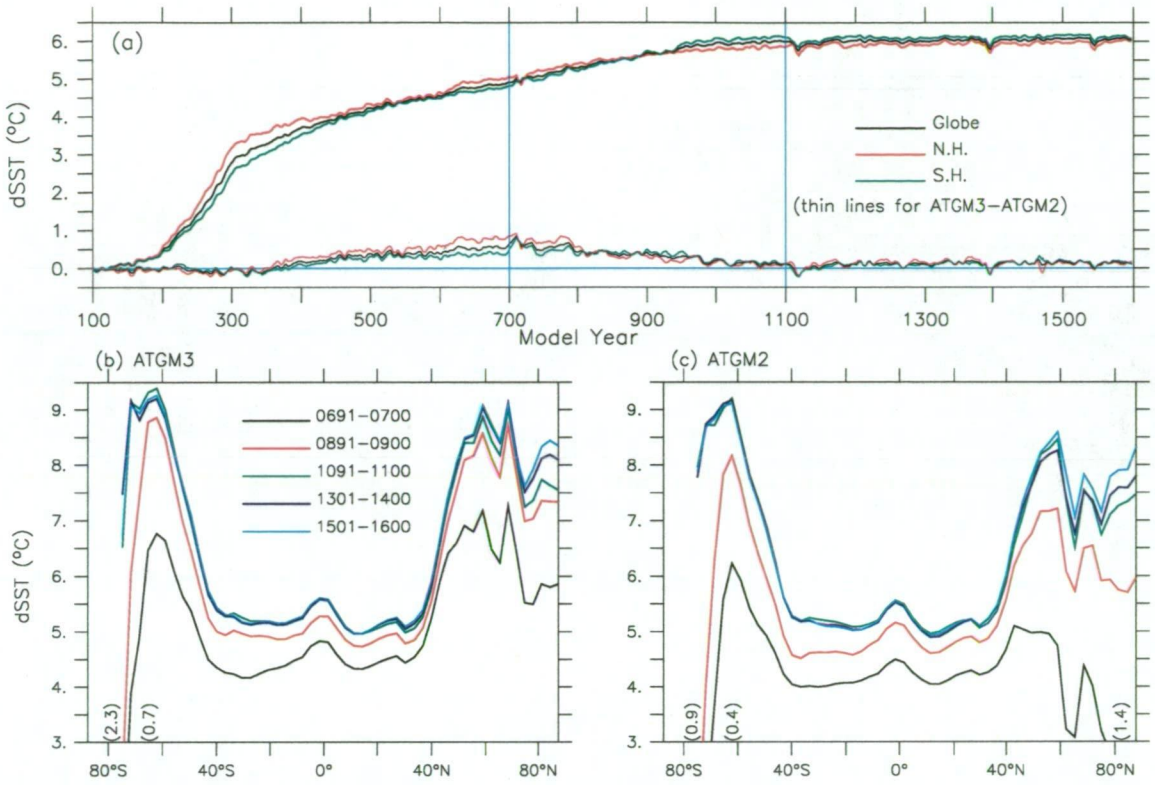

Figure 6.2: (a) Time series of SST changes for ATGM3 and and ATGM3 - ATGM2 over the globe, SH and NH; (b)(c) zonally averaged SST changes.

of the overall thermal state of the near surface atmosphere. In the following 500 year normal mode run, the averaged SAT hardly changes, showing a final global warming of about 7.3 °C, with the warming over land, oceans, SH and NH being 8.5, 6.7, 6.8 and 7.7 °C, respectively. For the ATGM2 run, the acceleration leads to a noticeably larger SAT increase in the first 300 years and also brings the system into a near steady state. This implies that the surface convergence in TGM3 is faster than that in TGM2 in the normal mode integration before year 700, probably due to the stronger oceanic circulation in TGM3 which causes a faster adjustment in the ocean and thus the whole climate system. The final equilibrium has a global mean temperature about 7.1 °C warmer than its initial state, and the warming is slightly smaller than its ATGM3 counterpart. The contrasts of SAT change between oceans and land and between two hemispheres are similar to that in ATGM3. Table 6.1 summarizes the surface temperature changes in both runs, giving an indication of the warming for the selected epochs and the final state.

Table 6.1: Accumulated surface warming (°C) relative to yr51-100 in ATGM3 (and *ATGM2*).

		yr0691-0700	yr0991-1000	yr1091-1100	yr1501-1600
SAT	Globe	6.11 (*5.48*)	7.13 (*6.98*)	7.22 (*7.14*)	7.28 (*7.16*)
	N.H.	6.73 (*5.88*)	7.52 (*7.41*)	7.60 (*7.53*)	7.73 (*7.60*)
	S.H.	5.48 (*5.08*)	6.74 (*6.56*)	6.83 (*6.76*)	6.84 (*6.71*)
	Land	7.32 (*6.65*)	8.29 (*8.20*)	8.39 (*8.36*)	8.52 (*8.36*)
	Oceans	5.56 (*4.96*)	6.61 (*6.45*)	6.70 (*6.60*)	6.74 (*6.62*)
SST	Globe	4.89 (*4.33*)	5.92 (*5.75*)	6.01 (*5.91*)	6.05 (*5.93*)
	N.H.	5.02 (*4.26*)	5.76 (*5.64*)	5.86 (*5.77*)	5.96 (*5.85*)
	S.H.	4.80 (*4.41*)	6.04 (*5.83*)	6.13 (*6.01*)	6.13 (*5.98*)

Fig.6.1c and 6.1d show the evolution of the latitudinal distribution of SAT change in the course of ATGM3 and ATGM2, respectively. At most latitudes the SAT is maintained nearly unchanged from the end of acceleration, but noticeable changes occur over both polar regions. Also evident is the slower convergence of the ATGM2 run over northern high latitudes in particular. Such a lagging of warming in ATGM2 is largely reduced by year 900 and finally removed in the last century of acceleration. The final SAT increase over the North Pole is about 20.5 °C due to the complete disappear of sea ice, in contrast to the warming of only 5.3 °C around the equator and 10.8 °C over the South Pole. This is the case for both runs.

The global and hemispheric mean SST evolve in a way similar to that of SAT, and the acceleration brings the SST into a quasi-stable state from around year 1000, as shown by Fig.6.2a. It is worth mentioning that, in contrast to the early stage of warming when the SST increases less in the SH than NH, the final equilibrium shows a slight but clearly stronger warming over the SH than the NH (e.g., 6.13 vs 5.96 °C for the ATGM3 run). The globally averaged SST increase is 6.05 °C, about 0.7 °C lower than the SAT change over the oceans. As discussed above, acceleration removes the lagging of sea surface warming in the ATGM2 run, particularly in the NH where the difference of SST change between the two runs is reduced from 0.8 °C before acceleration down to 0.1 °C by the end of acceleration. Fig.6.2b and 6.2c illustrate the zonal mean SST changes for the two runs. The largest warming during

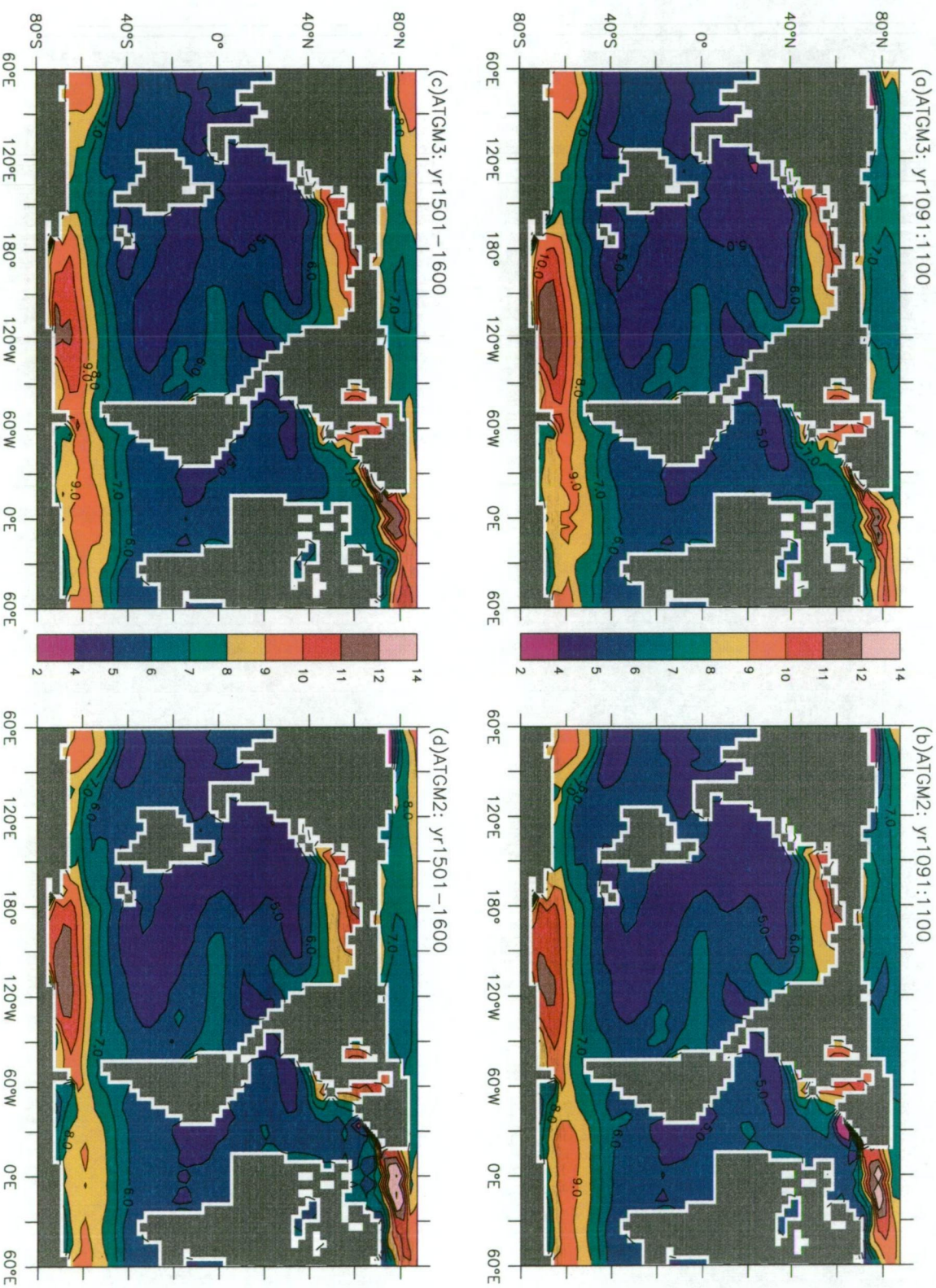

Figure 6.3: Geographical distributions of SST changes in ATGM3 and ATGM2: (a)(b) at the end of acceleration, (c)(d) last 100 year mean (normal run). (units: °C)

the ATGM3 integration is up to 6.0 °C, occurring at the southernmost latitude (in the Ross Sea), and for ATGM2 this warming is even larger (7.3 °C), both due to the complete removal of sea ice there. The final maximum SST increase caused by CO_2 forcing is more than 9 °C and is found over the Southern Ocean ACC band. In the Arctic Ocean, the SST still shows a trend of warming in the last few hundred years of the normal integration. This is more likely to be the effect of climate drift (as shown in the control runs) than the continuing impact of CO_2 forcing.

Examining the geographical distribution of SST anomalies at the end of acceleration and the end of the whole integration, as shown in Fig.6.3, we see that the low to mid latitude oceans keeps the annual mean SST nearly unchanged in the last 500 years normal integration for both runs. In those climatically sensitive regions such as the high latitude Southern Ocean, however, SST still undergoes some small changes during this period. In ATGM3, for example, the Ross Sea shows slight cooling whilst the Weddell Sea shows warming. In ATGM2, however, the above changes are reversed for these two regions, i.e., the Ross Sea is warmed a little whereas the Weddell Sea cools down. This kind of change obviously does not necessarily indicate a significant trend of continuing warming. Instead, it is more likely a result of long time scale variability. For the northern North Atlantic, ATGM2 sees more noticeable warming than ATGM3, especially off the eastern coast of Greenland. In general, the changes of global ocean SST are very small after the acceleration, indicating that the acceleration does result in a steady equilibrium state in terms of the annual mean SST distribution.

6.2.2 Sea Surface Heat Flux and Oceanic Heat Transport

We show the geographical distribution of changes in the oceanic surface heat flux (relative to yr51-100) for the periods yr1091-1100 and yr1501-1600 in Fig.6.4 for both runs. It can be seen that this quantity is in a very stable state over most parts of the global ocean after the acceleration, with minor changes occurring in the polar oceans such as the Ross Sea. This suggests that the adjustment of all the

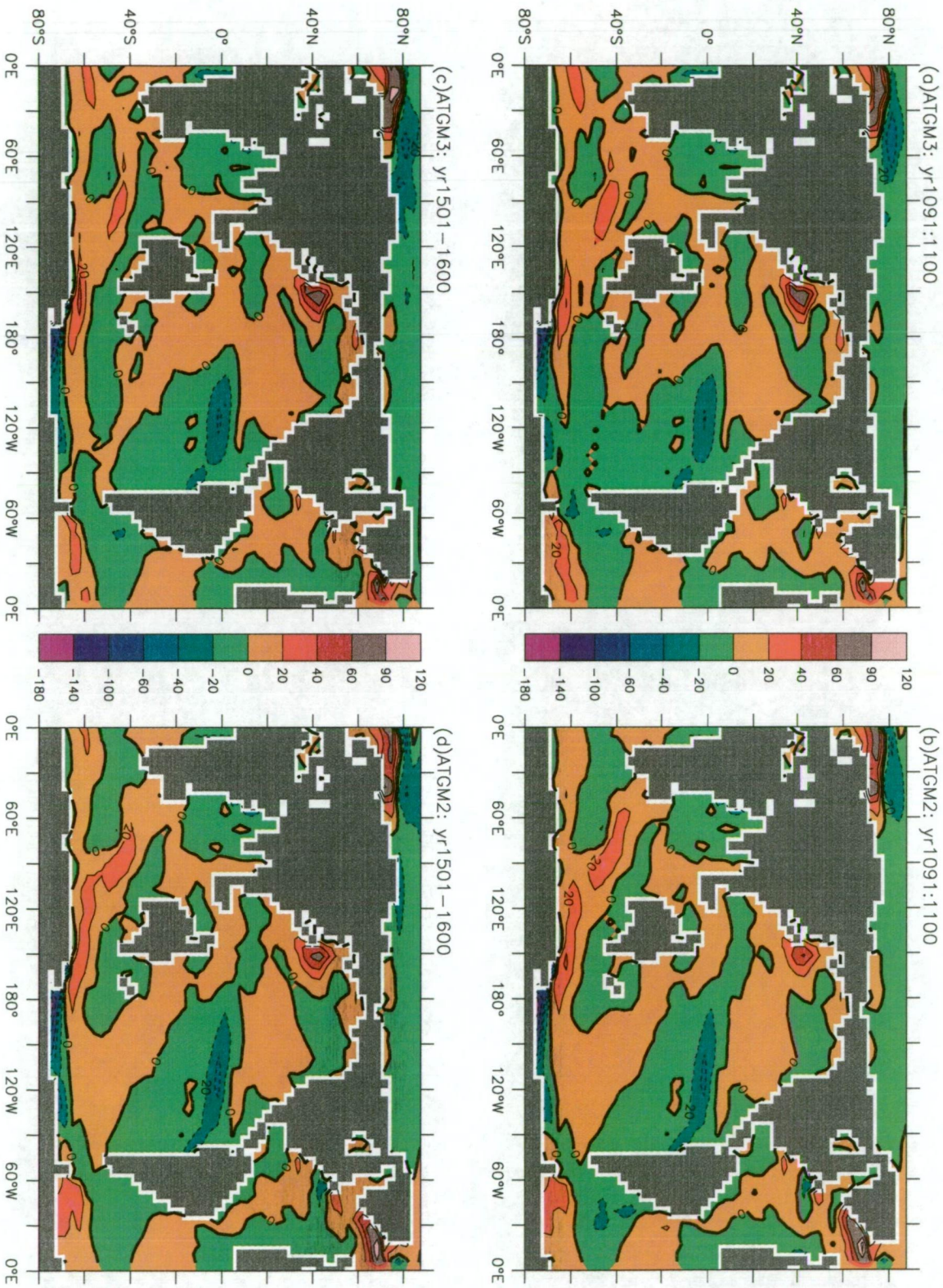

Figure 6.4: Changes of sea surface heat flux in ATGM3 and ATGM2: (a)(b) at the end of acceleration, (c)(d) last 100 year mean (normal run). (units: $\mathrm{W\,m^{-2}}$)

surface heat budget components (i.e., solar radiation, long-wave radiation, latent heat and sensible heat) under CO_2 forcing is completed and a new balance over the global ocean is established. Comparison between the new anomaly pattern and its counterpart in TGM3 (Fig.5.9c) shows that the surface heat budget only changes slightly from year 900 in TGM3 in most regions, but a fundamental difference is clearly seen in the Ross Sea where the surface layer loses a large amount of heat after acceleration, in sharp contrast to the results obtained in TGM3 (and TGM2). As already discussed in Chapter 5, the CO_2 induced shutdown of deep convection in the high latitude Southern Ocean and the collapse of overturning off Antarctica largely reduce the vertical mixing and the transport of heat sequestrated in the surface layer into the deep ocean, resulting in a net heat gain in the Ross and Weddell Seas. In the new equilibrium achieved after acceleration, as we will see, the Ross Sea deep convection is in operation again and the overturning/AABWF is reactivated and largely intensified. This results in active transport of heat from the surface layer into the deep ocean, plus the enhanced evaporation by the largely increased SST, causing a substantial heat loss there. However, such an important change is not found in the Weddell Sea, because the deep convection and overturning there do not recover at all due to the freshening being too strong at the surface, which is discussed later in this chapter.

Fig.6.5a and 6.5b show the evolution of the global ocean northward heat transport in ATGM3 and ATGM2, respectively. Also shown are variations of the contributions from individual basins, i.e., Fig.6.5cd for the Atlantic and Fig.6.5ef for the Indian-Pacific. Note that the total heat transport includes contributions from advection and isopycnal diffusion. Since the isopycnal component and its change due to CO_2 forcing are negligible compared to their advective counterparts in most oceans except for the mid to high southern latitudes, the changes of heat transport discussed below result almost completely from the changes of meridional advection, i.e., the evolutions of the wind driven Ekman drift and the thermohaline circulations. However, it must be born in mind that changes of the ocean interior thermal structure (i.e., meridional temperature gradient) also play an important role, which means that a

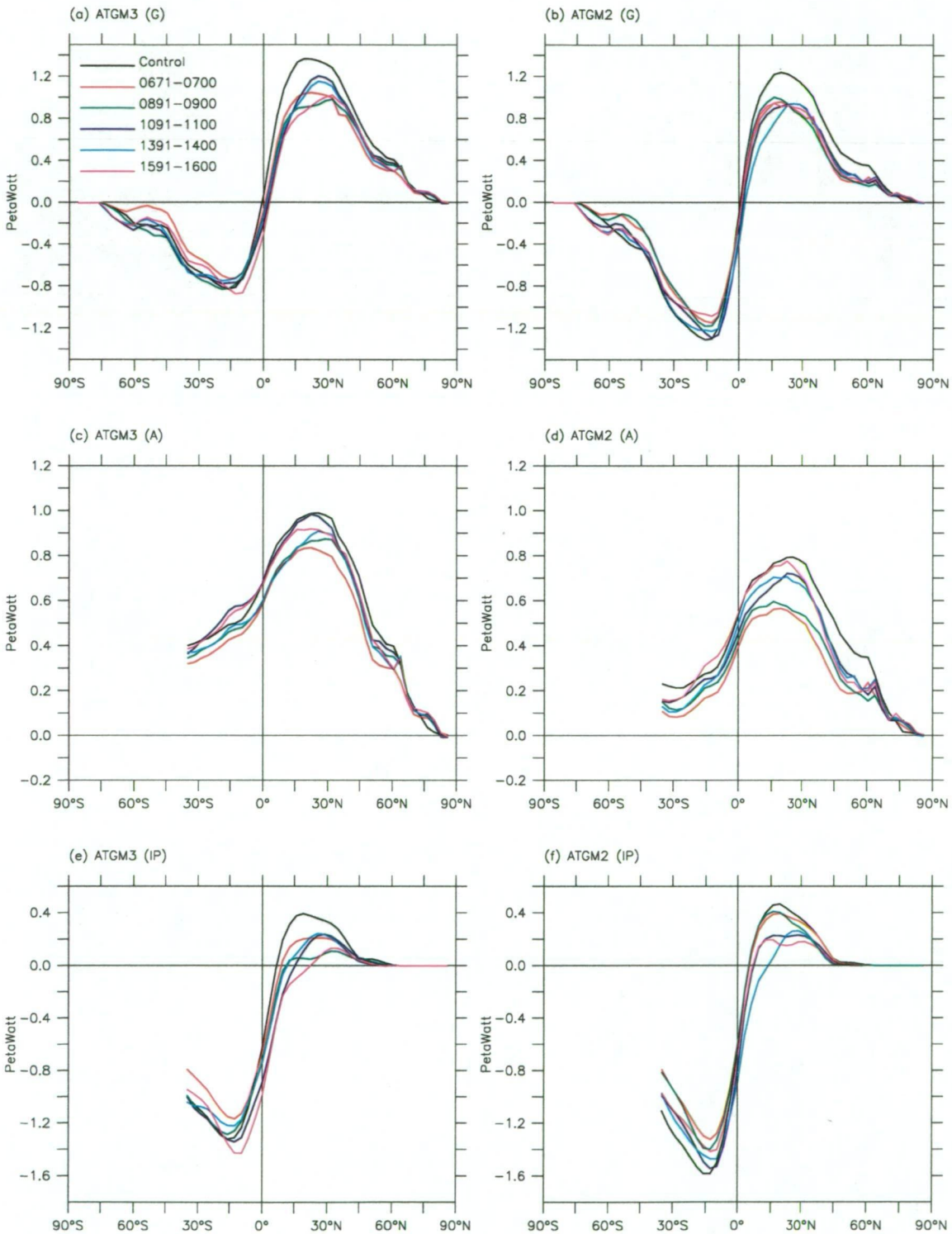

Figure 6.5: Evolution of northward heat transport for ATGM3 (left) and ATGM2 (right): (a)(b) global ocean, (c)(d) Atlantic, (e)(f) Indian-Pacific.

similar change of advection in the new equilibrium may result in a heat transport change of quite different magnitude from that before the acceleration.

It appears that, by year 700, both runs see largely reduced poleward oceanic heat transport in most latitudes of the NH. Examination of the individual basin components suggests that, at the early stage of CO_2 forcing (before the acceleration), most of the change in global ocean heat transport is attributed to the reduction in the Atlantic basin associated with the substantial weakening of the North Atlantic overturning circulation. Under the new equilibrium achieved by acceleration and the following adjustment, changes relative to that occurring before year 700 seems to be fairly small. However, factors responsible for the final total reduction (from the initial climate) are fundamentally different. Namely, most of the change occurs in the Indian-Pacific basin where the low latitude easterly winds are weakened considerably (see Fig.6.6) and therefore the heat transport by the northward Ekman drift in the upper layer is largely reduced. By that time, the Atlantic basin sees much smaller change of heat transport because the North Atlantic overturning circulation is fully functioning again, except for a considerable shoaling of the penetration depth.

In the SH, although the reduction of poleward heat transport is evident before the acceleration, the final state is generally quite close to the level of the initial climate in mid to high latitudes in particular. It is clear that changes in the individual basins play different roles in affecting the global ocean heat transport anomaly in the SH region. Before year 700, the Atlantic Ocean conveyor belt is weakened and the northward return flow in the upper layer is reduced. This overrides the effect of a slight weakening of the low latitude easterly winds, leading to a weakening of the northward heat transport in the southern Atlantic sector, resulting in an additional southward transport. In contrast, the Indian-Pacific basin experiences a much greater weakening in the low latitude westward windstress and thus a large reduction in the southward heat transport by Ekman drift. In the meanwhile, the largely reduced AABW outflow leads to a weakening of the southward return flow in the mid-depth layer. These reductions in the Indian-Pacific ocean more than cancel the increase in the Atlantic basin mentioned above, causing an overall decrease of

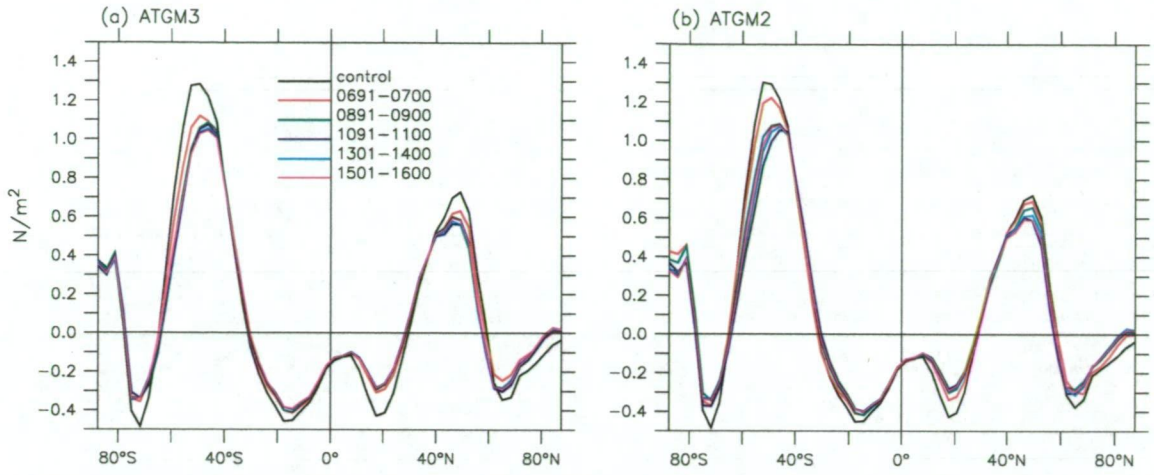

Figure 6.6: Evolution of zonally averaged annual mean zonal windstress in: (a) ATGM3, and (b) ATGM2.

the global ocean southward heat transport in low to mid latitudes. At the last stage of the experiments, the 'strengthening' of southward flow in the Atlantic Ocean is mostly cancelled by the re-intensification of the conveyor belt, and change occurs mainly in the Indian-Pacific basin. We will see that the deep ocean ventilation is in operation again and strengthened significantly there, leading to a stronger return flow to the south. In addition, the wind change at the surface also makes some contributions. In the low latitudes, the weakening of the easterly wind indeed causes a reduction of the southward Ekman drift, but the larger weakening of the westerly wind over (and north of) the ACC results in a weakening of the equatorward Ekman flow in the mid latitudes, which in effect enhances the southward heat transport. As a result, we see a generally 'recovered' southward heat transport for ATGM3 in particular.

It is noted that, after acceleration (and even in the last 200 years of the integration), the global ocean heat transport still fluctuates considerably, indicating a larger variability under the new equilibrium with the elevated level of CO_2. This is associated with the large adjustment and fluctuation of the global ocean THCs discussed later. It also needs be mentioned that, over the ACC region, changes of isopycnal diffusion (not shown) make considerable contribution to the local heat transport due to the tilting of the isopycnals. As discussed in chapter 5, the uneven warming in the ocean interior across the ACC causes a further sloping of the isopycnals down to

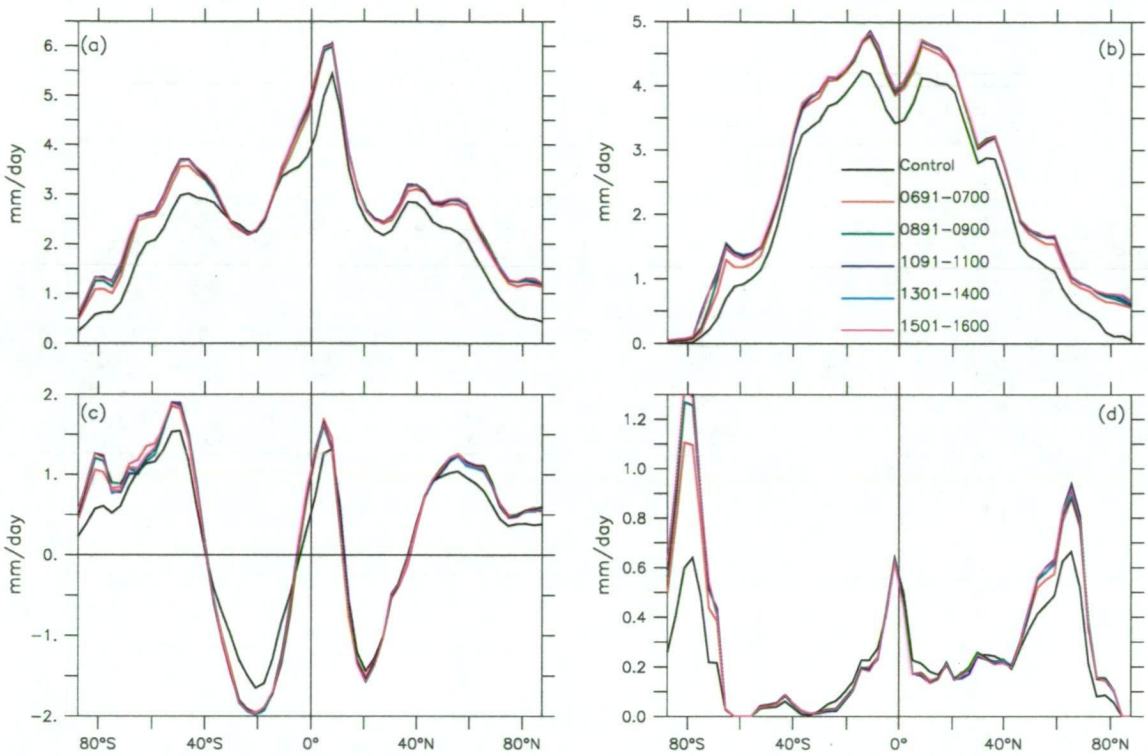

Figure 6.7: Latitudinal profiles of surface freshwater fluxes in ATGM3: (a) P, (b) E, (c) P - E, and (d) runoff.

the north, acting to reduce the southward isopycnal heat transport across the ACC. The 'bulge' shown in, say, Fig.6.5ab over the ACC band results mainly from the change of isopycnal heat transport there.

6.2.3 Hydrological Cycle and SSS

Fig.6.7a-d show the evolutions of the zonally averaged precipitation, evaporation, P - E and runoff, respectively, for ATGM3. All fields show little change from year 700 on until the end of the run for the whole NH and the low to mid latitudes in the SH. Small but noticeable changes from year 700 are seen in P - E (and thus runoff) over Antarctica, and this change does not occur at all after the end of acceleration, indicating that a very steady equilibrium is reached in terms of the global zonal mean hydrological cycle. In fact, the global geographical distributions of these fields are also very stable under the new equilibrium and, consequently, the global ocean sea surface freshwater flux is maintained nearly unchanged during the whole period

of the final 500 years normal mode integration.

Fig.6.8 illustrates the geographical distributions of SSS changes (relative to the control climate) at the end of acceleration and the end of integration for both runs. Most of the ocean, including nearly the whole Indian and Pacific Oceans and the mid to high latitude Atlantic Ocean, shows significant freshening at the surface. Meanwhile, SSS increase is evident over the inland seas, the Japan Sea, the low latitude Atlantic Ocean and the Arctic Ocean, but the overall change of global ocean SSS is a reduction of up to 0.54 psu by the end of acceleration. In general, the global SSS distribution evolves very little in the final 500 years over most of the oceans except for the Arctic region where the SSS is generally increasing. As mentioned repeatedly before, this increase is most likely the consequence of numerical noise. The local intensification of SSS due to this kind of numerical contamination, which has already been seen at the early stage of CO_2 forcing in TGM3 (Chapter 5), can finally cause a spurious thermohaline overturning in the Arctic Ocean as we will see later. This local circulation brings up more salt from the deep ocean and further enhances the SSS there. Also seen in the Arctic is the large reduction of SSS in the coastal region of Barents Sea, where the ATGM2 equilibrium SSS is over 10 psu lower than the initial climate, due to the largely enhanced runoff. In the Southern Ocean, we see a large surface freshening of over 4 psu in the Weddell Sea off Antarctica, due mainly to the enhancement of runoff there as well. In contrast, the Ross Sea sees only a modest reduction in SSS of around 1 psu. This is the case for both runs. It is this difference in surface freshening that causes substantially different equilibrium states of the convection and THCs in these two regions, i.e., as will be shown, the Ross Sea overturning fully recovers (and largely intensified) whereas the Weddell Sea overturning never comes back.

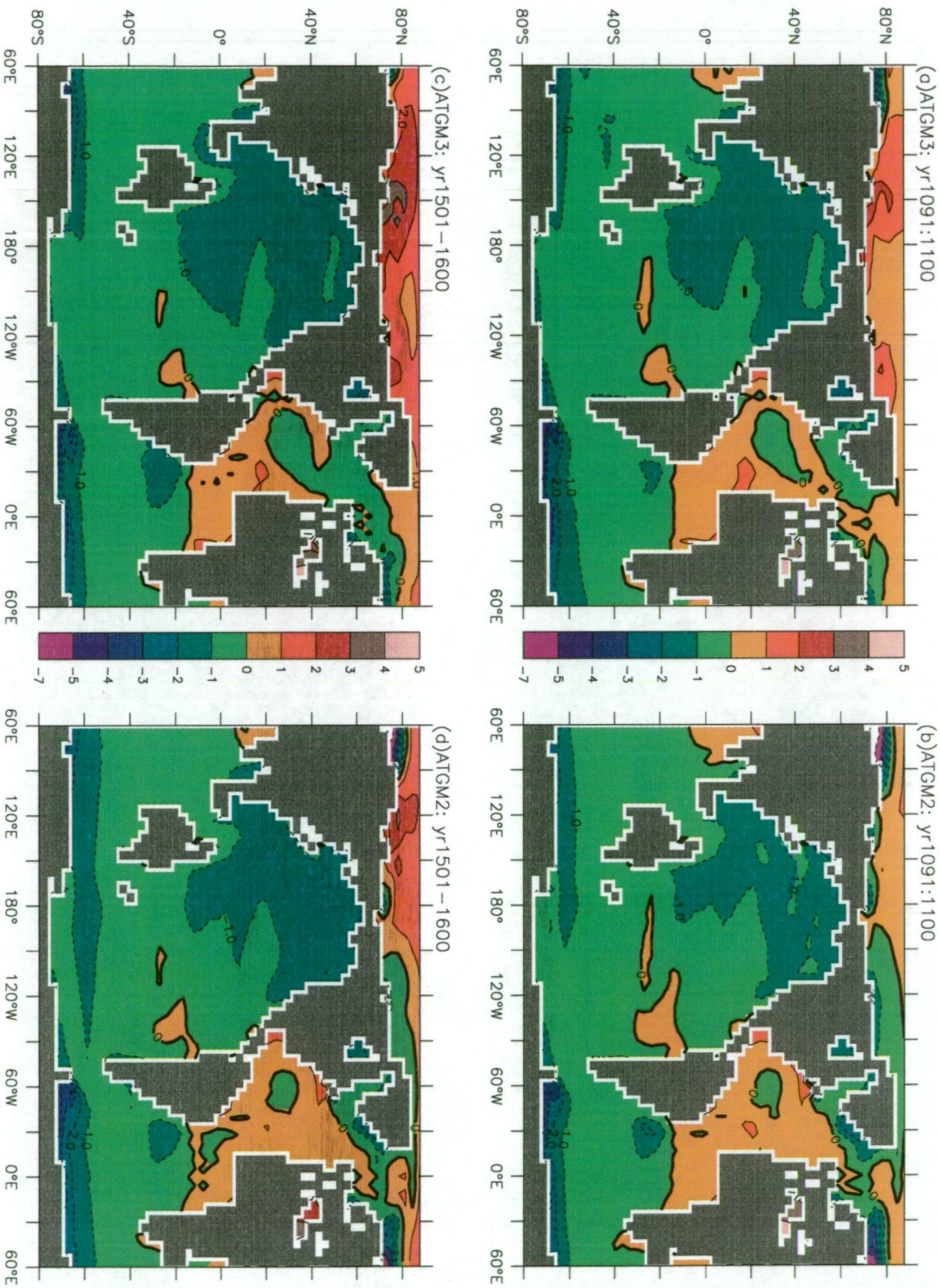

Figure 6.8: Geographical distributions of SSS changes in ATGM3 (left) and ATGM2 (right): (a)(b) at the end of acceleration, (c)(d) last 100 year mean. Contour interval is 1 (psu).

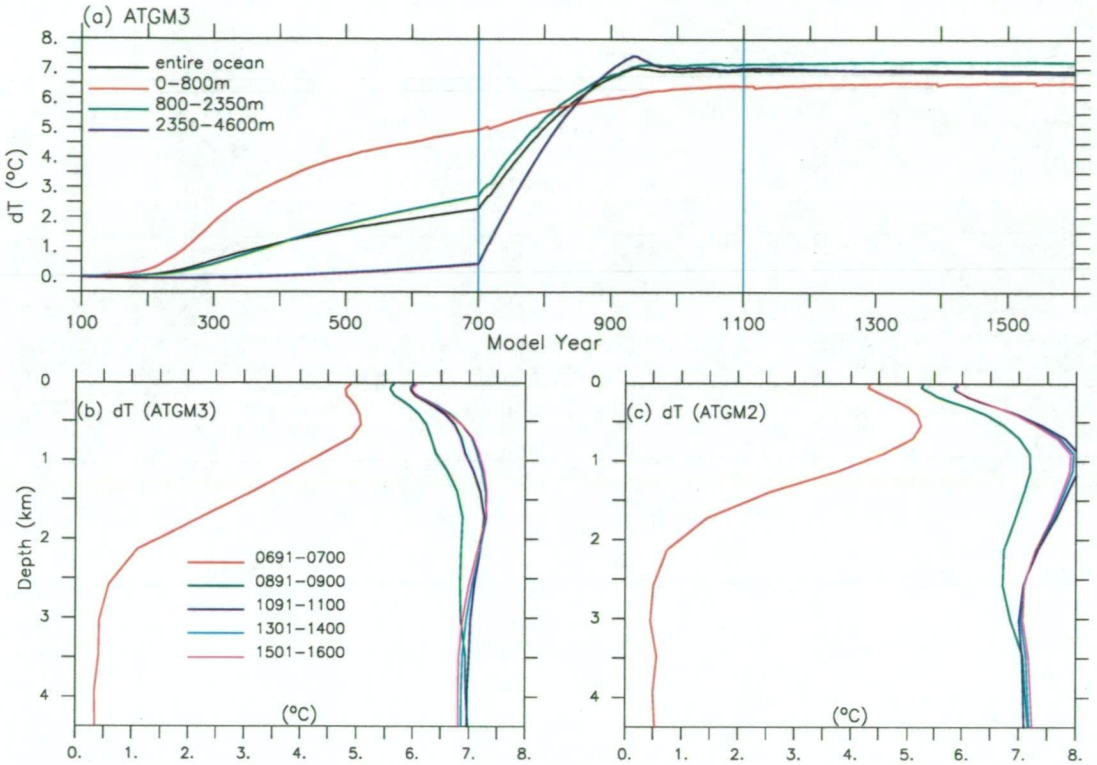

Figure 6.9: Changes of global ocean temperature: (a) time series of ΔT for the entire ocean and 3 sub-layers in ATGM3, (c)(d) vertical profiles of ΔT for the indicated epochs.

6.3 Ocean Interior Changes

We now examine the ocean interior change and the equilibrium state, especially that in the deep ocean, which is the goal we suppose to achieve using the acceleration technique. Focus is placed on the temperature evolution and the corresponding change in density. The change of salinity and its impact on density structure are relatively much smaller and are discussed in Appendix B.

6.3.1 Temperature

The acceleration appears to be very efficient in converging the deep ocean towards the equilibrium solution and thereby bringing the whole system into a quasi-steady state under elevated CO_2 conditions. As expected, this is especially true for the temperature evolution in the ocean interior. Fig.6.9a shows time series of changes in annual mean global ocean temperature for the whole column and three sublayers

in ATGM3. Clearly, from year 700 the warming in the mid-depth layer and abyssal ocean is speeded up substantially due to the use of enlarged time steps or say, equivalently, reduced heat capacities. The temperature change in the deep ocean catches up with that at the surface in the second century of acceleration and keeps ramping up for about one more hundred surface years before settling down at a level significantly higher than the surface warming. The upper layer sees a much slower but longer lasting warming during the acceleration period. We will see that the Southern Ocean overturning comes into operation again after 230-250 years' acceleration in the two runs and then the system adjusts quickly and evolves into a quasi-equilibrium within a few tens of surface years. Henceafter, i.e., from the fourth century of acceleration, the ocean interior temperature changes little. The final state of the global ocean is significantly warmer than the initial climate, with the entire ocean mean warming being 6.95 °C and 7.25 °C for ATGM3 and ATGM2, respectively, and the largest warming occurring in the mid-depth layer and the smallest warming in the upper layer for both runs.

Fig.6.9b and 6.9c show the vertical profiles of the global ocean temperature changes relative to the control climates for the two runs. It is evident that, for ATGM3, the bottom ocean is warmed to the greatest degree by the time of the (early) third century of acceleration and then cools down a little bit during the further adjustment period; the subsurface water is seen to be warmed further after acceleration and reaches a maximum warming of 7.3 °C by the end of the run; the uppermost few levels do not see any change after acceleration, maintaining a maximum warming of about 6 °C in the last 500 years of integration. For the case of ATGM2, while the surface water keeps a temperature anomaly of slightly less than 6 °C after acceleration, the bottom ocean is further warmed whereas the subsurface water is cooling down slightly, just in the opposite way to that for ATGM3. We see that in ATGM2 the final warming is up to 7.8 °C and 7.25 °C in the subsurface and bottom, respectively, both being about 0.5 °C more than their ATGM3 counterparts.

Fig.6.10 shows the accelerated results and the final states of the global ocean warming for both runs in terms of the zonal mean distribution. In general, no significant

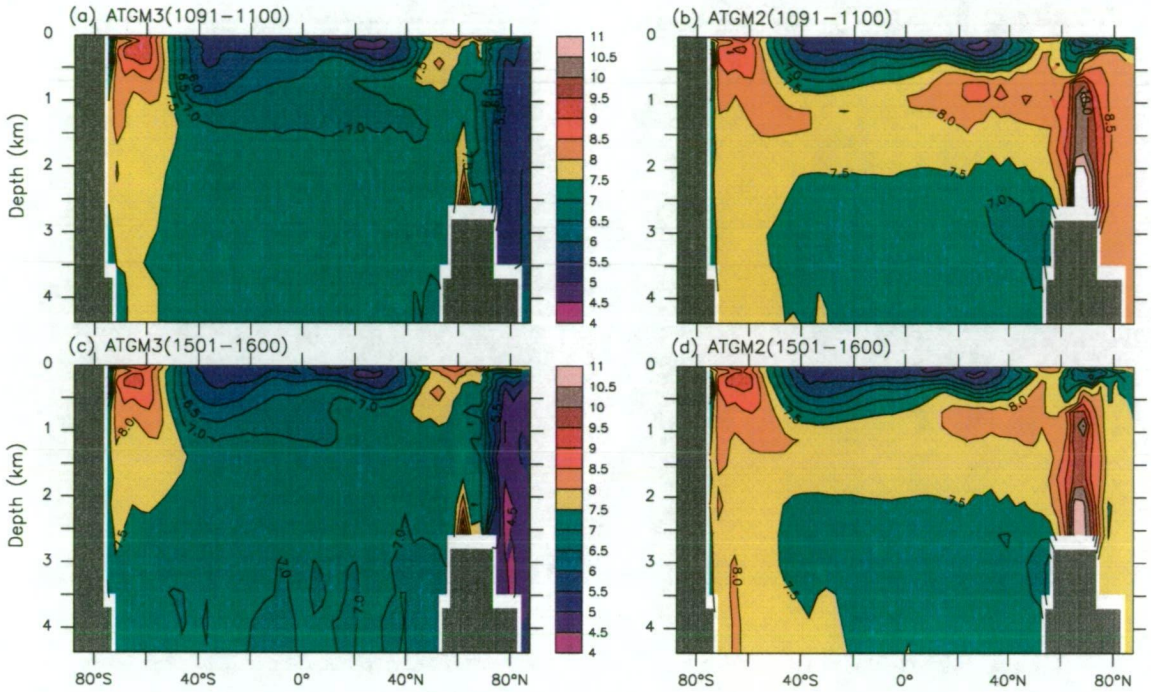

Figure 6.10: Zonal mean global ocean temperature changes in the ocean interior from ATGM3 (left) and ATGM2 (right) for indicated epochs. Contour interval is 0.5 °C.

change is evident during the last period of adjustment (except for the Arctic Ocean region), but the above mentioned small evolution in the bottom and subsurface layers can be seen in most latitudes, especially in the Southern Ocean, for both runs. Compared to the initial climate, the final equilibrium state sees the most pronounced changes of temperature in the Southern Ocean and the North Atlantic, where the strong warming at the surface is associated with the removal of sea ice and the deep ocean warming is attributable to the THC transporting heat down to depth. As for the extremely large warming located near the bottom of the Greenland/Norwegian/Iceland Seas for the ATGM2 run in particular, it is believed to be the result of topography related numerical noise as discussed before. The smallest warming is found in the near surface layer of low to mid latitude oceans, due mainly to the large evaporative heat loss cancelling the surface warming resulting from the radiative heat gain. We note that, in the interior of Arctic Ocean, there is significant difference of change between the two runs, i.e., ATGM3 sees a warming below 5 °C whereas the warming in ATGM2 is over 7.5 °C. This contrast of warming between the two runs in the Arctic Ocean seems unlikely to be a result of 'climate drift',

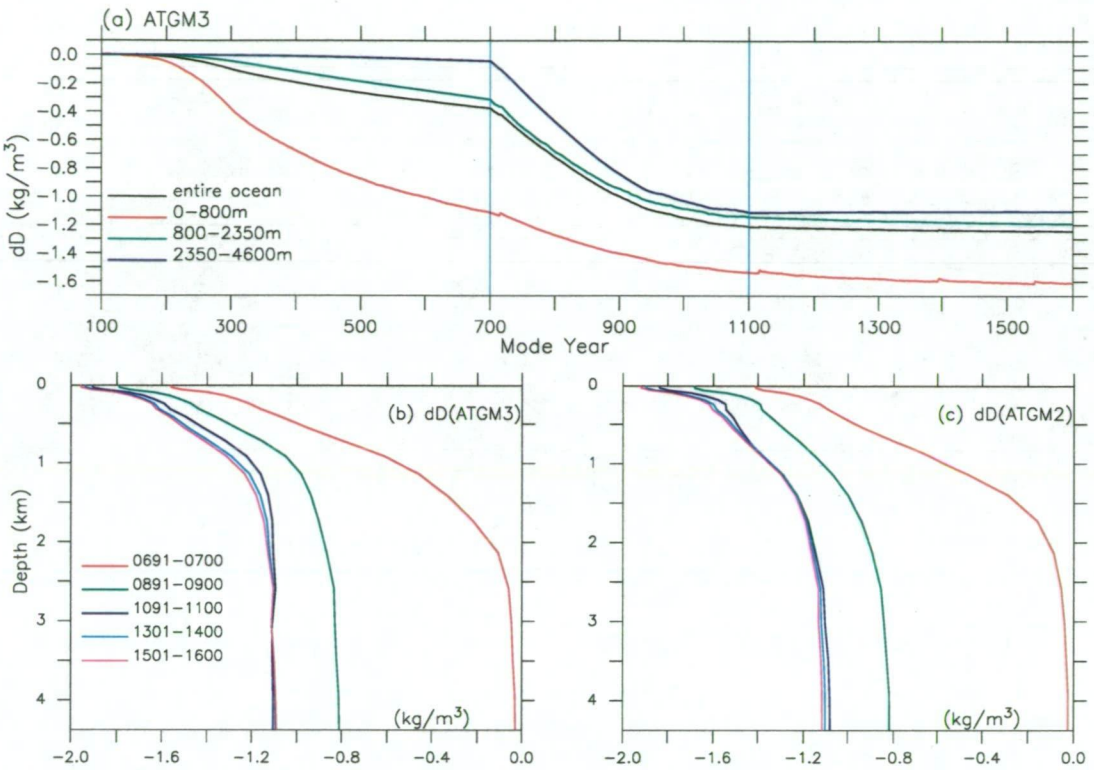

Figure 6.11: Same as Fig.6.9 but for density (σ_t)

because we have shown in Chapter 4 that the control run CGM3 suffers a drift of warming whereas CGM2 is subject to a drift of cooling in this region. It is more likely a consequence of numerical contamination and remains to be further explored.

6.3.2 Density

The acceleration of deep ocean convergence, especially the 'quick' adjustment of the ocean interior thermal state, causes a corresponding rapid evolution to equilibrium of the density structure. Fig.6.11a presents time series of annual mean density (σ_t) change relative to the initial state for ATGM3. Evident is the faster ramp-down of density in the deep oceans than that in the upper layer. Such a decrease in density is largely reduced at all depths in the last century of acceleration when a new near-stable climate of the world ocean THC is established (see the following section) due to the completion of ocean interior thermal adjustment. It may be worth mentioning that, as a consequence of thermal expansion, the global ocean in the final state has a

mean surface level about 443 cm and 460 cm higher than its initial level in ATGM3 and ATGM2, respectively. However, it is noted that the density field, unlike the temperature, maintains a noticeable although reducing trend of decline through the whole course of the accelerated integration, and remains so but at a very small rate through the last 500 years of integration with acceleration switched off, especially in the surface layer. This continuing evolution of the global ocean density structure is completely attributable to the spurious change in the salinity field, which is discussed in Appendix B.

Fig.6.11b and 6.11c show the vertical profiles of density change for the indicated epochs. The world ocean stratification is reduced substantially in the first two centuries of acceleration, as indicated by the much larger reduction of densities in deeper levels than upper levels. For ATGM3, by the end of the acceleration, the deep ocean density is reduced to a maximum and henceforth no change is evident, but densities of the surface and subsurface water maintain slight but noticeable trends of decrease as mentioned above, implying a further intensification of the water column stratification in terms of the global mean. ATGM2 sees somewhat different evolution after the acceleration, i.e., densities of both the deep and near-surface water continues to decline slightly whereas the mid-depth water keeps unchanged. Comparison with Fig.6.11 shows that the difference of temperature change after acceleration (i.e., ATGM3 suffers a slight cooling whilst ATGM2 sees a small warming) causes the contrast of density change between the two runs in the deep ocean. We note that, for the deep ocean density, the almost zero change in ATGM3 is the result of cooling cancelled by freshening, and the notable reduction in ATGM2 is the result of warming intensified by freshening. The continual reduction in surface density for both runs results from the decrease of salinity, as will be shown later. This kind of spurious reduction in density is evident over most latitudes for both runs, as revealed by the zonal mean density changes featured in the latitude-depth plots (not shown).

6.4 Recovery of the Thermohaline Circulation

As the intensification of stratification caused by the freshening and heating from the above results in the shutoff of Southern Ocean overturning and substantial reduction of the NADWF at the early stage of the transient runs, long-term warming in the ocean interior acts to destabilize the water column and, as anticipated, does finally bring back the world ocean deep THC. In the following discussion, we take the ATGM3 integration as the example to demonstrate the changes of global ocean THCs in the accelerated phase and the normal mode extension. Any noticeable difference of THC behaviour between the two runs is also addressed.

6.4.1 Evolution of the World Ocean THC

Fig.6.12a displays the temporal variation of NADWF (to 800 m) in the course of the two runs. During the period of acceleration, especially the first three centuries, we see a clear speed-up of recovery of the NADWF (compared to the normal evolution shown in Fig.5.21a) until it finally reaches a maximum near the end of the acceleration. From then on, the NADWF stays at this level through the whole course of the normal extension, showing that the acceleration brings a quite stable equilibrium for the NADWF, which appears to be the same as the solution of normal integration, with an intensity slightly stronger than the initial climate. However, despite a final stronger intensity, the recovery of NADWF can not be thought to be complete because its downward penetration is significantly reduced (by nearly 1000 m), as shown by Fig.6.12d. This change, as can be understood, has a significant impact on the mid-depth and deep ocean ventilation.

Much more complex is the case of AABWF, as illustrated in Fig.6.12b. The Antarctic downwelling through 1250 m depth is shown to be brought into a state of complete shutoff by the acceleration within a couple of decades (about 500 deepest ocean years), and then stays inactive during the following two centuries (5500 deepest ocean years) until it shows a relatively 'rapid' increase from zero to up to 10 Sv

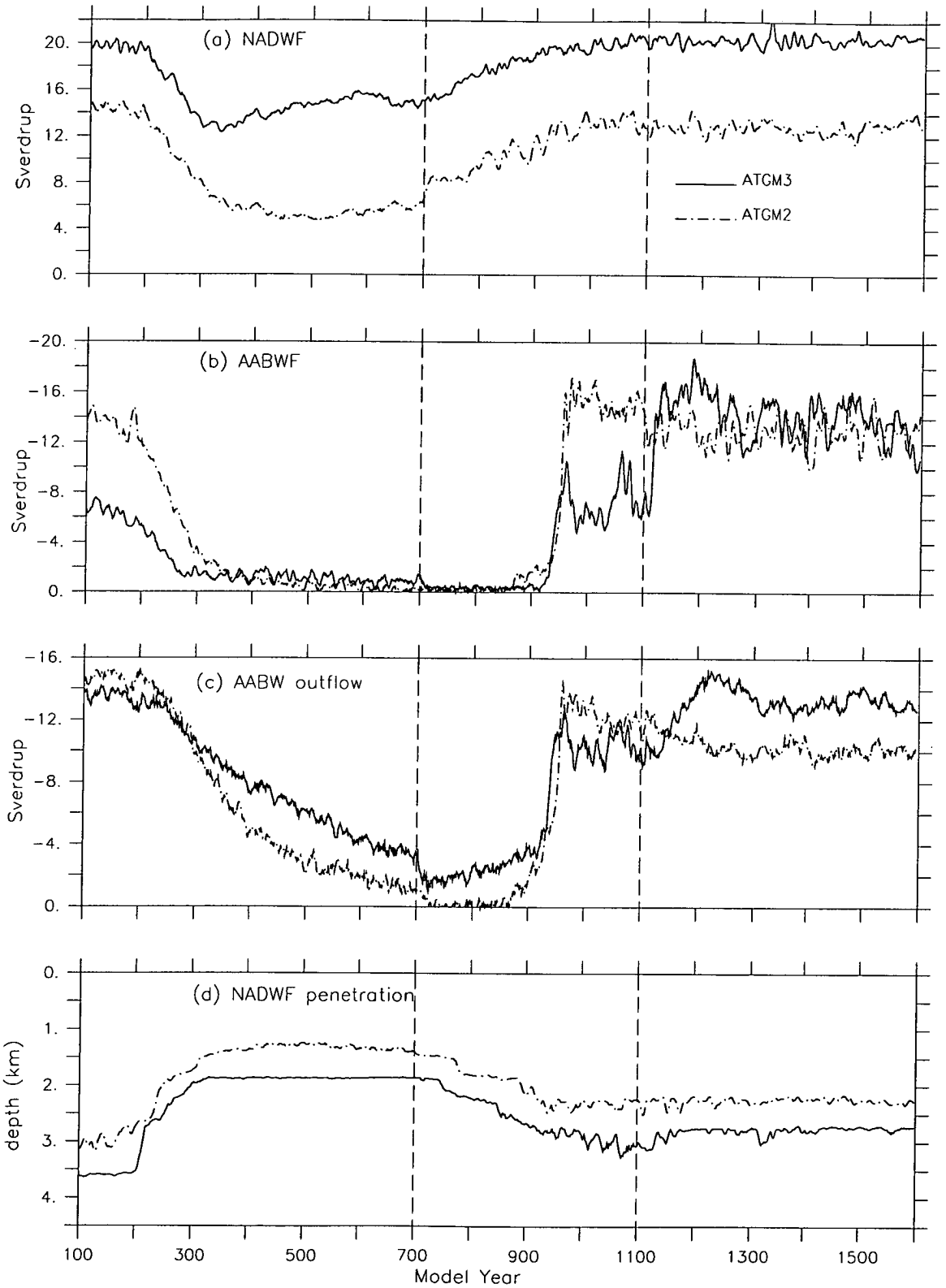

Figure 6.12: Time series of the global ocean THC in ATGM3 and ATGM2: (a) NADWF (44.6°N, 800 m), (b) AABWF (66.9°S, 1540 m), (c) outflow of AABF (35°S, 3250 m), and (d) penetration depth of the NABWF (40 – 60°N).

within 30 years (820 deepest ocean years). Thereafter, it fluctuates largely between 5 and 10 Sv for the remainder of the accelerated integration, generally stronger than for the control state. However, this accelerated solution is clearly not the same as that of the normal mode run, because we see a nearly immediate, significant change in the AABWF intensity following the switch-off of acceleration. Within the first 30 years of the normal mode extension, the AABWF is enhanced from around 6 Sv to over 16 Sv and, a few decades later, it even reaches a maximum of over 18 Sv. Thereafter AABWF ramps down to a minimum within about 100 years and then fluctuates between 11 and 16 Sv for most of the time during the last three centuries. This final quasi-equilibrium intensity for AABWF is nearly twice as strong as its initial climate, and with a much larger variability on interannual and interdecadal timescales.

With regard to the northward outflow of the AABW shown in Fig.6.12c, after quickly reaching its minimum soon after acceleration, it shows at first some minimal recovery in the following two centuries, but then comes back strongly with the resumption of downwelling off Antarctica as discussed above. However, the deep ocean meridional circulation unlike the AABWF does not recover to its initial intensity in the accelerated period. Instead, it fluctuates largely around a level of about 10 Sv after achieving a maximum at around year 960. Such a result is also far from the normal mode solution. Rapid intensification occurs soon after the switch-off of acceleration, similar to that of the AABWF but with a much more moderate rate of change. In the final 300 year normal integration, the deep cell shows a fairly stable state with an average intensity of about 13 Sv which is very close to the control climate, in contrast to the situation of AABWF.

We note the similarity and differences of the THC change in the ATGM3 and ATGM2 integrations. For the NADWF, ATGM2 sees an evolution qualitatively close to that found in ATGM3 but has a final equilibrium intensity smaller than the control climate, and the penetration depth shoals as well, indicating an incomplete recovery. On the other hand, both the AABWF and the associated AABW northward outflow in ATGM2 achieve their maximum intensities during the accel-

erated period and then gradually decline to a near-steady level in the latter half of the normal mode extension, with nearly no abrupt change occurring after the transition from accelerated mode to normal mode. In other words, the acceleration in ATGM2 seems to be more efficient in bringing the Southern Ocean into a 'real' quasi-equilibrium state than in ATGM3. It is also clear that the ATGM2 equilibrium intensities of the AABWF and the deep cell are weaker than their control climates, in contrast to their counterparts in ATGM3, especially for the case of AABWF. Nevertheless, the fact that both runs finally settle down to a quasi-equilibrium state in terms of a (near) stable world ocean thermal structure, stratification and overturning circulations, sheds light on the robustness of our results, i.e, the Bryan technique (1984) does a fairly good job in accelerating the convergence of the deep ocean towards its equilibrium under a CO_2 stabilization forcing, and the long-term warming in the ocean interior does generate the re-operation of the Southern Ocean overturning and the deep ocean ventilation.

Fig.6.13 shows patterns of overturning streamfunctions in ATGM3 for the end of the accelerated period and the last century of the normal extension. Presented are the world ocean (6.13ab), the Atlantic basin (6.13cd) and the Indian-Pacific basin (6.13ef). Comparison between Fig.6.13a and 6.13b reveals an intensification of the AABWF and the deep ocean circulation during the normal adjustment period. Also notable is that the NADWF is strengthened slightly but its penetration become shallower. In the Arctic Ocean we see a pair of developed local overturning cells which is associated with numerical noise and already noted in the latter part of the TGM3 run as discussed in chapter 5. Examination of the final state of THCs in the individual basins reveals a more important differences between the new equilibrium circulation under long-term global warming forcing and the control climate. Namely, the Weddell Sea does not see overturning anymore (Fig.6.13d) whereas the Ross Sea does see an overturning several times stronger than its initial state. Therefore the new equilibrium AABWF is totally a contribution from the Ross Sea due to the perpetual close-down of the Weddell Sea downwelling, in sharp contrast to the control climate which is dominated by the Weddell Sea overturning. As al-

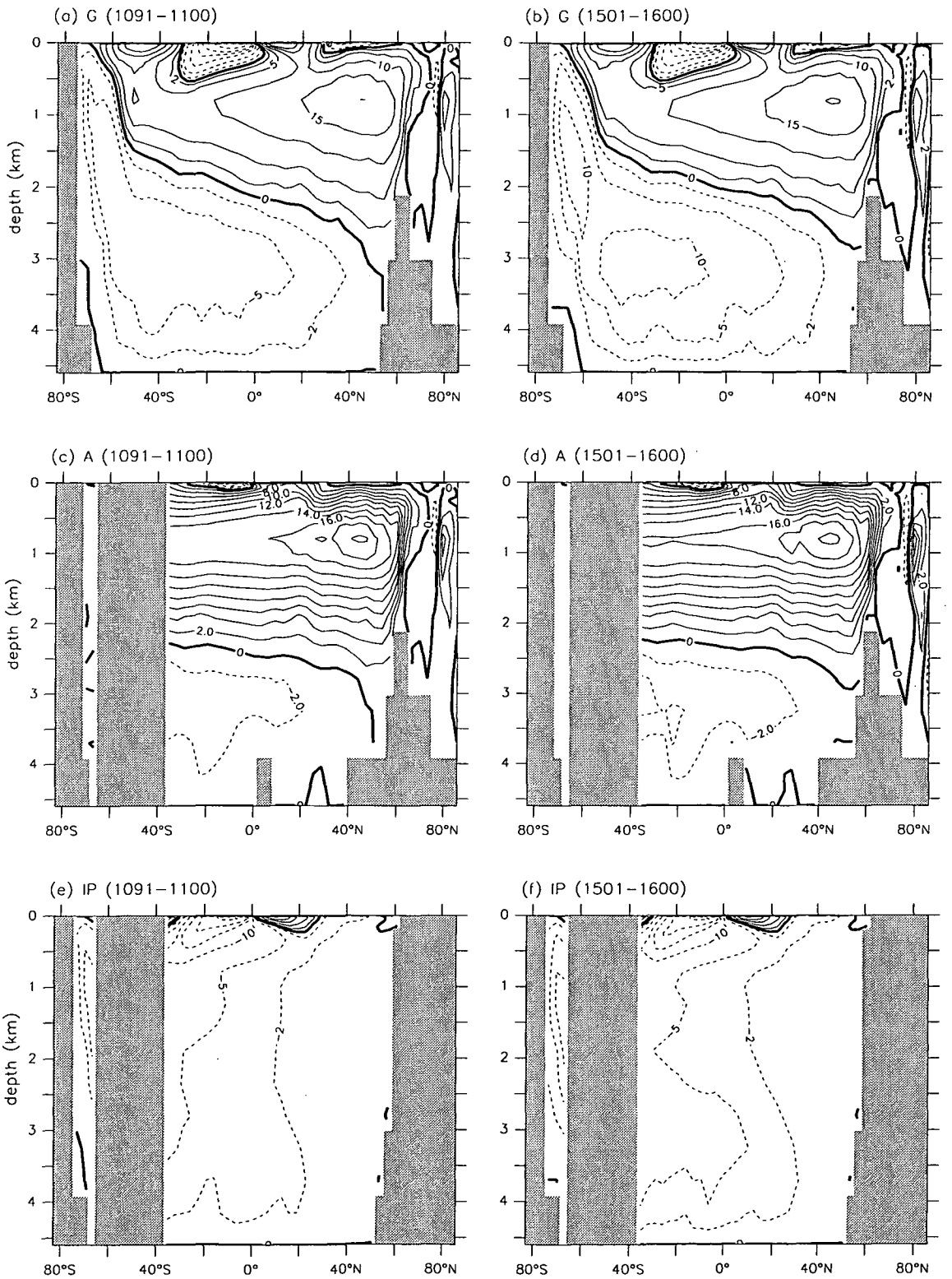

Figure 6.13: Overturning patterns for the indicated epochs in ATGM3. Contours: (a)(b) 0, ±2, ±5, ±10, ±15, ±20, ±30, ±40; (c)(d) -8 to 20 with interval 2; (e)(f) same as (a)(b).

ready mentioned, the extremely large freshening over the Weddell Sea prevents the occurrence of deep convection there and thus does not allow a resumption of the overturning. In ATGM2 (not shown), the situation is exactly the same, i.e., the Weddell Sea overturning never comes back after it is shut off. More details of the mechanism are discussed below.

6.4.2 Mechanism of the AABWF Resumption

In Chapter 5 we have shown that a hydrological balance over the southern high latitude ocean surface is achieved soon after CO_2 tripling and lasts through the rest of the transient runs. Under the accelerating mode and in the following normal extension period, such a stasis is generally well maintained in terms of the annual and area mean around Antarctica (not shown). However, the ongoing warming and evolution of convective activities can cause regional imbalance in the surface freshwater budget, especially over the climatically sensitive regions such as the Ross Sea and Weddell Seas, leading to a corresponding change in the local salinity field. Adjustments of the surface thermohaline conditions, plus the warming induced ocean interior changes in density fields, naturally affect the local water stratification and may cause an active response of the thermohaline overturning circulation, depending on the degree to which the stability is changed.

Fig.6.14a–c presents the annual mean SST, SSS and SSD changes over the Weddell and Ross Seas (south of 60°S) for the ATGM3 integration. From Fig.6.14a we see that, during the acceleration period, the Weddell Sea experiences a relatively smooth increase of SST and a small but noticeable decrease of SSS. In contrast, the Ross Sea sees a much stronger increase of SST at about the time that the Antarctic overturning is reactivated, and accordingly an evident increase of SSS over that time. It is noted that the Weddell Sea suffers a much larger salinity decrease than the Ross Sea in the whole course of the acceleration due to the very large freshening associated with the effect of the Antarctic catchment that leads a to large difference of runoff into the two regions as mentioned before. Consequently, the annual mean

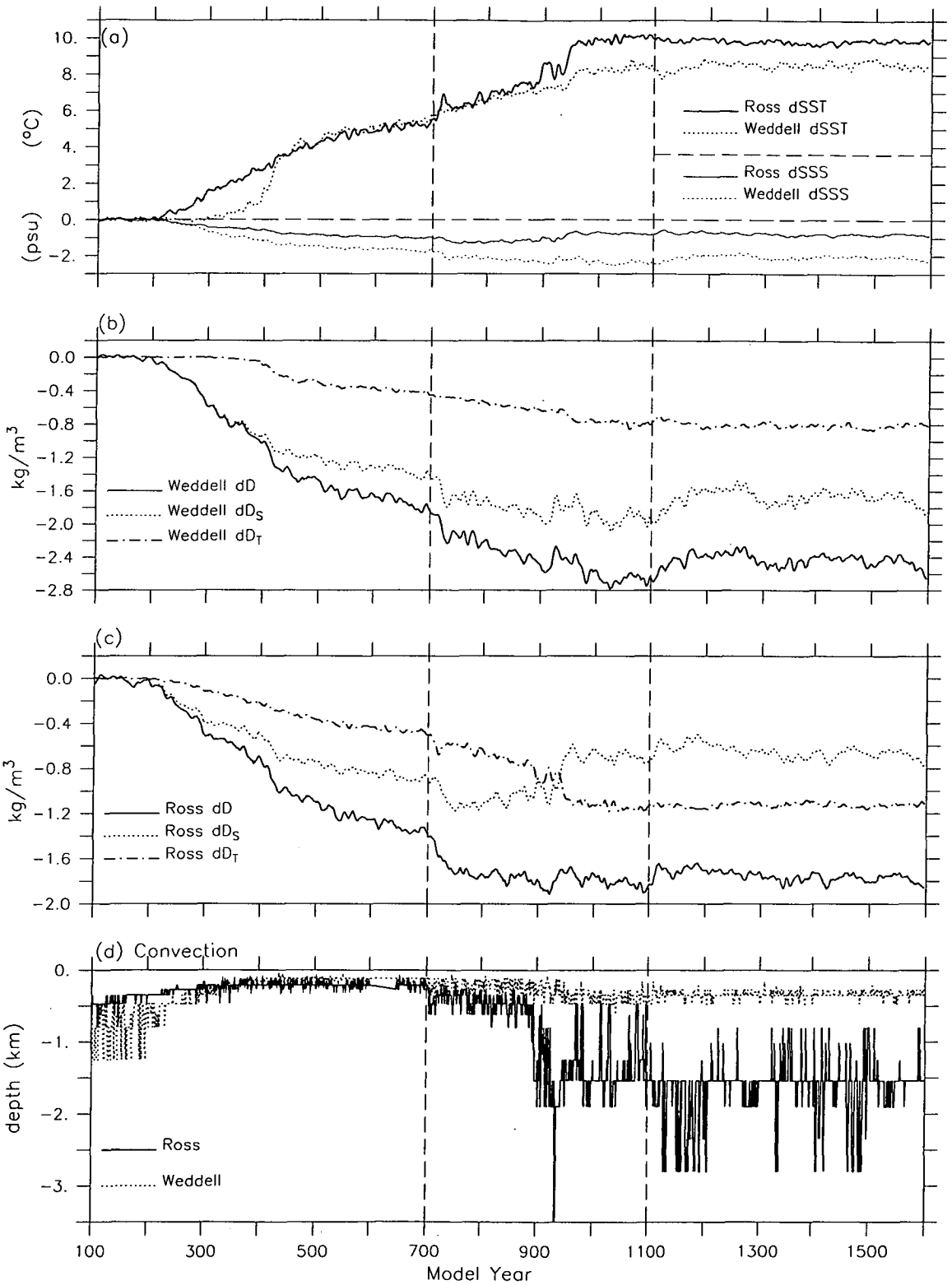

Figure 6.14: Time series of annual mean SSS, SST and SSD (σ_t) changes in ATGM3: (a) SST/SSS changes over Ross and Weddell Seas, (b) Weddell Sea SSD, (c) Ross Sea SSD. (d) shows the maximum convection depth in Ross and Weddell Seas. In (b) and (c), density changes induced by temperature alone and salinity alone are included.

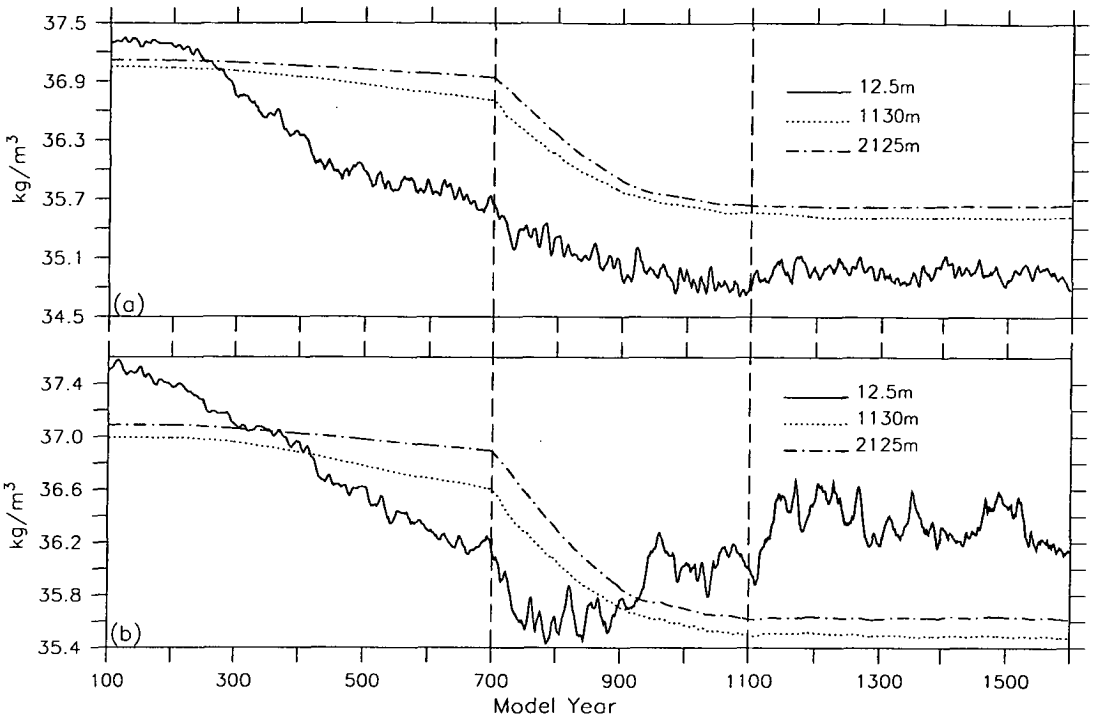

Figure 6.15: Time series for the ATGM3 winter peak SSD (σ_2) and densities at two deep levels in: (a) Weddell Sea and (b) Ross/Bellingshausen Seas (south of 60°S). (c) shows the deepest convecton depth in the annual cycle for the two regions.

SSD reduction in the Weddell Sea is significantly larger than that in the Ross Sea. This is clearly seen in Fig.6.14b and 6.14c, which show the SSD anomalies in ATGM3 induced by changes in SST, SSS and their joint effect. In fact, SSD reduction in the Weddell Sea induced by SSS change alone exceeds the total decrease of SSD in the Ross Sea. In realityi, for such long term changes the changes in the Antarctic ice sheet would need to be considered as given for example by Warner and Budd (1998). However, for the consideration of the mechanisms involved here those other factors are ignored.

The 'sudden' increases of SST and SSS seen in the Ross Sea are primarily the result of the rapid upmixing of warmed and salty deep water in association with the renewed Antarctic convection, and the consequent partial breakdown in the relatively fresh and cool surface capping layer. On the other hand, the enhanced SSS in winter (together with the cooled SST) causes a relatively large peak SSD that further strengthens the deep convection and may finally resume the overturning. This process is a positive feedback and critical for the AABWF recovery.

Following the idea of checking the relevant process of the AABWF shutoff, we examine the winter peak SSD and subsurface densities in the Ross Sea and the Weddell Sea in order to establish the circumstances of the resumption or lasting stagnancy of overturning. Fig.6.15 displays the maximum winter (Aug.–Oct.) surface density attained at any oceanic point to the south of 60°S in each year for both regions, together with the annual and area mean densities at the depths of 1130 m and 2125 m over the same regions in the ATGM3 integration.

In the Ross Sea region, densities at the two deeper levels decreases drastically in the first 200 years of the accelerated period due to the rapid development of warming in the ocean interior. Meanwhile, the surface winter peak SSD drops to a minimum value in the first century of acceleration and then fluctuates above this value until year 900 when it catches up with the dropping average density of the 1130 m depth. From that time, the water column stability is reduced to such an extent that intermittent deep convection is triggered off, as clearly shown in Fig.6.14d. As the convection occurs more and more frequently and penetrates deeper and deeper, it brings more and more salt and heat from the deep ocean up to the surface, increasing the SST more strongly and thus leading to more evaporation, producing somewhat denser surface water in winter, destabilizing the water column further. We can see that the winter peak SSD begins to surpasses the average density at 2125 m depth by around year 930, which immediately results in deep convection down to below 3500 m. Thereafter, the peak winter SSD continues to be significantly higher than the ambient subsurface densities, indicating that a stratification structure close to the initial state is becoming re-established, which finally initiates the re-operation of the overturning. After the switch-off of the acceleration, a dramatic increase of peak winter SSD occurs, which is responsible for the sudden jump of the AABWF intensity after acceleration, as shown in Fig.6.12b.

In the Weddell Sea, however, we do not see the above processes. Although the decrease of densities at the two deeper levels is as evident as those shown in the Ross Sea, the surface winter peak SSD is reduced so much at the early stage of normal integration and still keeps decreasing through the course of the acceleration

to such an extent that the surface water remains far less dense than the interior water beneath for the whole time. With such a stable stratification, deep convection is not able to occur (Fig.6.14d) in this region, and therefore the overturning off Antarctica there does not return.

The above discussion also applies to the ATGM2 run which sees a very similar destabilization of the water column stratification off Antarctica and thus a similar process of resumption of the Ross Sea overturning and a perpetual shutdown of the Weddell Sea overturning.

6.5 Barotropic Flow: ACC Transport

By the end of the ATGM3 and ATGM2 runs, the global ocean barotropic flow (not shown) settles down to a quite stable state under the 3×CO_2 condition, which is very similar in geographical pattern to the initial state, except for some changes in the intensities of all the major gyres. However, during the course of the accelerated integration and the following normal extension, significant adjustments occur in the world ocean currents in response to the substantial re-arrangement of the thermohaline conditions and the THC pattern, especially for the Southern Ocean overturning shown above, and to the continual change of surface windstress forcing. Examination of this evolution and the relevant processes may help our understanding of the association of barotropic flow, especially the ACC transport, with the water mass properties and the THC state.

Fig.6.16a shows the time series of ACC transport in the ATGM3 and ATGM2 runs. Dramatic variation occurs in the ACC flow during the Accelerated period in both runs. For the case of ATGM3, the ACC drops quickly from a level over 150 Sv to a minimum less than 110 Sv in the first two centuries, jumps back to a high level over 140 Sv within the next few decades and then fluctuates between 127 and 140 Sv on to the end of acceleration. In the following century of normal mode adjustment, the ACC increases to a level close to that achieved prior to the acceleration and

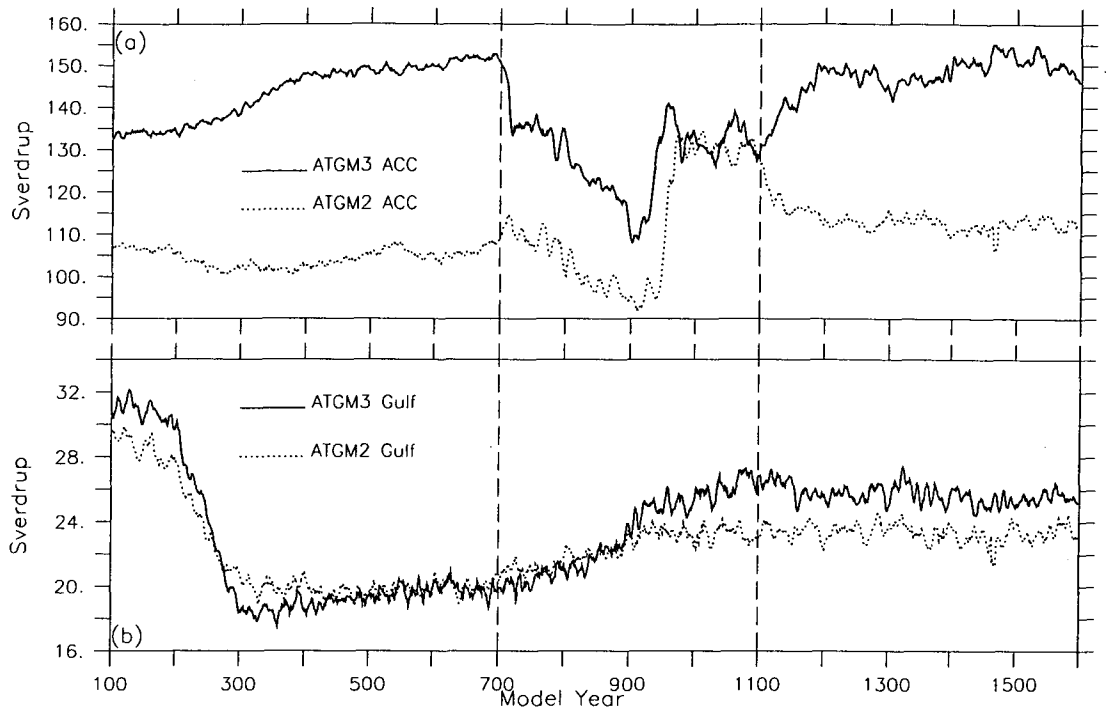

Figure 6.16: Time series of the ACC and Gulf Stream transports in ATGM3 and ATGM2: (a) ACC transport, (b) Gulf Stream.

then generally remains at this intensity through the rest of the run. This process of variation in the ACC transport can be readily explained by the evolution of the meridional density structure across the ACC and the re-organization of the Southern Ocean overturning, based on our discussion in Chapter 5. A similar analysis is performed and we present the time series of zonal mean density contrast (averaged over the layer from the surface to 2250 m depth) in Fig.6.17. In the first half of the accelerated integration, we see a large reduction in the meridional density gradient across the ACC, particularly the apparent 'straight drop' following the acceleration. This implies a flattening of the tilted 'sea surface', due to the accelerated warming in the interior of the high latitude Southern Ocean (south of the ACC). Such a change is responsible for the decline of the ACC during the same period, namely, a large reduction in the southward flow causes a slowdown of the geostrophic eastward current in the upper layer. From year 900 on, the reactivated overturning off Antarctica and the associated deep ocean northward flow (see Fig.6.12bc) lead to a rapid increase of the southward (return) flow in the mid-depth layer, which acts to accelerate the ACC current. In this period, the change in density contrast across the

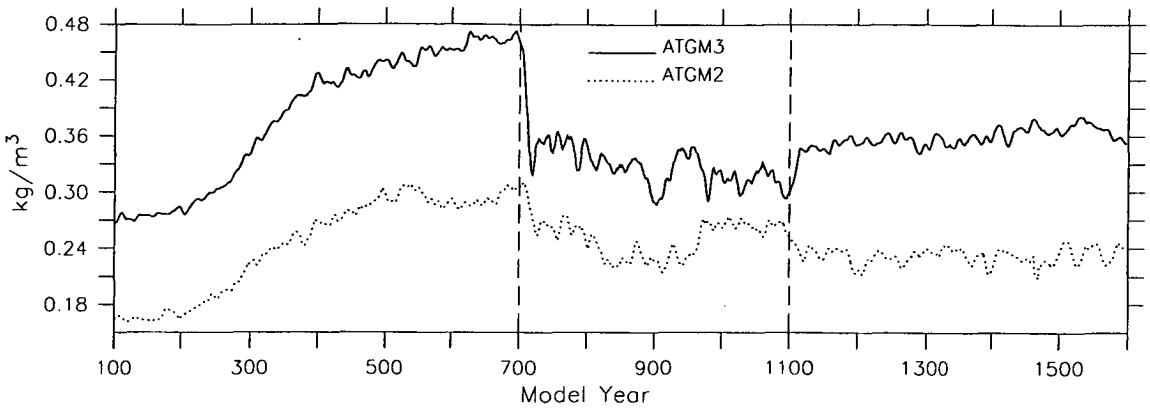

Figure 6.17: Time series of meridional density contrast across ACC, averaged over 0–2250 m depth and around the globe.

ACC also makes a contribution but its impact become secondary. During the final normal mode adjusting period, the AABWF is further enhanced, which, together with the small but sizeable increase of the meridional density gradient, brings the ACC transport back to a high level, the final quasi-equilibrium state.

For the case of the ATGM2 integration, we see a similar but much more moderate decline of the density contrast across the ACC in the first two centuries of acceleration. Accordingly, the ACC transport deceases steadily to a minimum during the same period. Thereafter, the resumption of AABWF brings the ACC to a maximum of about 135 Sv promptly. We note that the sudden increase of the ACC is up to 43 Sv in ATGM2, significantly larger than the 33 Sv for ATGM3 during (roughly) the same period. This is because the renewed AABWF in ATGM2 is much stronger than its ATGM3 counterpart (Fig.6.12b) in this period. In addition, due to the relatively stable AABWF plus a firstly enhanced and then little changed density gradient in ATGM2, the ACC remains quite stable through the latter period of the acceleration, whereas ATGM3 sees fairly strong fluctuation in ACC transport because of the largely varying AABWF and density structure. Following the switch-off of acceleration, a quick and large decline of the ACC transport is evident in ATGM2, in sharp contrast to the increase of the ACC in ATGM3. This is the consequence of the ramp-down of both the AABWF and the density gradient at the early stage of the normal mode adjustment.

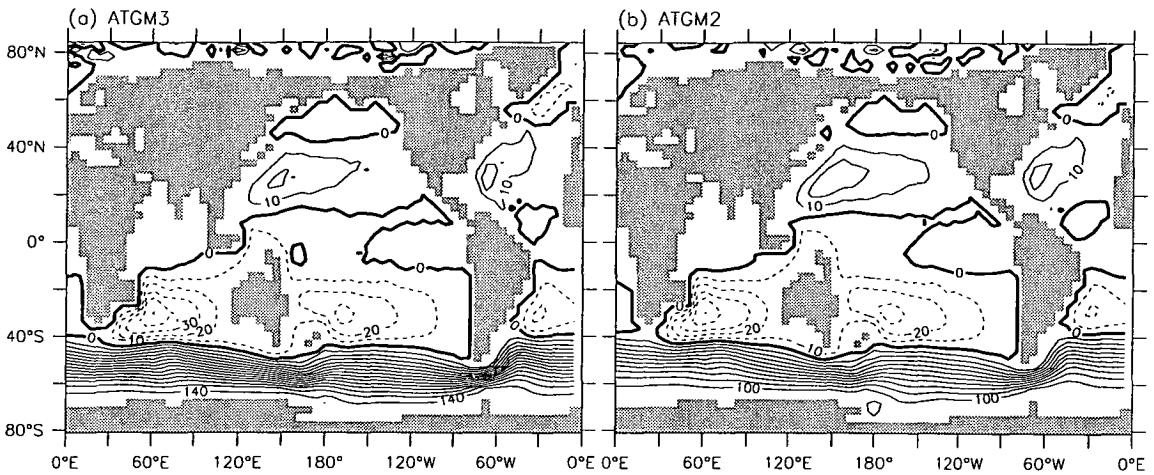

Figure 6.18: Last 100 year mean global ocean barotropic flow pattern in ATGM3 and ATGM2.

The above features of the ACC evolution during the accelerated period and normal mode extension, including both the similarity and differences between the two runs, further confirm our conclusion about the association of the ACC with the zonal and depth mean meridional density gradient and the downwelling off Antarctica, as addressed in Chapter 5.

We also show the evolution of the Gulf Stream in Fig.6.16b. It can be seen that the acceleration does speed up the recovery of the Gulf Stream transport in both runs but in general there are no sudden changes like those seen for the ACC. The increase stops from the second half of acceleration in ATGM2 but lasts for a much longer time in ATGM3. The final equilibrium of Gulf Stream is quite stable, with an intensity considerably weaker than its control climate, indicating an incomplete recovery in both runs. However, the initial deviation of intensity between the two runs is finally recovered, although we see a much larger reduction in ATGM3 during the period of CO_2 increase. As already discussed, the Gulf Stream is mainly driven by the surface windstress, and the NADWF also plays an important role in affecting its intensity. Fig.6.6 shows that the major driving factors, i.e., the low latitude easterly trades and the mid latitude westerlies, are further (slightly) reduced during the course of the integration after year 700 for both runs, and are largely responsible for the weakening of Gulf Stream intensity relative to the control climate. Another reason for this change may be the incomplete recovery of the NADWF. As already

shown, the NADWF penetrates significantly shallower in the new equilibrium, which results in a weakening or even no motion in the zonal flow below 2500 m depth in the North Atlantic, naturally reducing the vertically integrated barotropic flow there.

Finally, we present the last 100 year average global ocean geographical pattern of the barotropic flow in Fig.6.18. It may be regarded as the final (quasi-)equilibrium state under 3×CO_2 conditions for both runs. All the major gyres operating in the control runs are still evident and are basically the same as their initial climates except for some small changes in the intensities.

Chapter 7

Concluding Discussions

The primary aims of this study have been to realistically simulate the world ocean water mass properties and those of the major basins to global scale thermohaline circulations, such as the Southern Ocean overturning using the CSIRO OGCM, then to investigate the stability of world ocean THC, especially the responses of AABWF, to long-term global warming forcing induced by atmospheric CO_2 increase in the CSIRO coupled climate model. It is also aimed to explore the possible final equilibrium of the ocean system under a stable but elevated $3\times CO_2$ condition, and to examine the dependence of the ocean climatic responses to global warming on the basic state of ocean. In the following discussions, some concluding summaries are presented to highlight the results achieved from the above work, with a focus on the solution for the coupled climate model with the improved ocean sub-model (GM3).

Conclusion 1: *A new formulation of the ocean model, including a modification of the surface thermohaline forcing fields, a change of the dynamic boundary forcing data, and the use of more realistic isopycnal thickness diffusivity in the ocean interior, leads to a largely improved ocean spinup solution in terms of world ocean water mass properties, thermohaline circulations, and barotropic flows such as the ACC transport. This new solution provides the CSIRO cou-*

pled model with a more realistic initial state of the world ocean for climate change studies.

It is widely recognised that any model used to investigate climate change must be able to represent reasonably well the large scale features of the world ocean thermohaline circulation. Accordingly, the ability to realistically simulate the temperature and salinity distributions is essential for a prognostic ocean model. In this context, among various surface forcing strategies, we have chosen a modified form of the traditional relaxation method for the ocean spinup integration because it appears to be the most appropriate boundary condition for our model to generate a stable and realistic oceanic thermohaline climate. Clearly, whether or not the ocean spinup solution is reasonably close to the observations also strongly depends on the relaxation fields and the validity of the observations. Early versions of the CSIRO OGCM that restore the model SSS and SST to the original Levitus (1982) SSS and BMO SST climatologies show a considerable deficiency of water mass properties (e.g., too weak stratification in the high latitude Southern Ocean resulting from a low salinity bias at depth), and weak as well as shallow-penetrating North Atlantic overturning, due initially to the failure of the relaxation fields in yielding a reasonable annual cycle for the model surface water properties, especially the late winter peak surface density in the deep water mass formation regions. In addition, it is recognised that there are problems in the Levitus data set for winter conditions under the polar ice covered waters. Starting from this point, we carefully tune the above mentioned relaxation fields in the high latitude oceans, particularly the North Atlantic and the Southern Ocean, through the course of the annual cycle, for the purpose of producing more realistic model SST, SSS and SSD .

Our moderate modification to the tracer relaxation data leads to a significant improvement of the world ocean water mass production and a much stronger, deeper-penetrating North Atlantic overturning. (It is noted that, while the Southern Ocean stratification is largely strengthened and thus matches the observations quite closely, as a natural consequence, the intensity of the downwelling off Antarctica is considerably reduced). Furthermore, we replace the Hellerman and Rosenstein (1983) wind-

stress data with the NCEP reanalysis climatology based on the judgement that the NCEP data are generally more realistic over most regions, particularly the tropical oceans and the Circumpolar Ocean. This new dynamic boundary forcing, together with our use of a much smaller (and thus more realistic) isopycnal thickness diffusivity in the ocean interior, results in generally better depth-integrated oceanic flows. For example, the ACC transport is in very good agreement with observations.

This re-formulated spinup solution is thus used to initialize the coupled model ocean climate. It also benefits the climate model by a further suppression of climate drift in the coupled control run, which covers 800 years and now shows negligible long-term trends in terms of the world ocean THC and the water properties at the surface and in the ocean interior. The success of our model in representing an ocean climate which more closely matches the observations in both stand-alone and coupled modes strengthens our confidence that the coupled model can also do a better job in climate change simulations. For example, it might be expected to provide a more realistic sensitivity of the THC to surface thermohaline perturbations, and therefore more reliable climatic responses of the world ocean to external forcings, such as CO_2 induced global warming.

The above achievement of our new model version GM3 is validated mainly through comparisons of model results from GM3 and the prior version GM2 with the Levitus (1994) observation data compilation. The major differences between the two versions seen in the ocean spinup solutions are generally well maintained through the coupled control runs in most of the oceans, particularly those climatically sensitive regions. This makes it possible for us to examine the dependence of the ocean climatic response to CO_2 induced global warming forcing on the basic state of ocean.

Conclusion 2: *The world ocean THC, especially the Southern Ocean overturning is extremely sensitive to global warming forcing. In our integrations with a transient/stabilization CO_2 scenario, the NADWF weakens substantially in the first two centuries due to the joint effect of surface freshening and heating from above, while the AABWF essentially ceases by the time of CO_2 tripling, at-*

tributable almost completely to the surface freshening around Antarctica. During the subsequent millennium of stable 3×CO_2, NADWF recovers slightly but the AABWF shows no sign of returning. In addition, as a result of changes in the Southern Ocean meridional density structure, the ACC transport increases considerably.

We have examined the transient and long-term behaviour of the global ocean at the surface and in the interior under a scenario of transient increase of CO_2 (IPCC/IS92a) followed by a perpetual 3×CO_2 stabilization. Pronounced changes of world ocean THC occur during the CO_2 increase period: the NADWF weakens rapidly from near 20 Sv to a minimum of less than 12.5 Sv soon after CO_2 stabilization, and the Southern Ocean downwelling through the 1250 m depth drops dramatically to near zero before CO_2 tripling, which indicates an essential shutoff of the AABWF.

Surface freshening in the high latitude Southern Ocean is found to be responsible for the shutoff of AABWF. Three factors contribute to the surface freshening around Antarctica. Firstly, CO_2 increase warms the atmosphere, enhancing the poleward atmospheric moisture transport and leading to an increase in the excess of precipitation over evaporation over high latitude oceans. Secondly, due to the assumption of constant terrestrial water mass (i.e., ice-sheet/shelf) in our model, enhanced P-E over the Antarctic continent leads to an enhanced runoff into the surrounding oceans. Thirdly, surface warming reduces the ice formation near Antarctica and thus leads to a decrease in the northward transport of sea ice out of the Antarctic coast associated with Ekman drift, in effect causing a net freshwater gain in the coastal regions.

The above changes freshen the surface water near Antarctica rapidly, strengthening the stratification to such an extent that the deep convection off Antarctica is suppressed completely and the AABWF collapses. In this period, surface warming around Antarctica plays only a minor role in stabilizing the water column. Similarly, large freshening also occurs over the North Atlantic due to the enhancement of local P-E and runoff from the continents, acting to stabilize the water column. However,

the surface warming from above unlike that in the Southern Ocean is found to play a role at least as important as the freshening in weakening the NADWF. In fact, freshening over the North Atlantic, say, between 45 °N and 65 °N, dominates the reduction in sea surface density during the first century of CO_2 forcing but surface warming takes over thereafter. The shutoff state of AABWF is maintained through the whole period of CO_2 stabilization (1100 years), due to the persistent freshening around Antarctica. As a contrast, the NADWF appears to recover slowly after reaching its minimum soon after CO_2 tripling, resulting mainly from the relatively rapid warming in the ocean interior (due to the remaining NADWF) and the slight decrease of surface freshening (after year 400).

Accompanying the development of global warming, surface windstress fields are continuously adjusting. This leads to significant changes in the wind driven horizontal currents. All the subtropical gyres, as depicted by the depth-integrated barotropic flows, are more or less weakened in accordance to the weakening of overlying wind forcings. For the Circumpolar Ocean, even though it is the only part of the world oceans where there is no continental barrier, the ACC transport appears to be little influenced by the change of windstress. Instead, its strength largely determined by the thermodynamic and dynamic adjustments to the ocean interior off Antarctica and across the ACC, although the westerly wind is one of the major driving forces for setting up the basic state of the ACC control climate. Under CO_2 forcing, while surface warming in the high latitude Southern Ocean can not be efficiently transported into the ocean interior with the collapse of overturning, rapid warming occurs in the ocean interior, say, the subsurface layer to the north of the ACC, owing mainly to the southward heat transport by the world ocean conveyor belt. This causes larger and larger meridional density contrast across the ACC, strengthening the southward flow in the upper (and subsurface) layer, leading to an increase in the eastward current in this layer. Furthermore, the shutoff of AABWF and the decline of the deep overturning cell lead directly to a substantial reduction of southward return flow in the mid-depth layer, which causes a drag to decelerate the ACC flow. However, in the case of our TGM3 run, the effect of acceleration in the upper layer

dominates, and therefore the ACC transport shows a steady increase until it reaches a maximum by around year 700.

In the latter part of the $3\times CO_2$ stabilization period, a new balance seems to have been gradually established at the air-sea interface in terms of the thermal, hydrological and dynamic exchanges between the ocean and the atmosphere. In the meanwhile, with the collapse of AABWF and the cessation of deep ocean overturning, the global ocean climate evolves very slowly. An important scientific question for the long-term ventilation of the deep ocean is whether or not the Southern Ocean overturning eventually resumes under stable and elevated CO_2 levels. An additional run with accelerated deep ocean adjustment is conducted to address this question.

Conclusion 3: *Accelerating the convergence to equilibrium of the deep ocean solution under $3\times CO_2$ conditions, we see that the global THC eventually reaches a near-stable state with the deep ocean warming being over 7 °C. The NADWF is recovered to its initial intensity but with a shallower penetration, and the AABWF partly re-established. However, for this accelerated solution, especially the Southern Ocean overturning, it needs a few more hundred year synchronous integration to further adjust and finally settle down to a normal mode equilibrium.*

In the course of the transient/stabilization integration, the global ocean upper layer is warmed rapidly during the first few centuries, but thereafter the rate of change is considerably reduced. In contrast, the mid-depth and deep ocean respond very slowly at first, but the rate of warming gradually catches up with and finally exceeds that at the surface. A reasonable expectation is that the long-term deep ocean warming may eventually destabilize the water column to such an extent that the Southern Ocean overturning can be reactivated after, say, some thousands of years. In that case, the associated deep ocean ventilation will be in operation again and the world ocean naturally evolves into a new equilibrium under the $3\times CO_2$ condition.

The accelerated integration, which uses depth-dependent time steps in the ocean sub-model and lasts for 400 (surface) years from the end of year 700 (of the normal run) with stable $3\times CO_2$, has confirmed this speculation. After around 230 years' acceleration (i.e., 6300 deepest ocean years), the AABWF is seen to come back strongly from zero to nearly 10 Sv within 30 years (820 deepest ocean years) and then fluctuates between 5 and 10 Sv for the remainder of the integration, generally stronger than its control climate. The deep ocean overturning is also triggered in a sudden manner by the resumption of downwelling off Antarctica. The NADWF reintensifies much more moderately and eventually reaches its initial intensity after about 220 years (6030 deepest ocean years). Examination of the thermohaline conditions in the high latitude Southern Ocean reveals that the re-commencement of AABWF is initially the result of warming in the ocean interior. Under acceleration, deep ocean warming exceeds the near surface layer warming in due course, which gradually weakens the water column stability and activates intermittent convection in the region near Antarctica, especially the Ross Sea. As the convection occurs more and more frequently and penetrates deeper and deeper, it brings more and more salt and heat from the deep ocean up to the surface, increasing the SST more strongly and thus leading to more evaporation, producing somewhat denser surface water in winter, destabilizing the water column further. When the winter peak surface density surpasses the densities of ambient deep levels, a stratification structure close to the initial state becomes re-established, which finally initiates the re-operation of the overturning and brings the system into a new quasi-equilibrium.

We have noted that the recovery of world ocean THC under the perpetual $3\times CO_2$ condition is incomplete. Firstly, downward penetration of the North Atlantic overturning is significantly shoaled. Secondly, the Antarctic downwelling is only partly re-established: the Ross Sea sees largely enhanced overturning but the Weddell Sea, which initially contributes most of the AABWF for the global ocean, sees no overturning re-occurring due to the extremely large freshening at the surface suppressing the occurrence of deep convection there. In addition, this accelerated solution seems not to be exactly the final result of $3\times CO_2$ forcing. An extension of 500 years nor-

mal mode integration shows a noticeable adjustment in the world ocean THC, in particular the Southern Ocean overturning. AABWF further intensifies remarkably after the switch-off of acceleration and so does the deep ocean ventilation. However, no change is evident in the Weddell Sea during the final normal mode adjustment, and in particular, the overturning does not come back.

Both the paleoceanic records and modelling research in recent decades have revealed the possible existence of multiple equilibria in the ocean climate and the transition between different circulation modes under certain external forcings. Under the IPCC/IS92a scenario, the CO_2 equivalent of greenhouse gases in the atmosphere increase to three times the pre-industrial level before the end of this century. We have shown the transient and long-term behaviour of the global THC under stable $3\times CO_2$ forcing in the CSIRO climate model. A new oceanic climate, clearly different from the control state, is seen soon after CO_2 tripling. Such a state, mainly featured by the shutoff of AABWF, stagnancy of deep ocean ventilation, and a substantial weakening and shoaling in the NADWF, is maintained for such a long time, with little change in terms of the THC pattern, it may be thought to represent a quasi-equilibrium of the ocean under the stable $3\times CO_2$ condition. However, this state is not stable because the ongoing warming in ocean interior can eventually give rise to a reintensification of the global THC and thus a new equilibrium. This process of transition between different circulation modes under the *same forcing* is evident in our accelerated integration.

Conclusion 4: *Differences in the initial ocean state between model versions seems not to cause substantially different responses of the ocean and the coupled system to CO_2 induced global warming in terms of large scale climate features. We see generally similar changes of all major variables in the course of the two parallel runs and quite close final equilibria, despite some evident differences of details.*

An initial motivation for this study was the possibility that differences in the basic ocean state may lead to different behaviours of the world ocean THC under CO_2

anomaly forcing. The two parallel integrations documented in this thesis however show no substantial distinction of climate change in all the major climate variables at the surface or in the ocean interior, although one of the runs has clearly a more realistic control climate for the ocean, especially the stratification of the Southern Ocean, than the other. Both runs show a temporary decline of the NADWF, a long lasting shutoff of the AABWF, an eventual resumption of the Ross Sea overturning and a perpetual close-down of the Weddell Sea overturning, as already discussed. Therefore, no critical dependence of climate change on the basic state of ocean is evident in the CSIRO climate model, at least for these two versions with generally the same physics in the ocean.

One reason for this may be that, even though CGM2 had some offsets with observed ocean water mass properties, the pattern of the global distribution was generally reasonable and the global THC was not too unrealistic. Although these were improved in CGM3, the climate warming responses were not found to be greatly different. A carollory from this is that further improvements to the basic state of the ocean model are not expected to substantially change the response found here.

However, some differences of the oceanic changes under CO_2 forcing between the two versions are of scientific interest and thus deserve further discussion. In the North Atlantic, for example, the TGM2 integration shows a larger and longer lasting decrease in the NADWF intensity at the early stages of CO_2 forcing. Two centuries after CO_2 tripling, the NADWF drops to a minimum of 4.6 Sv from the initial value of 14.3 Sv, indicating a reduction up to nearly 70%, contrasting the largest reduction of 37% reached soon after CO_2 stabilization and a gradual recovery thereafter in TGM3. This difference in behaviour does result from the difference in the NADWF control climates between the runs. As can be understood, stronger overturning circulation in TGM3 transports warm water from low latitudes to the NADWF region more efficiently, causing larger buoyancy gain at the surface and therefore a more rapid reduction in the overturning intensity. At the same time, more heat is brought into the ocean interior, which destabilizes the water column, thereby resisting the weakening of NADWF and leading to a quicker restoration of the

NADWF thereafter.

Another example is the ACC transport, which behaves rather differently in the two runs during the first several centuries with CO_2 forcing. While TGM3 experiences a steady increase in the ACC flow until year 700, TGM2 suffers an evident decrease in the ACC flow in the CO_2 ramp-up period and a gradual recovery thereafter. Such a contrast is also closely associated with the difference in the THC control climate between the two versions. On the one hand, the stronger NADWF in TGM3 leads to a stronger world ocean conveyor belt, which transports more heat southward to the ocean interior north of the Circumpolar Ocean, causing a larger density contrast across the ACC and thus a stronger acceleration of the ACC flow in the upper layer. On the other hand, because the initial intensity of the AABWF in TGM2 is about 14 Sv, at least twice that in TGM3, it is much more important to the ACC transport in TGM2 based on the recognition that the contribution of AABWF to the ACC flow is (roughly) proportional to the AABWF intensity. Therefore, the decrease and shutoff of AABWF in TGM2 results in much larger reduction in the ACC transport, which more than cancels the acceleration in the upper layer, causing a decline in the ACC flow in the first few centuries of CO_2 forcing.

Remarks: *The coupled model's use of flux adjustment, the coarse horizontal resolution, the (steady state) treatment of the Antarctic ice sheet mass, and the neglect of the effect of anthropogenic sulfate aerosols in the forcing may all bring some uncertainty into the details of the results. Nevertheless, our experiments provide an indication of the possible future changes and evolution of a near-steady state for the global thermohaline circulation under enhanced CO_2 conditions in a fully coupled model of the current generation.*

We note that the question as to whether the flux adjustment technique, to accommodate the initial mismatches in atmosphere and ocean fluxes, is appropriate for the case with so large climate changes such as the THC breakdown, is still under debate (e.g., Manabe and Stouffer 1994, Egger 1995, Schmittner and Stocker 1999). Not taking into account the effect of anthropogenic sulfate aerosols, which offsets

some of the CO_2 induced global warming, especially in the Northern Hemisphere, may have caused a more or less overestimate of the model's climate sensitivity, although such an effect is expected to be much smaller later in the 21st century (P. Whetton 2001, personal communication). The model's resolution, especially the coarse horizontal resolution; causes difficulties of representing the fine features of the sea ice near Antarctica such as the ice edge and continental shelf region which are important for the surface heat flux and the thermohaline overturning, and of representing accurately the ocean topography and hence the water mass formation processes and locations in both the North Atlantic and the Southern Ocean. The assumption of constant mass for the terrestrial ice in the course of integrations under CO_2 forcing may lead to too much runoff from the Antarctic continent initially and thus an overestimate of the surface freshening around Antarctica. This is especially the case for the Weddell Sea due to the effect of Antarctic catchment which is also somewhat associated with the coarse resolution. On the other hand, for the longer term much more runoff may be expected from the basal melting and flow of the continental ice. Therefore, for long term climate change simulations lasting many centuries the effects of changes in the large ice sheets of Greenland and Antarctica need to be included in the freshwater fluxes for the global ocean.

In addition, the deep ocean acceleration method may also bring uncertainty to the details of the equilibrium solution of the ocean due to the deep ocean flushing of freshwater from the surface after the resumption of AABWF (see Appendix B). To eliminate the possible contamination of such a low salinity bias in the deep ocean, and/or to examine whether or not the flushing still occurs when the AABWF comes back 'naturally', i.e., with no acceleration, an additional normal mode integration initialized from the end of year 920 in the accelerated run ATGM3 (just prior to the re-operation of deep convection off Antarctica) is under way. Finally, a set of new runs using a more recent version of the CSIRO model (Mark2) are also under way, which takes into account the effect of aerosols and sets the Antarctic runoff fixed to the initial average control values (i.e., allowing for the accumulation of ice volume over the Antarctic continent). The response of AABWF to CO_2 forcing, especially

the Weddell Sea overturning in the new transient run is expected to be somewhat different from what we presented in this thesis. For a more complete analysis there is a need to include interactive coupling between the coupled climate model and ice sheet models for Greenland and Antarctica.

Appendix A

Surface Adjustments for CGM3/CGM2

A.1 Aim of Surface Adjustments

As is well known, in coupled atmospheric-ocean modelling, climate drift is a common deficiency for all the existing coupled models around the world. It is generally found that, when two separate submodels of the atmosphere and ocean are coupled together, the coupled system either tends to drift into a new climate equilibrium state which is far from the pre-coupling climate or just crashes before reaching a stead state. In the first case, the coupled model final state may be so unrealistic that climate response for sensitivity experiments relative to this state could become meaningless. Many studies have been conducted to investigate this drift extensively (e.g., Weaver and Hughes 1996; Cai and Gordon 1998) and revealed that it results from the systematic mismatches between model components in principal fields such as poleward heat and moisture transports and, obviously, it is an extremely sensitive indicator of some model imperfections.

To avoid the systematic climate drift of a coupled model, Sausen et al. (1988) proposed a flux adjustment method which *ensures that the coupled model operates at*

the reference climate state for which the individual model sub-systems were designed without affecting the dynamical response of the coupled system in climate variability experiments. Such a technique has since been employed in many coupled models (e.g., Cubasch et al. 1992; Manabe and Stouffer 1993, 1994; Murphy and Mitchell 1995; Lunkeit et al. 1996; Gordon and O'Farrell 1997; Hirst et al. 2000) and efficiently removed the major drift of the coupled system from the realistic pre-coupling spinup states of the components. It is generally believed that, as per Manabe and Stouffer (1994), the surface flux adjustments are independent of the magnitudes of the anomalies in temperature and salinity at the oceanic surface, and thus do not explicitly affect the damping rate of these anomalies. Furthermore, in spite of the systematic biases of the models, the flux adjustments do a generally good job in maintaining the SST and SSS near the initial states which are close to the observed distributions, and thus allow the model state to be perturbed or fluctuate around a realistic surface condition.

It must be mentioned, however, that the use of flux adjustments also brings in an undesirable effect which is not physically founded. In addition, the amounts of the adjustments are often larger than the climatological mean fluxes themselves, especially in some climatically sensitive regions. This kind of flux adjustment, as addressed by Weaver and Hughes (1996) and Nakamura et al. (1994), can cause difficulty for the coupled model in studying the oceanic climate stability/variability. For example, ocean modelling studies have revealed that the THC can behave diversely under "mixed boundary conditions", i.e., a specified freshwater flux with thermal damping (e.g., Weaver et al. 1993; Pierce et al. 1995; Osborn 1997), depending on the the imposed or spontaneous perturbations in the freshwater flux. Furthermore, Cai and Chu (1996) demonstrated that change in thermal damping can also cause anomalous climate variability and drift regardless of the forcing condition for salinity. Such an oceanic feature makes it difficult to study the variability in a coupled model which uses flux adjustments, in particular large amounts of flux adjustment, because the flux adjustments may also be a factor which generates oceanic variability and instability and thus contaminates the interpretation of the effect of external

forcing on the coupled system.

Despite the possible contaminating effect, flux adjustments are inevitable for maintaining a realistic climate in coupled model experiments unless the OGCM implied ocean heat and freshwater transports are used as constraints for tuning the AGCM to present day climatology (Weaver and Hughes 1996). On the other hand, the improvements in both the AGCM and OGCM, including finer model resolutions and more appropriate parameterizations of some important physical processes (such as clouds within the atmospheric component) can reduce the need for flux adjustments in the coupled model. For example, the NCAR Climate System Model (NCAR-CSM) (Boville and Gent 1998) which employs new state-of-the-art parameterizations in both its atmospheric and oceanic components, together with "the most appropriate boundary conditions", i.e., fluxes at the surface, for the component models, has been run for 300 years with no flux adjustments applied and the results show virtually no trend in the surface temperature. This is certainly marked progress in coupled model development. However, the success is still very limited because only part of the inconsistency between the model components is removed by tuning the pre-coupling spinups carefully, and, there occur significant drifts in many other fields, especially in the deep ocean. More recently, a new version of the Hadley Center coupled model (HadCM3, see, e.g., Gordon et al. 2000) that does not require flux adjustments to prevent large climate drifts has been run successfully for a simulation of 400 years, with very little global mean SST drift (less than 0.009 °C per century) being found. Again, the improved simulation is a consequence of a greater compatibility between the atmosphere and ocean model heat budgets, which is attributed mainly to the enhancement of the ocean model resolution (i.e., 1.25° × 1.25°) and more extensive validation with observations.

The CSIRO coupled model mark2 version used for this study runs with the fluxes adjusted. This is due to the inherent incompatibilities in the surface fluxes required by the coarse resolution model components to maintain realistic climatologies. On the one hand, like many other AGCMs of the current generation, the CSIRO AGCM (R21) yields implied surface heat and freshwater fluxes (and thus the corresponding

meridional transports) significantly different from the observed due primarily to the deficiency in cloud parameterization in particular (e.g., Gordon and O'Farrell 1997). On the other hand, the present GM versions of the coarse resolution ocean model give realistic representation of the present climate only when the restoring forcings on surface temperature and salinity are used. As already shown in Chapter 3, a kind of bulk-flux forcing, which is employed in the NCAR CSM and is regarded as a much more realistic boundary condition for ocean models due to its similarity to the real flux forcing mode in the coupled system, is not suitable for our ocean model in terms of the water production.

A.2 CSIRO Coupled model Surface Adjustments

The flux adjustments for the coupled model runs are determined in the following way. Firstly, the atmospheric model was integrated for many decades to reach equilibrium. The surface fluxes of the final 30 years were averaged to give monthly climate, i.e., $Q_a(x, y, t)$. Here $Q_a(x, y, t)$ stands for one of the four kinds of implied fluxes, namely, the heat, freshwater, zonal momentum and meridional momentum fluxes from the atmosphere model. Secondly, the average of the diagnosed ocean surface heat and freshwater fluxes over the final 100 years of oceanic spinup (GM3 or GM2) were obtained and denoted by $Q_o(x, y, t)$. Note $Q_o(x, y, t)$ also stands for NCEP or H-R windstresses (zonal or meridional components) used to force the uncoupled ocean model, i.e., GM3 or GM2. For each of the 4 kinds of fluxes, the corresponding flux adjustment can be simply calculated by

$$F_{adj}(x, y, t) = Q_a(x, y, t) - Q_o(x, y, t) \tag{A.1}$$

where x, y indicate geographical position and t is time throughout the annual cycle, i.e., 12 months.

In the coupled mode, the fluxes passed from the atmospheric component into the ocean are adjusted by above adjustments and the resulting coupled model interface

fluxes are therefore

$$Q_c(x, y, t) = Q_a(x, y, t) - F_{adj}(x, y, t) \tag{A.2}$$

It needs to be mentioned that the ocean surface windstress in the atmosphere model spinup and in the coupled experiments is derived from the surface windstress over the open water areas; and for ice regions it is a combination of surface windstress over the leads and an ice-ocean interface stress for the ice-covered part.

We note that the above approach for the surface flux adjustments ensures that at the starting point of the coupled runs the atmospheric component provides the ocean component at the surface with flux forcing fields which are close to the corresponding diagnosed flux fields or initial forcing fields (in the case of windstress) at the stable stage of the spinup. However, at the 'starting point' of the coupled run, neither the ocean nor the atmosphere is the same as their states at the end of the spinups since the coupled run is initialized with the last 500 year average of the ocean spinup solutions and the last 30 year mean of the atmosphere spinup results. An incompatibility, no matter how small it is, naturally exists within and between the components, and therefore a residual drift is inevitable for the system following the coupling.

A.2.1 Heat and freshwater flux adjustments

Fig.A.1 shows the zonal mean surface heat and freshwater fluxes (into the ocean) implied by the atmospheric spinup and diagnosed from the ocean spinup GM3, respectively, for DJF, JJA and the annual mean. Also shown are the corresponding adjustments for the coupled control run CGM3, and the adjustments for another coupled control run CGM2 which is based on the GM2 ocean. It can be seen that the adjustments for both the heat and freshwater fluxes are generally large in terms of the seasonal and annual mean for mid to high latitudes in particular.

In the case of heat flux, the major adjustments occur in the southern high lati-

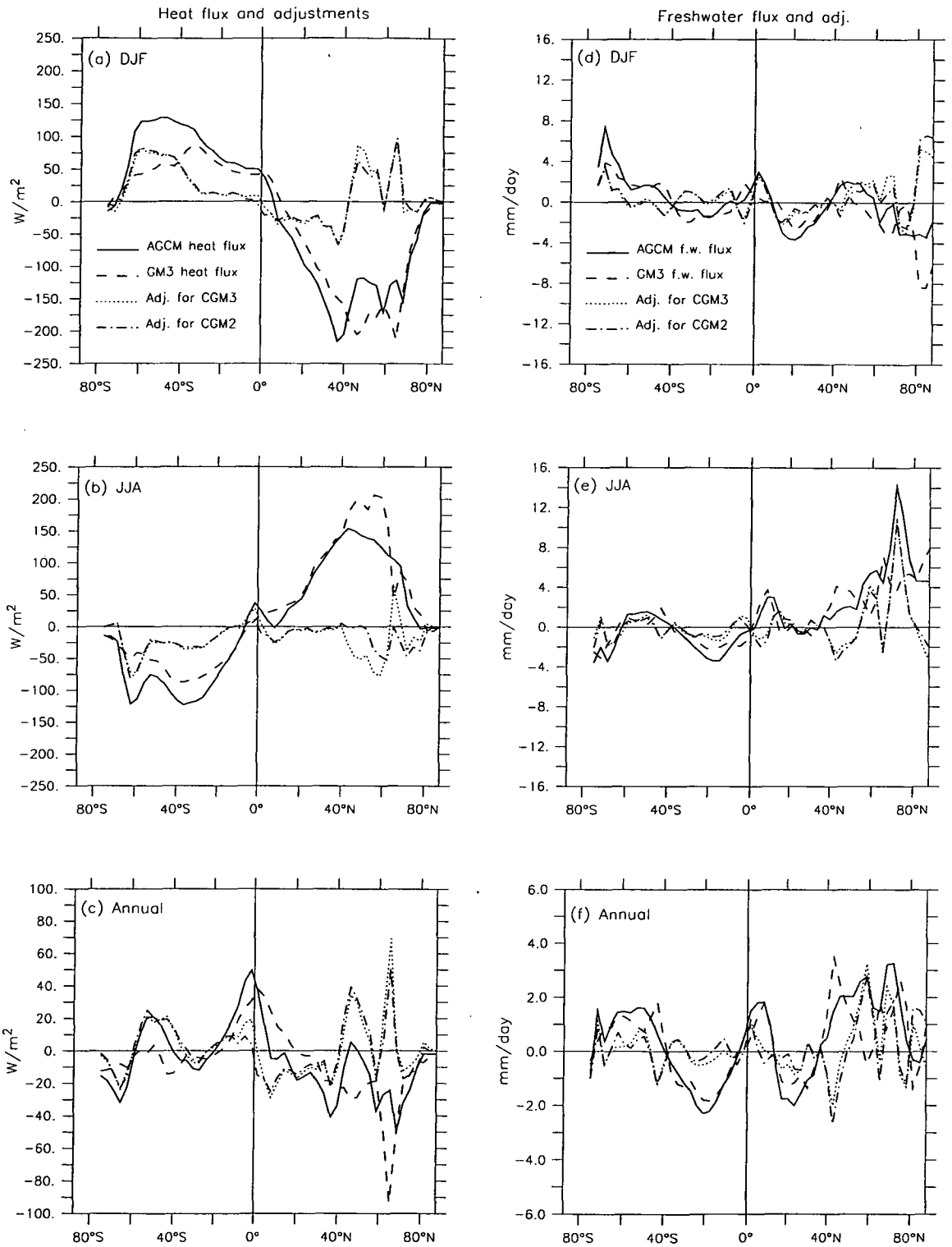

Figure A.1: Zonal mean surface heat and freshwater fluxes from AGCM and OGCM-GM3 and adjustments for CGM3 and CGM2.

tudes in winter and summer due partly to the insufficient cloud cover there (Gordon and O'Farrell 1997) and the region of the sea ice margin at around 60°S shows over 70W m^{-2} discrepancy between the atmospheric and ocean model implied heat fluxes in both seasons. In the NH, substantial adjustments are needed for nearly all latitudes in winter, with the largest value of 92W m^{-2} at around 65°N and a remarkable average of near 70W m^{-2} in the 45–55°N band. In JJA, the latitudinal distributions of oceanic and atmospheric implied heat fluxes are in very good agreement in the northern low to mid-latitudes but considerable extra heat flux (e.g., about 44.5W m^{-2} for the band 40–62°N) is needed to make up for the insufficiency of heat from the atmosphere into the GM3 ocean north of 40°N except for a narrow band centered at 65.3°N where the atmospheric heat flux outweighs that required by the ocean. The annual mean curves also show systematic disagreement between the submodel implied heat flux distributions and significant flux adjustments are made for most latitudinal bands, with the largest amount being about 69W m^{-2} at 65.3°N. Finally, we see slightly larger adjustment needed for CGM3 than that for CGM2 in the northern mid to high latitudes due to the modification (enhancement) of the surface thermal forcing in the GM3 North Atlantic Ocean. At other latitudes, the difference in heat flux adjustments for these two versions of coupled runs is negligible.

With regard to the freshwater flux, the submodel implied distributions suffer even larger discrepancies than those shown in the heat flux curves for northern high latitudes in particular. In DJF, the southern ocean polar region sees 7.4 mm/day implied freshwater flux into the ocean (by sea ice melt and water inflow off Antarctica), which is nearly twice the amount (3.9 mm/day) required by the ocean model, whereas the north pole region freshwater flux out of the ocean implied by the atmospheric model in this season (mainly by ice formation) is less than half of that diagnosed from the salinity relaxation in the ocean model, with the discrepancy being as large as 5 mm/day. The largest disagreement occurs at the northern high latitudes in JJA as shown in Fig.A.1(e), where the atmospheric model implied flux into the ocean (by sea ice melt and water inflow off the northernmost coast) at

around 71.7°N reaches 14.2 mm/day, being nearly 4 times the ocean model diagnosed value (3.55 mm/day). However, examination of the geographical distribution of the atmospheric model surface fluxes (not shown) reveals that such a large zonal mean freshwater flux results mainly from the model overestimated river runoff at a few individual locations along the northernmost coast. The annual mean adjustment for the freshwater flux is still evident but the magnitude is much smaller particularly in the norther high latitudes. It is also clear that, the modification of the surface saline forcing for GM3 has not caused significant change in the need for freshwater flux adjustment in terms of the latitudinal distribution shown here.

A.2.2 Momentum flux adjustments

The zonally averaged surface windstresses generated by the atmospheric model and the NCEP windstresses used to force the ocean model (GM3) are displayed in Fig.A.2. Clearly these two sets of momentum fluxes are in generally good agreement for the seasonal and annual mean at most latitudes, with large discrepancy existing only at northern high latitudes in winter, which leads to marked annual mean adjustments there as well. This is the case for both the zonal and meridional stresses. More importantly, the NCEP stresses correspond to the CSIRO AGCM stresses much better than the H-R climatology in terms of the geographical distribution features discussed in Chapter 3 and the resultant stress adjustments are thus significantly smaller for CGM3 than that for CGM2 at nearly all latitudes, as indicated by the dotted and dot-dashed curves in Fig.A.2. In fact, the global ocean annual area-weighted root-mean-square adjustments of the zonal and meridional windstresses for CGM3 are 0.23 and 0.13 $\mathrm{N\,m^{-2}}$, respectively, contrasting with their counterparts of 0.27 and 0.19 $\mathrm{N\,m^{-2}}$, respectively, for CGM2.

It is worthwhile mentioning that the windstress adjustments are not really necessary for the coupled model runs especially in the case of CGM3. This follows since the NCEP stresses and the AGCM generated stresses are very close and the ocean climate achieved under the CSIRO AGCM wind forcing, i.e., CW3 shown in Chap-

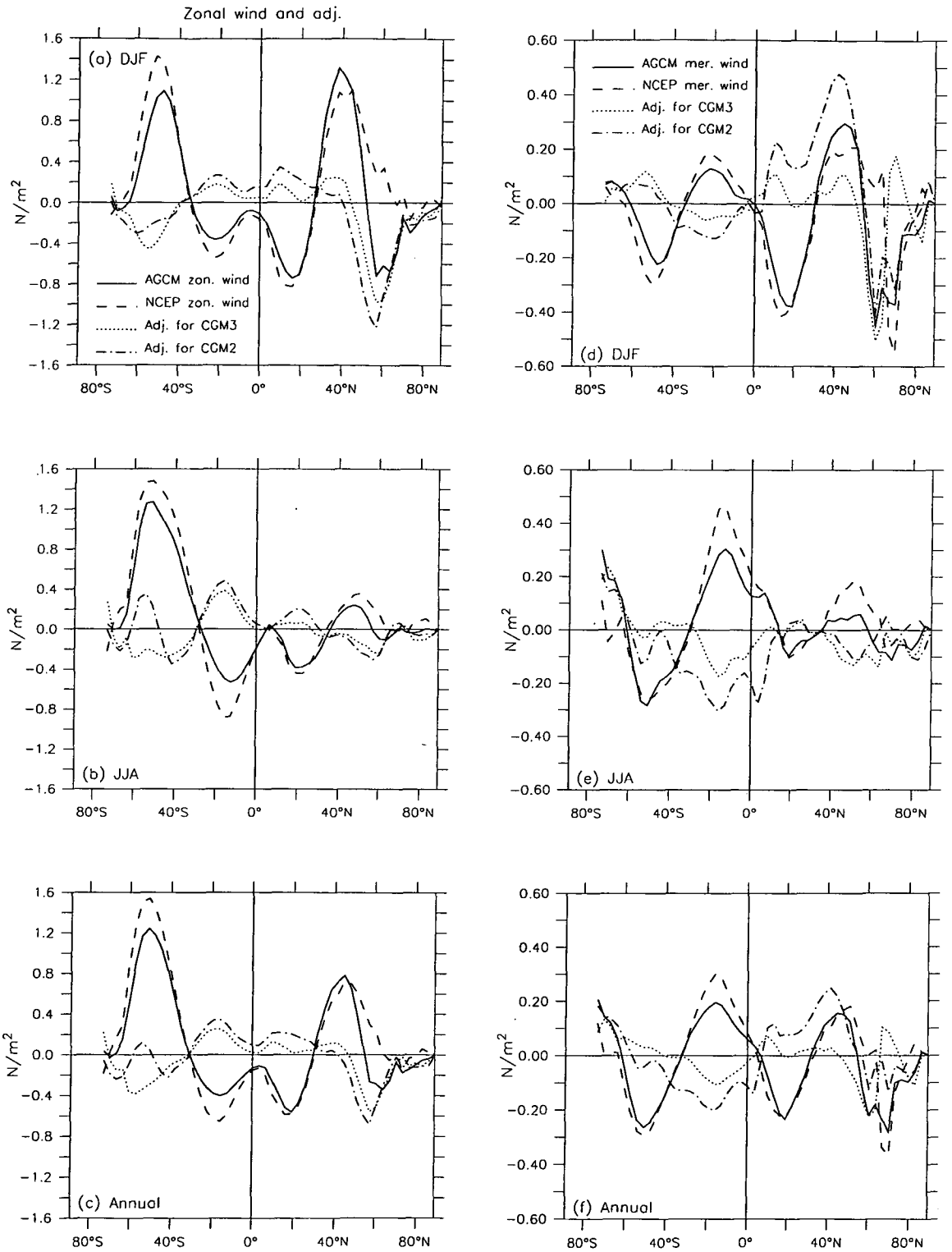

Figure A.2: Zonal mean surface windstresses from the AGCM and the NCEP data and the adjustments for CGM3 and CGM2.

ter 3, exhibits no significant difference from that of GM3. On the other hand, as addressed by Weaver and Hughes (1996), any small errors of the surface temperature and salinity in particular which arise from the AGCM windstress field will be indirectly adjusted through adjustments to the fluxes of heat and freshwater.

A.2.3 SST and SSS adjustments

In addition to the above flux adjustments, the CSIRO coupled model applies adjustments to the ocean surface temperature and salinity fields as well. The reason for doing such additional adjustment is as follows. Firstly, as is known, in order to ensure a realistic representation of the current ocean climate, the ocean model is usually forced at the surface using the observed SST and SSS climates, e.g., BMO SST and Levitus SSS for the GM2 integration. However, due to the imperfections in many aspects, ocean models especially those of coarse resolution have a common deficiency in that they yield surface temperatures different from the relaxation fields and these departures can be regionally very large (e.g., too low/high SST in the tropic/polar regions and large errors in and near the major western boundary currents). Such a deviation, on one hand, is used to diagnose the oceanic heat fluxes at the surface, and thus can not be removed by any means. On the other hand, it causes difficulty when the ocean model is coupled to the atmospheric-sea ice model, because the ice model, which is forced using the observed SST before coupling, requires that the SST yielded by the ocean model in the coupled system be at or very near the freezing point of sea water in the vicinity of the ice so as to maintain reasonable ice cover. Clearly, the warmer than observed SST in polar regions would seriously affect the performance of the ice model and thus must be adjusted before being passed to the ice model. The SST errors in other regions are adjusted at the same time in order to provide the atmospheric component with a realistic horizontal (meridional gradient in particular) distribution of the thermal forcing at the sea surface. For the GM3 version of the ocean model, although the surface relaxation SST field is modified based on the BMO SST climate and the resultant model SST

is a bit closer to the original BMO SST, there still exist marked deviations (e.g., as shown by Fig.2.1) which must be adjusted in the coupled model run, say, CGM3.

The details of the procedure for adjusting the surface temperature can be found in Gordon and O'Farrell (1997). For our study, no matter what the relaxation fields we use for the ocean spinups, the monthly adjustment term for each ocean grid point is obtained by

$$\delta T(x, y, t) = T_{BMO}(x, y, t) - T_{oc}(x, y, t) \tag{A.3}$$

where T_{oc} is the monthly averaged ocean model SST and the T_{BMO} the monthly climate of BMO SST which is used as the lower boundary condition for the atmospheric spinup in stand-alone mode.

For the coupled model, the SST simulated by the ocean sub-model are adjusted by adding δT before being applied as a lower boundary condition for the atmospheric sub-model. This approach enables, at least at the starting point of coupling, the atmospheric sub-model to have a suitable thermal forcing at the lower boundary. Fig.A.3a, A.3b and A.3c show the zonally averaged SST adjustments calculated from the ocean spinup uppermost level temperatures and the original BMO SST climate for DJF, JJA and annual mean, respectively. As already mentioned, the ocean model yields too warm SST in the tropical ocean and too cold SST at high latitudes and these errors are adjusted by increasing (decreasing) the tropical (polar region) SSTs for all seasons and annual mean. This is specially the case for GM2 which shows generally larger deviations from the BMO SST for the whole annual cycle compared with those of GM3. It is evident that the GM3 spinup yields colder and thus more realistic SST than GM2 in the southern high latitudes, especially the polar sea ice region off Antarctica. In summer, the southern polar ocean (south of 70°S) SST adjustment is 0.01 and -0.24 °C for CGM3 and CGM2, respectively, while the winter adjustment for a larger region in the Southern Ocean (south to 60°S) is -0.35 and -0.56 °C for CGM3 and CGM2, respectively. The adjustments in low to mid-latitudes are characterized by the changes of sign between seasons, i.e., increasing the ocean model SST in summer and decreasing it in winter, which enhances the

annual cycle of the ocean model SST in these regions and is apparently important to the atmospheric model simulation of the monsoons in particular. The largest adjustments for both seasons are found at the same latitude, i.e., around 43°N, which originate from the extremely large SST errors in and/or near the western boundary currents in the Pacific (i.e., up to -7 °C in the Kuroshio current in winter and 5 °C in the Japan and East China Sea in summer) and the Atlantic (i.e., up to -4 °C in winter and 3 °C in summer in the Gulf Stream). The reduced SST adjustments for CGM3 compared to CGM2 particularly in the southern polar region and the latitudes north of 40°N reflect the improvement in the GM3 SST simulation achieved by using modified thermal forcing fields, as addressed in Chapter 3.

The SSS simulated by the ocean sub-model is also adjusted in the coupled system (see Gordon and O'Farrell 1997 for details) and the corresponding zonally averaged adjustments for DJF, JJA and annual mean are displayed in Fig.A.3d, A.3e and A.3f, respectively. However, it must be mentioned that the adjustment on SSS is not so important as that on SST because SSS is not a direct forcing factor for either the atmospheric submodel or the ocean submodel in the coupled system. The SSS errors do have some effects on the calculation of the coupled model salinity forcing or rather the salt/freshwater flux, but with the employment of the freshwater flux adjustment, such effects are very small and have no appreciable impact on the coupled model performance. In fact, the SSS adjustment is not really necessary for our coupled model runs.

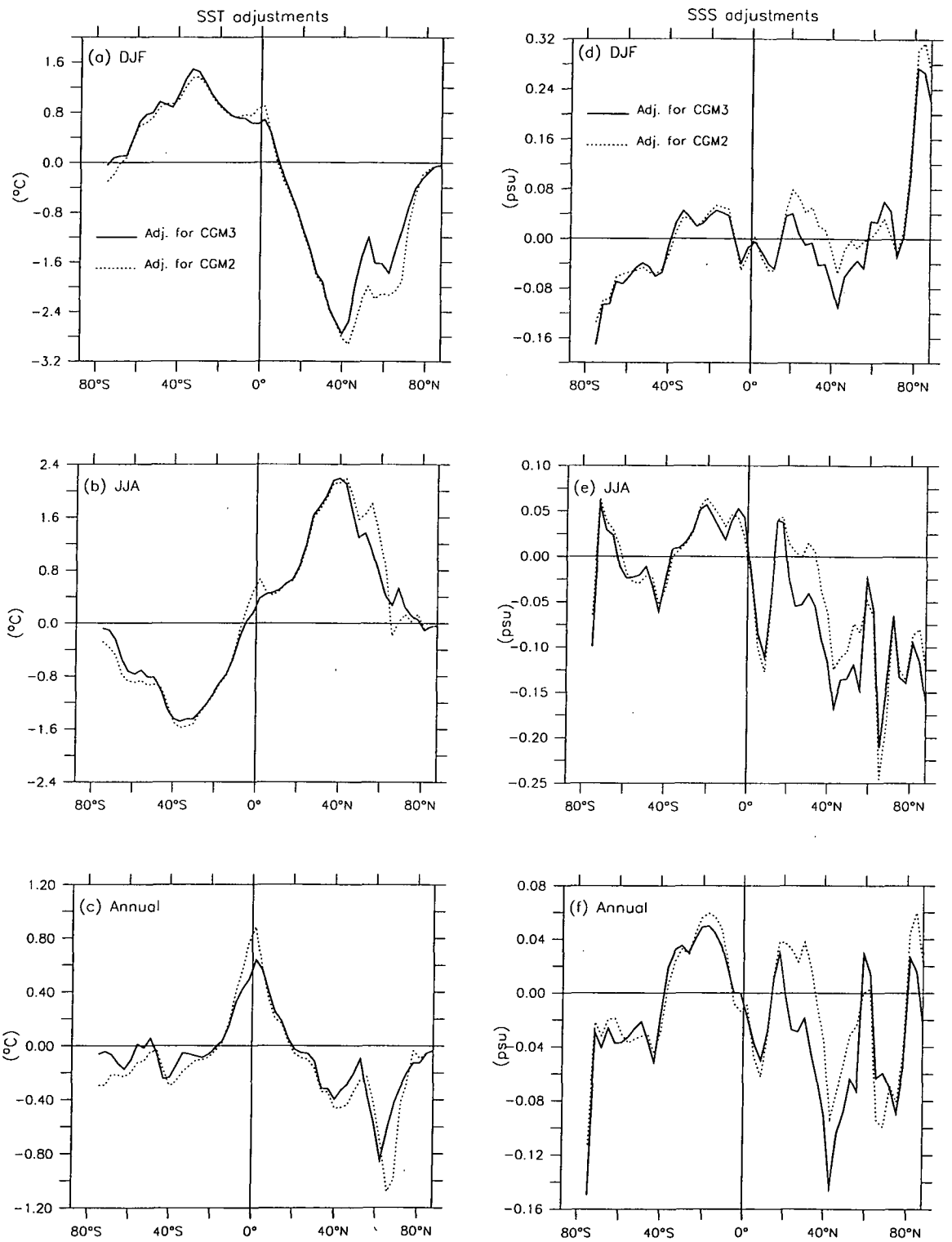

Figure A.3: Zonal mean SST (left) and SSS (right) adjustments for control runs CGM3 and CGM2

Appendix B

Remarks on Salinity Change

B.1 Salinity Changes in the Coupled Runs

In both the ATGM3 and ATGM2 integrations, the global ocean suffers a significant decrease in salinity at all levels. This gives rise to questions as to whether or not such a change is caused by the acceleration scheme itself and if it severely contaminates the real response of the THC to the warming in the ocean interior. Answers to these questions, especially to the second one, concern the validity of our use of the acceleration in the integrations and thus the reliability of the above conclusion about the new quasi-equilibrium of the world ocean under the elevated $3\times CO_2$ condition.

To address these questions, we examine the salinity change in detail and analyse its potential effect on the water column stratification in the Southern Ocean in particular.

Fig.B.1a illustrates the evolution of the globally averaged annual mean salinity anomaly relative to the initial climate for the entire ocean and three sub-layers in the ATGM3 run, including the preceding 600 year transient integration. The ATGM2 run sees generally similar change trends for all sub-layers, particularly for the entire ocean average, and is thus not shown. Salinity changes for the three sub-layers and entire ocean column observed in the normal integration period before

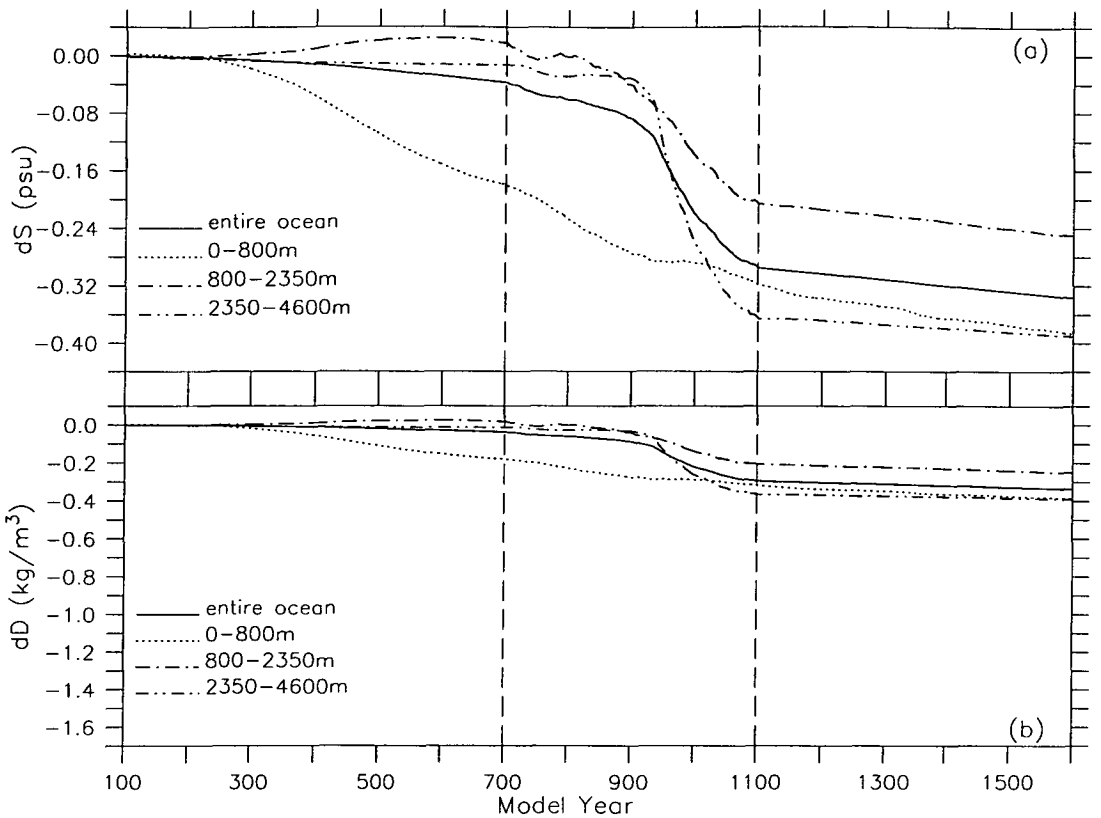

Figure B.1: (a) Changes of global ocean salinity and, (b) the corresponding changes of density (S-dependent only) in ATGM3 for the entire ocean and three sub-layers.

acceleration, the accelerated period which is further divided into two sub-periods, and the following 500 year normal extension are summarized in Table B.1.

Table B.1: Salinity changes (psu) of the ocean interior observed in the ATGM3 integration.

	yr100-700	yr700-900	yr900-1100	yr1100-1600	total
0-800m	-0.1815	-0.0955	-0.0425	-0.0695	-0.3890
800-2350m	0.0192	-0.0587	-0.1657	-0.0431	-0.2483
2350-4600m	-0.0117	-0.0194	-0.3331	-0.0250	-0.3892
whole column	-0.0366	-0.0507	-0.2070	-0.0415	-0.3357

We see that, in the period prior to acceleration, the upper layer is considerably freshened (more than 0.18 psu) while the other layers see very small change in salinity, and the entire ocean is freshened by 0.037 psu. It is noted that the mid-depth layer experiences a slight increase in salinity in this period due mainly to the shutoff of AABWF and shoaling of NADWF, as discussed in Chapter 5. Within

the first half of the accelerated period, salinity is reduced in all layers and the total column sees a freshening of about 0.051 psu. Except for the upper layer, the largest changes of salinity occur in the later period of acceleration, particularly in the deep ocean where the freshening is up to 0.333 psu, leading to a reduction in salinity of 0.207 psu for the entire ocean. Thereafter, a further freshening is still clearly seen during the last 500 year normal mode integration in all layers.

It must be pointed out that the large and lasting freshening in the world ocean is not possibly a natural result of global warming. In fact, it is most likely caused by some kind of model deficiency which breaks the rule of conservation for the volume integral of salinity. Hirst and Godfrey (1993) addressed such a potential problem with the asynchronous mode integration using the Bryan acceleration technique. However, our finding is that, under the CO_2 anomaly forcing, especially in the stabilization period, the volume integral of salinity is not so well conserved as in the control run, even with no acceleration applied. This is clear if we examine the salinity change in the TGM3 run and compare it with the control climate.

In Chapter 5 we have shown that the global ocean salinity in TGM3 suffers a reduction of nearly 0.1 psu by the end of the 1400 year integration (Fig.5.16a). Since our ocean model represents a total oceanic water volume (including inland seas) of about 1280×10^6 km^3 (in contrast to an estimate of 1370×10^6 km^3 for the real world ocean) and an average control salinity of about 34.7 psu, a freshening of 0.1 psu requires a net freshwater input to the ocean of about 3.7×10^6 km^3. As already addressed, for simplicity the CSIRO coupled model currently assumes a constant mass for the terrestrial ice (the Antarctic ice sheet plus ice shelves, as well as the Greenland ice sheet and other small glaciers) during the course of the integration. So the only freshwater source that is available for the oceanic freshening is the sea ice and snow cover. However, our model represents a total water equivalent snow cover over the globe of about 0.0811×10^6 km^3 and a sea ice volume of 0.0245×10^6 km^3 for the annual mean control climate, which together, when completely melted and incorporated into the ocean, can cause a maximum freshening for the entire ocean of only 0.00267 psu, provided we do not also take into account the increase of

water content in the significantly warmed atmosphere and changes of water content held in soil etc.). Therefore, the unrealistically large salinity reduction seen in the TGM3 run can only be taken as a spurious trend of the salinity field. It is noted that the control run CGM3 also sees a decrease in the entire ocean salinity, due mainly to the accumulated effect of a very small imbalance of the surface hydrological cycle, but the change is only 0.011 psu (Fig.4.11b) for the 800-year integration, far less than the change of 0.045 psu seen in TGM3 by year 800 (Fig.5.16a). We also note that, the trend of salinity decrease becomes more and more evident in the CO_2 stabilization period. The case for TGM2 is similar. The reason that the model ocean suffers much larger salinity reduction in transient experiment than the control run remains to be explained.

In the accelerated phase, due to the different time scales in the ocean, mixing between the upper and lower ocean can prolong an anomalous transient forcing from the upper ocean into a long-lived response in the lower ocean. In other words, trends of tracer changes in the upper ocean, i.e., warming due to the net radiative energy gain and freshening due to some kind of spurious freshwater source, are transfered into the deep ocean and prolonged there. This causes a speed-up of the warming and an enlargement of the freshening in the deep ocean. After the energy balance over the global ocean surface is finally achieved through various feedback processes, the thermal adjustment in the ocean interior can be completed very quickly, and thereafter the temperature field changes little under a 'thermal' equilibrium because there is (generally) no anomalous transient thermal forcing transferring between different levels. In this situation, acceleration does not modify the temperature fields any further. For the salinity field, however, there is no efficient feedbacks at the ocean surface to constrain the evolution of the spurious freshening. As a result, the anomalous transient (freshening) forcing keeps acting on the deep ocean, leading to more and more reduction of salinity there, and the ocean seems to never reach an equilibrium in terms of the salinity distribution. We see that, after switching off the acceleration, the freshening is still evident in the normal mode integration. Therefore, the acceleration technique itself may not be responsible for the spurious

change in the world ocean salinity.

However, we do note the dramatic decline of salinity in the ocean interior during the later period of acceleration (in fact, from around year 920 to year 1100). This is obviously associated with the resumption of the Southern Ocean overturning. Before the re-operation of the AABWF, the upper layer freshening signal is transported into the deep ocean by slow diffusive mixing and we see relatively little change of salinity there in spite of the effect of acceleration. When the AABWF and deep convection come into operation again around Antarctica, the largely freshened high latitude Southern Ocean surface water is 'suddenly' flushed into the deep ocean off Antarctica and is then transported northward into other basins by the reactivated deep overturning cell, thereby resulting in large decrease of salinity in the deep ocean and thus the whole water mass of the global ocean.

B.2 Impact on the Density Structure

As mentioned above, the drift of salinity in the ocean interior is not significant before the recovery of the AABWF. Moreover, the freshening in the upper layer is larger than that in the deep ocean, which acts to strengthen the water column stratification. This seems to ensure that the only factor responsible for destabilizing the water column and thus triggering off the re-commencement of Southern Ocean overturning is the warming in the ocean interior. Fig.B.1b shows the evolution of the global ocean density changes ($d\sigma_t$) induced by only the salinity changes for the three sub-layers and the entire ocean in the ATGM3 run. For convenience of comparison, the vertical scale in this plot is the same as that in Fig.6.11a which shows the total changes of density. We see that, before the AABWF is fully resumed (around year 935), the salinity induced density change is very small, actually negligible compared to that induced by the temperature change, especially from the subsurface to deep ocean levels. Even after the resumption, the contribution of salinity change still accounts for a minor portion of the total changes in terms of the global mean.

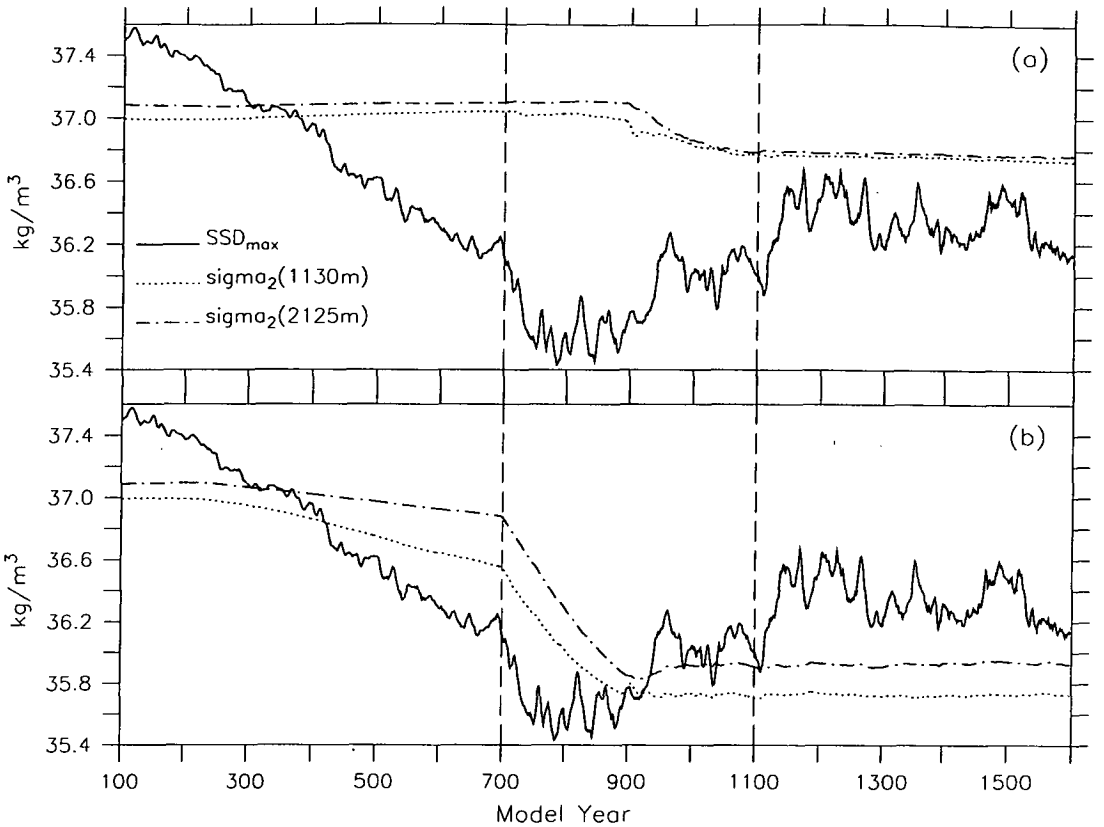

Figure B.2: Density changes due to: (a) salinity changes alone, and (b) temperature changes alone, in the Ross/Bellingshausen Seas (60°Ssouthward).

To further verify the above conclusion, it is necessary to examine the salinity change in the Southern Ocean, especially its effect in establishing the environment in which the AABWF may operate, as discussed in Chapter 6. For this purpose, we present Fig.B.2 to show time series of the winter peak SSD and densities at two deep levels in the the Ross/Bellingshausen Seas (60°S southward), in the context similar to that for Fig.6.15. Note that the deep level densities shown in Fig.B.2a and Fig.B.2b are salinity dependent ($\sigma_S = \sigma_2(S, T_0)$) and temperature-dependent ($\sigma_T = \sigma_2(S_0, T)$), respectively, whilst the winter peak SSD is determined by both the temperature and salinity. Fig.B.2a immediately discounts the possibility that the deep ocean freshening brings back the overturning, because the salinity induced density changes at the deeper levels are too small to permit an excess of the winter peak SSD over the underlying ambient densities. It is the temperature induced reduction in deep ocean densities that causes the re-operation of deep convection off Antarctica and thus the return of the AABWF, namely, the deep ocean warming alone can result

in the resumption of Southern Ocean Overturning, as clearly seen in Fig.B.2b.

Nevertheless, the spurious large reduction of salinity in the ocean interior does help further destabilize the water column off Antarctica after the resumption of AABWF. This seems to be partially responsible for the further intensification and large fluctuations of the AABWF after its resumption, and thus to some extent contaminates the final equilibrium solution, especially the variability. We note that it is necessary for us to eliminate the spurious effect of salinity changes by designing and conducting the accelerated integration more carefully. One of the practical approaches is to switch off the acceleration just before the resumption of AABWF and henceforth continue the run in normal mode like the last 500 years of the ATGM3 integration such that the deep ocean flushing can be avoided.

An additional experiment based on the above considerations is underway. This integration is started from year 920 (of the ATGM3 run), which is before the AABWF resumes in the accelerated run, then is continued running from there with the acceleration turned off. The evolution of the world ocean THC during the next 515 years (i.e., from year 921 to year 1435) of this additional run (ATGM3add) is shown in Fig.B.3 by the dot-dashed curves, together with the corresponding THC time series for the ATGM3 run. It is evident that the switchoff of the acceleration does not hinder the resumption of the AABWF and thus the return of the deep ocean ventilation, although the THC varies differently in this normal mode integration. However, we see that all the major indicators of the world ocean THC in this additional run appear to gradually approach their counterparts in the 'final' (normal mode) solution of the ATGM3 run, which generally validates the ATGM3 results discussed in Chapter 6. We note that this run may need a much longer time for the ocean to adjust and evolve into a final equilibrium.

What happens to the salinity field during the course of this 'normal mode' run? Fig.B.4b shows the evolution of the global ocean salinity during the period prior to year 920 of ATGM3, followed by that for the 515 years of this normal mode run. Clearly, as expected, the deep ocean rapid freshening occuring in ATGM3

(following the AABWF resumption, see Fig.B.1a) does not occur in this new run. In this circumstance, the reduction in deep ocean density due to freshening (shown in Fig.B.4d) is much smaller than that for the later period of ATGM3, i.e., after year 920 (Fig.B.1b), and therefore the fluctuations of AABWF (after its resumption) in ATGM3 is largely reduced in this normal mode integration. Further, this also confirms our conclusion that the resumption of the AABWF is attributable to the warming in the ocean interior rather than the spurious freshening in the deep ocean. It should be mentioned that, because the thermal adjustment in the ocean interior is nearly completed before year 920, switching off the acceleration has little impact on the world ocean temperature field, as indicated by Fig.B.4a and Fig.6.9a. However, Fig.B.1b shows that, with no acceleration, the globally averaged salinity still suffers noticeable decrease in the deep ocean in particular, which is consistent with the salinity decrease occuring in the normal mode period of ATGM3 shown in Fig.B.1a. This discounts the possibility that the implied thermal expansion of the water column under global warming forcing may contribute to the salinity decrease, because the global ocean temperature changes little after year 920 for both the ATGM3 run and this additional integration.

To eliminate the spurious decrease in the global ocean salinity, modification to the model configuration may be necessary for the relevant future work. For example, during the course of the integration, the surface freshwater flux over the global ocean may be examined regularly and the imbalance removed, or, alternatively, a kind of weak restoration may need be employed over the whole ocean interior for ensuring the salinity closure, both based on the current assumption of a constant terrestrial ice mass. However, these approaches raise the difficulties of choosing the most appropriate way for models to represent the real response of the world ocean to global warming. Finally, the expected changes in the climate system such as the large ice sheets, which are not considered here, would need to be taken into account in a more comprehensive balance constraint for the salinity in the global ocean.

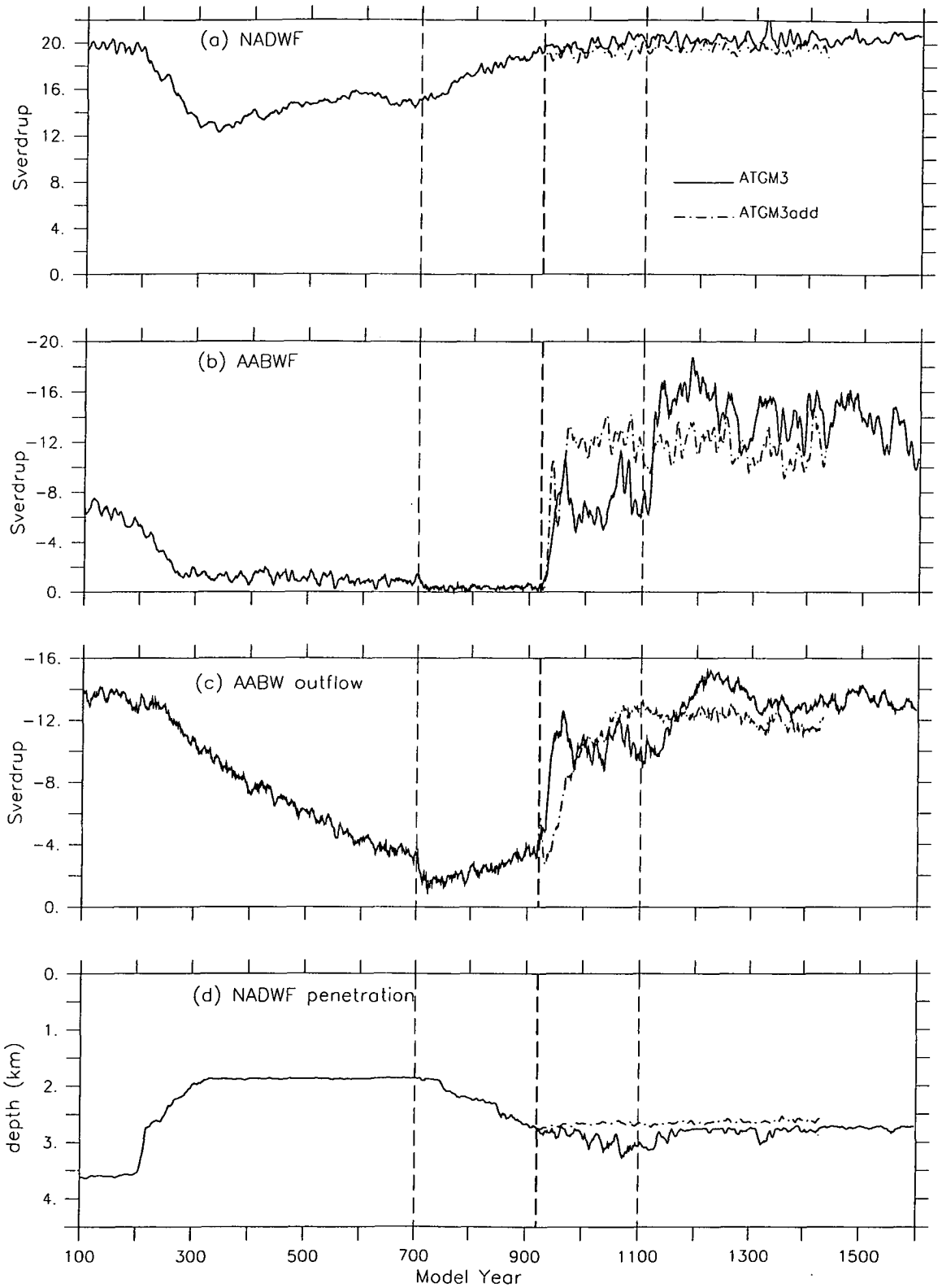

Figure B.3: Time series of the global ocean THC in ATGM3 and an additional run (ATGM3add): (a) NADWF (44.6°N, 800 m), (b) AABWF (66.9°S, 1540 m), (c) outflow of AABF (35°S, 3250 m), and (d) penetration depth of the NABWF (40 - 60°N).

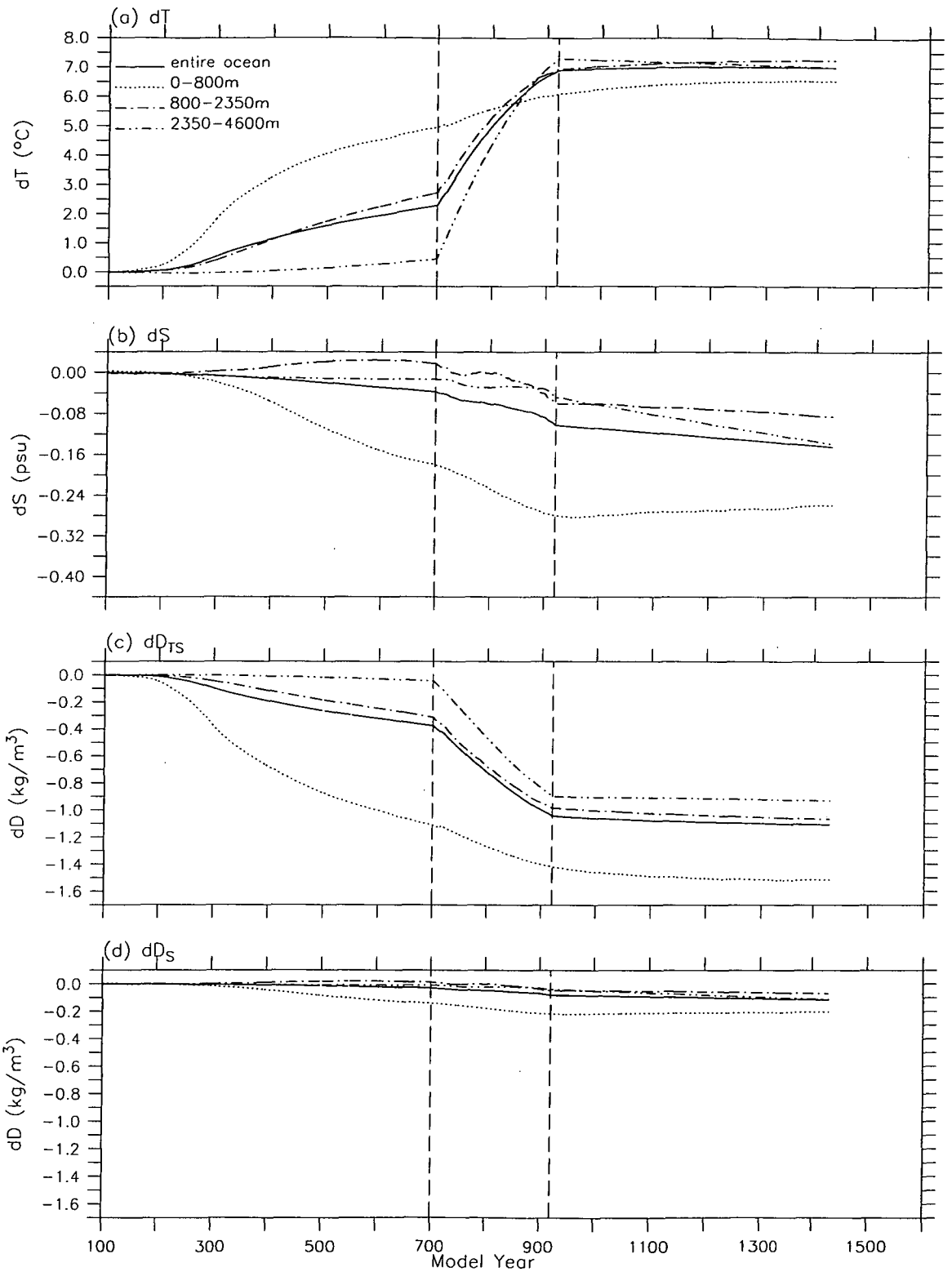

Figure B.4: Time series of global ocean temperature, salinity and density changes in ATGM3add: (a) temperature change, (b) salinity change, (c) density change (joint effect of T and S changes), and (d) density change induced by S change alone.

References

Barnier, B., L. Siefridt and P. Marchesiello, 1995: Surface thermal boundary condition for a global ocean circulation model from a three-year climatology of ECMWF analyses. *J. Mar. Res.*, **6**, 363-380.

Bigg, G.R., 1996: *The Oceans and Climate.* Cambridge University Press, pp 266.

Böning, C.W., W.R. Holland, F.O. Bryan, G. Ganabasoglu, and J.C. McWilliams, 1995: An overlooked problem in model simulations of the thermohaline circulation and heat heat transport in the Atlantic Ocean, *J. Climate*, **8**, 515-523.

Böning, C.W., F.O. Bryan, W.R. Holland, and R. Döscher, 1996: Deep-water formation and meridional ocerturning in a high-resolution model of North Atlantic. *J. Phys. Oceanogr.*, **26**, 1142-1164.

Boville, B.A., and P.R. Gent, 1998: The NCAR Climate System Model, Version One. *J. Climate*, **11**, 1115-1130.

Boyle, E.A. and Keigwin, L.D., 1987: North Atlantic thermohaline circulation during the past 20,000 years linked to high-latitude surface temperature. *Nature*, **330**, 35-40.

Broecker, W.S., D. Peteet, and D. Rind, 1985: Does the ocean-atmosphere system have more than one stable mode of operation? *Nature*, **315**, 21-25.

Broecker, W.S., 1987: The biggest chill. *Natural History Magazine*, October, 74-82.

Broecker, W.S., 1991: The great conveyor belt. *Oceanography*, **4**, 79-89.

Bryan, F., 1986: High latitude salinity effects and interhemispheric thermohaline circulations. *Nature*, **323**, 301-304.

Bryan, F.O., 1998: Climate drift in a multi-century integration of the NCAR climate System Model. *J. Climate*, **11**, 1455-1471.

Bryan, K., 1969: A numerical method for the study of the circulation of the world ocean. *J. Comput. Phys.*, **4**, 347-376.

Bryan, K., F.G. Komro, S. Manabe, and M.J. Spelman, 1982: Transient climate response to increasing atmospheric carbon dioxide. *Science*, **18**, 851-867.

Bryan, K., 1984: Accelerating the convergence to equilibrium of ocean-climate models. *J. Phys. Oceanogr.*, **14**, 666-673.

Bryan K. and L.J. Lewis, 1979: A water mass model of the world ocean. *J. Geophys. Res.*, **84**, 347-376.

Bryan K. and M.J. Spelman, 1985: The ocean's response to a carbon dioxide-induced warming. *J. Geophys. Res.*, **90**, 11679-11688.

Bryan, K., S. Manabe, and R.C. Pacanowski, 1975: A global ocean-atmosphere climate model. Part II. The ocean circulation. *J. Phys. Oceanogr.*, **5**, 30-46.

Bryan, K., S. Manabe, and M.J., Spelman, 1988: Interhemispheric asymmetry in the transient response of a coupled ocean-atmopshere model to a CO_2 forcing. *J. Phys. Oceanogr.*, **18**, 851-867.

Cai, W.J., 1995: Interdecadal variability driven by mismatch between surface flux forcing and oceanic freshwater/heat transport. *J. Phys. Oceanogr.*, **25**, 2643-2666.

Cai, W.J., 1996a: Surface thermohaline forcing conditions and the response of the present-day global ocean climate to global warming. *J. Geophys. Res.*, **101**, 1079-1093.

Cai, W.J., 1996b, The Stability of NADWF under mixed boundary conditions with an improved diagnosed freshwater flux. *J. Phys. Oceanogr.*, **26**, 1081-1087.

Cai, W.J., and P.C. Chu, 1996: Ocean climate drift and interdecadal Oscillation due to a change in thermal damping. *J. Climate*, **9**, 2822-2833.

Cai, W.J., and P.G. Baines, 1996: Interactions between thermohaline- and wind-driven circulations and their relevance to the dynamics of the Antarctic Circumpolar Current, In a coarse-resolution global ocean general circulation model. *J. Geophys. Res.*, **101**, 14073-14093.

Cai, W.J., J. Syktus, H.B. Gordon, and S. O'Farrell, 1997: Response of a global coupled ocean-atmopshere-sea ice climate model to an imposed North Atlantic high-latitude freshening. *J. Climate*, **10**, 929-948.

Cai, W.J., and H.B. Gordon, 1999:, Southern high-latitude ocean climate drift in a coupled model. *J. Climate*, **12**, 132-146.

Carmack, E.C., 1986: Circulation and mixing in ice covered waters. In: *The Geophysics of Sea Ice.*, N. Untersteiner (ed.), 641-712, Plenum, New York, New York.

Clarke, R.A., J.H. Swift, J.L. Reid, and K.P. Koltermann, 1990: The formation of Greenland Sea deep water: Double diffusion of deep convection? *Deep-Sea Res.*, **37**, 1385-1424.

Cubasch, U.K., K. Hasselmann, H. Hock, E. Maier-Reimer, U. Mikolajewicz, A. Stossel, and R. Voss, 1992: Time-dependent greenhouse warming computations with a coupled ocean-atmosphere model. *Climate Dyn.*, 8, 55-69.

Cox, M.D., 1984: A primitive equation three dimensional model of the ocean. GFDL Ocean Group Tech. Rep. No.1, GFDL/NOAA, Princeton University, Princeton, 250 pp.

Cox, M.D., 1987: Isopycnal diffusion in a z-coordinate ocean model. *Ocean Modelling*, **74**, 1-5.

Cummins, P.F., G. Holloway, and A.E. Gargett, 1990: Sensitivity of the GFDL ocean model to a parameterization of vertical diffusion. *J. Phys. Oceanogr.*, **20**, 817-830.

Curry, J.C., and P.J. Webster, 1992: *Thermodynamics of Atmospheres and Oceans.* Academic Press., 408 pp.

Danabasoglu, G., 1998: On the wind-driven circulation of the uncoupled and coupled NCAR Climate System ocean model. *J. Climate*, **11**, 1442-1454.

Danabasoglu, G., and J.C. Williams, 1995: Sensitivity of the global ocean circulation to parameterizations of mesoscale tracer transports. *J. Climate*, **8**, 2967-2987.

Danabasoglu, G., J.C. Williams, and P.R. Gent, 1994: The role of mesoscale tracer transports in the global ocean circulation. *Science*, **264**, 1123-1126.

Dickson, R.R., J. Meincke, S.A. Malmberg, and A.L. Lee. 1988: "Great Salinity Anomaly" in the northern North Atlantic, 1968-82. *Progress in Oceanography*, Vol. 20, Pergamon Press, 103-151.

Doney, S.C., W.G., Large, and F.O. Bryan, 1998: Surface ocean fluxes and water-mass transformation rates in the coupled NCAR Climate System Model, *J. Climate*, **11**, 1420-1441.

Döös, K., and D. J. Webb, 1994: The Deacon Cell and the other meridional cells of the Southern Ocean. *J. Phys. Oceanogr.*, **24**, 429-442.

Duffy, P.B., D. Eliason, A.J. Bourgeois, and C. Covey, 1995: Simulation of bomb radiocarbon in two ocean general circulation models. *J. Geophys. Res.*, **100**, 22545-22565.

Duplessy, J.-C., N.J. Shackleton, R.G. Fairbanks, L. Labeyrie, O. Oppo, and N. Kallel, 1988: Deep water source variation during the last climate cycle and their impact on the global deep water circulation. *Paleoceanography*, **3**, 343-360.

Egger, J., 1995: Flux correction: Tests with a simple ocean-atmosphere model, *Climate Dyn.*, **13**, 285-292.

England, M. H. and A. C. Hirst, 1997: Chlorofluorocarbon uptake in a world ocean model. 2. Sensitivity to surface thermohaline forcing and subsurface mixing parameterization. *J. Geophys. Res.*, **102**, 15,709-15,731.

England, M.H., 1995: Using chlorofluorocarbons to assess ocean climate models. *Geophys. Res. Lett.*, **22**, 3051-3054.

England, M.H., 1993: Representing the global-scale water masses in ocean general circulation models. *J. Phys. Oceanogr.*, **23**, 1523-1552.

Fieux, M., C. Andrie, P. Delecluse, A.G. Ilahude, A. Kartavtseff, F. Mantisi, R. Molcard, and J.C. Swallow, 1994: Measurements within the Pacific-Indian Oceans throughflow region. *Deep-Sea Res.*, **41**, 1091-1130.

Flato, G.M., and W.D. Hibler, 1990: On a simple sea-ice dynamics model for climate studies. *Ann. Glaciol*, **14**, 72-77.

Gargett, A.E., 1984: Vertical eddy diffusivity in the ocean interior. *J. Mar. Res.*, **42**, 359-393.

Gates, W.L., and A.B. Nelson, 1975: A new (revised) tabulation of the Scripps topography on a 1^o global grid. Part I: Terrain heights. Tech. Rep. R-1276-1-ARPA, The Rand Corporation, 132 pp.

Gent, P.R., F.O. Bryan, G.Danabasoglu, S.c. Doney, W.R. Holland, W.G. Large, and J.C. McWilliams, 1998: The NCAR Climate System Model global ocean component. *J. Climate*, **11**, 1287-1306.

Gent, P.R., and J.C. McWilliams, 1990: Isopycnal mixing in ocean circulation models. *J. Phys. Oceanogr.*, **22**, 626-651.

Gent, P.R., J. Willebrand, T.J. McDougall, and J.C. McWilliams, 1995: Parameterizing eddy-induced tracer transports in ocean circulation models. *J. Phys. Oceanogr.*, **25**, 463-474.

Gent, P.R., and J.C. McWilliams, 1996: Eliassen-Palm fluxes and the momentum equation in non-eddy-resolving ocean circulation models. *J. Phys. Oceanogr.*, **26**, 2539-2546.

Gent, P.R., W.G. Large, and F.O. Bryan, 2001: What sets the mean transport through Drake Passage? *J. Geophys. Res.*, **106**, 2693-2712.

Gerdes, R., C. Koberle, and J. Willebrand, 1991: The influence of numerical advection schemes on the results of ocean general circulation models. *Climate Dyn.*, **5**, 211-226.

Godfrey, J.S., 1989: A Sverdrup model of the depth-integrated flow for the World Ocean allowing for island circulations. *Geophys. Astrophys. Fluid Dyn.*, **45**, 89-112.

Gordon, C., C. Cooper, C.A. Senior, H. Banks, J.M. Gregory, T.C. Johns, J.F.B. Mitchell, and R.A. Wood, 2000: The simulation of SST, sea ice extents and ocean heat transports in a version of the Hadley Centre coupled model without flux adjustments. *Climate Dyn.*, **16**, 147-168.

Gordon, H.B., and S.P. O'Farrell, 1997: Transient climate chnage in CSIRO coupled model with dynamic sea ice. *Mon. Wea. Rev.*, **125**, 875-907.

Gough, W.A., 1997: Isopycnal mixing and convective adjustment in an ocean general circulation model. *Atmosphere-Ocean*, **35**, 495-511.

Gough, W.A., and W.J. Welch, 1994: Parameter space exploration of an ocean general circulation model using an isopycnal mixing parameterization. *J. Mar. Res.*, **52**, 773-796.

Gregory, J.M., J. Oerlemans, 1998: Simulated future sea-level rise due to glacier melt based on regionally and seasonally resolved temperature changes. *nature*, **391**, 474-476.

Grootes, P.M., M. Stulver, J.W.C. White, S. Johnson, and J. Jouzel, 1993: Comparison of oxygen isotope records from the GISP2 and GRIP Greenland ice

cores. *Nature*, **366**, 552-554.

Han, Y-J., 1984: A numerical world ocean general circulation model. Part II. A baroclinic experiment. *Dyn. Atmos. Oceans*, **8**, 141-172.

Haney, R.L., 1971: Surface thermal boundary condition for ocean circulation models. *J. Phys. Oceanogr.*, **1**, 241-248.

Hellerman, S., and M. Rosenstein, 1983: Normal monthly wind stress over the world ocean with error estimates. *J. Phys. Oceanogr.*, **13**, 1093-1104.

Hirst, A.C., 1999: the Southern Ocean response to global warming in the CSIRO coupled ocean-atmosphere model. *Environmental Modeling and Software: Special issue on Global Change*, 227-241.

Hirst, A. C., and J.S. Godfrey, 1993: The role of Indonesian Throughflow in a global ocean GCM. *J. Phys. Oceanogr.*, **23**, 1057-1086.

Hirst, A. C., D. R. Jackett, and T. J. McDougall, 1996: The meridional overturning cells of a world ocean model in neutral density coordinates. *J. Phys. Oceanogr.*, **26**, 775-791.

Hirst, A.C., H.B. Gordon, and S.P. O'Farrell, 1996: Global warming in a coupled climate model including oceanic eddy-induced advection. *Geophys. Res. Letters*, **23**, 3361-3364.

Hirst, A.C., S.P. O'Farrell, and H.B. Gordon, 2000: Comparison of a coupled ocean-atmosphere model with and without oceanic eddy-induced advection. Part I: Ocean spinup and control integrations. *J. Climate*, **13**, 139-163.

Hirst, A. C., and T. J. McDougall, 1996: Deep water properties and surface buoyancy flux as simulated by a z-coordinate model including eddy-induced advection. *J. Phys. Oceanogr.*, **26**, 1320-1343.

Hirst, A.C., and T.J. McDougall, 1998: Meridional overturning and dianeutral transport in a z-coordinate ocean model including eddy-induced advection. *J. Phys. Oceanogr.*, **28**, 1205-1223.

Hirst, A.C., and W.J. Cai, 1994: Sensitivity of a world ocean GCM to changes in subsurface mixing parameterization. *J. Phys. Oceanogr.*, **24**, 1256-1278.

Huybrechts, P., and J. de Wolde, 1999: The dynamic response of the Greenland and Antarctic ice sheets to multiple-century climate warming, *J. Climate*, **12**, 2169-2188.

Jacobs, S.S., R.G. Fairbanks, and Y. Horibe, 1985: Origin and evolution of water masses near the Antarctic continental margin: Evidence from $H_2^{18}O/H_2^{16}O$ ratios in seawater. *Oceanology of the Antarctic Continental Shelf*, Antarctic Res. Ser., Vol. 43, American Geophysical Union, 59-85.

Johns, T.C., R.E. Carnell, J.F. Crossley, J.M. Gregory, J.F.B. Mitchell, C.A. Senior, S.F.B. Tett, and A.R. Wood, 1997: The second Hadley Center coupled ocen-atmopshere GCM: model description, spinup and validation. *Climate Dyn.*, **13**, 103-134.

Karpuz, Z., and E. Jansen, 1992: A high-resolution diatom record of the last deglaciation from the SE Norwegian Sea: Documentation of rapid climatic changes. *Paleoceanography*, **7**, 499-520.

Kattenberg, A., F. Giorgi, H. Grassl, G.A. Meehl, J.F.B. Mitchell, R.J. Stouffer, T. Tokioka, A.J. Weaver, and T.M.L. Wigley, 1996: Climate models–projections of future climate. *Climate Change 1995: The Science of Climate*, Houghton, J.T. et al. (eds.), Cambridge University Press, 285-357.

Keigwin, L.D., and S.J. Lehman, 1994: Deep circulation change linked to Heinrich event 1 and Younger Dryas in a middepth North Atlantic core. *Paleoceanography*, **9**, 185-194.

Killworth, P.D., 1983: Deep Convection in the World Ocean. *Rev. Geophys. Space Phys.*, **21**, 1-26.

Killworth, P.D., 1987: Topographic instabilities in level model OGCMs. *Ocean Modelling*, **75**, 9-12.

Kowalczyk, E.A., J.R. Garratt, and P.B. Krummel, 1991: A soil-canopy scheme for use in a numerical model of the atmosphere–1D stand-alone model. *CSIRO DAR Res. Tech. Pap.*, No. 23, 56 pp.

Kowalczyk, E.A., J.R. Garratt, and P.B. Krummel, 1994: Implementation of a soil-canopy scheme into the CSIRO GCM–Regional aspects of the model response. *CSIRO DAR Res. Tech. Pap.*, No. 32, 59 pp.

Kraus, E.B., 1990: Diapycnal mixing. *Climate-Ocean Interaction*, M.E. Schlesinger, Ed., Kluwer, 269-293.

Large, W.G., G. Danabasoglu, S.C. Doney, and J.C. Williams, 1997: Sensitivity to surface forcing and boundary layer mixing in a global ocean model: Annual-mean climatology. *J. Phys. Oceanogr.*, **27**, 2418-2447.

Latif, M., E. Roeckner, U. Mikolajewicz, and R. Voss, 2000: Tropical stability of the thermohaline circulation in a greenhouse warming simulation. *J. Climate*, **13**, 1809-1813.

Levitus, S., 1982: *Climatological Atlas of the World Ocean.* National Oceanic and Atmospheric Adminstration, 173 pp.

Levitus, S., and T.P. Boyer, 1994: *Temperature.* Vol.4, *World Ocean Atlas 1994*, National Oceanic and Atmospheric Adminstration, 117 pp.

Levitus, S., R. Burgett, and T.P. Boyer, 1994: *Salinity.* Vol.3, *World Ocean Atlas 1994*, National Oceanic and Atmospheric Adminstration, 99 pp.

Macdonald, A.M., and C. Wunsch, 1996: An estimate of global ocean circulation and heat fluxes. *Nature*, **382**, 436-439.

Manabe, S., and R.J. Stouffer, 1993: Century-scale effects of increased atmospheric CO_2 on the ocean-atmosphere system. *Nature*, **364**, 215-218.

Manabe, S., and R.J. Stouffer, 1994: Multiple-century response of a coupled ocean-atmosphere model to an increase of atmospheric carbon dioxide. *J. Climate*, **4**, 5-23.

Manabe, S., K. Bryan, and M.J. Spelman, 1990: Transient response of a global ocean-atmosphere model to a doubling of atmospheric carbon dioxide. *J. Phys. Oceanogr.*, **20**, 722-749.

Manabe, S., R.J. Stouffer, M.J. Spelman, and K. Bryan, 1991: Transient response of a coupled ocean-atmosphere model to gradual changes of atmospheric CO_2. Part I: Annual mean response. *J. Climate*, **4**, 785-818.

Manabe, S., and R.J. Stouffer, 1995: Simulation of abrupt climate change induced by freshwater input to the North Atlantic Ocean. *Nature*, **378**, 165-167.

Manabe, S., and F.J. Stouffer, 1996: Low-frequency variability of surface air temperature in a 1000-year integration of a coupled atmosphere-ocean-land surface model. *J. Climate*, **9**, 376-393.

Manabe, S., and R.J. Stouffer, 1999: The role of thermohaline circulation in climate. *Tellus*, **51**A, 91-109.

Manabe, S., R. J. Stouffer, M. J. Spelman, and K. Bryan, 1991: Transient responses of a coupled ocean-atmosphere model to gradual changes of atmospheric carbon dioxide. Part I: Annual mean response. *J. Climate*, **4**, 785-818.

Marotzke, J., 1989: Instability and multiple steady states of the thermohaline circulation. *Oceanic Circulation Models: Combining Data and Dynamics*, D.L.T. Anderson and J. Willebrand (eds.), NATO ASI Series, Kluwer, 501-511.

Marotzke, J., 1991: Influence of convective adjustment on the stability of the thermohaline circulation. *J. Phys. Oceanogr.*, **21**, 903-907.

Marshall J. et al. (The Lab Sea Group), 1998: The Labrador Sea deep convection experiment. *Bull. Amer. Meteor. Soc.*, **79**, 2033-2058.

McDougall, T.J., 1987: Neutral surfaces. *J. Phys. Oceanogr.*, **17**, 1950-1964.

McDougall, T.J., and J.A. Church, 1986: Pitfalls with the numerical representation of isopycnal and diapycnal mixing. *J. Phys. Oceanogr.*, **16**, 196-199.

McGregor J.L., H.B. Gordon, I.G. Watterson, M.R. Dix, and L.D. Rotstayn, 1993: The CSIRO 9-level atmospheric general circulation model. *CSIRO DAR Techn. Pap.*, No. 26, 89 pp.

McIntosh, P.C., and T.J. McDougall, 1996: Isopycnal averaging and the residual mean circulation. *J. Phys. Oceanogr.*, **26**, 1655-1660.

Mikolajewicz, U. and R. Voss, 2000: The role of the individual air-sea flux components in CO_2-induced changes of the ocean's circulation and climate. *Climate Dyn.*, **16**, 627-642.

Moore, A.M., and H.B. Gordon, 1994: An investigation of climate drift in a coupled atmosphere-ocean-sea ice model. *Climate Dyn.*, **10**, 81-95.

Moore, A.M., and C.J.C. Reason, 1993: The response of a global OGCM to climatological surface boundary conditions for temperature and salinity. *J. Phys. Oceanogr.*, **23**, 300-328.

Moum, J.N., and T.R. Osborn, 1986: Mixing in the main thermocline. *J. Phys. Oceanogr.*, **16**, 1250-1259.

Murphy, J.M., and J.F.B. Mitchell, 1995: Transient response of the Hadley Centre coupled ocean-atmosphere model to increasing carbon dioxide. Part II: Spatial and temporal structure of response. *J. Climate*, **8**, 57-80.

Nakamura, M., P.H. Stone, and J. Marotzke, 1994: Destabilization of the thermohaline circulation by atmospheric eddy transports. *J. Climate*, **7**, 1870-1882.

Nicholls, N., G.V. Gruza, J. Jouzel, T.R. Karl, L.A. Ogallo, and D.E. Parker, 1996: Observed climate variability and Change. *Climate Change 1995: The Science of Climate Change*, J.T. et al. (eds.), Cambridge University Press, 133-192.

Oberhuber, J.M., 1988: An atlas based on the 'COADS' data set: The budget of heat, buoyancy and turbulent kinetic energy at the surface of the global ocean. Max-Plank-Institute für Meteorology Rep. 15, 20 pp.

Oberhuber, J.M., 1993a: Simulation of the Atlantic circulation with a coupled sea ice-mixed layer-isopycnal general circulation model. Part I: Model description. *J. Phys. Oceanogr.*, **23**, 808-829.

Oberhuber, J.M., 1993b: Simulation of the Atlantic circulation with a coupled sea ice-mixed layer-isopycnal general circulation model. Part II: Model experiment. *J. Phys. Oceanogr.*, **23**, 830-860.

Olbers, D., V. Gouretzki, G. Seiβ, and J. Schroeter, 1992: *The hydrographic atlas of the Southern Ocean*, Alfred-Wegener-Inst. for Polar and Mar. Res., Bremerhaven, Germany.

Olbers, D., 1998: Comments on "On the obscurantist physics of form drag in theorizing about the Circumpolar Current". *J. Phys. Oceanogr.*, **28**, 1647-1654.

O'Farrell, S.P., 1998: Sensitivity study of a dynamical sea ice model: The effect of the external stresses and land boundary conditions on ice thickness distribution. *J. Geophys. Res.*, **103**, 15751-15782.

O'Farrell, S.P., J.L. McGregor, L.D. Rotstayn, W.F. Budd, C. Zweck, and R. Warner, 1997: Impact of transient increases in atmospheric CO_2 on the accumulation and mass balance of the Antarctic ice sheet. *Ann. Glaciol*, **25**, 137-144.

Peterson, R.G., and L. Stramma, 1991: Upper-level circulation in the South Atlantic Ocean. *Progress in Oceanography*, Vol. 26, Pergamon Press, 1-73.

Power, S.B., A.M. Moore, D.A. Post, N.R. Smith, and R. Kleeman, 1994: Stability of North Atlantic deep water formation in a global general circulation model. *J. Phys. Oceanogr.*, **24**, 904-916.

Qiu, B., and T.M. Joyce, 1992: Interannual variability in the mid and low-latitude western North Pacific. *J. Phys. Oceanogr.*, **22**, 1062-1079.

Rahmstorf, S., 1996: On the freshwater forcing and transport of the Atlantic thermohaline circulation. *Climate Dyn.*, **12**, 799-811.

Rahmstorf, S., and J. Willebrand, 1995: The role of temperature feedback in stabilizing the thermohaline circulation. *J. Phys. Oceanogr.*, **25**, 778-805.

Redi, M.H., 1982: Oceanic isopycnal mixing by coordinate rotation. *J. Phys. Oceanogr.*, **12**, 1154-1158.

Robitaille, D.Y., and A.J. Weaver, 1995: Validation of subgrid-scale mixing schemes using CFCs in a global ocean model. *J. Geophys. Lett.*, **22**, 2917-2920.

Roemmich, D., and C. Wunsch, 1985: Two transatlantic sections: Meridional circulation and heat flux in the subtropical North Atlantic ocean. *Deep-Sea Res.*, **32**, 619-664.

Warner, R., and W.F. Budd, 1998: Modeling the long-term response of the Antarctic ice sheet to global warming. *Ann. Glaciol*, **27**, 161-168.

Rosati, A., and K. Miyakoda, 1988: A general circulation model for upper ocean simulation. *J. Phys. Oceanogr.*, **18**, 1601-1626.

Rudels, B., D. Quadfasel, H. Friedrich, and M.-N. Houssais, 1989: Greenland Sea convection in the winter of 1987-1988. *J. Geophys. Res.*, **94**, 3223-3227.

Russell, G.L., and D. Rind, 1999: Response to CO_2 transient increase in the GISS coupled model: regional coolings in a warming climate, *J. Climate*, **12**, 531-939.

Saravanan, R., and J.C. McWilliams, 1995: Multiple equilibria, natural variability, and climate transitions in an idealized ocean-atmosphere model. *J. Climate*, **8**, 2296-2323.

Sarmiento, J.L., and C.L. Quere, 1996: Oceanic carbon dioxide uptake in a model of century-scale global warming. *Science*, **274**, 1346-1350.

Sarmiento J.L., T.M.C. Hughes, 1999: Anthropogenic CO_2 uptake in a warming ocean. *Tellus*, **51B**, 560-561.

Sarnthein, M., K. Winn, S.A. Jung, J.-C., Duplessy, L. Labeyrie, H. Erlenkeuser, and G. Gaussen, 1994: Changes in east Atlantic depp water circulation over the past 30,000 years: Eight time slice reconstruction. *Paleoceanography*, **9**, 209-267.

Sausen R., K. Barthel and K. Hasselmann, 1988: Coupled ocean-atmosphere models with flux correction, *Climate Dyn.*, **2**, 154-163.

Schmittner, A., and T.F. Stocker, 1999: The stability of the thermohaline circulation in global warming experiments. *J. Climate*, **12**, 1117-1133.

Seager, R., Y. Kushnir, and M.A. Cane, 1995: On heat flux boundary conditions for ocean models. *J. Phys. Oceanogr.*, **25**, 3219-3230.

Semtner, A.J., 1976: A model for the thermodynamics growth of sea ice in numerical investigations of climate. *J. Phys. Oceanogr.*, **6**, 379-389.

Shea, D.J., K.E. Trenberth, and R.W. Reynolds, 1990: A global monthly sea surface temperature climatology. NCAR Tech. Note TN-435-STR, 167 pp.

Shine, K.P., R.G. Derwent, D.J. Wuebbles, and J-J. Morcrette, 1990: Radiative forcing of climate. *Climate Change: The IPCC Scientific Assessment*, Houghton, J.T. et al. (eds.), Cambridge University Press, 41-68.

Spelman, M.J., and S. Manabe, 1984: Influence of oceanic heat transport upon the sensitivity of a model climate. *J. Geophys. Res.*, **89**, 571-586.

Stouffer, R.J., S. Manabe, and K. Bryan, 1989: Interhemispheric asymmetry in climate response to a gradual increase of atmospheric CO_2. *Nature*, **342**, 660-662.

Stramma, L., and J,R,E, Lutjeharms, 1997: The flow field of the subtropical gyre of the South Indian Ocean. *J. Geophys. Res.*, **102**, 5513-5530.

Toggweiler, J.R. and B. Samuels, 1995: Effect of sea ice on the salinity of Antarctic Bottom Waters. *J. Phys. Oceanogr.*, **25**, 1980-1997.

Tomczak, M., and J.S. Godfrey, 1994: *Regional Oceanography: An Introduction*, Pergamon Press. 420 pp.

Trenberth, K.E., and A. Solomon, 1994: The global heat balance: Heat transports in atmosphere and ocean. *Climate Dyn.*, **10**, 107-134.

Voss, R., and U. Mikolajewicz, 2001: Long-term climate changes due to increased CO_2 concentration in the coupled atmosphere-ocean general circulation model ECHAM3/LSG. *Climate Dyn.*, **17**, 45-60.

Walsh, J.E, and W.L. Chapman, 1990: Arctic contribution to upper ocean variability in the North Atlantic. J. Climate, **3**, 1725-1743.

Warrick, R.A., C. Le Provost, M.F. Merer, J. Oerlemans, and P.L. Woodworth, 1996: Changes in sea level. *Climate Change 1995: The Science of Climate Change*, J.T. et al. (eds.), Cambridge University Press, 359-405.

Washington, W.M., and G.A. Meehl, 1989: Climate sensitivity due to increased CO_2: Experiments with a coupled atmosphere and ocean general circulation model. *Climate Dyn.*, **4**, 1-38.

Watterson, I.G., M.R., Dix, H.B. Gordon, and J.L. McGregor, 1995: The CSIRO9 AGCM and its equilibrium present and doubled CO_2 climates. *Aus. Meteorol. Mag.*, **44**, 111-125.

Wang, X., P.H. Stone, and J. Marotzke, 1999: Global thermohaline circulation. Part II: sensitivity with interactive atmospheric transports. *J. Climate*, **12**, 83-91.

Weaver, A.J., and E.S. Sarachik, 1990: On the importance of vertical resolution in certain ocean circulation models. *J. Phys. Oceanogr.*, **20**, 600-609.

Weaver, A.J., and T.M.C. Hughes, 1996: On the incompatibility of ocean and atmosphere models and the need for flux adjustments. *Climate Dyn.*, **12**, 141-170.

Weller, R.A., and P.K. Taylor, 1993: Surface conditions and air-sea fluxes. CCCO-JSC Ocean Observing System Development Pabel, Taxas A&M University, College Station, TX, 131 pp.

Whetton, P.H., M.H. England, S.P. O'Farrell, I.G. Watterson and A.B. Pittock, 1996: Global comparison of the regional rainfall results of enhanced greenhouse coupled and mixed layer ocean experiments: Implications for climate change scenario development. *Climate Change*, **33** (4), 497-519.

Whitworth, T., III, 1983: Monitoring the transport of the Antarctic Circumpolar Current at Drake Passage. *J. Phys. Oceanogr.*, **13**, 2045-2057.

Wijffels, S.E., R.W. Schmitt, H.L. Bryden, and A. Stigebrandt, 1992: Transport of freshwater by the oceans. *J. Phys. Oceanogr.*, **22**, 155-162.

Wright, D.G., and T.F. Stocker, 1991: A zonally averaged ocean model for the thermohaline circulation. Part I: Model development and flow dynamics. *J. Phys. Oceanogr.*, **21**, 1713-1724.

Wu, X., I. Simmonds, and W.F. Budd, 1997: Modeling of Antarctic sea ice in a general circulation model. J. Climate, **10**, 593-609.

Wu, X., W.F., Budd, 2001: Antarctic changes during global warming towards equilibrium for different levels of stabilization of greenhouse gases. Sixth conference on polar meteorology and oceanography, May 2001, San Diego, USA. 41-44.

Zwally, H.J., J.C. Comiso, and A.L. Gordon, 1985: Antarctic offshore leads and polynyas and oceanographic effects. *Oceanology of the Antarctic Continental Shelf*, Jocobs, S. (ed), Antarctic Res. Ser., AGU, Vol. 43, 203-226.